Modelling Curvilinear Beamline Effects on Beam- and Spin-Dynamics in the Fermilab Muon $g-2$ Storage Ring

Thesis submitted in accordance with the requirements of the University of Liverpool for the degree of Doctor in Philosophy by

Alexander Thomas Herrod

September, 2019

Supervisors:
Andrzej Wolski
Christopher Edmonds

"I see you've brought a marker. Is there a *fundamental* reason for this?
Does it signify new physics?"

– Robert T. Herrod (December 2018)

Declaration

I confirm that I have read and understood the University's PGR Policy on Plagiarism and Dishonest Use of Data. I have acted honestly, ethically and professionally in conduct leading to assessment for the programme of study. I have not copied material from another source nor committed plagiarism nor fabricated, falsified or embellished data when completing the attached material. I have not colluded with any other student in the preparation and production of this material. If an allegation of suspected academic malpractice is made, I give permission to the University to use source-matching software to ensure that the submitted material is all my own work.

Dedication

Dedicated to my wise parents, who taught me that persistence can solve any problem, regardless of difficulty, to my brother, whose intelligence, humour and (kinetic) energy has always kept me on my toes; and to my fiancée, whose support through all things has been unwavering.

Also dedicated to my late supervisors David Newton and Barry King, both of whom demonstrated the kindness, compassion and enthusiasm that helped inspire and motivate countless undergraduate students, as well as myself.

Acknowledgements

I should like to acknowledge the members of the Fermilab Muon $g-2$ Collaboration for their data, support and friendliness, particularly during my time at Fermilab.

I should particularly like to acknowledge my supervisors, Andrzej Wolski and Christopher Edmonds, for the time and effort which they have expended for my benefit, over the course of these studies.

Alexander Thomas Herrod

Modelling Curvilinear Beamline Effects on Beam- and Spin-Dynamics in the Fermilab Muon $g-2$ Storage Ring

Abstract

A model of the Fermilab Muon $g-2$ Experiment storage ring is developed with the BMAD simulation library for beam- and spin-dynamics studies. Particular focus is given to the electrostatic quadrupoles, the plates of which follow the curvature of the particle design trajectory of the magnetically uniform storage ring. To model these, standard electric multipoles and a novel method based on cylindrical harmonics are investigated and found to accurately match the electric field maps produced for the bulk and fringe regions of the curved quadrupoles respectively, despite these methods being specifically for straight beamlines. The toroidal multipole description is then developed, to include curvature and longitudinal field variations (to model the fringe field regions). Various combinations of the different descriptions (including use of the field maps) are used for the bulk and fringe fields of the quadrupoles, and the toroidal multipoles are found to provide the best agreement with the measured tunes of the storage ring. Two integrators are also developed, based on the method of Wu, Forest and Robin. The first of these describes motion in a uniform magnetic dipole field with arbitrary electric field, and produces results comparable to those of the adaptive-step fourth-order Runge–Kutta integrator implemented in BMAD, suitable for tracking over thousands of turns. The second is a generalisation of the first to arbitrary magnetic vector potentials superimposed on that of the uniform dipole, with arbitrary electric fields, and was also found to agree with the Runge–Kutta integrator. Simulations of antimuon storage for 2000 turns of the storage ring were performed, where losses were studied along with the evolution of beam polarisation. The storage losses, important for reducing the systematic error in the measurement of the muon $g-2$, were found to be largely due to collimator shape. The correlation between momentum and spin precession frequency reflect the effects expected from the electric field correction in the T-BMT equation, on the order of 10^{-6}. Particle injection was also studied, for various injection angles, quadrupole strengths and strengths of injection kick, and in the cases where experimental data was provided, the model was found to be consistent with the experiment.

Contents

Chapter 1

Introduction

1.1 Motivation for Measuring the Muon $g-2$

When performing an experiment, one usually has some expectation of the result. On a more objective level, in physics we have developed models and theories to express these expectations based on previous experience. In particle physics experiments, such experience has been absorbed in to the Standard Model, which is a collection of physical theories and laws which describe (to varying levels of precision) almost all particle interactions (with the current exception of gravity [1]).

A clear route to a better understanding of nature is to observe effects and particles as yet undiscovered, in an unambiguous manner. From these, new patterns in nature may be realised, for which new laws and theories can be derived. Experiments searching for new particles are either investigating those which could be extremely weakly interacting (the "intensity frontier") or extremely massive (the "energy frontier"). However, there are methods to probe our knowledge of the particles that can exist in nature, along with their electromagnetic interactions, without creating or detecting them directly.

Measurement of the gyromagnetic ratio, or "g" factor, of a particle involves subjecting it to a strong magnetic (and/or electric) field and measuring the precession of the spin vector about some axis. The theoretical value for the precession rate may be calculated (for leptons) from the Dirac equation, to which one must apply perturbative Quantum Electrodynamics corrections, caused by all particles that can exist in nature appearing and disappearing in the interaction with the external field. If knowledge of the particles that can exist in nature or their interactions is incomplete, theory and experiment should differ – frequently put: we would have "broken the Standard Model".

For such experiments, leptons are used as they are described by the Dirac

equation, which predicts a gyromagnetic ratio of exactly $g_{\text{lepton}} = 2$ [2]. The perturbative corrections from this are collectively referred to as the "anomalous magnetic moment" a_{lepton}:

$$a_{\text{lepton}} \equiv \frac{g_{\text{lepton}}}{2} - 1. \tag{1.1}$$

The choice of which lepton to use depends on the intended particle mass range for study. For example: the electron is stable and therefore easier than the muon to study, although the effects of heavier particles on its measured anomalous magnetic moment (a_e) as opposed to that of the muon (a_μ) are suppressed by the factor $(m_e/m_\mu)^2$ [3]. This effect continues for the tau lepton, although the lifetime of the tau lepton prohibits it from any precise measurement [4]. Through this reasoning, the conclusion was drawn that a precise measurement of a_μ is an important part of validating our understanding of nature.

Another benefit of using the muon is that it decays in to an electron, preferentially emitted along the spin axis [5]. This provides a simple way to detect the spin orientation of the muon as it decays. Given a high-population bunch of muons with parallel spins, this method can show the "polarisation" (average spin direction) of the bunch over time.

Theoretical calculations of a_μ are on-going [6, 7, 8] in an effort to reduce the uncertainty on the result, which currently stands at [9]:

$$a_\mu^{\text{SM}} = 165918204 \pm 356 \times 10^{-12} \tag{1.2}$$

where the limit in accuracy is combined from those of the calculations of the different Standard Model contributions. The greatest contribution to this uncertainty is from QCD corrections, in particular from the running strong coupling (determined from experiment).

1.2 Previous Measurements of the Muon $g - 2$

The first two experiments to measure the muon anomalous magnetic moment a_μ were performed at CERN [10, 11], with a constant, near-uniform magnetic field, using spatial variation of the field to confine the muons. The first of these experiments initially used a magnet borrowed from the University of Liverpool, within which the muons would perform a helical motion into a detector.

The second of these experiments incorporated a storage ring with a diameter of 5 m, with detectors on the inside of the ring to catch the lower-momentum decay electrons. This design made use of a convenient geometrical

feature: such placement of the detectors results in their measuring the difference between the spin precession frequency ω_s and the cyclotron frequency ω_c. This is shown in Appendix A (from the T-BMT spin precession formula [12]) to be:

$$\omega_a = \omega_s - \omega_c = \frac{-q}{\gamma m}\left(\gamma a_\mu \boldsymbol{B} - \frac{\gamma^2 a_\mu}{\gamma+1}(\boldsymbol{B}\cdot\boldsymbol{\beta})\boldsymbol{\beta} + \left(a_\mu - \frac{1}{\gamma^2-1}\right)\frac{\gamma \boldsymbol{E}}{c}\times\boldsymbol{\beta}\right) \tag{1.3}$$

where q and m are particle charge and mass respectively, and $\boldsymbol{B}$, $\boldsymbol{E}$, γ and $\boldsymbol{\beta}$ are the magnetic and electric fields, Lorentz factor and normalised particle velocity ($\boldsymbol{\beta} = \boldsymbol{v}/c$ where $\boldsymbol{v}$ is particle velocity) respectively.

The third experiment, also at CERN [13], and consequent BNL experiment [14], sought to minimise any variations in the magnetic field by using a single dipole ring magnet. The final term in the brackets in (1.3) was also minimised by choosing the "magic" momentum value of $\gamma_0 = \sqrt{1/a_\mu + 1} = 29.3$, corresponding to $p_0 = 3.1\,\mathrm{GeVc}^{-1}$. Assuming that the beam is also perpendicular to the field, the beam rigidity formula $B\rho = p/q$ (where we use dipole bend radius ρ and particle momentum $p = \gamma m \beta c$) allows us to reduce (1.3) to:

$$\omega_a = \frac{-\beta}{\rho}\gamma c a_\mu. \tag{1.4}$$

Thus one can measure a_μ directly, having minimised the two latter terms in the outermost brackets in (1.3). Clearly, the muon/antimuon bunches used must have a narrow range of momenta to maintain accuracy when dropping the last term in (1.3).

The experimental measurements of a_μ thus far yield the combined result [14, 15]:

$$a_\mu = 16592091(54)(33) \times 10^{-11} \tag{1.5}$$

where the errors are statistical and systematic, respectively. Statistically, this result differs from that of theory by 3.6 standard deviations. Thus, it would serve well to perform an experiment of higher precision to better determine this discrepancy, potentially to greater than the 5 standard deviation difference from theory required to claim a discovery.

1.3 Brief Overview of Twiss Parameters and Beam Dynamics

In the interest of comprehension of the research presented in the following chapters, a basic introduction of beam dynamics and Twiss parameters is presented here.

In beam dynamics models, a "design trajectory" is defined, with respect to which particle motion is described. In the case here, the design trajectory of the storage ring is the circle of radius $\rho = 7.112\,\mathrm{m}$, centred in the middle of the storage ring.

Some of the properties of particle beams along accelerator lines can be described by the (inter-related) Twiss parameters α_i, β_i and γ_i ($i \in x, y$), for each axis (β and γ here not to be confused with v/c and the Lorentz factor, respectively), also referred to as the Courant–Snyder parameters. For the case of "uncoupled" periodic motion (independent motion along the different axes), and with momentum approximately parallel to the longitudinal axis (s), these obey the relations:

$$\alpha_i^2 = \beta_i \gamma_i + 1, \qquad -2\alpha_i = \frac{d\beta_i}{ds}, \qquad i \in x, y. \tag{1.6}$$

Of the Twiss parameters, the β_i function is the most commonly used (and will be the only one discussed in the following chapters), as this is proportional to the square of the size of a (mono-energetic) beam along that axis:

$$\sigma_i^2(s) = \epsilon_i \beta_i(s), \qquad i \in x, y. \tag{1.7}$$

Here, ϵ_i is the beam emittance; a quantity used to describe the beam spread in phase-space for that axis (this is effectively a constant for the studies considered here and so will not be discussed further). The quantity σ_i is, as a function of longitudinal coordinate s, the average spread of the bunch around the design trajectory, defined by:

$$\sigma_i(s) = \sqrt{\langle [x_i(s) - \bar{x}_i(s)]^2 \rangle}, \qquad i \in x, y, \tag{1.8}$$

where $\bar{x}_i$ denotes the average value of coordinate x_i in the bunch.

The beta functions oscillate as the bunch undergoes focusing and defocusing in each axis as it moves along a beamline, and may also be calculated using the transfer map for the position and momentum of a particle with small deviations from the design trajectory and momentum. Assuming uncoupled motion (where the particle moves in each axis independently of motion in the other axes), each axis can be treated separately. For the motion in each axis we can write:

$$\begin{pmatrix} x_i(s) \\ p_i(s) \end{pmatrix} = \mathcal{M}_i \begin{pmatrix} x_i(0) \\ p_i(0) \end{pmatrix}, \qquad i \in x, y, \tag{1.9}$$

where $x_i(0)$ and $p_i(0)$ are the initial position and momentum in each transverse axis. Assuming a periodic lattice, in which the particles undergo peri-

odic motion in the transverse axes, we can write:

$$\mathcal{M}_i = \begin{bmatrix} \cos(\mu_i) + \alpha_i(0)\sin(\mu_i) & \beta_i(0)\sin(\mu_i) \\ -\gamma_i(0)\sin(\mu_i) & \cos(\mu_i) - \alpha_i(0)\sin(\mu_i) \end{bmatrix}, \qquad i \in x, y, \tag{1.10}$$

where μ_i are the oscillation phase advances of the particle, in each transverse axis, over the section of beamline described by the transfer matrices $\mathcal{M}_i$, and the Twiss parameters are taken at the initial position, defined here as $s = 0$.

In a closed ring, particles undergo a set number of these oscillations during each orbit of the ring, referred to as the ring "tunes" ν_i for each axis. If the transfer matrices $\mathcal{M}_i$ are for one orbit of the ring, then we can write the tunes as:

$$\nu_i = \frac{\mu_i}{2\pi}, \qquad i \in x, y. \tag{1.11}$$

Given a closed ring, "resonance" conditions can be met by the tunes, under which the particles perform an integer number of oscillations in an axis (referred to as the resonance order) over an integer number of orbits, and so will have the same oscillation phases at the same points in the ring:

$$L\nu_x = N \qquad \text{for any } L, N \in \mathbb{Z}, \tag{1.12}$$

and

$$M\nu_y = N \qquad \text{for any } M, N \in \mathbb{Z}. \tag{1.13}$$

In the case of an inter-dependency between motion in the transverse axes, caused here by the use of circular collimators, the resonance condition can also depend on the tunes of both axes:

$$L\nu_x + M\nu_y = N \qquad \text{for any } L, M, N \in \mathbb{Z} \tag{1.14}$$

where the resonance order is given as $L+M$ (where L and M are the number of oscillations in x and y, respectively), and N is the number of ring orbits these oscillations are performed over.

Particles undergoing resonance are typically driven by a field (caused by either a misalignment or field nonuniformity) which works to pull particles on a specific resonance from the storage region (increasing their "action" in that axis). By this mechanism, lower-order resonances (with small, integer values of L and/or M) typically encounter greater losses, although some higher-order resonances may cause higher particle loss than some lower-order resonances. By avoiding the most driven resonances, substantial particle loss can be avoided.

The "dispersions" of a beamline η_i relate the momentum of a particle (to first order) to the average position it will occupy on that axis in the beamline

$x_{i,\mathrm{Equil}}$, typically caused by the beam passing through a bend in that axis:

$$x_{i,\mathrm{Equil}}(s) = \eta_i(s)\delta(s), \qquad i \in x, y, \tag{1.15}$$

where $x_{i,\mathrm{Equil}}$ are the average positions of the particles of a given momentum δ on each transverse axis with respect to the design orbit. The quantity δ is the momentum of the particle relative to, and normalised to, the design momentum:

$$\delta = \frac{P - P_0}{P_0} \tag{1.16}$$

where P and P_0 are the total momentum of the particle and of the design particle, respectively (such that $\delta = 0$ corresponds to the design momentum and $\delta = 1$ corresponds to twice the design momentum). Variations of the dispersions along a beamline (for example, in bending magnets), in each axis, give rise to an average transverse momentum $p_{i,\mathrm{Equil}}$ in that axis, for a given δ:

$$p_{x,\mathrm{Equil}}(s) = \eta'_x(s)\delta(s), \qquad i \in x, y, \tag{1.17}$$

where η'_i is the derivative of η_i with respect to longitudinal position s.

We may also define the action J_i and angle $\phi_i(s)$ of a particle for each transverse axis. The action (multiplied by 2π) describes the area enclosed in phase space by the oscillation of a particle in that axis and, similarly to the emittance, is effectively constant in the $g-2$ ring:

$$2J_i = \gamma_i(s)x_i^2(s) + 2\alpha_i(s)x_i(s)p_i(s) + \beta_i(s)p_i^2(s), \qquad i \in x, y. \tag{1.18}$$

The angles ϕ_i are the phases of oscillation of the particle at any given position in s, in each transverse axis, such that:

$$x_i(s) = \sqrt{2\beta_i(s)J_i}\cos(\phi_i(s)), \tag{1.19}$$

$$p_i(s) = -\sqrt{\frac{2J_i}{\beta_i(s)}}\Big(\sin(\phi_i(s)) + \alpha_i(s)\cos(\phi_i(s)\Big), \qquad i \in x, y. \tag{1.20}$$

However, the values for x_i and p_i in (1.18), (1.19) and (1.20) must be corrected to take in to account any non-zero dispersion, using (1.15) and (1.17):

$$x_{i,\mathrm{Correc}}(s) = x_i(s) - x_{i,\mathrm{Equil}}(s), \tag{1.21}$$

$$p_{i,\mathrm{Correc}}(s) = p_i(s) - p_{i,\mathrm{Equil}}(s), \qquad i \in x, y, \tag{1.22}$$

where we now use the values $x_{i,\mathrm{Correc}}$ and $p_{i,\mathrm{Correc}}$ in place of x_i and p_i in (1.18), (1.19) and (1.20).

Due to the entire storage ring being in a uniform, vertical magnetic dipole field, the dispersion in the y-axis, η_y, can be assumed to be zero, so dispersive corrections will be applied to J_x and ϕ_x (by means of correcting x and p_x).

1.4 Design Overview of the Fermilab Muon $g-2$ Experiment (E989)

1.4.1 A Direct Measurement of a_μ by Spin Precession

As with the previous two experiments, summarised in Section 1.2, the method employed by the Fermilab Muon $g-2$ Experiment (also referred to as E989) is to use the difference between the cyclotron and spin precession frequencies as given in (1.3) to measure a_μ directly. The goal is to reach a precision on the measured value of a_μ at least four times greater than that recorded by the previous BNL experiment [16].

Using the same, $\rho = 7.112\,\text{m}$ radius, highly-uniform storage ring magnet as in the BNL experiment, shown in Figure 1.1, the second term in (1.3) is non-zero only if the particle has a component of velocity parallel to the magnetic field. In addition to this, using the magic momentum $\gamma_0 = 29.3$, the last term in (1.3) is also minimised, and only contributes for off-momentum muons in non-zero electric field.

The new experiment currently uses antimuons only, as these decay to positrons, which are easier to detect over the noise of electron showers. However, the experiment design also allows the use of negatively-charged muons [16], requiring only an inversion of the magnetic and electric fields. Typically, using a proton beam it is easier to produce antimuons than muons. However the Fermilab accelerator complex is equipped to also supply antiproton beams and hence has the capability to produce muons.

1.4.2 Antimuon Production at the Fermilab Accelerator Complex

The antimuon beam starts its life as free protons, from hydrogen gas, at the upstream end of the Fermilab linear accelerator. From here, the protons are accelerated to 400 MeV and injected into the Booster, which accelerates the circulating beam to 8 GeV before sending it on to the Recycler Ring (see Figure 1.2). Here, the protons are stored before being syphoned off to the muon/pion-production target.

The target produces 1.2500×10^{-2} protons, 1.172×10^{-3} positive pions and 3×10^{-6} antimuons for each incident proton [17]. These are focused immediately after the target by passing through an electrically pulsed lithium lens [18], which uses a 170 kA pulse of current parallel to the beam to produce a universally focusing magnetic field. This is followed by a sequence of quadrupoles and dipoles, which direct the mixed-particle beam towards the Delivery Ring, as in Figure 1.3.

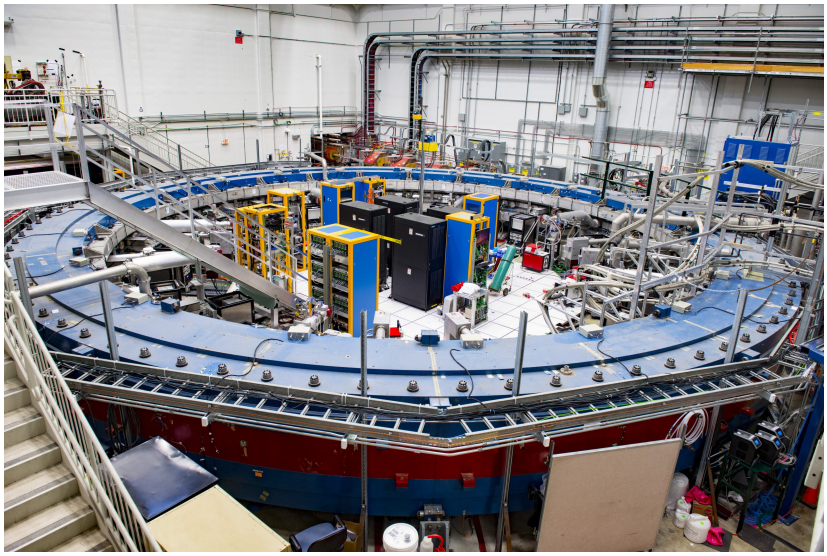

Figure 1.1: The Fermilab Muon $g-2$ Experiment dipole magnet (the blue ring occupying the full width of the image), sitting in the experiment hall at Fermilab. [Reidar Hahn, Fermilab]

The Delivery Ring has two purposes: the first is to separate out the protons from the beam, and the second is to allow the pions to decay to more antimuons for the experiment. To fulfil these tasks, the ensemble circulates four times. On the final turn a kicker magnet extracts the proton bunch, lagging behind due to the higher momentum and increased paths through the bends, to a beam dump [19].

We also make use of the fact that pion weak decay (which produces about 80% of the final antimuon distribution [20]) produces antimuons with spins oriented parallel to the muon velocity in the pion rest frame [2], and so the antimuons of highest longitudinal momentum in the lab frame have spins oriented parallel to the beam. By appropriate use of magnets in the Delivery Ring for particle selection, this enables the production of a beam of antimions with spins largely parallel, collectively referred to as a "highly polarised" beam.

Once the 3.1 GeV antimuons have been extracted from the delivery ring, they are focused and directed to the $g-2$ experiment hall, and pass through a piece of lead which catches positrons from decayed antimuons. Overall, the complex yields 7.7×10^{-7} antimuons arriving at the experiment hall for each incident proton [21].

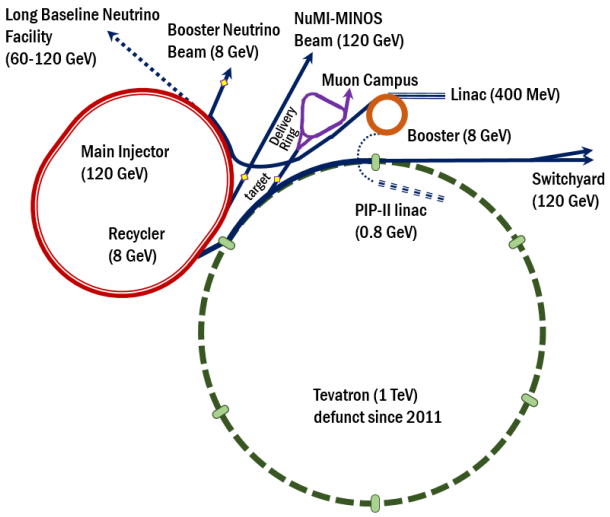

Figure 1.2: The current (at time of writing) Fermilab accelerator complex. A proton bunch is accelerated to 400 MeV down the Linac (top-right, blue) in to the Booster Ring (top, orange), where it is accelerated to 8 GeV before being transferred to the Recycler Ring (left, red) from which it is sent to strike the target in the target hall via part of the Tevatron. The consequent bunch of positive pions traverses the Delivery Ring, decaying in to antimuons, before arriving at the $g-2$ experiment hall. [Vladimir Shiltsev, Fermilab]

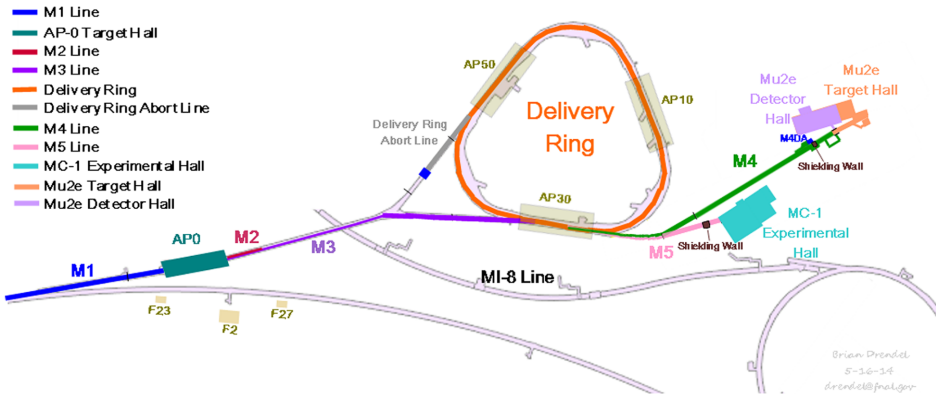

Figure 1.3: Fermilab muon campus, showing the relative locations of the Production Target Hall ("AP0", green, left) where the proton bunch strikes the target to produce positive pions, the Relivery Ring (red, centre) where the pions decay to antimuons and stray protons are removed, and MC-1 experiment hall for the Fermilab Muon $g-2$ Experiment (cyan, right). [Brian Drendel, Fermilab]

1.4.3 Beam Injection and Collimation

The incoming beam of antimuons traverses three quadrupoles known as the "final focus" on entry to the experiment hall, which determine the beam angle, dispersion and Twiss parameters on injection into the experiment ring.

The experiment storage ring incorporates an inflector magnet (see Figure 1.4) to cancel out the magnetic dipole field of the storage ring as the beam approaches the storage region.

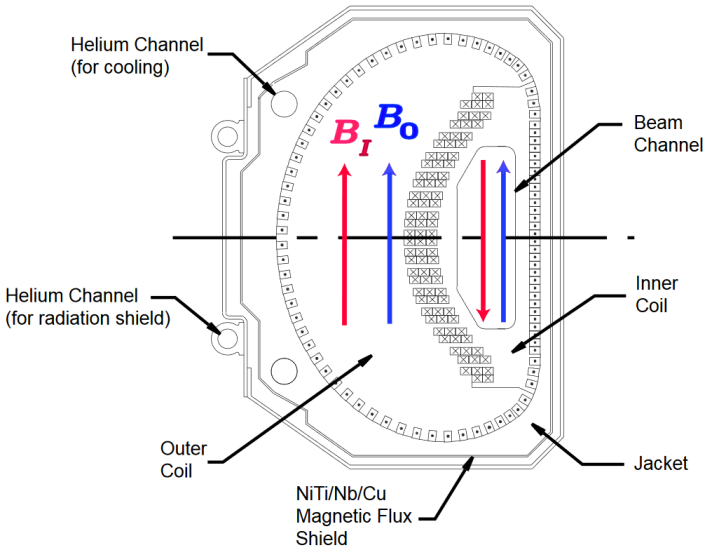

Figure 1.4: Downstream-facing cross-section of the 2.025 m long superconducting inflector magnet, which produces a magnetic field B_I (red) to cancel that of the storage magnet, B_o (blue), in the beam channel (on the right). The beam channel is 56 mm vertical by 18 mm horizontal, and the longitudinal axis is clocked 2.4 mrad radially inward with respect to the ring tangent at the downstream end. At this point, the inflector is 77 mm radially outward from the storage axis of the ring (to the right-hand-side of the inflector as viewed here) – see also Figure 1.5. [16]

Use of the inflector introduces a difficulty for the beam dynamics: the aperture of the inflector, shown in Figure 1.4, is much smaller than the storage region aperture of 90 mm, while the inflector itself is relatively long. As this small aperture requires the antimuon beam (which has a spread in momentum of approximately 1% [22]) to have zero dispersion on injection, not matched to the 8.6 m dispersion of the ring [22] (which would cause particles to undergo large oscillations about their equilibrium orbits, calculable from (1.15)), we expect high injection losses.

As shown in Figure 1.5, pulsed magnetic kickers are used to adjust the beam trajectory on the first turn after injection. As the beam length of $\approx$ 40 m is approximately 5 m less than the circumference of the ring on injection, the kickers are given a 20 ns time window to turn off [16]. Unfortunately, the kickers installed in the experiment do not perform to this specification, and "ring" for approximately 3 µs (the first 20 turns), which may likely result in unpredictable beam dynamics effects, and beam dynamics models requiring the inclusion of computationally expensive kicker effects for a period much longer than one orbit period.

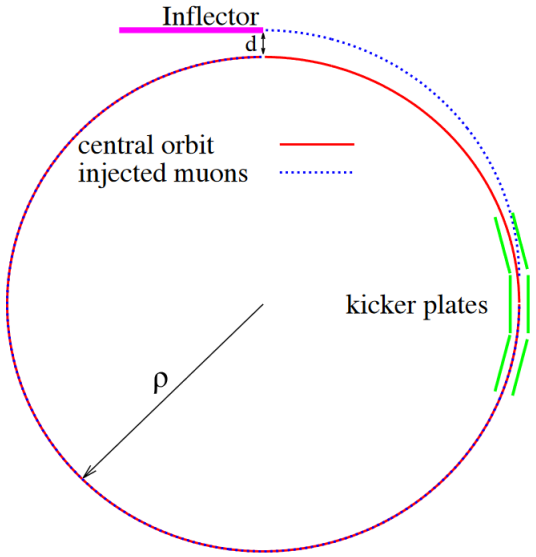

Figure 1.5: Schematic showing the layout of the $g-2$ storage ring injection components. The inflector (top, magenta) injects the incoming antimuon beam (blue dotted line) at $d = 77$ mm radially outward from the design orbit of radius $\rho = 7.112$ m (red) and the incoming beam is consequently kicked by the kickers (right, green). The desired result of the kick is for the incoming beam to be given zero horizontal momentum, relative to the design orbit, just as the incoming beam crosses the design orbit. [16]

Circular collimators, of 45 mm radius aperture, are used at 5 points around the ring in a configuration shown in Figure 1.6. The collimators can be automatically inserted or removed as deemed preferable for the experiment [16].

These are used to rapidly remove antimuons that could otherwise spend time outside the storage region, potentially being affected by objects and external fields not intended during design. Different configurations of colli-

mators naturally lead to different rates of antimuon loss and different qualities of the stored beam (as shall be seen later in Section 4.3).

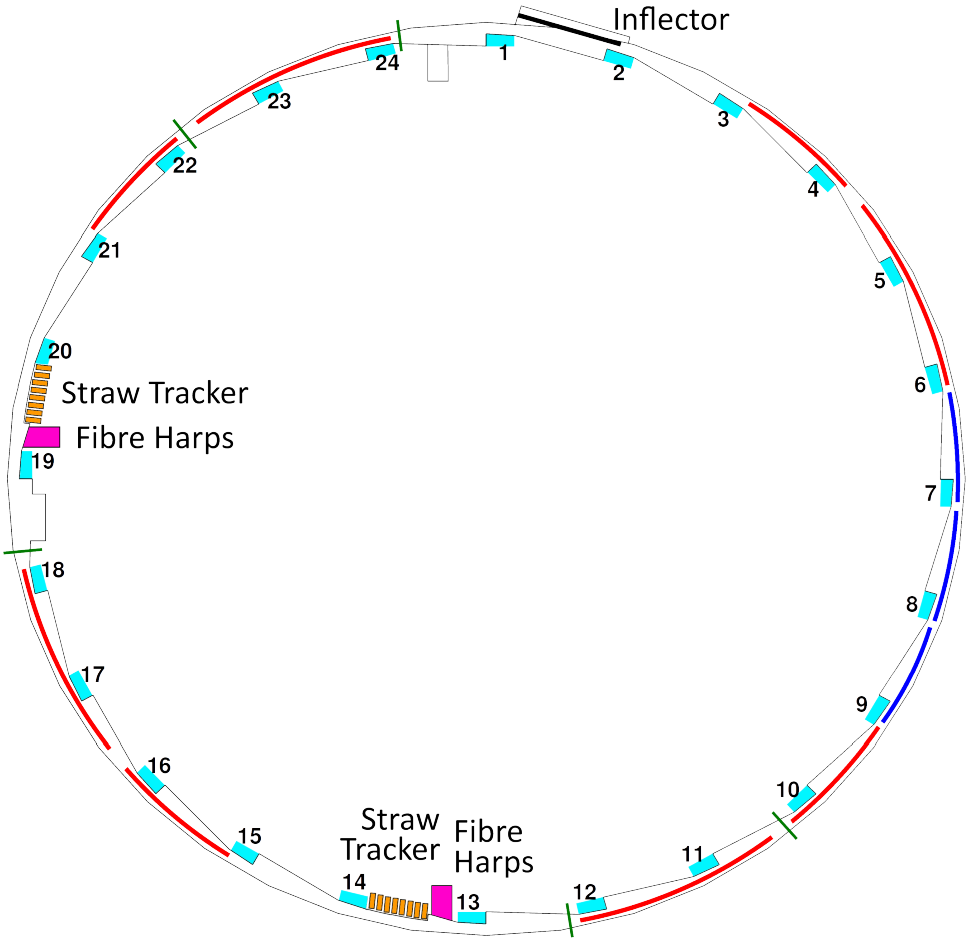

Figure 1.6: Diagram of the Fermilab Muon $g-2$ Ring, showing the relative locations of the (pairs of x- and y-) fibre harps (magenta), straw trackers (orange) and 24 calorimeters (cyan). Also shown are the quadrupoles (red), kickers (blue), collimators (dark-green) and inflector (black).

1.4.4 Beam Storage in Electric and Magnetic Fields

The magnetic dipole ring and electrically charged plates (shown together in Figure 1.7) are used to keep the antimuons within the designated circular aperture, centred on a ("major") radius of $\rho = 7.112\,\mathrm{m}$ and kept within a storage region with circular transverse cross-section of ("minor") radius

$r = 0.045\,\mathrm{m}$ from the design orbit. The dipole has adjustable pole pieces, configured to give a magnetic field variation around the ring of less than 50 ppm, with adjustable coils providing active shimming which results in an azimuthally-averaged deviation from the design field of less than 1 ppm [23].

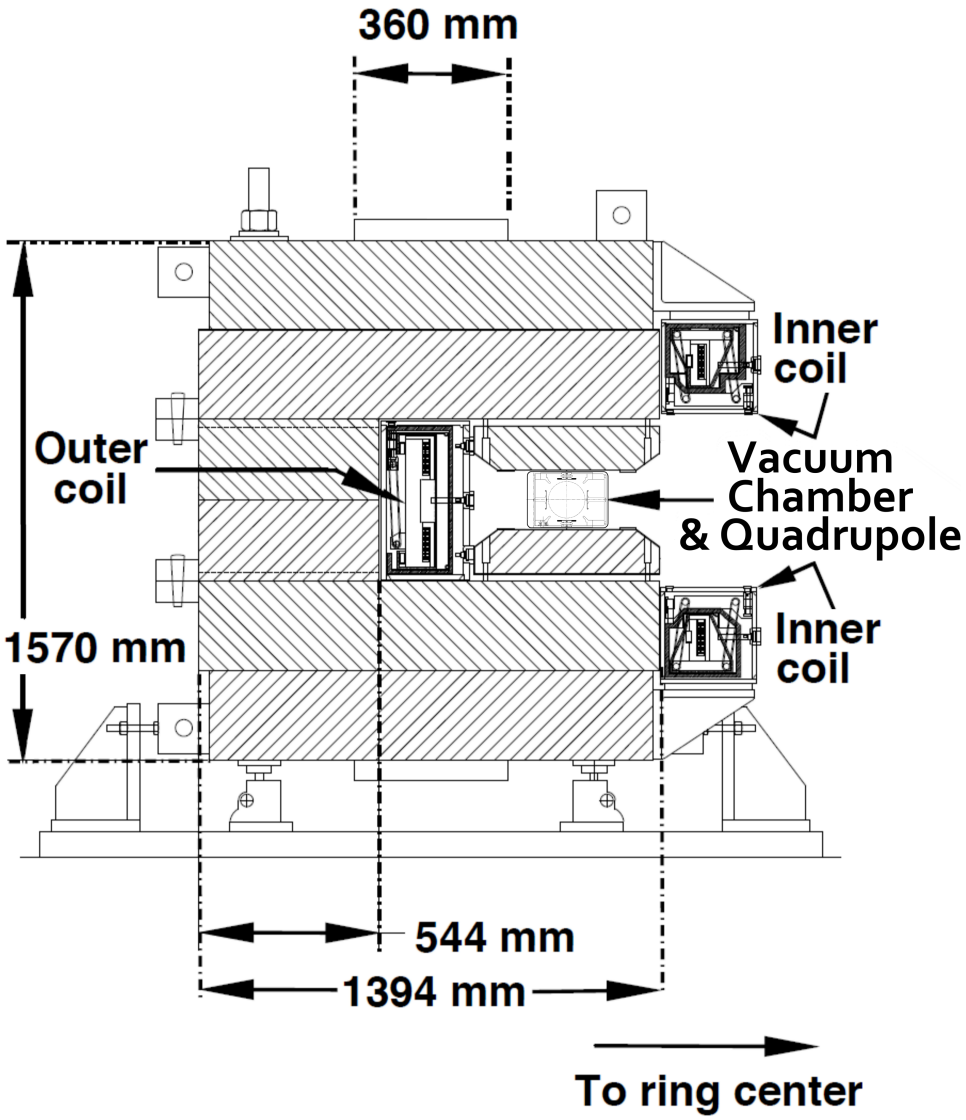

Figure 1.7: Cross-section diagram of the dipole magnet, with the vacuum chamber and quadrupole plates (shown in greater detail in Figure 1.8). [16]

There are eight sets of flat-electrode electrostatic quadrupole plates positioned around the ring, configured as four short/long quadrupole pairs, used

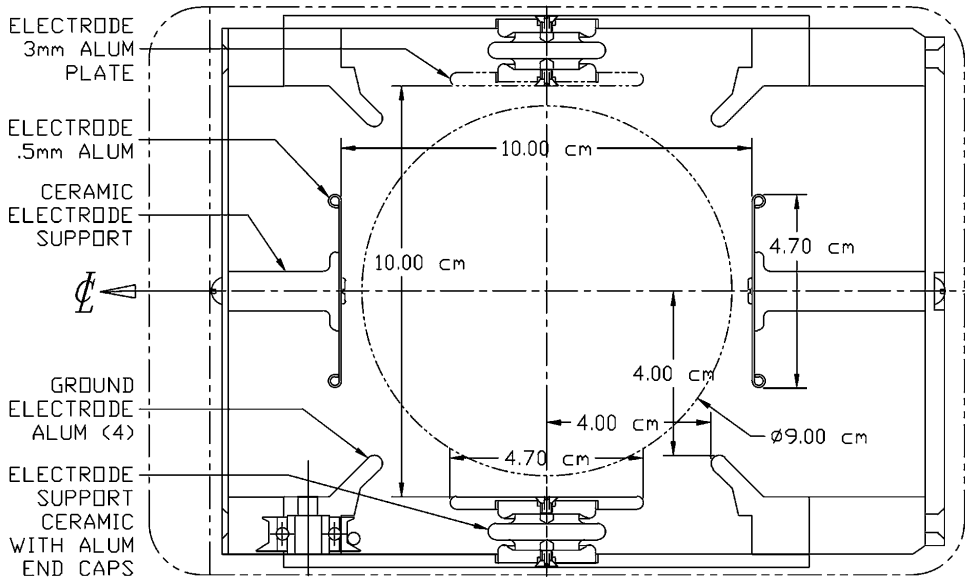

Figure 1.8: Cross-section diagram of the electrostatic quadrupoles, showing the flat electrode plates on the left and right of the storage region (negatively-charged) and top and bottom of the storage region (positively charged). [16]

to confine the beam to the designated storage region. A technical drawing of the transverse plane within a quadrupole is shown in Figure 1.8. All quadrupoles are horizontally defocusing (vertically focusing). Horizontal focusing is provided by the (weak focusing effect of) the main dipole magnet, resulting in overall focusing in both the horizontal- and vertical-transverse directions. As there are no accelerating cavities in the beamlines following the target, there is no longitudinal focusing. This results in a beam length of approximately 40 m at the point of injection and, following this, the bunch naturally spreads longitudinally to encompass the full circumference of the ring after some time.

The electrostatic quadrupoles have a range of operation voltages, providing the main means to control beam focusing in the ring (the other being the strength of the dipole magnet). This, in turn, determines the transverse horizontal and vertical tunes ν_x and ν_y respectively, which indicate the number of betatron oscillations performed by a nearly on-axis antimuon during one ring rotation. We wish to find an operation point far from resonances (operation points satisfying (1.14)), plotted in Figure 1.9, and which may cause continual, slow antimuon collimation over time. One way to locate a significant loss-causing resonance is to measure the number of stored antimuons

(via detected positron flux) as a function of quadrupole voltage. In this case, a drop in positron flux indicates a drop in stored antimuons and thus that a resonance has been encountered.

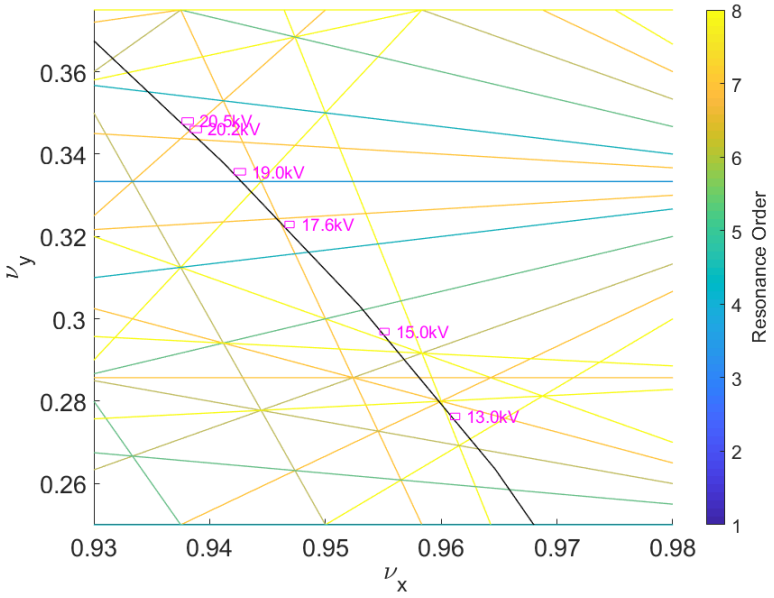

Figure 1.9: Plot of tune space, where straight lines indicate resonances satisfying (1.14), the curved line (black) indicates the operating range for a ring with quadrupoles covering the full azimuth, and the rectangles (magenta) indicate the measured tunes/uncertainties [24] of the E989 ring for various set potentials of the quadrupoles.

During the injection process, and before data-taking, a scraping scheme can be activated which forces a field asymmetry between the quadrupole plates. This moves the beam vertically down and horizontally to opposite sides in the second and fourth quadrupoles, so as to scrape the edge against the collimators with the intention of removing any particles that would otherwise be collimated during the data-taking period. Indeed, losing antimuons through collimation during data-taking was the largest contributor to systematic uncertainty in the previous experiment [14].

To complement the basic scraping scheme incorporated in to the original design of the experiment [16]; a more complicated RF scraping scheme has been developed [25], during which the potentials of some of the plates are changed at RF frequencies. This is intended to operate in two stages.

The first stage, lasting for 5 μs, reduces the coherent betatron oscillation (CBO) of particles of similar phase by applying an RF dipole. This is tuned

to the horizontal and, separately, vertical oscillation frequencies of these particles, out of phase with the particle oscillation so as to reduce the oscillation amplitudes.

The second stage, lasting for 10 μs, further reduces the horizontal CBO by using an RF quadrupole when the particles of momentum higher and lower than the design momentum are, on average, completely out of phase. Due to the higher/lower momentum particles having average positions on the radial outside/inside of the ring respectively, an RF quadrupole tuned to the horizontal betatron frequency (and with correctly chosen phase) will effectively push the particles of both high and low momentum towards their respective dispersive orbits simultaneously.

These RF scraping systems, with several other potential RF methods, are currently undergoing testing in the experiment ring. [26]

Once scraping schemes have been completed, the potential on the plates returns to the symmetric voltages asymptotically, with decay time of 5 μs. The data-taking period then starts, 20 μs after injection.

1.4.5 Particle Detectors

There are three kinds of detectors used in the experiment, each optimised to detect antimuons and positrons in different ways. This allows us to observe the behaviour of the beam at multiple locations in the ring, and validate observations by comparing results from the various detectors.

The "fibre harps" each consist of 7 scintillating fibres in the horizontal (x) or vertical (y) transverse directions, with one harp for each direction. Pairs of these (one x and one y) can be swung in to the beam at approximately 180 and 270 degrees from the injection point (as shown in Figure 1.6), to observe the behaviour of the stored antimuons with time, which makes the harps instrumental for understanding the beam dynamics. Despite the somewhat low resolution offered, this achieves a reasonable compromise with degradation of beam quality over time. Thus, the fibre harps can be used to provide information on the behaviour of the beam for some time after injection, although no $g-2$ measurement data can be recorded with the harps swung in to the storage region.

The static "straw trackers" consist of many gas-filled metal tubes containing a high voltage filament. Two banks of straw trackers, one just after each pair of fibre harps (as shown in Figure 1.6), are used to detect the trajectories of decay positrons on approaching a calorimeter. Through detection and reconstruction of positron trajectories, along with correlations inferred from Monte-Carlo simulations, the straw trackers allow the measurement of the approximate decay point of their parent antimuons. From the perspec-

tive of beam dynamics, this works as an effective confirmation tool for the fibre harp measurements of beam position, and a useful tool for estimating the beam cross-section shape for a range of ring azimuth. However, as the trace-back methods are based on fast Monte-Carlo simulations using a simple model of the ring, caution should be applied when considering the accuracy of the given antimuon decay points.

For the main experimental result (ie. measurement of the antimuon precession frequency), 24 calorimeters are distributed at 15° intervals around the inside of the ring, shown in Figure 1.6. Each calorimeter consists of 54 lead fluoride crystals with silicon photomultipliers, with uniform laser pulses used for calibration. These are of limited use for beam dynamics, although efforts are being made to use the multiple calorimeter crystals to provide beam position measurements, albeit with low resolution [27].

1.5 Purpose and Requirements of Modelling the Experiment

To understand the effects of antimuon beam behaviour on the final measured result of a_μ an accurate model of the ring is required, including the fields produced by the dipole magnet and the electrostatic quadrupoles.

In particular, the beam "polarisation" (distribution of antimuon spins), and the collective motion of antimuons (which may cause long-term antimuon losses – a significant effect in the previous experiment [14]) should be studied in simulations, as these might affect the results. Indeed, as antimuons experiencing different non-uniformity in the magnetic field will differ in their measured precession frequency ω_a, it is clear that the polarisation will have some dependence on the beam dynamics in the ring.

To these ends, we require a simulation tool that can track antimuons, with their spins, through custom electric and magnetic fields. Due to the curved geometry of the elements in the ring, it would be useful to use an advanced tracking code already incorporating as many of the necessary features as possible.

The beam dynamics studies for the experiment already use models of the ring developed in Geant4 [28, 29] (which can model matter effects, mainly used to simulate large numbers of positrons for mock data analysis), COSY [30, 31] (which can track large numbers of particles quickly using transfer maps, mainly used for resonance loss analysis) and BMAD [32, 33] (which can model spin precession through kickers with multiple tracking methods, used mainly for kicker simulations).

The objective of the work reported here is to produce a model which

differs from these, while simulating the same experiment and phenomena as accurately as possible, such that greater confidence can be placed on the results of the simulation team if all models agree. With results from beam dynamics measurements from the experiment, the models can be calibrated and be evaluated in how well they reflect the experiment, and used accordingly for making predictions about possible future configurations of the experiment.

1.5.1 Difficulties

Having the elements of the ring all within a bend (dipole field) is not typical in storage rings, where elements are usually separate and do not interact significantly with each other (efforts are often made to ensure this [34]). Hence, no particle tracking codes were found which permit the use of standard beamline elements superimposed with curvature in the design trajectory and accompanying magnetic dipole field (with the exception of magnetic dipoles).

Indeed, various studies of multipoles in curvilinear coordinates have been performed [35, 36, 37] but have not resulted in simple methods to fit these to field maps. This lack of accurate fitting to realistic fields suggests that these methods are unsuitable for modelling any possible subtle effects of the curvature of the coordinate system.

Further, longitudinally-varying fields (those which vary around the ring) need to be modelled. Due to the unique behaviour of the electric field within the storage region at the ends of the quadrupoles (discussed in Chapter 2, see Figure 2.5), a hard-edge model of the electrostatic quadrupoles cannot simply be expected to describe the case studied here to high precision, particularly where antimuons pass these fringe regions in close proximity to the quadrupole plates.

In the ideal case, we would be able to combine longitudinally-varying fields and the curvilinear coordinate system, such that the variation of the magnetic field about the ring, as well as the quadrupole fringes, can be accurately modelled. This would also provide the freedom to model any other static field present in the ring.

The first step to overcoming these difficulties is to choose a versatile modelling tool, which should ideally already contain some of the desired functionality, whilst allowing customisation for bespoke field descriptions. Once a basic model of the experiment is developed with the tool, new modelling methods can be developed and tested against the basic model.

We will then use the chosen accelerator modelling tool to implement electric multipoles to model the quadrupoles before investigating more complex methods which incorporate the curvature and non-continuous nature of the quadrupoles. We will also look to develop new particle motion integration

methods, and compare with those available in the used modelling tool.

The next step is to compare the results from each of these methods with other storage ring models as well as the experiment, and identify the most accurate and the optimal modelling methods. With these, various aspects of the experiment can be modelled, including a long-term simulation run under conditions accurately reflecting the experiment, and conclusions can then be drawn from the results regarding the beam- and spin-dynamics of the experiment.

Chapter 2

Modelling the Fermilab Muon $g-2$ Storage Ring

2.1 BMAD: A Tracking Library for Particle Accelerators

The particle tracking code chosen for this research was BMAD [32]. The main reason for this is that it can track spin to high precision (necessary for quantities of interest in a storage ring, where particles undergo multiple orbits). In addition to this, BMAD is an open-source library, not a self-contained executable, allowing customisation of any aspect of the model.

In BMAD, tracking is performed on the set of coordinates:

$$\boldsymbol{r} = (x, p_x, y, p_y, z, \delta) \tag{2.1}$$

where x, p_x are the transverse horizontal position (in metres) and momentum (as a fraction of the design momentum) respectively, y, p_y are the transverse vertical position (in metres) and momentum (as a fraction of the design momentum) respectively, and z, δ are the longitudinal position relative to the design particle (in metres) and momentum deviation normalised to that of the design particle, respectively. The normalised spin vector, which is stored and tracked for each particle, takes the form:

$$\boldsymbol{s} = (s_x, s_y, s_z) \tag{2.2}$$

where the components are those of the spin along the respective coordinate axes.

Conveniently, BMAD contains a selection of "dummy methods", supplied with the package, that can be customised by a user and called when BMAD

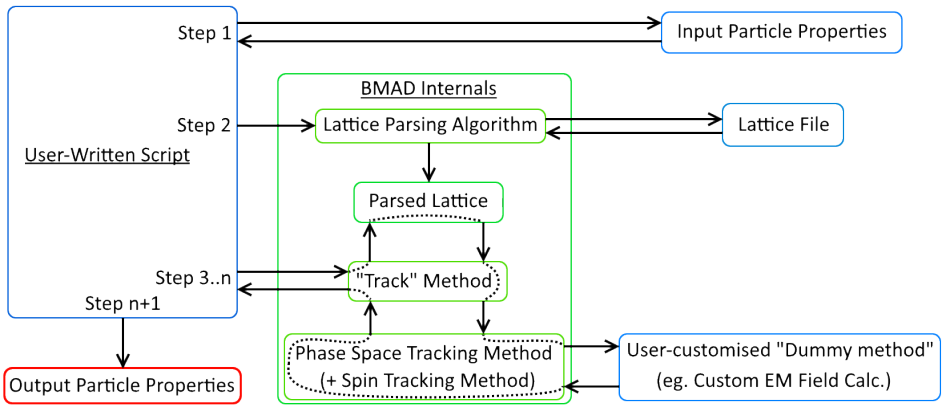

Figure 2.1: The structure for the model developed in this research, using the BMAD library. Firstly, the properties of injected particles are read in from a file ("Step 1"), then a call is made to BMAD to parse the "lattice" file containing the structure of the storage ring ("Step 2"), where the parsed "lattice" remains in memory. In consequent steps (ie. within the tracking loop), calls are made to BMAD to track particles through the parsed lattice, using a specified (in some cases custom) tracking method, which integrates the equations of motion through the electromagnetic fields supplied either by the lattice (in the case of multipoles, dipoles or other simple components) or supplied by a user-customised method (in the case of the field descriptions presented in Chapter 3). During this tracking loop, particle properties can be output as they are tracked past the injection point and all four fibre harp locations.

tracks through a specific element. The most relevant of these methods (for the purposes of the research presented here) allow the specification of field values on each integrator step, the implementation of custom tracking methods, and custom tasks to be performed after having tracked each time step (useful for decay simulations). These customised methods can be packaged with a tracking script which calls the BMAD functions necessary to perform the tracking tasks. A schematic description of the particular case employed in this study is presented in Figure 2.1.

In order to use field maps directly in the model (as these will be used for comparison in Chapters 4 and 5), whilst maintaining a high level of accuracy, we will use a built-in tracking method that invokes a fourth-order time-based Runge–Kutta integrator. We choose a time-based, rather than the standard space-based, integrator to make the modelling of decays simple (as particle decays have a known temporal, rather than spatial, distribution). We also

wish to use fourth-order as this should provide the accuracy required for tracking over thousands of turns. This integrator also permits tracking backwards about the ring, although this is not intended for the studies presented here.

This "Time-RK" integrator is implemented in BMAD with an adaptive-step algorithm [32, 38], which determines each consequent (temporal) step size by tracking a particle through the fields using one standard step, and tracking through the same space using two steps of half the size. If the results of tracking from these two methods varies by more than the relative or absolute tolerances, a further calculation will be performed with a quarter of the step size, and compared to the half step-size results. This procedure repeats until a suitable step size is found, at which point the tracking of that step is already complete.

Tracking through field maps (supplied through the lattice file) requires some form of interpolation. In BMAD, this is provided through a simple linear interpolation between the given field map grid points. While this can be expected to work well for a high-resolution field map, the resulting discontinuities in field gradients from poor meshing or noise in the map cause irregular behaviour for certain studies later on (most notably the tune and chromaticity studies in Chapter 4). However, for use in shorter elements and for simple tracking to compare with later, this method is deemed sufficient.

Spin tracking can be performed in multiple ways in BMAD. However, only one of these is permitted for tracking through field maps (or indeed custom fields). The BMAD "*tracking*" method effectively uses the field calculations in the Time-RK integration steps to perform its own integration of spin vector motion.

Similarly to a number of tracking codes (most notably MAD [39]), BMAD uses lattice files to express the structure of the accelerator being modelled. In BMAD, one can specify field maps, apertures, custom tracking methods and custom fields for each element of the accelerator, as well as the design particle energy in the lattice files. This allows many of the bespoke aspects of the storage ring layout (such as the measured component positions shown in Appendix L) to be contained within the lattice file.

2.2 Injection and Collimation

2.2.1 Incoming Bunch Modelling

The beamline simulations track up to (and in some cases include) the inflector magnet using BMAD [40, 41], G4Beamline [42] and COSY [43]. The results of these simulations provide an estimate of the beam properties on entry in to

the storage ring, and a convenient set of data with which to start simulations of dynamics within the ring.

However, there is the inherent limitation in this approach that the number of particles used is restricted to those produced by a specific beamline simulation. While some beamline simulations are capable of generating arbitrary numbers of antimuons, whilst approximately maintaining the distribution in 8-dimensional phase space (3 spatial co-ordinates, 3 momenta and 2 angles of spin), these may introduce artificial noise or amplify small, artificial correlations. For this reason, the data sets used are restricted to those produced directly by a given model.

Due to the starting points of all beamline simulations being the pion production target (simulated in MARS [44]), in multiple runs of each model one could expect to see some antimuons with the same properties each time, having survived from the target to the end of the beamline. This causes problems when trying to merge the results of multiple runs of beamline simulations of the same configuration, as duplicate particles cannot be removed (as this would taint the distribution, as would moving them very slightly), nor can they remain (as identical particles are not suitable in a continuous distribution and are an effective waste of simulation time).

Only one simulation produced enough antimuons in a single run for meaningful statistics, with 168924 antimuons at the downstream end of the inflector resulting in approximately 5000 to 7000 being stored in the storage ring. This was produced by the Geant4Beamline simulation [42], with tracking through the dipole magnet backleg and inflector magnet performed by the Cornell BMAD simulation [41].

One of the main studies performed by combined beamline and ring simulation teams has involved attempts to match Twiss parameters and dispersion (particularly β_x, β_y and η_x) of the incoming beam with those of the ring. However, the horizontal dispersion of the ring being $\eta_x \approx 8\,\mathrm{m}$ [16], along with a ring momentum acceptance of about $\delta = P/P_0 - 1 \approx 0.003$ (and neglecting contributions from beam emittance) would result in a beam width of approximately:

$$\eta_x \delta = 0.024\,\mathrm{m}.$$

Given that the horizontal aperture of the 1.8 m long inflector magnet is 18 mm [16], it would be impossible to achieve a good match to the ring optics without substantial beam losses.

The other extreme is to inject with the aim of maximum transmission through the inflector. However, this in turn would cause substantial medium term losses in the storage ring due to phase space mismatch.

Much focus in combined beamline-ring models has been given to finding

a compromise between these two approaches which results in the largest number of antimuons surviving in the ring. The optimum configuration was used to produce the post-inflector data used for the studies discussed in Chapter 4.

2.2.2 Pulsed Electromagnet Kickers

In the experiment, it was deemed necessary to measure the kicker pulse waveform so that accurate simulations of the kicker pulse could be performed [45]. During these measurements, the kicker pulses were all found to have a long oscillating tail, shown in Figure 2.2, presumed to be due to impedance mismatch between the power supplies and the kicker plates.

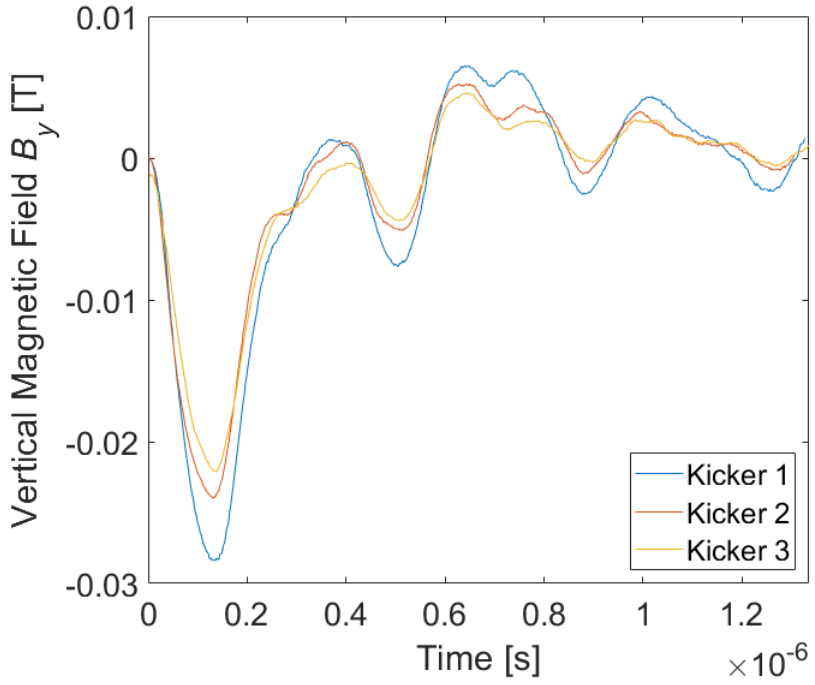

Figure 2.2: Measured time dependencies of the magnetic fields of Kicker 1 (blue), 2 (dark orange) and 3 (light orange) [45]. The ideal kick would have no oscillation beyond the first peak, which should also have a flat top (to provide near-constant field when the antimuons traverse the kickers). The kickers appear to exhibit different kick strengths, although the behaviours of the pulses are near identical and so we shall use only the Kicker 1 pulse (with a peak field of 270 gauss) for modelling.

This pulse was modelled in BMAD using *ac_kicker* elements, which can represent a time-dependent field described by a field map (shown in Figure 2.3 for the kickers). The start time of the simulated pulse had to be synchronised relative to the incoming beam so as to match the experiment.

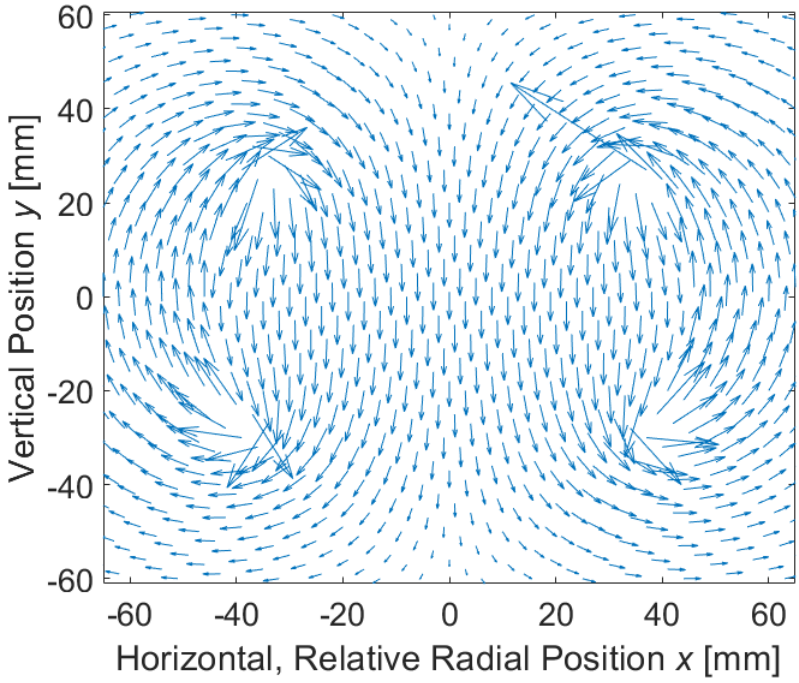

Figure 2.3: Transverse, 2D magnetic field map of the kickers, calculated by a finite element analysis code. The plates are circular at a radius of approximately 46 mm from the beam axis, pulsed so at to produce a magnetic field pointing vertically down to counteract the magnetic dipole field. It is noted that particles travel through the plates of Kicker 1 just after injection, and the kicker plates have tapers at the ends.

The kicker plates end in tapers, which are omitted from simulation due to their short length relative to the rest of the kicker plates, and the small number of turns for which the kick strength is high. However, due to the long active time of the kicker pulse (over which the particles may pass these regions many times) this may need to be considered when comparing the simulation results to those from the experiment.

One feature of the kickers that is difficult to model is that the absolute magnitude of the kicker field has not been measured, so field maps combined with the time dependence must still be scaled by a factor determined

by simulation. The estimates for kicker magnetic field are in the range of $250 - 320$ Gauss ($0.025 - 0.032$ T), which constrains the parameter space for analysis. The chosen starting value for the peak of the pulse is 270 Gauss, as the higher values are thought less likely due to the kick pulse not being optimal.

Another difficulty is that the incoming antimuon beam may be partially behind the radially-outside plate of the first kicker, which prevents the use of a multipole expansion (which is valid only in regions without a source of magnetic flux). This leaves only the possibility of using a field map. However, this is also not trivial, as discontinuities in the field (such as at the surfaces of the plates) cause the field map interpolation to break down.

To avoid the discontinuity problem, a region tightly encompassing the plates in the given field map is manually set to have zero kicker field within the simulation. This avoids field map interpolation difficulties in a way which allows the adaptive-step integrator to track particles through the plates.

Although magnetic fields from each of the three kickers were measured (Figure 2.2), they are sufficiently similar that the Kicker 1 pulse may be used for all three kickers.

2.2.3 Circular Collimators and Apertures

By default in BMAD, all element apertures work on an eliminate-on-hit basis, whereby any particle outside the specified aperture is "lost" and not tracked further. Simulations of the beamlines in BMAD [40] and Geant4Beamline [42] suggested that eliminating particles in this manner provides good agreement with a code which instead invokes matter effects. [46]

During scraping, the transverse aperture used in the lattice (with the exclusion of collimators), was a rectangle of height 128 mm and width 160 mm (almost the full aperture of the quadrupole field maps), allowing incoming antimuons injected at the $x = 77$ mm offset to encounter realistic fields from the quadrupoles and avoid getting unnecessarily collimated before being kicked by the kickers. After scraping, if the multipole fit methods are enabled, this aperture reduces within the quadrupoles to be a circle of radius 48 mm, so as to avoid particles being tracked through the poorly represented fields at the edges of (and behind) the charged plates (at $x, y = \pm 50$ mm, shown in Figure 1.8 in Chapter 1).

The precise shape of the collimators [47] is difficult to reproduce in BMAD, so the approximation was made that the collimators were circular in cross-section and followed the curvature of the ring. This resulted in the simulated collimator thickness on the radially outside edge being 0.25 mm greater than that on the radially inside edge. For the real collimators, this

difference is 7 mm.

The effects of the subtle differences in collimator shape in the model and in the experiment may be worth investigating further, as would the implementation of matter effects in the collimation scheme (rather than an eliminate-on-hit scheme). However, while these may indeed have consequences for beam dynamics, it is not the main objective of the study, so this approximate model of the collimators is used.

2.3 Modelling of Electric and Magnetic Fields in Approximately Straight Elements

2.3.1 Measured and Calculated Field Maps

The field maps used were created in the finite element analysis tool Opera3D [48]. In the case of the steady state quadrupoles (no scraping), field maps were supplied for the upstream and downstream fringe regions, each covering 2° of ring azimuth Θ (corresponding to 0.25 m of path along the design trajectory) centred on the start/end of the plates ($-1° \leq \Theta \leq 1°$), and for the 2D transverse field within the bulk of the quadrupole. The regions covered by each of these field maps is shown in Figure 2.4.

All field maps were calculated with plate potentials of ± 27.2 kV and resolution of 1 mm in the transverse (x, y) plane, and $\Delta\Theta = \frac{1}{40}° \approx 3$ mm in the longitudinal/azimuthal (Θ) direction. Each of the three field maps were also calculated for each plate being at full potential individually (with the other plates at 0 V).

On analysis of the provided field maps, we notice electric field peaking at the edges of the plates. Such effects are expected due to the plate geometry, and we can expect these to introduce higher-order multipoles in analysis of the transverse plane. As seen in Figure 2.5, this effect also amplifies the fringe fields, causing a peak in field at either end of the quadrupoles.

Here, we make the assumption that the field maps can be scaled with the plate potential, such that relative charge distribution on the plates remains constant regardless of plate potential. As the plates are mostly aluminium, with very low electrical resistivity to affect the free distributing of electric charge across the plate, this assumption is considered acceptable.

The ring azimuth covered by each 2° fringe field map of 0.25 m is small with respect to the ring radius $\rho = 7.112$ m, so we may approximate the fringe fields as being taken from a straight element, for the purposes of fitting to analytical functions. In the case of the 26° "long" quadrupoles, which each occupy 3.2 m of orbit path, the same approximation for the bulk fields must

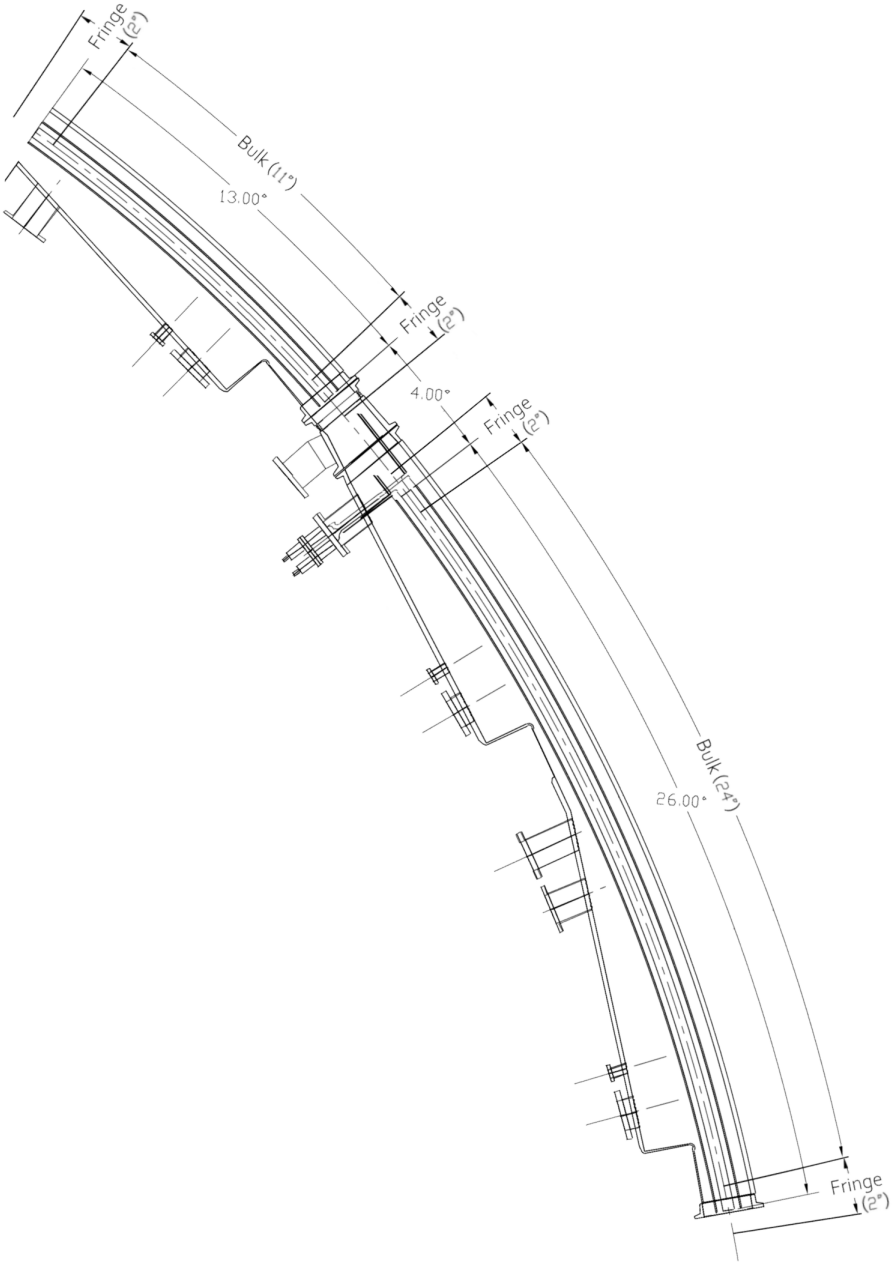

Figure 2.4: Diagram of a quadrupole pair, showing the extent in azimuth of the short (13° of ring azimuth) and long (26° of ring azimuth) quadrupoles and the corresponding bulk and fringe regions. The fringe regions occupy the space between 1° of ring azimuth outside of each end of a quadrupole and 1° within, and the bulk regions occupy the space between these (the regions of space more than 1° of ring azimuth within the quadrupoles). [16]

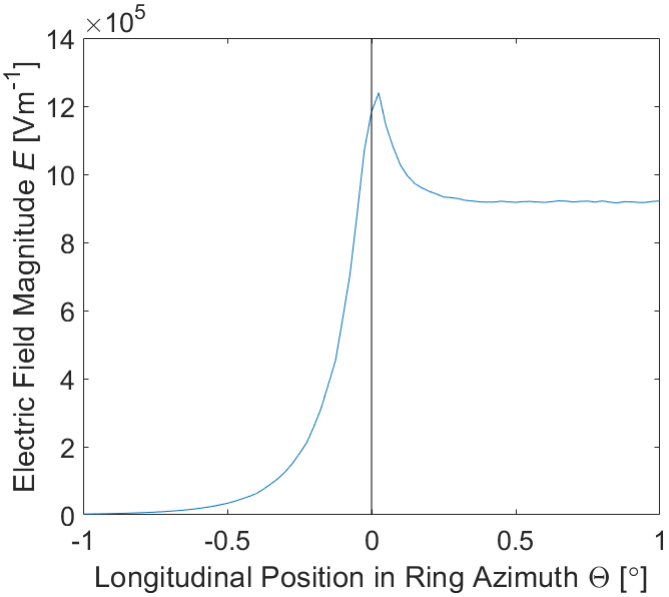

Figure 2.5: Electric field magnitude for the quadrupole fringe fields over longitudinal position Θ, taken at $(x, y) = (45\,\text{mm}, 0)$, as calculated from the field map. There is a clear peak at the start of the quadrupole (at $\Theta = 0°$), where the field reaches 135% of the value field within the quadrupole bulk.

be made with caution.

2.3.2 Highly Uniform Dipole Magnet

Sector bend elements in a lattice use a coordinate system which follows the curvature of the design orbit. Due to the uniform magnetic dipole field around the ring of 1.45131 T, a curved reference trajectory of radius $\rho = 7.112\,\text{m}$ is used for all elements in the storage ring model.

Efforts have been made to achieve a magnetic dipole field in the experiment that is as uniform as possible [49], with much of the correction of non-uniformities carried out by use of coils in the walls of the vacuum chambers [50].

The magnitude of the resulting residuals, in the beam storage region, have been measured by 17 NMR probes mounted on a trolley that can be positioned around the ring [16, 51]. Due to the measurements being of field magnitude only, a reliable multipole expansion could not be obtained from the measurement data.

For simplicity, it is assumed that the measured residual field is purely

radial (attempts have been made to separate the measured field into components, without success [23]). Fortunately, a residual transverse field that is uniform around the ring can be simply implemented in the model using magnetic multipole components, applied to the template sector bend element in the lattice file.

2.3.3 Electrostatic Quadrupole Bulk Fields as a Multipole Expansion

To model the bulk section of the quadrupole field (the region of space more than 1° of ring azimuth within the quadrupole), we can utilise the field map directly in BMAD. However, the fast interpolation used by BMAD causes the derivatives of the field to be badly behaved, causing the tunes to exhibit the erratic behaviour shown in Figure 2.6.

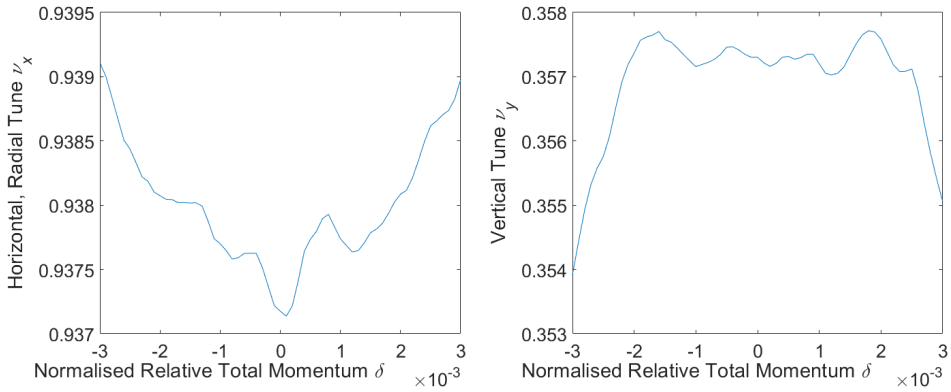

Figure 2.6: Horizontal, radial tune ν_x (left) and vertical tune ν_y (right) as a function of closed orbit momentum, with the quadrupoles at 20.5 kV, where the quadrupoles comprise of field maps for both the bulk and fringe descriptions. The many bumps in the plots are artefacts of the interpolation of the field maps, although the divergences at the extrema of δ are also exhibited by the continuous descriptions of quadrupoles described in Chapter 3 and plotted in Figure 4.6 in Chapter 4.

Given this difficulty, and in the pursuit of shorter tracking times, a multipole expansion of the field map was chosen, so as to have a continuous description of the field in BMAD.

On a straight reference trajectory, the electric multipole expansion (which obeys Laplace's equation in a region of space free from electric charge) takes

the following form:

$$E_\phi(r,\phi) + iE_r(r,\phi) = \sum_{n=1}^{\infty} c_n \left(\frac{r}{r_0}\right)^{n-1} e^{in\phi} \tag{2.3}$$

where r and ϕ are the circular polar coordinates in the transverse plane, relative to the beam axis, r_0 is the "expansion radius" at which the fit was made and c_n are the multipole coefficients.

Taking the Fourier transform of (2.3) (shown in Appendix C.1), one can show the coefficients c_n to be calculable as:

$$c_n = \frac{1}{N_\phi} \sum_{n_\phi=0}^{N_\phi-1} \Big(E_\phi(r_0, 2\pi n_\phi/N_\phi) + iE_r\left(r_0, 2\pi n_\phi/N_\phi\right) \Big) e^{-2\pi i n n_\phi/N_\phi} \tag{2.4}$$

where N_ϕ is the number of points at which the field is sampled on the circle of radius r_0 about the beam axis.

To obtain the multipole coefficients in this case, studies (described in Appendix C.2) suggested an optimal value of $r_0 = 45\,\text{mm}$ for the expansion radius about the design orbit. This was chosen so as to maximise the area within the expansion region (increasing the accuracy of the field within) whilst keeping sufficient distance from the plates to avoid a sharp drop in accuracy. As the field map resolution is 1 mm and the circumference of the ($r_0 = 45\,\text{mm}$) circle on which the fit is performed is 282 mm, the number of equidistant samples chosen to perform the fit was $N_\phi = 120$ (allowing approximately two field map points for each sample to reduce noise, whilst providing ample resolution for an accurate fit up to the $n = 22$ mode).

As the provided field map (shown in Figure 2.7) was in Cartesian coordinates (in the plane perpendicular to the reference trajectory), a MatLab 2D spline fit was used to obtain field values on the $r_0 = 45\,\text{mm}$ circle. The resulting coefficients c_n of this fit were calculated up to $n = 22$, and are are shown in Table 2.1.

To compare the field map with that produced by the multipole expansion, we use a transverse Cartesian grid with the same mesh as the field map (1 mm squares), within the region bounded by the plates ($-50\,\text{mm} \leq x \leq 50\,\text{mm}$ and $-50\,\text{mm} \leq y \leq 50\,\text{mm}$). The Cartesian field components calculated from the multipole expansion were subtracted from those from the field map, and plotted in Figure 2.8. As this is the bulk field, and we are making the approximation that the reference trajectory is straight, the longitudinal component is assumed to be zero so that analysis using only the transverse components is necessary.

These residual fields show agreement down to $10^4\,\text{Vm}^{-1}$, which is less than 1% of the maximum field values of $10^6\,\text{Vm}^{-1}$ on the fitted surface. Fits

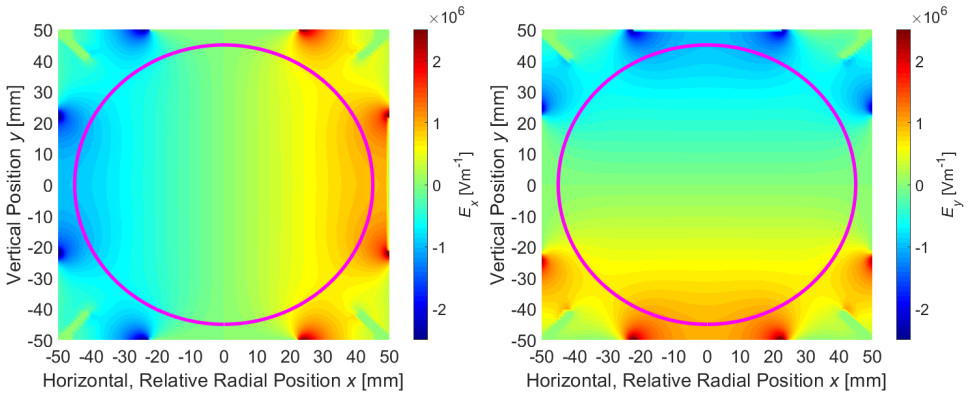

Figure 2.7: Field map for the electrostatic quadrupole field components E_x (left) and E_y (right), calculated using a finite element analysis code [48]. The edge of the $r = 45\,\text{mm}$ storage region is shown in magenta.

to different orders n were compared in this way, in an effort to find an optimal fit order, as calculating to higher order n requires higher computation time.

As can be seen in Figure 2.8, $n = 22$ provides excellent agreement with the field map up to a distance of 48 mm from the design orbit (2 mm from the electrode plates). However, $n = 14$ retains a similar level of agreement, to a distance of 45 mm from the design orbit. While dropping orders further (eg. to $n = 12$) may reduce computation time, Figure 2.8 demonstrates that it would greatly reduce the accuracy of the field within the full $r = 45\,\text{mm}$ storage region. This is consistent with the multipole coefficients in Table 2.1, given that the $n = 14$ multipole has a large amplitude as compared to the other multipoles, with the exclusion of the quadrupole term (dropping higher-amplitude multipoles causes large drops in field fit accuracy).

The residuals of the multipole fit within the storage region in Figure 2.8 appear to be dominated by noise with an amplitude of approximately $2 \times 10^3\,\text{Vm}^{-1}$ (0.2% of the peak field, and not substantially larger than the field map noise, taken as the random fluctuations in E_y along the x-axis, approximately $500\,\text{Vm}^{-1}$ to $1000\,\text{Vm}^{-1}$)). This suggests that the coefficients obtained are sufficient for describing the quadrupole field bulk.

The working point of the ring in tune space, using the multipole expansion of the quadrupole bulk fields, was compared to that using the field maps for bulk and fringe fields. As can be seen in Figure 2.9, using the multipole representation brings the model far closer to the measured working points of the ring.

Table 2.1: Multipole expansion coefficients (calculated from(2.4)) for the electrostatic quadrupole bulk field with expansion radius of $r_0 = 45\,\text{mm}$, where $2n$ is the number of poles. By not absorbing the factor of $r_0^{-(n-1)}$ in to these coefficients, they can be interpreted as the field magnitude contributed by that multipole on the fit circle (at distance r_0 from the reference trajectory). The largest component is due to the skew quadrupole ($n = 2$), with skew 8-, 20-, 28- and 36-poles ($n = 4, 10, 14$ and 18) also contributing more than the other multipoles.

Order n	$\mathbb{R}\text{e}\,(c_n)$ [Vm^{-1}]	$\mathbb{I}\text{m}\,(c_n)$ [Vm^{-1}]
1	-53	-492
2	3	1015576
3	15	-284
4	-33	-13105
5	-20	-274
6	8	-6671
7	-14	101
8	44	358
9	4	-45
10	-10	-95166
11	-21	10
12	-15	4302
13	-36	37
14	-6	15580
15	73	-31
16	-23	-2120
17	78	-12
18	-6	9936
19	-16	51
20	7	62
21	-27	17
22	-6	-3354

2.3.4 Electrostatic Quadrupole Fringe Fields as Cylindrical Harmonics

Due to the quadrupole fringe field regions (32° of ring azimuth) occupying far less ring azimuth than the quadrupole bulk field regions (140°), replacement of the fringe field maps in the model is not as significant. However, the uncertainties on the measured tune values (in Figure 2.9) were small enough that different fringe field descriptions could result in tune variations of similar size to the measurement errors.

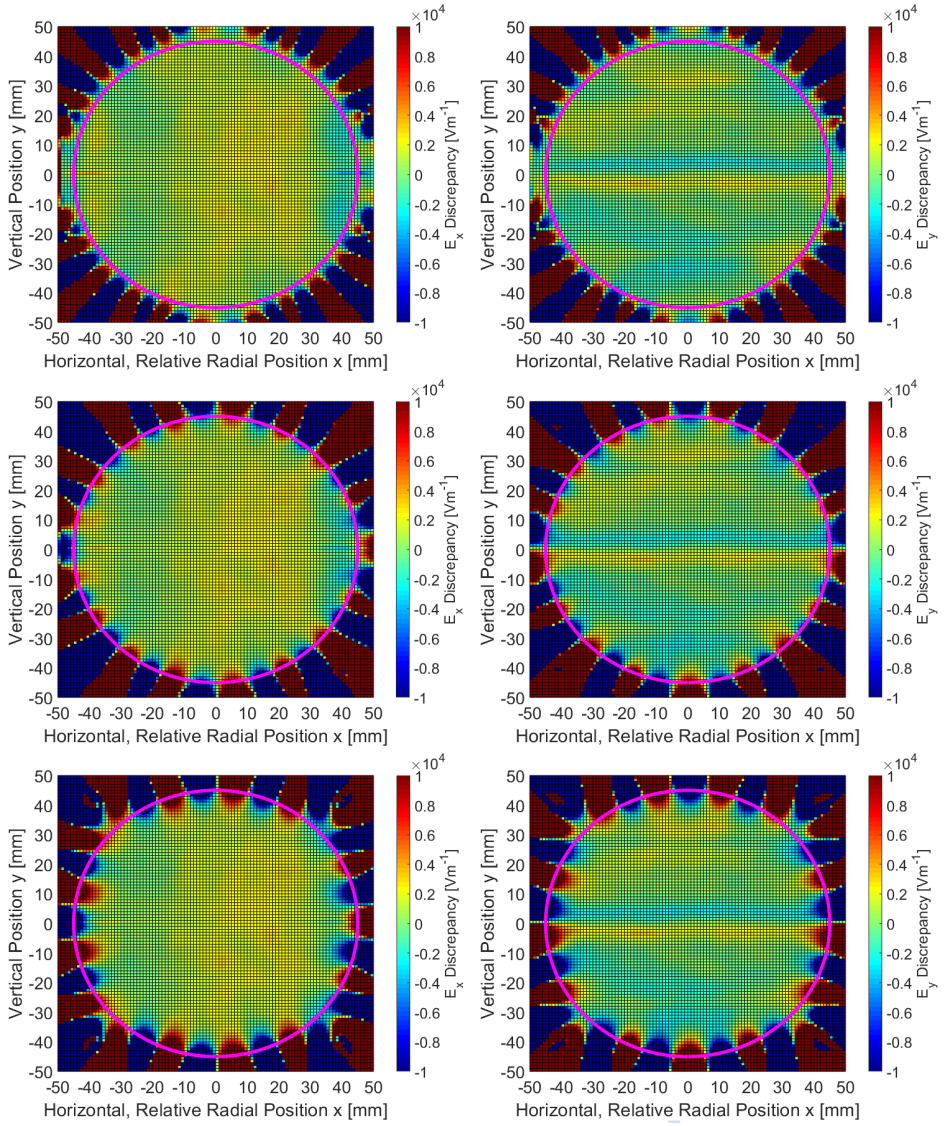

Figure 2.8: Difference between field map (shown in Figure 2.7) and field reproduced by multipole expansion with expansion radius $r_0 = 45\,\mathrm{mm}$, shown for E_x (left) and E_y (right) for $n \leq 22$ (up to 44-pole, top row), $n \leq 14$ (up to 28-pole, middle row) and $n \leq 12$ (up to 24-pole, bottom row) order expansions. The $n = 14$ expansion is considered a suitable compromise between order (which increases computation time) and accuracy of fit within the storage region, shown in magenta. For perspective, these differences can be compared with the approximate field strength at the plate surfaces of $10^6\,\mathrm{Vm}^{-1}$ and noise level of the field maps of approximately $10^3\,\mathrm{Vm}^{-1}$.

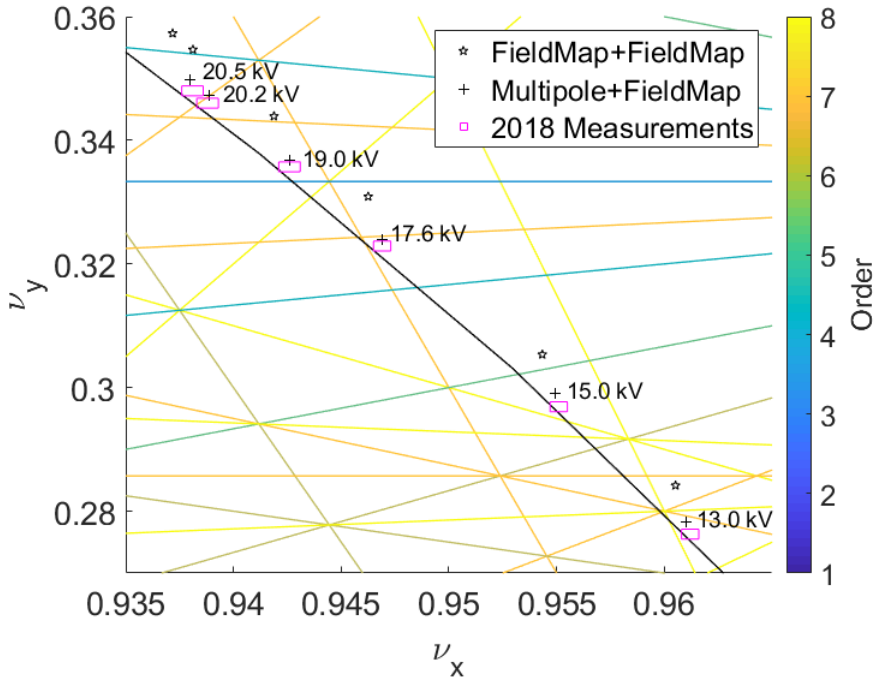

Figure 2.9: Working point of the ring in tune space, showing measured tunes [24] (magenta boxes, where the edges of each box are the bounds of the uncertainties for that measurement) alongside calculated tunes for the case of both bulk and fringe fields being described by field maps, and for the case of the bulk fields described by $n = 14$ multipoles, with fringe fields described by field maps. We see that using the field map to describe the bulk fields causes a much greater discrepancy with the measured data than for bulk fields described by a multipole expansion, possibly due to the interpolation method of the field map in BMAD.

In order to obtain a description of a longitudinally-varying field in a source-free region, we must find an expression for the scalar potential ψ by solving Laplace's equation $\nabla^2\psi = 0$ in cylindrical coordinates about the reference trajectory, which we approximate here as being straight. For a radius r from (and angle ϕ about) the design trajectory, the new coordinate system is defined by:

$$x = r\cos(\phi), \qquad y = r\sin(\phi), \qquad s = z, \tag{2.5}$$

where s is the longitudinal position in the ring.

The solution to the Laplace equation here consists of a sum of cylindrical harmonics, described by modified Bessel functions of the first kind $I_m(k)$ [52]:

$$\psi = \sum_{m=-\infty}^{\infty} \int_{-\infty}^{\infty} f_m(k') I_m(k'r) e^{ik'z} e^{im\phi} dk' \tag{2.6}$$

where we use cylindrical coordinates about the design orbit (ϕ, r) and the longitudinal position z, k' is the wavenumber (which we are integrating over), and $f_m(k')$ are complex coefficients. The iteration over m is effectively a sum over multipoles in the transverse plane.

We now proceed by defining k in terms of k' (above) as:

$$k' = nk = n\frac{2\pi}{4L} = n\frac{45}{R} \tag{2.7}$$

where L is the physical length of one of the fringe field regions. We normalise to $4L$ because four fringe regions are required to produce a form similar to a wave in the longitudinal direction. This comprises one upstream fringe field (shown in Figure 2.5) followed by a downstream fringe field (effectively an upstream fringe reflected along the longitudinal axis), then followed by negated copies of the two, effectively producing a full waveform.

With this definition of k, we can convert the integral over wavenumbers to a sum over only the wavenumbers corresponding to an integer number of wavelengths within the analysis region (four fringe field lengths). We also select only the longitudinal sine terms (which fit the boundary condition $\psi(z = 0) = 0$). If we also define a new set of constants $A_{n,m}$, given by:

$$A_{n,m} = \begin{cases} 1 & \text{for } n = m = 0 \\ 2 & \text{for } n = 0 \text{ or } m = 0 \text{ exclusive} \\ 4 & \text{for } n > 0 \text{ and } m > 0 \end{cases}, \tag{2.8}$$

then we can write:

$$\psi = \sum_{m=0}^{\infty} \sum_{n=0}^{\infty} -A_{n,m}\, c_{n,m} \sin(nkz) e^{im\phi} \frac{I_m(nkr)}{nk}, \tag{2.9}$$

due to the reduction of both sum limits from $-\infty \to \infty$ to $0 \to \infty$. In doing this, we have changed the coefficients from $f_m(k')$ to $c_{n,m}$ and absorbed factors into these coefficients, and have made use of the fact that $I_{-m}(k) = I_m(k)$. It is also important to note the following special cases for the modified Bessel function:

$$\lim_{k' \to 0} \frac{I_m(k'r)}{k'} = \begin{cases} r & \text{for } m = 0 \\ r/2 & \text{for } m = 1 \\ 0 & \text{for } m > 1 \end{cases} \tag{2.10}$$

which are necessary to avoid a singularity in the $n = 0$ term.

With this expression for the potential, we can calculate the coefficients $c_{n,m}$ using a discrete Fourier transform (performed in Appendix D.2):

$$c_{n,m} = \frac{nk}{N_\phi N_z I_m(nkr_0)} \sum_{n_\phi=0}^{N_\phi-1} \sum_{n_z=0}^{N_z} e^{-m2\pi i n_\phi/N_\phi} \sin(n2\pi n_z/N_z)\psi(r_0,\phi,z) \tag{2.11}$$

where N_ϕ and N_z are the number of available modes in ϕ (number of ϕ samples, as ϕ is cyclical) and in z (number of z samples minus 1), respectively.

For this description to be of immediate use in BMAD, the field components must be calculated, requiring the derivative of the Modified Bessel Function:

$$\frac{dI_m(x)}{dx} = \begin{cases} I_1(x) & \text{for } m = 0 \\ \frac{1}{2}\Big(I_{m-1}(x) + I_{m+1}(x)\Big) & \text{for } m > 0 \end{cases}. \tag{2.12}$$

Hence, for the x- and y-components E_x and E_y we separate out the $m = 0$ cases (whose sum is $E_{x,m=0}$). As shown in Appendix D.3, the x-component is:

$$\begin{aligned} E_x = E_{x,m=0} + \sum_{n=0}^{\infty}\sum_{m=1}^{\infty} A_{n,m}\frac{\sin(nkz)}{2} \\ \Bigg(\mathbb{R}\mathrm{e}\,(c_{n,m}) \Big(I_{m-1}(nkr)\cos\big((m-1)\phi\big) + I_{m+1}(nkr)\cos\big((m+1)\phi\big)\Big) \\ - \mathbb{I}\mathrm{m}\,(c_{n,m}) \Big(I_{m-1}(nkr)\sin\big((m-1)\phi\big) + I_{m+1}(nkr)\sin\big((m+1)\phi\big)\Big)\Bigg) \end{aligned} \tag{2.13}$$

where $E_{x,m=0}$ can be calculated from the first case in (2.12):

$$E_{x,m=0} = \cos(\phi)\sum_{n=0}^{\infty} A_{n,0}\,\mathbb{R}\mathrm{e}\,(c_{n,0})\sin(nkz)I_1(nkr). \tag{2.14}$$

Following a similar procedure for E_y (shown in Appendix D.4), we obtain:

$$E_y = E_{y,m=0} - \sum_{n=0}^{\infty}\sum_{m=1}^{\infty} A_{n,m}\frac{\sin(nkz)}{2}$$
$$\Bigg(\mathbb{R}\mathrm{e}\,(c_{n,m}) \Big(I_{m-1}(nkr)\sin\big((m-1)\phi\big) - I_{m+1}(nkr)\sin\big((m+1)\phi\big)\Big)$$
$$+ \mathbb{I}\mathrm{m}\,(c_{n,m}) \Big(I_{m-1}(nkr)\cos\big((m-1)\phi\big) - I_{m+1}(nkr)\cos\big((m+1)\phi\big)\Big)\Bigg) \quad (2.15)$$

where, for $E_{y,m=0}$, we have:

$$E_{y,m=0} = \sin(\phi)\sum_{n=0}^{\infty} A_{n,0}\,\mathbb{R}\mathrm{e}\,(c_{n,0})\sin(nkz)I_1(nkr). \quad (2.16)$$

For E_z we obtain:

$$E_z = \sum_{n=0}^{\infty}\sum_{m=0}^{\infty} A_{n,m}\cos(nkz)I_m(nkr)\Big(\mathbb{R}\mathrm{e}\,(c_{n,m})\cos(m\phi) - \mathbb{I}\mathrm{m}\,(c_{n,m})\sin(m\phi)\Big) \quad (2.17)$$

which requires no special treatment for $m = 0$.

To obtain the coefficients $c_{n,m}$, we use $r_0 = 45\,\mathrm{mm}$, as was found to be a suitable choice for the multipole expansion. To fit to the electric potential, we use $N_\phi = 180$ (close to the 1 mm transverse resolution of the field map) and the longitudinal resolution of the supplied field map $N_z = 320$. The potentials at these points were calculated from the cartesian grid field points using the MatLab [53] 3D spline interpolation function, and are plotted in Figure 2.10.

To reproduce the field, the optimal multipole order limit of $m \leq 14$ is used with the longitudinal order limit of $n \leq 80$, corresponding to wavelengths spanning 5 or more data points longitudinally. The reproduced potential on the fitted surface is shown in Figure 2.11. Using a similar quantification method to that employed for the multipoles, we see that the potential and all field components agree to within 5% of the 23 kV and $10^6\,\mathrm{Vm}^{-1}$ peaks, respectively.

The fit was also compared to the field map (shown in Figure 2.12) on the transverse plane at half-degree increments in ring azimuth – see Figure 2.13 (more plots in Appendix D.5). The only substantial change in discrepancy occurs at the plate ends, where the field gradient is greatest.

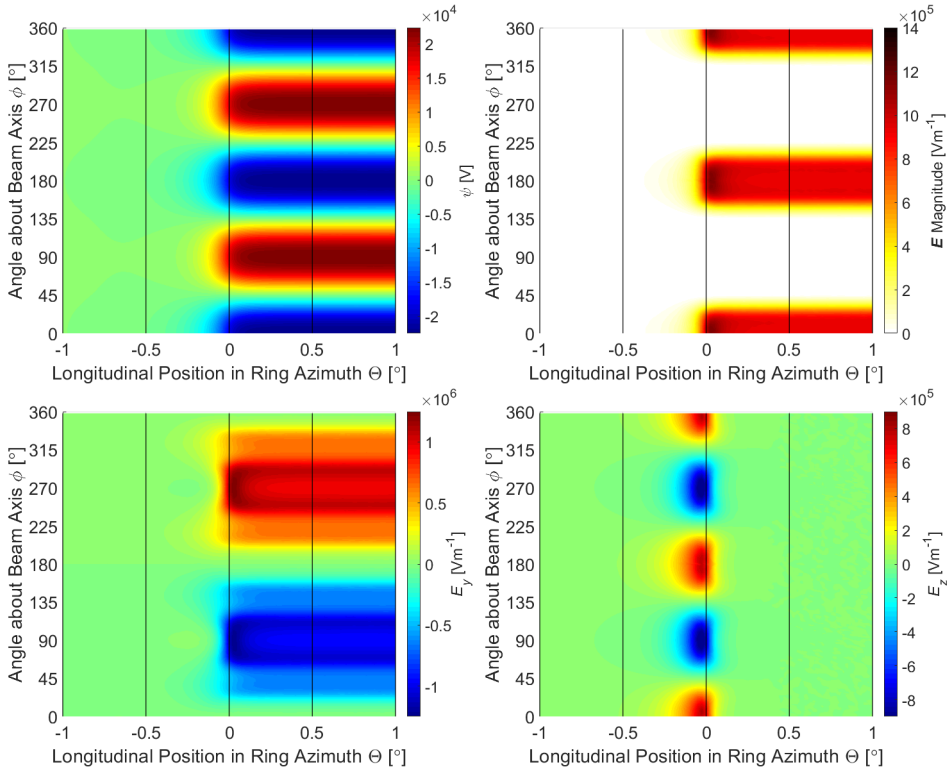

Figure 2.10: Interpolated quadrupole field map on the fitted surface with radius $r_0 = 45\,\text{mm}$ from the reference trajectory, shown for potential ψ (top-left), field magnitude E (top-right), E_y (bottom-left) and E_z (bottom-right).

To better understand how the field discrepancy changes with distance from the reference trajectory, in Figure 2.14 we plot the residuals of E_x with respect to longitudinal position (in ring azimuth) for various locations in x. The results here appear to confirm the improvement in fit closer to the origin, and show that the residuals at the edge of the storage region (on the fitted surface) at $r = 45\,\text{mm}$ are several times larger than those 10 mm closer to the reference trajectory.

As the description so far assumes a straight design trajectory, we investigated the asymmetry along the x-axis by looking at E_x along the design orbit in Figure 2.15. The on-axis field changes from zero on the order of $10^2\,\text{Vm}^{-1}$ on approach to the quadrupole, due to a dipole component in the fit. However the noise here appears to be of order $10^3\,\text{Vm}^{-1}$, so there is no

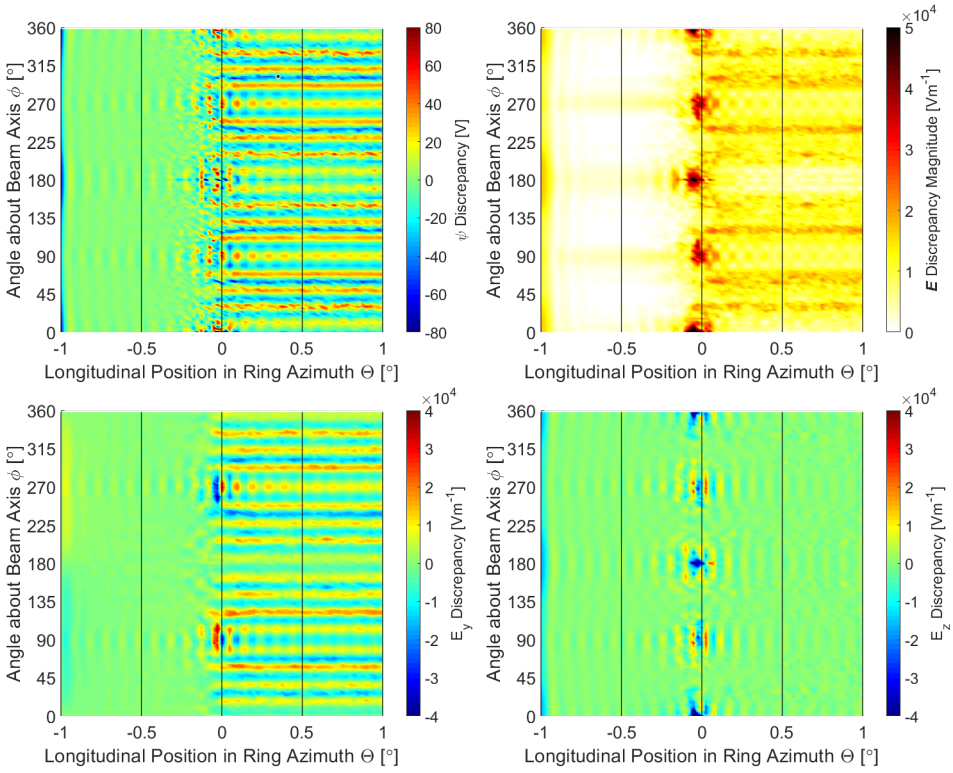

Figure 2.11: Difference between field map (shown in Figure 2.10) and field reproduced by the cylindrical harmonics description on the fitted surface with radius $r_0 = 45\,\text{mm}$ from the reference trajectory, shown for potential ψ (top-left), E_y (bottom-left) and E_z (bottom-right). The magnitude of the difference in field is shown in the top-right. We see a peak discrepancy of around $5 \times 10^4\,\text{Vm}^{-1}$, corresponding to 5% of the field value at the plate surfaces (although this is far above the field map noise of approximately $10^3\,\text{Vm}^{-1}$). Residuals of E_x, E_y and E_z are plotted separately in Appendix D.5.

evidence that this description is insufficient.

Noting again that we here assumed a straight reference trajectory to be sufficient, so on some small scale we are in violation of the divergence-free condition of Maxwell's equations, given this description is being applied to the curved storage ring.

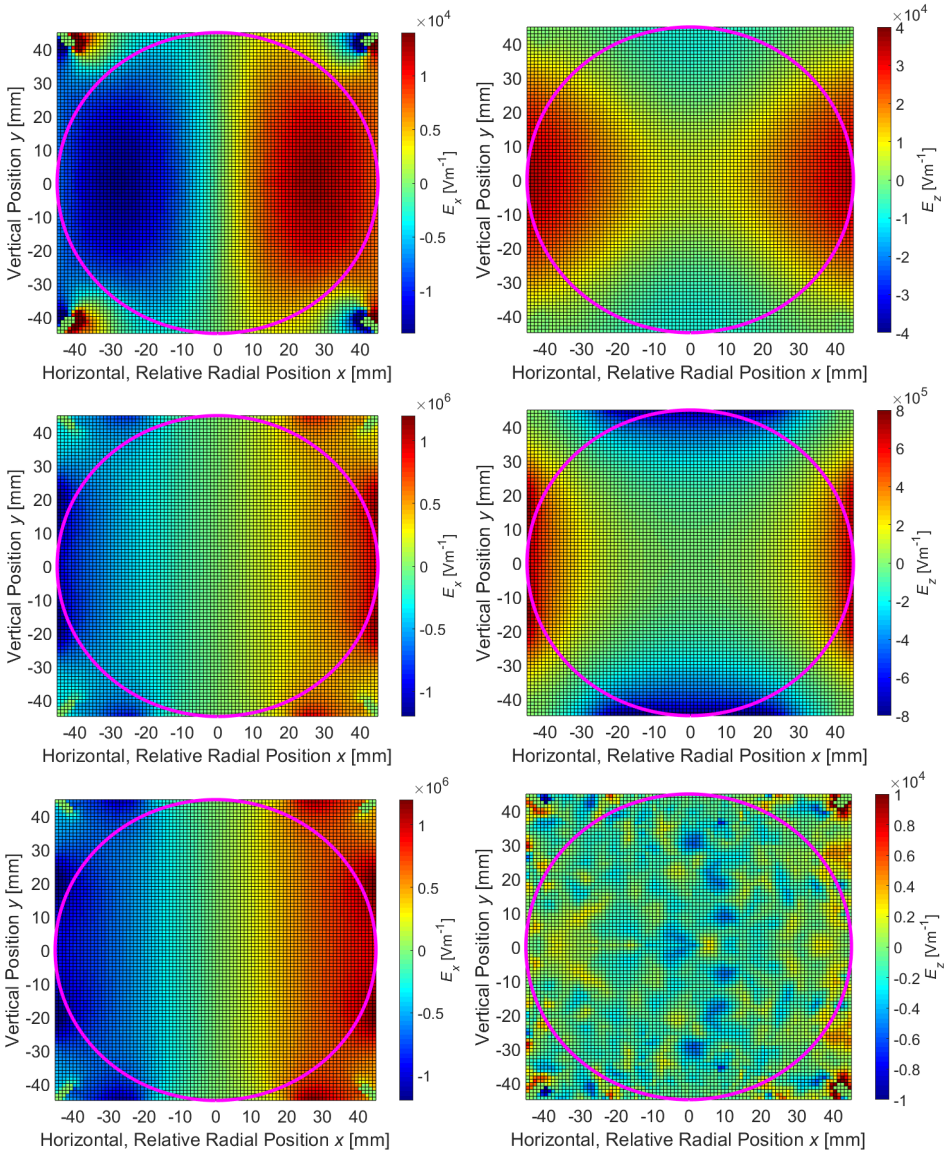

Figure 2.12: Field map components E_x (left column) and E_z (right column) on the transverse plane at 0.5° of ring azimuth before the quadrupole (top row), at the start of the quadrupole (middle row) and 0.5° of ring azimuth within the quadrupole (bottom row).

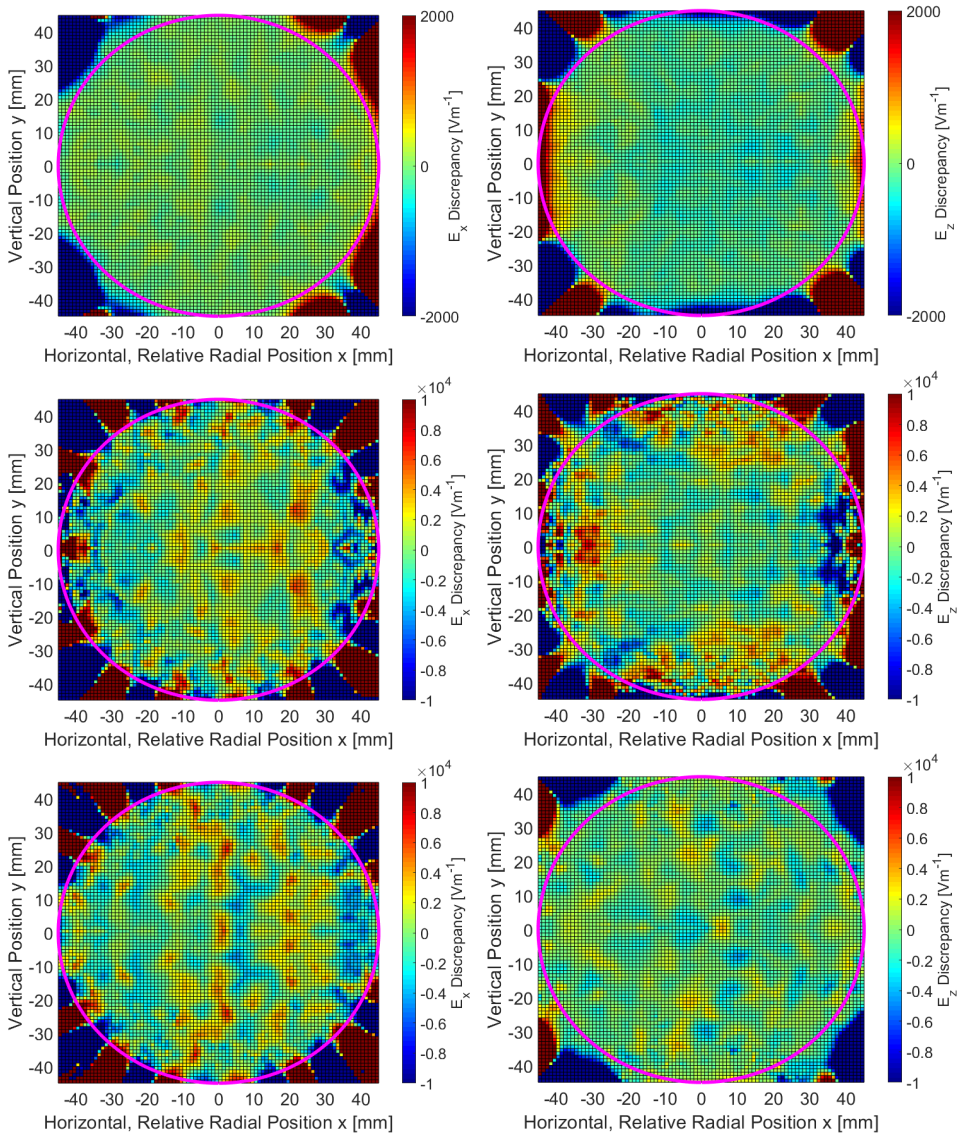

Figure 2.13: Difference between field map (shown in Figure 2.12) and field reproduced by the cylindrical harmonics description of E_x (left column) and E_z (right column) on the transverse plane at 0.5° of ring azimuth before the quadrupole (top row), at the start of the quadrupole (middle row) and 0.5° of ring azimuth within the quadrupole (bottom row). The residuals of the field components within the storage region at the plate ends (where the field peaks) peak at approximately $2 \times 10^4\,\mathrm{Vm}^{-1}$, which is 2% of the $10^6\,\mathrm{Vm}^{-1}$ field at the quadrupole plates. The average deviation of field within the storage region is $2.7 \times 10^3\,\mathrm{Vm}^{-1}$, which is between two and three times the noise level of the field map.

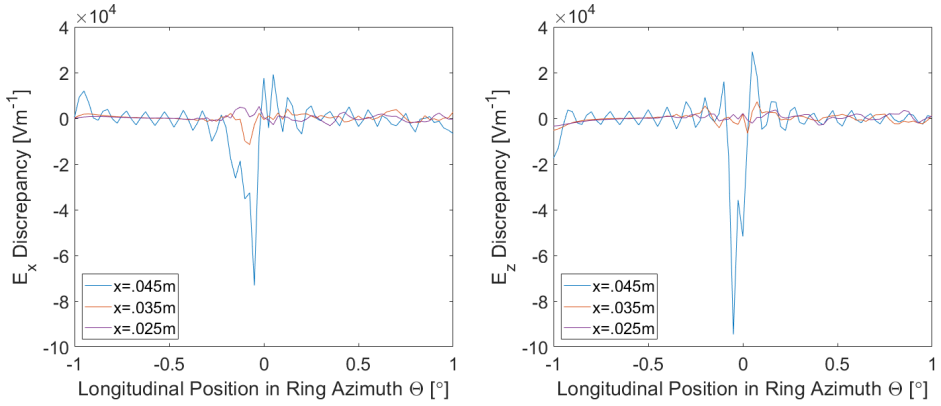

Figure 2.14: Residuals of E_x (left) and E_z (right) along ring azimuth, at $y = 0$ and $x = 45\,\text{mm}$ (blue), $x = 35\,\text{mm}$ (orange) and $x = 25\,\text{mm}$ (purple). The background wiggle is due to the limited number of longitudinal modes (of wavelength 0.1°).

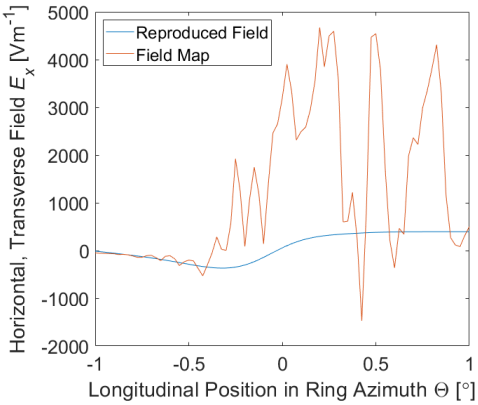

Figure 2.15: On-axis field component E_x, from field map (orange) and reconstructed field from the cylindrical harmonic description (blue), sampled over the fringe-field range of 1° of ring azimuth before the start of the quadrupole plates to 1° within the quadrupole. The noise in the field map values (taken as the random fluctuations in E_y along the x-axis, approximately $500\,\text{Vm}^{-1}$ to $1000\,\text{Vm}^{-1}$), on the order of 0.2% of the field strength at the quadrupole plates, is clearly more substantial than the field values from the reconstruction. Any effects due to curvature that we might have seen here in the field map data may be hidden in this noise, and so are not evident here.

2.3.5 Verifying the Model

The multipole and cylindrical harmonic descriptions of the bulk and fringe fields respectively, were implemented in BMAD and used for simulations to investigate tune. This is calculated in BMAD using one-turn tracking of particles with deviations of 10^{-5} in position (in metres) and (normalised) momentum from the reference trajectory. [54]

The locations in tune space of the design orbit particle, for different quadrupole potentials in a simulation, using the multipole bulk description and cylindrical harmonic fringe field description, were found to differ from those of the multipole bulk and field map fringes by 2×10^{-4} in both ν_x and ν_y.

We can conclude that the biggest change comes from replacing the field map of the quadrupole bulk field with the multipole description. This is to be expected, as the "bulk" covers a total of 140° of ring azimuth, as opposed to the 32° of ring azimuth covered by the fringe fields. The fringe fields also contain regions where the field drops off, so the bulk fields in fact have a greater effect than indicated by the ratio of azimuthal extents of the bulk and fringe field regions.

The tunes from the different descriptions, for quadrupole potentials of 20.5 kV and 15 kV, are tabulated in Table 2.2 with tunes from the storage ring model developed at MSU [55] and those measured in the machine [24].

Table 2.2: Tunes for the ring with electric fields described by different permutations of field maps, multipoles and cylindrical harmonics, at quadrupole potentials of 20.5 kV and 15 kV. We see that using field maps for the bulk description causes the tunes to be differ from the others by 5×10^{-3} in ν_y, and to be further from the measured tunes, while changing the fringe field description results in a negligible difference (with respect to the accuracy of measurement of the machine tunes of 10^{-3} [24]). The tunes from the continuous descriptions of the quadrupole bulk also agree with those of the MSU model of the storage ring [55, 56].

Bulk / Fringe Description	(ν_x, ν_y) at 20.5 kV	(ν_x, ν_y) at 15 kV
Field Map/Field Map	0.9372, 0.3573	0.9543, 0.3051
Multipole/Field Map	0.9376, 0.3507	0.9547, 0.2998
Multipole/Cylindrical Harm.	0.9377, 0.3499	0.9547, 0.2990
MSU Model	0.9376, 0.3503	0.9547, 0.2993
Machine Measurement	0.9381, 0.3480	0.9551, 0.2969

We notice that the difference in tunes between using the field map and cylindrical harmonic fringe field descriptions are on the order of 10^{-4}. Com-

pared to the accuracy level of the measured machine tunes (10^{-3}), we may consider these tunes identical. However, the changes in tune resulting from switching the description of the quadrupole bulk field, also plotted in Figure 2.9, are on the order of 10^{-3} in ν_y, which is substantial with respect to the measured tune accuracy. Using field maps for the description of the bulk field also moves the tunes further from those of the MSU model and machine.

2.4 Particle Tracking Methods

A proper understanding of the tracking results from a simulation, requires knowledge of the techniques used in the code to integrate the equations of motion. Two such methods have been employed for these studies: a fourth-order, time-based, Runge–Kutta integrator, integral to BMAD, and a new symplectic integrator, intended to make tracking faster and symplectic whilst maintaining sufficient accuracy for tracking over thousands of ring orbits.

2.4.1 BMAD's Runge–Kutta Integrators

The path integrators available in BMAD, for tracking particles through field maps, are fourth-order Runge–Kutta integrators, one of which uses longitudinal displacement s for the independent variable, while the other integrator is time-based.

Although the position-based R–K integrator is more efficient than the time-based integrator (due to the field depending on location), the ease with which the time-based integrator can be used to effect particle decay makes it the preferred choice. Apart from the differing independent variable, the two integrators use the same adaptive-step, fourth-order integration.

In BMAD, these methods also incorporate spin tracking, using the fields calculated for the coordinate tracking to calculate the precession of the particle spin axis. BMAD performs spin tracking by integrating the equation of motion of the spin vector in the local frame which, in a curved reference trajectory, is [32, 57]:

$$\frac{d\boldsymbol{S}}{ds} = \left(\frac{1 + \boldsymbol{r} \cdot \boldsymbol{r}_{\text{Bend}}}{c\beta_z} \left(\omega_s + \omega_{\text{EDM}} \right) - \boldsymbol{r}_{\text{Bend}} \times \hat{\boldsymbol{z}} \right) \times \boldsymbol{S} \tag{2.18}$$

where $\boldsymbol{r}$ is the particle position in local coordinates and $c\beta_z$ is the component of velocity parallel to to the design trajectory (the z-axis). The frequencies ω_s and ω_{EDM} are the T-BMT precession frequency (due to the magnetic dipole moment, equation given in Appendix A) and the spin precession frequency due to an electric dipole moment respectively. The vector $\boldsymbol{r}_{\text{Bend}}$ represents the local curvature (pointing radially outward such that, at all points in the

$g-2$ ring, $\boldsymbol{r}_{\text{Bend}} = (h, 0, 0)$ where $h = \rho^{-1}$). A summary of this and other spin tracking methods can be found in [58].

In Figure 4.21 in Section 4.4.3, we demonstrate that the polarisation precession simulated by BMAD is accurate to within 1 ppm over 2000 ring turns (corresponding to approximately half of the experiment storage period). The simulation is not expected to perform to higher accuracy than 1 ppm, given that the simulation is performed with double-precision numbers, and can thus have an expected accuracy of roughly single-precision numbers of circa six significant figures (and the electric fields represented by the multipole in Figure 2.8 are only accurate to approximately 100-1000 ppm). We thus consider the spin tracking to be sufficiently accurate for this usage case.

2.4.2 Explicit Symplectic Integrator for Static Electric Fields in Curved Coordinate Systems

The purpose of developing a new integrator is to attempt to provide a method for fast, symplectic (energy-conserving) tracking through a general (3D) static electric field in a curved reference trajectory (with uniform vertical magnetic field). Tracking time is the critical problem to address, as although the Runge–Kutta integrator is highly accurate, the time taken to perform simulations would be on the order of months for a complete fill of $600,000$ antimuons. It is also noted that other simulation teams (based on Geant4 and BMAD) also use R–K integration, so a new integrator would remove this similarity, and thus be desirable from the perspective of simulation diversity.

The second such weakness we wish to address is that of symplecticity, whereby particles tracked with the Runge–Kutta integrator can unphysically gain/lose momentum/energy over many turns of the storage ring. To address this, we make use of a Wu–Forest–Robin integrator [59], tailored for motion in static electric fields in a static, uniform dipole magnet.

The development of the integrator starts with the exact Hamiltonian H for a charged particle in a static electric field with potential field ψ and static, uniform magnetic field with vector potential $\boldsymbol{A} = (A_x, A_y, A_z)$ [12]:

$$H = \frac{\tilde{\delta}}{\beta_0} - (1+hx)\left(a_s + \sqrt{\left(\tilde{\delta} + \frac{1}{\beta_0} - \tilde{\psi}\right)^2 - (\tilde{p_x} - a_x)^2 - (\tilde{p_y} - a_y)^2 - \frac{1}{\beta_0^2\gamma_0^2}}\right) \tag{2.19}$$

where the field potentials scaled by the design momentum P_0 are:

$$\boldsymbol{a} = \frac{q\boldsymbol{A}}{P_0}, \qquad \tilde{\psi} = \frac{q\psi}{P_0 c}. \tag{2.20}$$

The canonical, transverse conjugate momenta $\tilde{p_x}$ and $\tilde{p_y}$ are:

$$\tilde{p}_x \;=\; \frac{\gamma m v_x}{P_0} + a_x \;=\; p_x + a_x, \qquad \tilde{p}_y \;=\; \frac{\gamma m v_y}{P_0} + a_y \;=\; p_y + a_y \tag{2.21}$$

and the longitudinal conjugate momentum is:

$$\tilde{\delta} \quad = \quad \frac{E}{P_0 c} - \frac{1}{\beta_0} + \tilde{\psi} \quad = \quad \frac{1}{\beta_0}\left(\frac{\gamma}{\gamma_0} - 1\right) + \tilde{\psi} \tag{2.22}$$

(where $\beta_0 = v_0/c$), or, written in terms of the normalised momentum deviation δ (used in BMAD):

$$\tilde{\delta} = \sqrt{(\delta+1)^2 + \frac{1}{\beta_0^2\gamma_0^2}} - \frac{1}{\beta_0} + \tilde{\psi}. \tag{2.23}$$

Since the electric field varies with longitudinal position, we need to treat the position s as a canonical variable, rather than use it as the independent variable in the Hamiltonian system. This requires the introduction of a new, independent variable σ, and a new variable p_s, which is the conjugate momentum to s. The Hamiltonian can then be written as $K(x, \tilde{p_x}, y, \tilde{p_y}, z, \tilde{\delta}, s, p_s; \sigma)$. If we assume the only magnetic field is transverse and uniform (the general case is investigated in Section 3.2), then only the s-component of $\boldsymbol{a}$ is required and the the canonical momenta reduce to the kinematic momenta ($\tilde{p_x} = p_x$, $\tilde{p_y} = p_y$). Hence, we obtain:

$$K = p_s + \frac{\tilde{\delta}}{\beta_0} - (1+hx)\left(a_s + \sqrt{\left(\tilde{\delta} + \frac{1}{\beta_0} - \tilde{\psi}\right)^2 - p_x^2 - p_y^2 - \frac{1}{\beta_0^2\gamma_0^2}}\right). \tag{2.24}$$

If we assume a constant, uniform, vertical dipole field, described purely by $\boldsymbol{a} = (0, 0, a_s)$, then we can use the expression for a_s [12] (which is shown in Appendix E.1 to be that for a dipole):

$$a_s = -k_0 x\left(1 - \frac{hx}{2(1+hx)}\right), \tag{2.25}$$

where the second term is due to the curvilinear coordinate system. This term describes the magnetic "weak focusing" of particles in the ring (which is partially counteracted by the horizontal defocusing of the electrostatic quadrupoles).

In (2.24), we assume that all dynamic variables are sufficiently small for a Taylor expansion (the paraxial approximation). By performing a Taylor expansion to third order (performed in Appendix E.2), K can be approximated as:

$$K \approx H_1 + H_2 + H_3 - 1. \tag{2.26}$$

Where and H_1, H_2 and H_3 are integrable Hamiltonian terms, containing terms of various orders in the dynamical variables. These are chosen here to be:

$$H_1 = p_s + \frac{p_x^2 + p_y^2}{2}\left(1 - \frac{\delta}{\beta_0}\right) + \frac{hk_0x^2}{2}, \tag{2.27}$$

$$H_2 = \frac{\tilde{\psi}}{\beta_0} + \frac{(\tilde{\psi}-\delta)^2}{2\beta_0^2\gamma_0^2}\left(1 + hx + \frac{\tilde{\psi}-\delta}{\beta_0}\right) + (k_0 - h)x + \frac{\tilde{\psi}-\delta}{\beta_0}hx, \tag{2.28}$$

$$H_3 = \frac{p_x^2 + p_y^2}{2}\left(\frac{\tilde{\psi}}{\beta_0} + hx\right). \tag{2.29}$$

Following the Wu–Forest–Robin method [59], the map generated by K can be produced (approximately) by combining the component Hamiltonian maps:

$$e^{-\Delta s:K:} \approx e^{-\frac{\Delta s}{2}:H_1:} e^{-\Delta s:H_2:} e^{-\frac{\Delta s}{2}:H_1:}. \tag{2.30}$$

We have discarded H_3 because it is third-order in the dynamic variables and therefore small, and is not integrable. While H_1 can be integrated, and represents a simple harmonic oscillator for the conjugate pair (x, p_x) (as the relevant terms can be written $ax^2 + bp_x^2$), the remaining part H_2 is not directly integrable.

For the dynamic variable transformations corresponding to the map generated by the Hamiltonian, we can make use of Hamilton's equations:

$$\frac{d\boldsymbol{p}}{d\sigma} = -\frac{\partial H}{\partial \boldsymbol{q}}, \qquad \frac{d\boldsymbol{q}}{d\sigma} = \frac{\partial H}{\partial \boldsymbol{p}} \tag{2.31}$$

where $\boldsymbol{p} = (p_x, p_y, \delta, p_s)$ and $\boldsymbol{q} = (x, y, z, s)$. Using the fact that H_1 represents simple harmonic motion in the x direction, the transformations (in Appendix E.3) $e^{\frac{-\Delta s}{2}:H_1:}$ can be expressed:

$$e^{-\frac{\Delta s}{2}:H_1:}x = x\cos\left(\frac{\Delta s}{2}\omega\right) + \frac{\omega}{hk_0}p_x\sin\left(\frac{\Delta s}{2}\omega\right), \tag{2.32}$$

$$e^{-\frac{\Delta s}{2}:H_1:}y = y + \frac{\Delta s}{2}\left(1 - \frac{\delta}{\beta_0}\right)p_y, \tag{2.33}$$

$$e^{-\frac{\Delta s}{2}:H_1:}z = z - \frac{\Delta s}{2}\frac{p_x^2 + p_y^2}{2\beta_0}, \tag{2.34}$$

$$e^{-\frac{\Delta s}{2}:H_1:}s = s + \frac{\Delta s}{2}, \tag{2.35}$$

$$e^{-\frac{\Delta s}{2}:H_1:}p_x = p_x\cos\left(\frac{\Delta s}{2}\omega\right) - \frac{hk_0}{\omega}x\sin\left(\frac{\Delta s}{2}\omega\right), \tag{2.36}$$

where

$$\omega = \sqrt{\left(1 - \frac{\delta}{\beta_0}\right) hk_0}, \tag{2.37}$$

and the transformations of the remaining momenta are the identity (no change). Of course, using the paraxial approximation further, the transformations for x and p_x can instead be written as:

$$e^{-\frac{\Delta s}{2}:H_1:}x = x + \frac{\Delta s}{2}\left(1 - \frac{\delta}{\beta_0}\right)p_x, \tag{2.38}$$

$$e^{-\frac{\Delta s}{2}:H_1:}p_x = p_x - \frac{\Delta s}{2}hk_0 x. \tag{2.39}$$

It is evident that, in the case of small Δs, these transformations are equivalent to those in (2.32) and (2.36). Typically, the calculation of a square-root is expensive, although the loss in accuracy from using (2.38) and (2.39) will require more integration steps. We will investigate both here.

As H_2 is not directly integrable, we transform the dynamic variables with a mixed-variable generating function of the third kind [60] $F_3(\boldsymbol{Q}, \boldsymbol{p}; \sigma)$:

$$F_3 = \tilde{\psi}(X, Y, S)Z - Xp_x - Yp_y - Z\delta - Sp_s, \tag{2.40}$$

where $\boldsymbol{Q} = (X, Y, Z, S)$ and $\tilde{\boldsymbol{P}} = (P_X, P_Y, P_Z, P_S)$ are the post-transformation variables. From this, we can calculate the relationships between the pre- and post-transformation dynamic variables:

$$\boldsymbol{Q} = -\frac{\partial F_3}{\partial \boldsymbol{p}} = \boldsymbol{q}, \tag{2.41}$$

$$P_X = -\frac{\partial F_3}{\partial X} = p_x - Z\frac{\partial \tilde{\psi}}{\partial X}, \tag{2.42}$$

$$P_Y = -\frac{\partial F_3}{\partial Y} = p_y - Z\frac{\partial \tilde{\psi}}{\partial Y}, \tag{2.43}$$

$$P_Z = -\frac{\partial F_3}{\partial Z} = \delta - \tilde{\psi}, \tag{2.44}$$

$$P_S = -\frac{\partial F_3}{\partial S} = p_s - Z\frac{\partial \tilde{\psi}}{\partial S}. \tag{2.45}$$

Given this transformation, H_2 can be re-written as:

$$H_2 = \frac{\tilde{\psi}}{\beta_0} + \frac{P_Z^2}{2\beta_0^2\gamma_0^2}\left(1 + hX - \frac{P_Z}{\beta_0}\right) + (k_0 - h)X - \frac{P_Z}{\beta_0}hX, \tag{2.46}$$

which can be integrated. Using the same method as for H_1 (shown in Appendix E.3), the map $e^{-\Delta s:H_2:}$ can be shown to transform these variables

as:

$$e^{-\Delta s:H_2:}Z = Z - \Delta s\left(\frac{h}{\beta_0}X - \frac{P_Z}{\beta_0^2\gamma_0^2}\left(1 + hX - \frac{3P_Z}{2\beta_0}\right)\right), \tag{2.47}$$

$$e^{-\Delta s:H_2:}P_X = P_X - \Delta s\left(\frac{1}{\beta_0}\left(\frac{\partial\tilde{\psi}}{\partial X} - hP_Z\right) + \frac{hP_Z^2}{2\beta_0^2\gamma_0^2} - (k_0 - h)\right), \tag{2.48}$$

$$e^{-\Delta s:H_2:}P_Y = P_Y - \frac{\Delta s}{\beta_0}\frac{\partial\tilde{\psi}}{\partial Y}, \tag{2.49}$$

$$e^{-\Delta s:H_2:}P_S = P_S - \frac{\Delta s}{\beta_0}\frac{\partial\tilde{\psi}}{\partial S}, \tag{2.50}$$

where the transformations of the X,Y,S and P_Z are the identity (no change). After performing this operation, the variables must be transformed back to the original set of dynamic variables $(\boldsymbol{q}, \boldsymbol{p})$, using (2.41), before applying $e^{-\frac{\Delta s}{2}:H_1:}$ again.

We wish to compare the speed and accuracy of the two versions of the integrator; the first "approximated" integrator using the operations in (2.38) and (2.39), and the "standard" integrator using the operations in (2.32) and (2.36). To do this, particles with 10 mm deviations from the design orbit in both the x and y-axes were tracked for 1000 turns of an hypothetical storage ring, where the electric multipole description in Section 2.3.3 was applied over the entire ring azimuth. The tracking was performed with a step of $\Delta s = .01$ m, corresponding to approximately 4.5 million steps.

For the case of the x-axis, we consider the action:

$$J_x = \frac{\gamma_x x^{*2} + 2\alpha_x x^* p_x^* + \beta_x p_x^{*2}}{2} \tag{2.51}$$

where the Twiss parameters α_x, β_x and γ_x are calculated for the new integrator in Appendix F and x^* and p_x^* are the dispersion-corrected position and momentum respectively:

$$x^* = x - \eta_x\delta, \qquad p_x^* = p_x - \eta_x'\delta. \tag{2.52}$$

As the value of J_x should be constant for symplectic tracking, we investigate the behaviour of J_x for both versions of the integrator, for 1 mm steps over 50 ring turns. The hypothetical ring uses the cylindrical harmonic fringe fields described in Section 2.3.4 and assumes the bulk regions to be identical to the field at the inside end of the fringe region.

The results shown in Figure 2.16 reveal that the action for the approximated integrator shows a steady, systematic increase with distance tracked,

but the action in the exact integrator does not. The simulation time for both integrators (implemented in MatLab [53]) for these 50 turns was virtually identical, so the integrator using the coordinate operations in (2.32) and (2.36) is clearly preferable. The other version should be discarded, given antimuons will be tracked around the ring on the order of 10^3 times.

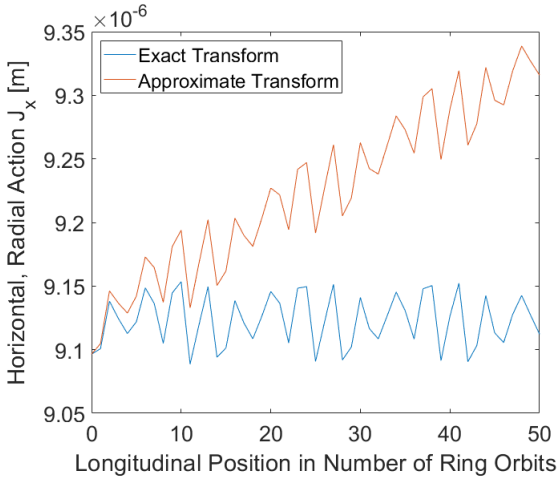

Figure 2.16: Horizontal action of particle tracked 50 times around the ring with integration steps of $\Delta s = 1\,\text{mm}$ with both the standard version of the new integrator (blue) and the approximated version (orange). Particle was initiated with $x = y = .01\,\text{m}$. The integrator with approximate x-axis transforms can be seen to increase steadily with tracked distance, while the "exact" version of the integrator is constant.

To compare the symplectic integrator with the BMAD Runge–Kutta integrator, the same ring setup was used, and a particle with only non-zero coordinates was tracked for 30 turns, with steps of $\Delta s = 1\,\text{mm}$ taken in the symplectic integrator. The phases:

$$\phi_x = \arctan\left(-\beta_x \frac{p_x^*}{x^*} - \alpha_x\right), \qquad \phi_y = \arctan\left(-\beta_y \frac{p_y}{y} - \alpha_y\right) \tag{2.53}$$

(where we ignore the negligible vertical dispersion) and actions in the x and y directions are shown in Figure 2.17.

For the actions: we see both integrators agreeing and maintaining the actions as constant to within 3 s.f. for the horizontal action, and to approximately the numerical precision for the vertical action. For the phases: we see differences oscillate but are bounded within $10^{-3}\,\text{rad}$, while the phases linearly increase with tracked distance. This suggests that the phase differ-

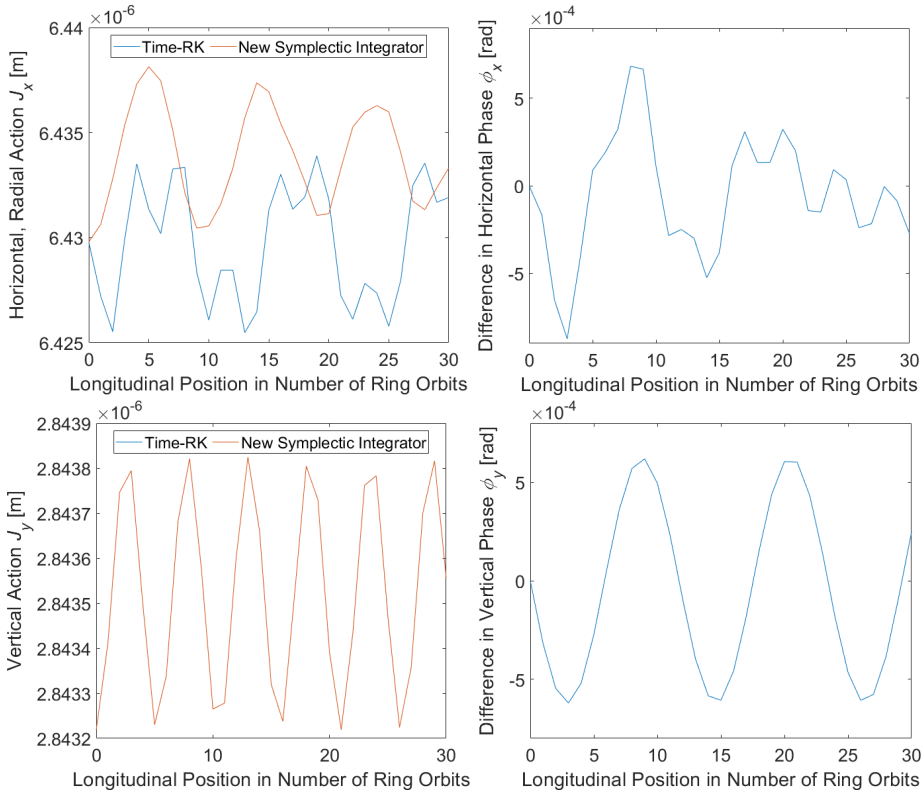

Figure 2.17: Horizontal (top-left) and vertical (bottom-left) action of particle tracked 30 times around the ring with BMAD's time-based adaptive-step Runge–Kutta integrator (blue) and the new symplectic integrator with steps of $\Delta s = 1\,\text{mm}$ (orange), with the differences in horizontal (top-right) and vertical (bottom-right) phases between the two integrators. We compare the actions and phases (as opposed to the usual phase space variables) because these take in to account the oscillating of the particles around the ring, so that subtle differences in tracking results are clearer. The horizontal actions agree to the third significant figure, with the visible oscillation possibly due to a slight mismatch in horizontal Twiss parameters or dispersion, while the vertical actions agree down to $10^{-12}\,\text{m}$ (close to the numerical precision available), hence why only one line is visible. The phase differences appear to oscillate, which may again be due to the accuracy of the supplied Twiss parameters. As neither the actions nor phases appear to have a disagreement which increases with tracking distance, as one might expect from comparison between symplectic and non-symplectic integrators, we conclude that the integrator could be implemented for use in long-term tracking.

ences will not increase over a longer tracking distance, and thus that the new integrator may be suitable for tracking over thousands of turns.

We note that the studies performed using the new integrator used 1 mm steps and that, for the new integrator to be a viable alternative for tracking, an adaptive-step algorithm must be implemented (similar to that used by the Runge–Kutta integrator in BMAD). The integrator does not track particle spins, so would also require the addition of a spin integrator. As both of these features are already incorporated in to the Runge–Kutta integrator in BMAD, and as we shall derive another integrator later (compatible with more general magnetic fields), we shall continue to use the time Runge–Kutta integrator in BMAD for the following field and beam/spin dynamics studies.

Chapter 3

Modelling of Curvilinear Elements

A significant challenge for modelling the beam dynamics in the Fermilab Muon $g-2$ storage ring is the curvature of the elements along the design trajectory within the constant, uniform dipole field. Efforts have been made to develop a curvilinear field description [35, 36, 37]. However, we find here that the existing descriptions are insufficient for the robust, accurate modelling required for the experiment.

3.1 Expanding Quadrupole Bulk Fields as Curvilinear Multipoles

As described by McMillan, Mane and Zolkin [35, 36, 37], the longitudinally-invariant field of a curved beamline element can be given in terms of solutions for the potential ψ to the Laplacian for a cylindrical coordinate system with no variation along the beamline:

$$\Delta\psi = 0 = \frac{1}{\tilde{R}}\frac{\partial}{\partial\tilde{R}}\left(\tilde{R}\frac{\partial\psi}{\partial\tilde{R}}\right) + \frac{\partial^2\psi}{\partial\tilde{y}^2} \tag{3.1}$$

where $\tilde{R} = R/\rho = (x+\rho)/\rho$, and $\tilde{y} = y/\rho$ (for ring radius ρ). These solutions take the forms:

$$\psi_m^{\mathbb{R}\mathrm{e}} = -\sum_{p=0}^{\mathrm{flr}(m/2)} \frac{(i\tilde{y})^{2p}}{m}\begin{pmatrix} m \\ 2p \end{pmatrix} F_{m-2p}(\tilde{R}) \tag{3.2}$$

$$\psi_m^{\mathbb{I}\mathrm{m}} = \sum_{p=0}^{\mathrm{flr}((m-1)/2)} i\frac{(i\tilde{y})^{2p+1}}{m}\begin{pmatrix} m \\ 2p+1 \end{pmatrix} F_{m-2p-1}(\tilde{R}) \tag{3.3}$$

where $\binom{n}{r}$ is the ${}_nC_r$ binomial coefficient (combination) operator, $\psi_m^{\mathbb{R}\mathrm{e}}$ and $\psi_m^{\mathbb{I}\mathrm{m}}$ are solutions representing the skew and normal components, respectively, and the *flr* function is the floor (round-down) function.

The functions F_p can be expressed:

$$F_p(\tilde{R}) = \sum_{n=0}^{\mathrm{flr}(p/2)} \tilde{R}^{2n} \left(\alpha_{p,n} \log(\tilde{R}) + \beta_{p,n} \right) \tag{3.4}$$

where $\alpha_{p,n}$ and $\beta_{p,n}$ satisfy:

$$\alpha_{0,0} = 0, \quad \beta_{0,0} = 1; \qquad \alpha_{1,0} = 1, \quad \beta_{1,0} = 0; \tag{3.5}$$

$$(\alpha, \beta)_{>1,0} = (p^2 - p) \sum_{k=1}^{\mathrm{flr}(p/2)} \left(\frac{\alpha_{p-2,k-1} - 2k\beta_{p-2,k-1}}{4k^2}, \frac{\alpha_{p-2,k-1} - k\beta_{p-2,k-1}}{4k^3} \right); \tag{3.6}$$

$$(\alpha,\, \beta)_{>1,>0} = (p^2 - p) \left(\frac{\alpha_{p-2,n-1}}{4n^2}, \frac{n\beta_{p-2,n-1} - \alpha_{p-2,n-1}}{4n^3} \right). \tag{3.7}$$

With these definitions, the electric scalar potential can be written as:

$$\psi = \sum_{m=1}^{\infty} \rho^m \left(a_m \psi_m^{\mathbb{I}\mathrm{m}} + b_m \psi_m^{\mathbb{R}\mathrm{e}} \right) \tag{3.8}$$

where we note there is no $m = 0$ solenoid term, as the bulk field has zero longitudinal component. This potential results in the electric field:

$$\boldsymbol{E} = -\sum_{m=1}^{\infty} \rho^m \left(a_m \boldsymbol{\nabla} \psi_m^{\mathbb{I}\mathrm{m}} + b_m \boldsymbol{\nabla} \psi_m^{\mathbb{R}\mathrm{e}} \right) \tag{3.9}$$

where a_m and b_m are coefficients for the normal and skew components, respectively, to be determined by fitting.

As demonstrated in [61], the fitting can be performed by making use of the fact that F_p is independent of the y coordinate, and making use also of quadrupole symmetry, whereby we assume the absence of all poles of odd order such that $a_{\mathrm{odd}} = b_{\mathrm{odd}} = 0$. If we also assume that only skew multipoles are present ($a_m = 0$), and take the value $x = 0$ (such that $\tilde{R} = 1$), we may simplify the expression for F_p so that the expression for ψ becomes:

$$\psi(x = 0) = \sum_{m=1}^{\infty} \rho^m b_m \left(-\sum_{p=0}^{\mathrm{flr}(m/2)} \frac{(i\tilde{y})^{2p}}{m} \begin{pmatrix} m \\ 2p \end{pmatrix} \sum_{n=0}^{\mathrm{flr}(m/2-p)} \beta_{m-2p,n} \right) \tag{3.10}$$

and so the expression for E_y becomes:

$$E_y(x=0) = \sum_{m=1}^{\infty} \rho^{m-1} b_m \left(\sum_{p=1}^{\mathrm{flr}(m/2)} \frac{2p}{m} i^{2p} \tilde{y}^{2p-1} \begin{pmatrix} m \\ 2p \end{pmatrix} \sum_{n=0}^{\mathrm{flr}(m/2-p)} \beta_{m-2p,n} \right), \tag{3.11}$$

where we have removed the first term of the sum over p, which is zero for $p = 0$. As this expression is simply a polynomial in $\tilde{y}$, it may be fitted to the E_y field map to fix the coefficients b_m.

3.1.1 Fitting to Field Maps

To fit the expression (3.11) to a bulk field map, a polynomial of even-only orders up to $m = 12$ is fitted to the E_y field along the y-axis at $x = 0$. The fit can be written:

$$E_{y\mathrm{Fit}}(x=0) = \sum_{m=1}^{6} A_{2m} y^{2m}. \tag{3.12}$$

Then, we can obtain expressions for the relevant A_m in terms of the coefficients b_m of the curvilinear multipole by expanding the expression for E_y in (3.11) over multipole orders $m \leq 12$ for even orders only. As demonstrated in Appendix G, the result for ψ is:

$$\psi(x=0) = \sum_{m=1}^{6} (-1)^{m+1} \frac{b_{2m}}{2m} y^{2m} \tag{3.13}$$

which leads to the result for E_y:

$$E_y(x=0) = \sum_{m=1}^{6} (-1)^m b_{2m} y^{2m-1}. \tag{3.14}$$

Hence, the resulting expression for the coefficients b_m of the curvilinear multipole in terms of polynomial fit coefficients A_m is:

$$b_m = (-1)^{\frac{m}{2}} A_m \qquad \text{for even } m. \tag{3.15}$$

The polynomial fit was performed in Microsoft Excel, using a 12th-order polynomial with only even powers (fit shown in Figure 3.1). This was applied to the range $-48\,\mathrm{mm} \leq y \leq 48\,\mathrm{mm}$, chosen as it was found that this provided the best agreement with the field maps. The values for A_m found from the fitting, and the resulting b_m are shown in Table 3.1, with the fit exhibiting an average deviation from the field map values of $587\,\mathrm{Vm}^{-1}$, which is .06% of the field at the plates.

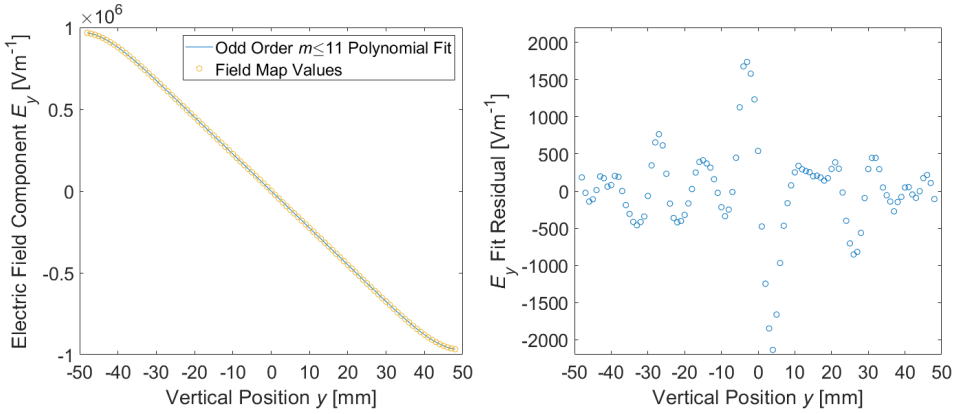

Figure 3.1: Plot of the y-component of electric field in the quadrupole bulk versus vertical position relative to the beamline at $x = 0$ (left), with data from both the field map (yellow) and the odd-order, $m \leq 11$ polynomial fit (blue), and a plot of the residuals for E_y along the fit line (right). The fit was made for values in the range $-48\,\text{mm} \leq y \leq 48\,\text{mm}$, chosen because of the optimal agreement with the field map (see Figure 3.2). The RMS deviation of the sets is $587\,\text{Vm}^{-1}$, approximately .06% of the field at the plates (where $y = \pm 50\,\text{mm}$) indicating a good fit to roughly the noise level of the field map (taken as the random fluctuations in E_y along the x-axis, approximately $500\,\text{Vm}^{-1}$ to $1000\,\text{Vm}^{-1}$).

With these coefficients, the transverse bulk field components were calculated at points in space on the same grid as the field map, and compared with those from the field map (Figure 2.7 in Chapter 2). The results of this comparison are shown in Figure 3.2, and exhibit an RMS deviation in electric field of $5.0 \times 10^4\,\text{Vm}^{-1}$ within the storage region, which is more than two orders of magnitude greater than the same deviation calculated for the standard multipole fit, of $15\,\text{Vm}^{-1}$.

There is clearly difficulty in fitting this curvilinear multipole to accurately reflect the field maps, partly due to the fact that different terms in a polynomial fit are not orthogonal, unlike those from a Fourier series. The other reason is that the fit is not performed on a surface enclosing the volume of interest, as was the case for the multipole description in Section 2.3.3 and for the cylindical harmonic description in Section 2.3.4. Because of these shortcomings, the standard multipole may be considered to provide a superior description of the fields despite not obeying Maxwell's equations in the curved coordinate system of the storage ring. However, we shall see more suitable methods developed in Section 3.3.

Table 3.1: Fit coefficients for a quadratic of even order up to order 12 of the quadrupole bulk electric potential along the line $x = 0$ for $-48\,\text{mm} \leq y \leq 48\,\text{mm}$ (left), and the resulting values of the b_m coefficient for the relevant curvilinear multipole (right). The latter have also been multiplied by the m-th power of the multipole expansion radius used in Section 2.3.3, so that the relative multipole strengths here may be compared to those of the straight multipole. As with the straight multipole case, the most prevalent multipoles are the $m = 2$ quadrupole and the $m = 10$ 20-pole, with the coefficient for the former between 10^1 and 10^2 times greater than those of the other even, skew multipoles.

m	A_m [Vm^{-m}]
2	-2.262×10^7
4	2.719×10^8
6	-4.182×10^{11}
8	1.265×10^{14}
10	1.839×10^{17}
12	-4.093×10^{19}

m	b_m [Vm^{-m}]	$b_m(.045\,\text{m})^m$ [V]
2	2.262×10^7	1017820
4	2.719×10^8	24773
6	4.182×10^{11}	77165
8	1.265×10^{14}	47284
10	-1.839×10^{17}	-139152
12	-4.093×10^{19}	-62723

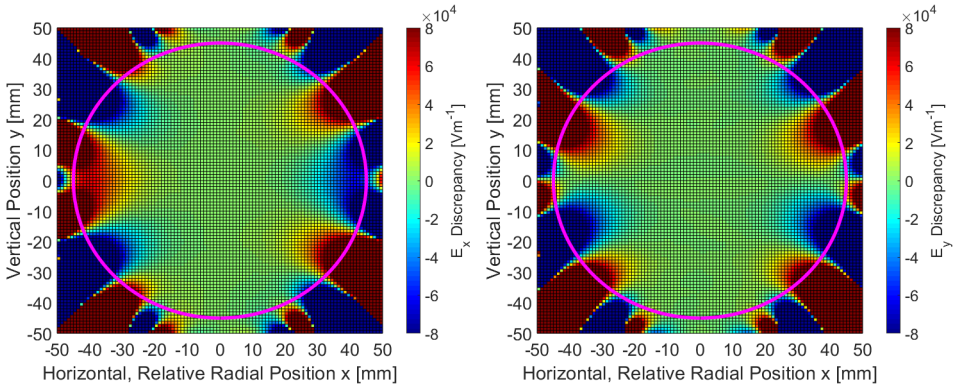

Figure 3.2: Difference in the x- (left) and y-component (right) of the electric field as described by the field map (shown in Figure 2.7 in Chapter 2) and the fitted curvilinear multipole, with the pink circle representing the edge of the storage region. The agreement along the $x = 0$ line (along which the curvilinear multipoles were fit) can be clearly seen, with the deviation growing with distance from this line up to approximately $10^5\,\text{Vm}^{-1}$ at the edge of the storage region (i.e. 10% of the field at the plates). Compared to the straight multipole residuals in Figure 2.8, and given that the experiment requires accurate knowledge of beam position/behaviour to make a precise measurement, this deviation of field along the radial direction is unacceptable.

3.2 Explicit Symplectic Integrator for Static Electric and Magnetic Fields in Curved Coordinate Systems

The integrator derived and tested in Section 2.4.2 does not describe motion in a magnetic field other than that of a constant, uniform dipole. Motivated by the slight variations in magnetic field measured across the storage region around the storage ring [23], we desire a further development of this integrator such that motion through general, static 3D magnetic fields can be described.

To this end, as demonstrated in [62], we include x and y components of the vector field $\boldsymbol{a} = (a_x, a_y, a_s)$ in the canonical momenta in (2.24). The Hamiltonian can thus be written:

$$K = p_s + \frac{\tilde{\delta}}{\beta_0} - (1 + hx)\left(a_s + \sqrt{\left(\tilde{\delta} + \frac{1}{\beta_0} - \tilde{\psi} \right)^2 - (\tilde{p}_x - a_x)^2 - (\tilde{p}_y - a_y)^2 - \frac{1}{\beta_0^2 \gamma_0^2}} \right) \tag{3.16}$$

where the canonical momenta $\tilde{p}_x$ and $\tilde{p}_y$ (2.21) now contain non-zero components of the vector field, and so are not equal to the kinematic momenta (p_x, p_y).

As this description is to be applied in a bend, we again define a_s as in (2.25), and after applying the paraxial approximation (where variables are small with respect to the orbit radius), K can be expanded in a Taylor series to third order (similar to that performed in Appendix E.2). The result can be written as:

$$K \approx H_1 + H_2 + H_3 - 1 \tag{3.17}$$

where

$$H_1 = H_{1,x} + H_{1,y} + H_{1,s}. \tag{3.18}$$

These terms take the form:

$$H_{1,x} = \frac{(\tilde{p_x} - a_x)^2}{2}\left(1 + hx - \frac{\tilde{\delta}}{\beta_0}\right), \tag{3.19}$$

$$H_{1,y} = \frac{(\tilde{p_y} - a_y)^2}{2}\left(1 + hx - \frac{\tilde{\delta}}{\beta_0}\right), \tag{3.20}$$

$$H_{1,s} = p_s + (k_0 - h) + \frac{hk_0x^2}{2}, \tag{3.21}$$

$$H_2 = \frac{\bar{\psi}}{\beta_0} + \frac{(\bar{\psi} - \tilde{\delta})^2}{2\beta_0^2\gamma_0^2}\left(1 + hx + \frac{\bar{\psi} - \tilde{\delta}}{\beta_0}\right) + \frac{\bar{\psi} - \tilde{\delta}}{\beta_0}hx, \tag{3.22}$$

$$H_3 = \frac{(\tilde{p_x} - a_x)^2 + (\tilde{p_y} - a_y)^2}{2}\frac{\bar{\psi}}{\beta_0}. \tag{3.23}$$

Making the choice of independent variable such that $\Delta\sigma = \Delta s$, the map corresponding to K is:

$$e^{-\Delta s:K:} \approx e^{-\frac{\Delta s}{2}:H_1:}e^{-\Delta s:H_2:}e^{\frac{\Delta s}{2}:H_1:}, \tag{3.24}$$

where:

$$e^{-\frac{\Delta s}{2}:H_1:} = \left(e^{-\frac{\Delta s}{8}:H_{1,s}:}e^{-\frac{\Delta s}{4}:H_{1,y}:}e^{-\frac{\Delta s}{8}:H_{1,s}:}\right)e^{-\frac{\Delta s}{2}:H_{1,x}:}\left(e^{-\frac{\Delta s}{8}:H_{1,s}:}e^{-\frac{\Delta s}{4}:H_{1,y}:}e^{-\frac{\Delta s}{8}:H_{1,s}:}\right). \tag{3.25}$$

While it may appear that this integrator will involve many sub-steps, we shall see that each sub-step involves few transformations as compared to those in Section 2.4.2.

As $H_{1,s}$ is directly integrable, the transformations corresponding to the map with generator $H_{1,s}$ are found using Hamilton's equations (2.31). Solving this system with appropriate boundary conditions (that the variables are unchanged when $\Delta s = 0$) provides the results:

$$e^{-\frac{\Delta s}{8}:H_{1,s}:}s = s + \frac{\Delta s}{8}, \tag{3.26}$$

$$e^{-\frac{\Delta s}{8}:H_{1,s}:}\tilde{p_x} = \tilde{p_x} - \frac{\Delta s}{8}(k_0 - h + k_0hx) \tag{3.27}$$

where transformations of all other variables are the identity (those variables are unchanged).

For $H_{1,x}$ and $H_{1,y}$, we must perform a change of variables to obtain an integrable form. As in Section 2.4.2, this can be done with mixed-variable

generating functions of the third kind which relate the new coordinates $\boldsymbol{Q_a} = (X_a, Y_a, Z_a, S_a)$ for $H_{1,x}$ and $\boldsymbol{Q_b} = (X_b, Y_b, Z_b, S_b)$ for $H_{1,y}$, to the old momenta $\tilde{\boldsymbol{p}} = (\tilde{p}_x, \tilde{p}_y, \tilde{\delta}, p_s)$.

In the case of $H_{1,x}$, the generating function $F_{3,a}$ can be chosen to be:

$$F_{3,a}(\tilde{\boldsymbol{p}}, \boldsymbol{Q_a}) = I_x(\boldsymbol{Q_a}) - X_a\tilde{p}_x - Y_a\tilde{p}_y - Z_a\tilde{\delta} - S_a p_s, \tag{3.28}$$

where we can define:

$$I_x(\boldsymbol{Q_a}) = \int_0^{X_a} a_x(\bar{X}, Y_a, S_a) d\bar{X}. \tag{3.29}$$

The new variables produced by $F_{3,a}$ are then:

$$\begin{aligned}
\boldsymbol{Q_a} &= -\frac{\partial F_{3,a}}{\partial \tilde{\boldsymbol{p}}} = \boldsymbol{q}, && (3.30)\\
P_{X,a} &= -\frac{\partial F_{3,a}}{\partial X_a} = \tilde{p}_x - a_x, && (3.31)\\
P_{Y,a} &= -\frac{\partial F_{3,a}}{\partial Y_a} = \tilde{p}_y - \frac{\partial I_x}{\partial Y_a}, && (3.32)\\
P_{Z,a} &= -\frac{\partial F_{3,a}}{\partial Z_a} = \tilde{\delta}, && (3.33)\\
P_{S,a} &= -\frac{\partial F_{3,a}}{\partial S_a} = p_s - \frac{\partial I_x}{\partial S_a} && (3.34)
\end{aligned}$$

where $(P_{X,a}, P_{Y,a}, P_{Z,a}, P_{S,a}) = \tilde{\boldsymbol{P}}_{\boldsymbol{a}}$ are the new momenta. This allows us to write $H_{1,x}$ as:

$$H_{1,x} = \frac{P_{X,a}^2}{2}\left(1 + hX_a - \frac{P_{Z,a}}{\beta_0}\right). \tag{3.35}$$

With this, we can use Hamilton's equations to derive the coordinate transformations (as shown for the simpler integrator in Appendix E.3):

$$e^{-\frac{\Delta s}{2}:H_{1,x}:}X_a = \frac{\Delta s}{2}P_{X,a}\left(1 - \frac{\tilde{\delta}}{\beta_0}\right)\left(1 + \frac{\Delta s}{8}hP_{X,a}\right) + \left(1 + \frac{\Delta s}{4}hP_{X,a}\right)^2 X_a \tag{3.36}$$

$$\begin{aligned}
e^{-\frac{\Delta s}{2}:H_{1,x}:}Z_a &= Z_a - \frac{\Delta s}{4\beta_0}\frac{P_{X,a}^2}{1 + \frac{\Delta s}{4}hP_{X,a}} && (3.37)\\
e^{-\frac{\Delta s}{2}:H_{1,x}:}P_{X,a} &= \frac{P_{X,a}}{1 + \frac{\Delta s}{4}hP_{X,a}} && (3.38)
\end{aligned}$$

where all other new coordinates remain unchanged. However, as the definitions of the new coordinates change with location, these transformations imply that $\tilde{p}_x$, $\tilde{p}_y$ and p_s transform as:

$$e^{-\frac{\Delta s}{2}:H_{1,x}:}\tilde{p}_x = \frac{(\tilde{p}_x - a_x(x_0,y,s))}{1+\frac{\Delta s}{4}h(\tilde{p}_x - a_x(x_0,y,s))} + a_x(x_1,y,s), \quad (3.39)$$

$$e^{-\frac{\Delta s}{2}:H_{1,x}:}\tilde{p}_y = \tilde{p}_y + \int_{x_0}^{x_1}\frac{\partial}{\partial y}a_x(\bar{x},y,s)d\bar{x}, \quad (3.40)$$

$$e^{-\frac{\Delta s}{2}:H_{1,x}:}p_s = p_s + \int_{x_0}^{x_1}\frac{\partial}{\partial s}a_x(\bar{x},y,s)d\bar{x} \quad (3.41)$$

where x_0 and x_1 are the values of x before and after the transformation, respectively.

For the case of $H_{1,y}$, we choose the generating function $F_{3,b}$, in terms of new coordinates $\boldsymbol{Q_b} = (X_b, Y_b, Z_b, S_b)$, to be:

$$F_{3,b}(\tilde{\boldsymbol{p}}, \boldsymbol{Q_b}) = I_y(\boldsymbol{Q_b}) - X_b\tilde{p}_x - Y_b\tilde{p}_y - Z_b\tilde{\delta} - S_b p_s, \quad (3.42)$$

with the definition:

$$I_y(\boldsymbol{Q_b}) = \int_0^{Y_b} a_y(X_b, \bar{Y}, S_b)d\bar{Y}, \quad (3.43)$$

which leads to the new variables being defined by:

$$\boldsymbol{Q_b} = -\frac{\partial F_{3,b}}{\partial \tilde{\boldsymbol{p}}} = \boldsymbol{q}, \quad (3.44)$$

$$P_{X,b} = -\frac{\partial F_{3,b}}{\partial X_b} = \tilde{p}_x - \frac{\partial I_y}{\partial X_a}, \quad (3.45)$$

$$P_{Y,b} = -\frac{\partial F_{3,b}}{\partial Y_b} = \tilde{p}_y - a_y, \quad (3.46)$$

$$P_{Z,b} = -\frac{\partial F_{3,b}}{\partial Z_b} = \tilde{\delta}, \quad (3.47)$$

$$P_{S,b} = -\frac{\partial F_{3,b}}{\partial S_b} = p_s - \frac{\partial I_y}{\partial S_a} \quad (3.48)$$

where the new momenta here are $(P_{X,b}, P_{Y,b}, P_{Z,b}, P_{S,b}) = \tilde{\boldsymbol{P}}_{\boldsymbol{b}}$. With this, we can write $H_{1,y}$ as:

$$H_{1,y} = \frac{P_{Y,b}^2}{2}\left(1 + hX_b - \frac{P_{Z,b}}{\beta_0}\right) \quad (3.49)$$

which can be used to find the coordinate transformations:

$$e^{-\frac{\Delta s}{4}:H_{1,y}:}Y_b = Y_b + \frac{\Delta s}{4}P_{Y,b}\left(1 + hX_b - \frac{P_{Z,b}}{\beta_0}\right), \tag{3.50}$$

$$e^{-\frac{\Delta s}{4}:H_{1,y}:}Z_b = Z_b - \frac{\Delta s}{8\beta_0}P_{Y,b}^2, \tag{3.51}$$

$$e^{-\frac{\Delta s}{4}:H_{1,y}:}P_{X,b} = P_{X,b} - \frac{\Delta s}{8}hP_{Y,b}^2 \tag{3.52}$$

where all other new coordinates are unchanged. Converting back to the original coordinates results in the momentum transformations:

$$e^{-\frac{\Delta s}{4}:H_{1,y}:}\tilde{p}_x = \tilde{p}_x - \frac{\Delta s}{8}h\big(\tilde{p}_y - a_y(x,y_0,s)\big)^2 + \int_{y_0}^{y_1}\frac{\partial}{\partial x}a_y(x,\bar{y},s)d\bar{y}, \tag{3.53}$$

$$e^{-\frac{\Delta s}{4}:H_{1,y}:}\tilde{p}_y = \tilde{p}_y + a_y(x,y_1,s) - a_y(x,y_0,s), \tag{3.54}$$

$$e^{-\frac{\Delta s}{4}:H_{1,y}:}p_s = p_s + \int_{y_0}^{y_1}\frac{\partial}{\partial s}a_y(x,\bar{y},s)d\bar{y}, \tag{3.55}$$

where y_0 and y_1 are the values of y before and after the transformation, respectively.

For H_2, we again require a generating function to provide suitable coordinates which simplify the expression for H_2 in to an integrable form. We choose the same form as used in Section 2.4.2, specifically:

$$F_{3,c}(\tilde{\boldsymbol{p}},\boldsymbol{Q_c}) = \tilde{\psi}(X_c,Y_c,S_c)Z_c - X_c\tilde{p}_x - Y_c\tilde{p}_y - Z_c\tilde{\delta} - S_cp_s \tag{3.56}$$

where we introduce $\boldsymbol{Q_c} = (X_c, Y_c, Z_c, S_c)$ and $\tilde{\boldsymbol{P}}_{\boldsymbol{c}} = (P_{X,c}, P_{Y,c}, P_{Z,c}, P_{S,c})$, defined in terms of the old coordinates as:

$$\boldsymbol{Q_c} = -\frac{\partial F_{3,c}}{\partial\tilde{\boldsymbol{p}}} = \boldsymbol{q}, \tag{3.57}$$

$$P_{X,c} = -\frac{\partial F_{3,c}}{\partial X_c} = \tilde{p}_x - Z_c\frac{\partial\tilde{\psi}}{\partial X_c}, \tag{3.58}$$

$$P_{Y,c} = -\frac{\partial F_{3,c}}{\partial Y_c} = \tilde{p}_y - Z_c\frac{\partial\tilde{\psi}}{\partial Y_c}, \tag{3.59}$$

$$P_{Z,c} = -\frac{\partial F_{3,c}}{\partial Z_c} = \tilde{\delta} - \tilde{\psi}, \tag{3.60}$$

$$P_{S,c} = -\frac{\partial F_{3,c}}{\partial S_c} = p_s - Z_c\frac{\partial\tilde{\psi}}{\partial S_c}. \tag{3.61}$$

These definitions allow us to re-write H_2 as:

$$H_2 = \frac{\bar{\psi}}{\beta_0} + \frac{P_{Z,c}^2}{2\beta_0^2\gamma_0^2}\left(1 + hX_c - \frac{P_{Z,c}}{\beta_0}\right) - \frac{P_{Z,c}}{\beta_0}hX_c \tag{3.62}$$

with which we can derive an explicit form of the transformation with generator H_2 (as shown for the simpler integrator in Appendix E.3):

$$e^{-\Delta s:H_2:}Z_c = Z_c - \frac{\Delta s}{\beta_0}hX_c + \Delta s\frac{P_{Z,c}}{\beta_0^2\gamma_0^2}\left(1 + hX_c - \frac{3P_{Z,c}}{2\beta_0}\right), \quad (3.63)$$

$$e^{-\Delta s:H_2:}P_{X,c} = P_{X,c} - \frac{\Delta s}{\beta_0}\frac{\partial\tilde{\psi}}{\partial X_c} - h\Delta s\frac{P_{Z,c}^2}{2\beta_0^2\gamma_0^2} + h\Delta s\frac{P_{Z,c}}{\beta_0}, \quad (3.64)$$

$$e^{-\Delta s:H_2:}P_{Y,c} = P_{Y,c} - \frac{\Delta s}{\beta_0}\frac{\partial\tilde{\psi}}{\partial Y_c}, \quad (3.65)$$

$$e^{-\Delta s:H_2:}P_{S,c} = P_{S,c} - \frac{\Delta s}{\beta_0}\frac{\partial\tilde{\psi}}{\partial S_c}. \quad (3.66)$$

As the parameters X_c, Y_c and S_c for $\tilde{\psi}(X_c, Y_c, S_c)$ remain constant, there is no need to re-evaluate $\tilde{\psi}$ or its derivatives when converting back to the original canonical coordinates $\boldsymbol{q}$ and $\tilde{\boldsymbol{p}}$ from $\boldsymbol{Q_c}$ and $\tilde{\boldsymbol{P}}_{\boldsymbol{c}}$. However, the scalar and vector potentials $\tilde{\psi}$ and $\boldsymbol{a}$ must be re-evaluated to convert the conjugate momenta $\tilde{p}_x$, $\tilde{p}_y$ and $\tilde{\delta}$ back to the kinematic values p_x, p_y and δ respectively.

To summarise; this results in an integrator with 15 sub-steps, 6 of which require the calculation of integrals over (some derivative of) the vector potential. Although this integrator includes the description of a general magnetic field, as well as electric field, it is apparent that the computation cost may be much greater than a (non-symplectic) Runge–Kutta integrator with the same longitudinal step Δs and similar accuracy.

3.2.1 Verifying the Integrator

Testing of the integrator was performed in BMAD, using the same uniform magnetic dipole field and continuous electric quadrupole field used in Section 2.4.2. In addition to this, we used a longitudinally-varying magnetic solenoid fringe field with a single period, consisting of two pairs of solenoid entry and exit fringes with field oriented both parallel and then antiparallel to the beam axis, covering the full azimuth of the ring. The solenoid field is superimposed with the uniform dipole field, and was chosen so that the behaviour of the integrator with non-zero a_x and a_y components of the vector field can be tested.

The "Cylindrical Map" field description used for the solenoid fringe field is developed in BMAD [63], which is different from that developed in Section 2.3.4 in that mode coefficients $B_{n,m}$ can be chosen arbitrarily without affecting agreement with Maxwell's equations. The equations for the vector

potential for a solenoid are given as:

$$A_r = 0, \tag{3.67}$$

$$A_\phi = \mathbb{R}\mathrm{e}\left(\sum_{n=-N/2}^{N/2-1} B_{n,0} i e^{ik_n z} \frac{I_1(k_n r)}{k_n}\right), \tag{3.68}$$

$$A_s = 0 \tag{3.69}$$

where

$$k_n = \frac{2\pi n}{N dz}, \tag{3.70}$$

I_n is the modified Bessel function of the first kind and N and dz are the total number of longitudinal modes and $1/(N-1)$th of the fringe-field length (a quarter of the ring circumference here), respectively.

In the interest of simplicity, mode coefficients $B_{n,m}$ are chosen such that:

$$B_{n,0} = \begin{cases} 1.0 & \text{for } n = 1 \\ 0.0 & \text{otherwise.} \end{cases} \tag{3.71}$$

The choice of $B_{1,0}$ is arbitrary, but is such that it produces a magnetic field of strength comparable to that of the dipole, but which does not cause loss of the tracked particles. For this purpose, the choice of $B_{1,0} = 1.0$ causes a peak longitudinal field of 1.0 T which is sufficient and caused none of the test particles to be lost during tracking studies.

For the tracking studies, eight test particles were tracked from various points in transverse phase space for 30 turns with 1 mm steps. This was done both with the new, symplectic integrator and the fixed-step Runge–Kutta integrator used in BMAD. The tracking results for the BMAD 6D phase space $(x, p_x, y, p_y, z, \delta)$ are shown in Figure 3.3, and the dispersion-corrected transverse actions and phases are shown in Figure 3.4.

From the tracking results, we found the deviations listed in Table 3.2. These values varied between the particles tracked, with those with the greatest orbit apogee exhibiting the greatest deviations from the Runge–Kutta integrator. This is expected, due to the ("paraxial") assumption that the coordinates (i.e. deviations from the design trajectory) are small, made when deriving the new integrator (for the Taylor expansion of K).

Despite the factor of 10 increase in time required to run the new integrator with respect to the Runge–Kutta integrator, the results are encouraging. Given a magnetic vector potential which varies little over the storage region, the integration required for the transformations for $H_{1,x}$ and $H_{1,y}$ can be performed with fewer steps, requiring fewer calculations of $\boldsymbol{a}$.

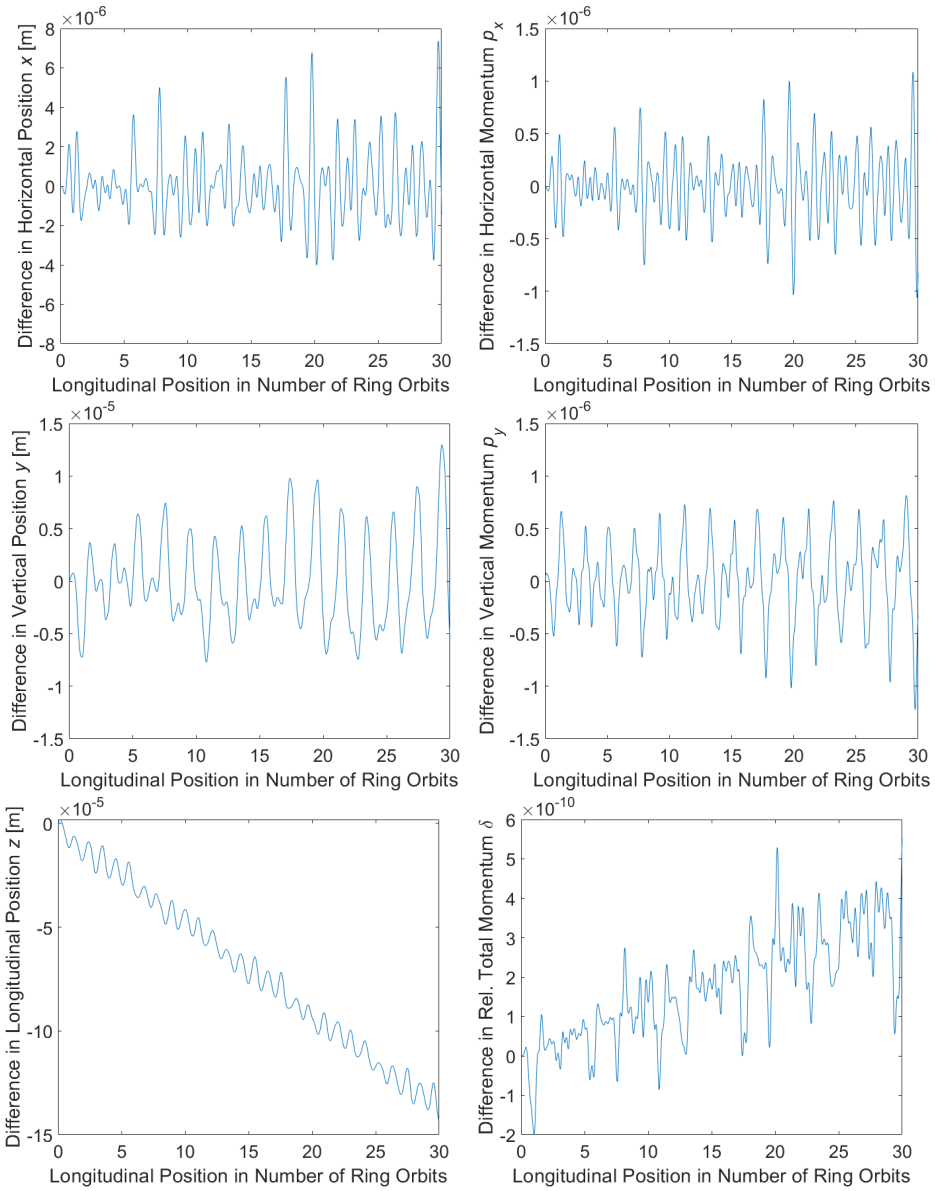

Figure 3.3: Differences in tracking results in 6D phase space (top-left to bottom-right: $x, p_x, y, p_y, z, \delta$) between the new, symplectic integrator and fixed-step Runge–Kutta integrator with 1 mm step, in the test ring consisting of uniform magnetic dipole field, electric quadrupole around the full ring azimuth and magnetic solenoid fringe field with periodicity of the ring circumference. The only increasing differences are those of the longitudinal position (relative to the design trajectory) z and the relative total momentum δ. However, if these trends continued on the visible linear trend over 2000 turns of the test ring, the differences would be approximately 4×10^{-8} for δ and 10 mm for z. While the former is negligible (at approximately 100 eV), the latter is measurable and we can associate this with the use of the paraxial approximation in deriving the integrator.

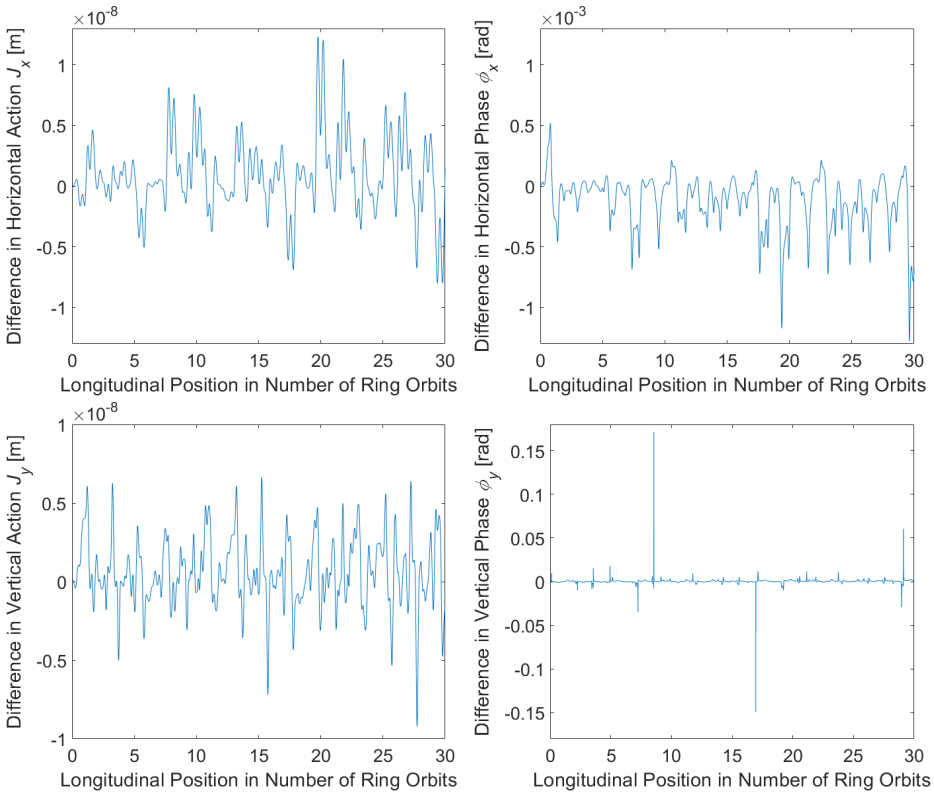

Figure 3.4: Differences in tracking results for horizontal (top) and vertical (bottom) action (left column) and phase (right column) between the new, symplectic integrator and fixed-step Runge–Kutta integrator with 1 mm step, in the test ring consisting of uniform magnetic dipole field, electric quadrupole around the full ring azimuth and magnetic solenoid fringe field with periodicity of the ring circumference. After 30 turns, the results agree to within 8.3×10^{-11} m, 0.03 mrad, 1.2×10^{-10} m and 0.18 mrad for J_x, ϕ_x, J_y and ϕ_y respectively. Although we see some random spikes in the vertical phase difference (understood to be part of the otherwise low-level noise), none of the differences appear to be increasing with tracked distance, so it may be possible to track through thousands of turns of the test ring accurately.

While the accuracy of the integrator also decreases for particles at the edge of the storage ring aperture, this is unlikely to lead to substantial deviations (on the mm scale) from the Runge–Kutta integrator. However, as well as the increased computation time, use of this integrator for the Fermilab Muon $g-2$ Experiment would require the implementation of a robust spin-tracking code (some examples of which are summarised in [58]) and an adaptive-step algorithm. For these reasons, it is concluded that using

Table 3.2: Differences between the new integrator and the Runge–Kutta integrator in BMAD, after tracking a particle 30 turns of the test ring with both integrators.

Variable	Difference
J_x	$8.3 \times 10^{-11}\,\mathrm{m}$
ϕ_x	$0.03\,\mathrm{mrad}$
J_y	$1.2 \times 10^{-10}\,\mathrm{m}$
ϕ_y	$0.18\,\mathrm{mrad}$

Variable	Difference
x	$1.4 \times 10^{-6}\,\mathrm{m}$
p_x	8.5×10^{-7}
y	$5.5 \times 10^{-6}\,\mathrm{m}$
p_y	3.4×10^{-7}
z	$1.4 \times 10^{-4}\,\mathrm{m}$
δ	5.7×10^{-10}

the Runge–Kutta integrator already implemented in BMAD is optimal for beam- and spin-dynamics studies where symplecticity is not a strong requirement. This choice allows us to replace the field map descriptions with more computationally expensive, continuous field descriptions in the studies.

3.3 Expanding Quadrupole Fields as Associated Legendre Polynomials

3.3.1 Toroidal Coordinates

In Section 3.1 we used cylindrical coordinates globally to describe the circular ring, with the cylinder axis parallel to the y-axis. In place of this, one may use toroidal coordinates as in [62], which better reflect the limited vertical extent of the ring. In addition, toroidal coordinates can be oriented about the design trajectory (see Figure 3.5), rather than the centre of the ring, so are potentially more suited to application within the storage region. Unlike the local (straight) cylindrical coordinates used to derive the cylindrical harmonics description of the fringe fields in Section 2.3.4, the toroidal coordinate system also follows the curvature of the design trajectory.

The toroidal coordinates u, v and Θ [64] are defined by:

$$x = \rho\left(\frac{\sinh(u)}{\cosh(u)-\cos(v)} - 1\right) \tag{3.72}$$

$$y = \rho\frac{\sin(v)}{\cosh(u)-\cos(v)} \tag{3.73}$$

$$s = \rho\Theta \tag{3.74}$$

where Θ is the global ring azimuth. As derived in Appendix H.1, the con-

versions from the local x, y and s coordinates are then:

$$u = \frac{1}{2}\log\left(\frac{(x+2\rho)^2+y^2}{x^2+y^2}\right) = \frac{1}{2}\log\left(1+4\frac{\rho x+\rho^2}{x^2+y^2}\right), \quad (3.75)$$

$$v = \mathrm{sgn}(y)\left|\arccos\left(\frac{x^2+y^2+2\rho x}{\sqrt{\big((x+2\rho)^2+y^2\big)(x^2+y^2)}}\right)\right|, \quad (3.76)$$

$$\Theta = \frac{s}{\rho}, \quad (3.77)$$

where $sgn(y)$ returns 1 with the same sign as y, and ensures the correct sign for v. We can derive some elements of the Jacobian for later use:

$$\frac{\partial u}{\partial x} = -\frac{\partial v}{\partial y} = \frac{-2\rho\big((x+2\rho)x-y^2\big)}{\big((x+2\rho)^2+y^2\big)(x^2+y^2)} = \frac{1-\cosh(u)\cos(v)}{\rho}, \quad (3.78)$$

$$\frac{\partial u}{\partial y} = \frac{\partial v}{\partial x} = \frac{4y\rho(x+\rho)}{\big((x+2\rho)^2+y^2\big)(x^2+y^2)} = \frac{-\sinh(u)\sin(v)}{\rho}. \quad (3.79)$$

To illustrate these new coordinates, we refer to the lines of constant u and v plotted in Figure 3.5. We understand u as being similar to the reciprocal of r in the cylindrical coordinates used in Section 2.3.4 as it increases towards, and diverges at, the beam axis. Close to the beam axis, the coordinate v can be understood as being similar to the angle about the beam axis in the transverse plane and, as such, also has an undefined value at the beam axis. While these descriptions of u and v are not strict or quantitative, they provide an intuition that can be useful when working in this new coordinate system.

We follow the approach outlined in [62], in which the solution to the Laplacian in toroidal coordinates (given in Appendix H.2) is expressed in the form (derived from [65, 66, 67]):

$$\psi = \sum_{n=-\infty}^{\infty}\sum_{m=-\infty}^{\infty} f_{n,m}\sqrt{\frac{\cosh(u)-\cos(v)}{\sinh(u)}}(-i)^m P_{n-\frac{1}{2}}^{-|m|}\left(\coth(u)\right)e^{imv}e^{in\Theta} \quad (3.80)$$

where $P_n^m(z)$ is the associated Legendre polynomial of z, of order m and degree n. To obtain values of $P_n^m(z)$ in the regime of negative m, we use the identity [68]:

$$P_n^{-|m|}(z) \equiv \frac{\Gamma\big(n-|m|+1\big)}{\Gamma\big(n+|m|+1\big)}\left(P_n^{|m|}(z) - \frac{2}{\pi}e^{-i\pi|m|}\sin\big(|m|\pi\big)Q_n^{|m|}(z)\right)$$
$$\equiv \frac{\Gamma\big(n-|m|+1\big)}{\Gamma\big(n+|m|+1\big)}P_n^{|m|}(z) \text{ for integer } m \quad (3.81)$$

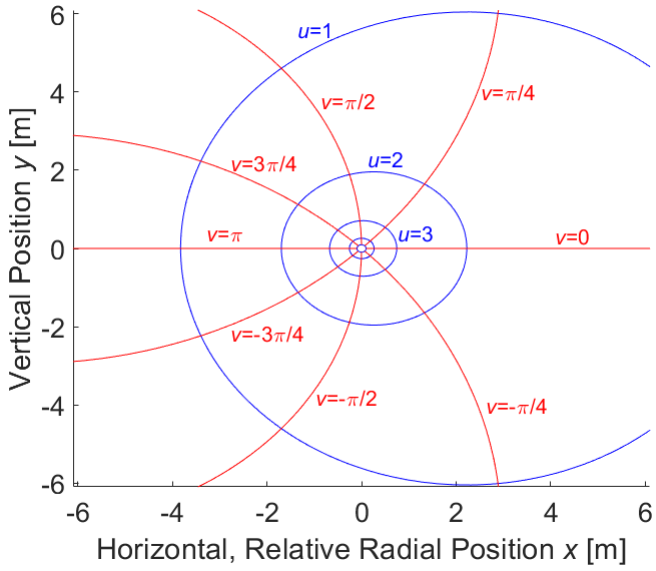

Figure 3.5: Lines of constant u (blue) and v (red) in the transverse plane of the beamline. We see that the u coordinate diverges towards the beam axis, and elongates along $+x$ more with lower u values. We also see that v is similar to the coordinate describing azimuth about the beam axis (ϕ in Section 2.3.4), although this breaks down further from the beam axis.

where $Q_n^m(z)$ is the associated Legendre polynomial of the second kind, and the second term in the brackets is discarded as m is always an integer.

From the definitions of coordinates u and v in (3.72) and (3.73), we can obtain the relation:

$$\frac{\cosh(u) - \cos(v)}{\sinh(u)} = \frac{\rho}{\rho + x}. \tag{3.82}$$

The factor $(-i)^m$ in (3.80) combines with the associated Legendre polynomial to generate a strictly real number, such that the only complex quantities remaining are the coefficients $f_{n,m}$ and the Euler exponents. As such, the factor and Legendre polynomial may be merged to create a new function $\tilde{P}$:

$$\tilde{P}^m_{n-\frac{1}{2}}(u) = (-i)^m P^{-|m|}_{n-\frac{1}{2}}\left(\coth(u)\right), \tag{3.83}$$

such that ψ can be written:

$$\psi = \sum_{n=-\infty}^{\infty} \sum_{m=-\infty}^{\infty} f_{n,m} \sqrt{\frac{\rho}{\rho + x}} \tilde{P}^m_{n-\frac{1}{2}}(u) e^{imv} e^{in\Theta}. \tag{3.84}$$

In order to find the coefficients $f_{n,m}$, we wish to perform a Fourier transform of (3.80). Fortunately, the form is such that we may choose a constant value for u, designated u_0, and transform with respect to v and Θ. This represents a surface (enclosing, and extending along, the design trajectory) on which we will use field values to fit the coefficients. Hence, the Fourier transform yields:

$$f_{n,m} = \frac{1}{4\pi^2}\int_0^{2\pi}\int_0^{2\pi}\psi(u_0,v,\Theta)\sqrt{\frac{\sinh(u_0)}{\cosh(u_0)-\cos(v)}}\frac{e^{-imv}e^{-in\Theta}dvd\Theta}{\tilde{P}^m_{n-\frac{1}{2}}(u_0)} \tag{3.85}$$

where we can take various factors out of the integrals, to simplify evaluation:

$$f_{n,m} = \frac{\sqrt{\sinh(u_0)}}{4\pi^2\tilde{P}^m_{n-\frac{1}{2}}(u_0)}\int_0^{2\pi}\int_0^{2\pi}\psi(u_0,v,\Theta)\frac{e^{-imv}e^{-in\Theta}dvd\Theta}{\sqrt{\cosh(u_0)-\cos(v)}} \tag{3.86}$$

from which, the coefficients $f_{n,m}$ can be determined from a known potential $\psi(u_0,v,\Theta)$.

In the interests of efficiency, it is possible to reduce the summation in (3.84) such that n and m start at 0. The value of $\tilde{P}^m_{n-\frac{1}{2}}$ is the same when we replace n with $-n$ (shown in Appendix H.3) and although $\tilde{P}^{-m} = (-1)^m\tilde{P}^m$ (due to the hidden factor of $(-i)^m$), the expression for the coefficients (3.86) results in the sign for m cancelling contributions for field for $n < 0$ and $m < 0$ being identical to those with $n > 0$ and $m > 0$. Due to this, we apply a factor $A_{n,m}$ (assuming this is not done when calculating the coefficients), and omitting the argument of $\tilde{P}^m_{n-\frac{1}{2}}(u)$ for convenience, we have:

$$\begin{aligned}\psi = \sum_{n=0}^{\infty}\sum_{m=0}^{\infty}\frac{A_{n,m}}{4}\sqrt{\frac{\rho}{\rho+x}}\big(&f_{n,m}e^{imv}e^{in\Theta} + f^*_{n,m}e^{imv}e^{-in\Theta}\\ &+ f_{n,m}e^{-imv}e^{in\Theta} + f^*_{n,m}e^{-imv}e^{-in\Theta}\big)\tilde{P}^m_{n-\frac{1}{2}}.\end{aligned} \tag{3.87}$$

In this, we have defined $A_{n,m} = 4$ for $n, m > 0$, $A_{n,m} = 2$ for $n = 0$ or $m = 0$, and $A_{n,m} = 1$ for $n = m = 0$, and used the relations:

$$f_{n,m} = -f^*_{-n,-m} = -f_{n,-m} = f^*_{-n,m} \tag{3.88}$$

discussed in Appendix H.4.

Combining the exponents in our expression for ψ results in:

$$\psi = \sum_{n=0}^{\infty}\sum_{m=0}^{\infty}\frac{A_{n,m}}{2}\sqrt{\frac{\rho}{\rho+x}}\cos(mv)\big(f_{n,m}e^{in\Theta} + f^*_{n,m}e^{-in\Theta}\big)\tilde{P}^m_{n-\frac{1}{2}} \tag{3.89}$$

where separating out the real and imaginary parts of $f_{n,m}$ gives:

$$\psi = \sum_{n=0}^{\infty}\sum_{m=0}^{\infty} A_{n,m}\sqrt{\frac{\rho}{\rho+x}}\cos(mv) \times \left(\mathbb{R}\mathrm{e}\left(f_{n,m}\right)\cos(n\Theta) - \mathbb{I}\mathrm{m}\left(f_{n,m}\right)\sin(n\Theta)\right)\tilde{P}^{m}_{n-\frac{1}{2}} \quad (3.90)$$

where we have dropped the complex part, as the potential ψ must be real (although the real and imaginary parts each separately satisfy the Laplace equation). Including the argument for $\tilde{P}$ leaves us with:

$$\psi = \sum_{n=0}^{\infty}\sum_{m=0}^{\infty} A_{n,m}\sqrt{\frac{\rho}{\rho+x}}\tilde{P}^{m}_{n-\frac{1}{2}}(u)\cos(mv)\,\mathbb{R}\mathrm{e}\left(e^{in\Theta}f_{n,m}\right). \quad (3.91)$$

In order to be useful in a typical accelerator code, we must obtain the Cartesian components of electric field from this expression. For the x component, again dropping the argument for $\tilde{P}$, we have:

$$E_x = -\frac{\partial\psi}{\partial x} = \sum_{n=0}^{\infty}\sum_{m=0}^{\infty} -A_{n,m}\,\mathbb{R}\mathrm{e}\left(e^{in\Theta}f_{n,m}\right) \times \left(\left(\frac{\partial}{\partial x}\sqrt{\frac{\rho}{\rho+x}}\right)\cos(mv)\tilde{P}^{m}_{n-\frac{1}{2}} + \sqrt{\frac{\rho}{\rho+x}}\left(\frac{\partial u}{\partial x}\frac{\partial}{\partial u}\tilde{P}^{m}_{n-\frac{1}{2}}\right)\cos(mv) + \sqrt{\frac{\rho}{\rho+x}}\left(\frac{\partial v}{\partial x}\frac{\partial}{\partial v}\cos(mv)\right)\tilde{P}^{m}_{n-\frac{1}{2}}\right). \quad (3.92)$$

We can use the derivative of the associated Legendre polynomial to show that:

$$\frac{\partial}{\partial u}\tilde{P}^{m}_{n-\frac{1}{2}}(u) = \frac{n+\frac{1}{2}}{\tanh(u)}\tilde{P}^{m}_{n-\frac{1}{2}}(u) - \left(m+n+\frac{1}{2}\right)\tilde{P}^{m}_{n+\frac{1}{2}}(u), \quad (3.93)$$

which can be used to evaluate the middle term in the brackets in (3.92), producing:

$$E_x = \sum_{n=0}^{\infty}\sum_{m=0}^{\infty} -A_{n,m}\,\mathbb{R}\mathrm{e}\left(e^{in\Theta}f_{n,m}\right)\sqrt{\frac{\rho}{\rho+x}} \times \left(\frac{-1}{2(\rho+x)}\cos(mv)\tilde{P}^{m}_{n-\frac{1}{2}} - \frac{\partial v}{\partial x}m\sin(mv)\tilde{P}^{m}_{n-\frac{1}{2}} + \frac{\partial u}{\partial x}\left(\frac{n+\frac{1}{2}}{\tanh(u)}\tilde{P}^{m}_{n-\frac{1}{2}} - \left(m+n+\tfrac{1}{2}\right)\tilde{P}^{m}_{n+\frac{1}{2}}\right)\cos(mv)\right). \quad (3.94)$$

We can use the derivatives of u and v with respect to x (from (3.78) and (3.79)) to obtain:

$$E_x = \sum_{n=0}^{\infty}\sum_{m=0}^{\infty} A_{n,m}\,\mathbb{R}\mathrm{e}\left(e^{in\Theta} f_{n,m}\right)\sqrt{\frac{\rho}{\rho+x}}\Bigg(\Big(-\frac{m}{\rho}\sinh(u)\sin(v)\sin(mv) + \frac{\cos(mv)}{2(\rho+x)} - \frac{1-\cosh(u)\cos(v)}{\rho}\frac{\left(n+\frac{1}{2}\right)}{\tanh(u)}\cos(mv)\Big)\tilde{P}^m_{n-\frac{1}{2}} + \frac{1-\cosh(u)\cos(v)}{\rho}\cos(mv)\left(m+n+\tfrac{1}{2}\right)\tilde{P}^m_{n+\frac{1}{2}}\Bigg) \quad (3.95)$$

which, in the interest of rapid computation, can be written as:

$$E_x = \sum_{n=0}^{\infty}\sum_{m=0}^{\infty}\frac{A_{n,m}}{2}\left(\mathbb{R}\mathrm{e}\left(f_{n,m}\right)\cos(n\Theta) - \mathbb{I}\mathrm{m}\left(f_{n,m}\right)\sin(n\Theta)\right)B \times\Bigg(\Big(\big(C-(2n+1)D\big)\cos(mv) - 2mF\sin(mv)\Big)\tilde{P}^m_{n-\frac{1}{2}} + G\cos(mv)\left(2m+2n+1\right)\tilde{P}^m_{n+\frac{1}{2}}\Bigg) \quad (3.96)$$

where B, C, D, F and G are functions of the coordinates only, and thus need only be calculated once for each field evaluation:

$$B = \sqrt{\frac{\rho}{\rho+x}}, \qquad C = \frac{1}{\rho+x}, \qquad D = \frac{G}{\tanh(u)}, \qquad F = \frac{\sinh(u)\sin(v)}{\rho}, \qquad G = \frac{1-\cosh(u)\cos(v)}{\rho}. \quad (3.97)$$

For the y component, we start with (3.94), expressed in terms of derivatives with respect to y, and using the derivatives from (3.78) and (3.79) (as in Appendix H.5):

$$E_y = \sum_{n=0}^{\infty}\sum_{m=0}^{\infty} A_{n,m}\,\mathbb{R}\mathrm{e}\left(e^{in\Theta} f_{n,m}\right)\sqrt{\frac{\rho}{\rho+x}} \times\Bigg(\Big(\frac{\sinh(u)\sin(v)}{\rho\tanh(u)}(n+\tfrac{1}{2})\cos(mv) - m\frac{1-\cosh(u)\cos(v)}{\rho}\sin(mv)\Big)\tilde{P}^m_{n-\frac{1}{2}} - \frac{\sinh(u)\sin(v)}{\rho}\left(m+n+\tfrac{1}{2}\right)\cos(mv)\tilde{P}^m_{n+\frac{1}{2}}\Bigg), \quad (3.98)$$

which can be written as:

$$E_y = \sum_{n=0}^{\infty}\sum_{m=0}^{\infty}\frac{A_{n,m}}{2}\big(\,\mathbb{R}\mathrm{e}\,(f_{n,m})\cos(n\Theta) - \mathbb{I}\mathrm{m}\,(f_{n,m})\sin(n\Theta)\big)B \times\left(\Big((2n+1)J\cos(mv) - 2mG\sin(mv)\Big)\tilde{P}^m_{n-\frac{1}{2}} - (2m+2n+1)\,F\cos(mv)\tilde{P}^m_{n+\frac{1}{2}}\right) \quad (3.99)$$

where we have introduced one more function, dependent only on the coordinates:

$$J = \frac{F}{\tanh(u)}. \quad (3.100)$$

Finally, the z (s) field component is simply:

$$E_z = -\frac{\partial\psi}{\partial s} = \sum_{n=0}^{\infty}\sum_{m=0}^{\infty} -A_{n,m}\sqrt{\frac{\rho}{\rho+x}}\tilde{P}^m_{n-\frac{1}{2}}\cos(mv)\frac{\partial\Theta}{\partial s}\,\mathbb{R}\mathrm{e}\left(ine^{in\Theta}f_{n,m}\right)$$
$$=\sum_{n=0}^{\infty}\sum_{m=0}^{\infty}A_{n,m}\frac{B}{\rho}n\tilde{P}^m_{n-\frac{1}{2}}\cos(mv)\big(\,\mathbb{R}\mathrm{e}\,(f_{n,m})\sin(n\Theta) + \mathbb{I}\mathrm{m}\,(f_{n,m})\cos(n\Theta)\big). \quad (3.101)$$

With these definitions, we now have a means of representing any longitudinally-varying electric field in a bend in terms of a set of coefficients $f_{n,m}$, that may be determined from a known potential ψ. If ψ is given in terms of values on a grid (e.g. from a finite element analysis code), the description in terms of coefficients $f_{n,m}$ provides a continuous, analytical description of the field.

3.3.2 Application to Fringe Fields

Due to the fact that the fringe fields cover only 2° of ring azimuth each, only the values of n which reflect structure on this scale need be considered. Taking four copies of the fringe field: upstream, downstream and then the same again reversed, as for the cylindrical harmonic expansion in Chapter 2, we obtain one full period of field, occupying 8°, or 1/45 of ring azimuth. This is the length in which we wish to fit an integer number of wavelengths (each representing a longitudinal field mode described by n), as such n must be selected as:

$$n' = 45(n+1) \quad (3.102)$$

where $n+1$ determines the number of wavelengths fit in to the fringe field wave (8° of ring azimuth).

Replacing n with n' in the equations for ψ, E_x, E_y and E_z (whilst keeping the sum over n) applies this boundary condition to the model field. This reduces the number of values of n for which the expressions must be evaluated and, thus, computation times.

Fitting to Field Maps

To fit these "toroidal multipoles" to a field map using (3.86), we wish to calculate values of $f_{n',m}$ where n' is from (3.102), ie. we wish to calculate $f_{45(n+1),m}$. To do this, we require values of the potential on a surface $\psi(u_0, v, \Theta)$, which may be obtained from a field map on a Cartesian grid by interpolating the field on to the surface $u = u_0$.

A value of u_0 for the fit was calculated from values of $x = 0.046\,\mathrm{m}$, $y = 0$ and $\rho = 7.112\,\mathrm{m}$, corresponding to $u_0 = 5.737$ in (3.75). This value was chosen by varying x and finding the best fit to the field. The field map of electric potential ψ must then be interpolated from the Cartesian grid to the chosen surface of $u = u_0 = 5.737$. This was performed using the 3D spline interpolation method in MatLab [53], using 180 evenly-spaced sample points in v and 80 evenly-spaced points in Θ.

A constant of $-40.7544\,\mathrm{V}$ is then added to this field, such that the potentials along the fit surface at the upstream end ($\Theta = -1°$ in Figure 3.6) have an average potential of $0\,\mathrm{V}$, so that the potentials more closely resemble a sine wave, and thus can be more accurately modelled. The surface is then mirrored along the longitudinal axis to produce a downstream fringe, and the field of the combined upstream and downstream fringes is then reflected, both in $\psi = 0\,\mathrm{V}$ and along the longitudinal axis as in Figure 3.6, such that the supplied field has 320 points in Θ (which ranges from $-1°$ to $7°$).

Using ψ on the surface $u = u_0$, the integration over v and Θ in (3.86) was performed both with the simple rectangle and trapezoidal methods, using 180 evenly-spaced sample points in v and 320 such points in Θ. Though the difference between using these two methods was found to be in and below the fourth significant figure (so that more advanced integration methods were not needed), the results from the trapezoidal method are used here.

The fit to the interpolated field map values (shown in Figure 3.7) was performed up to $m = 14$ and $n = 100$, as the accuracy of the fits at and within the surface of the fit were substantially worse if smaller values were used. The values obtained for $f_{n,m}$ are given in Appendix H.6 (up to $n = 8$), and the resulting fit residuals on the fitted surface are shown in Figure 3.8. These show similar discrepancy to the case of fitting cylindrical harmonics

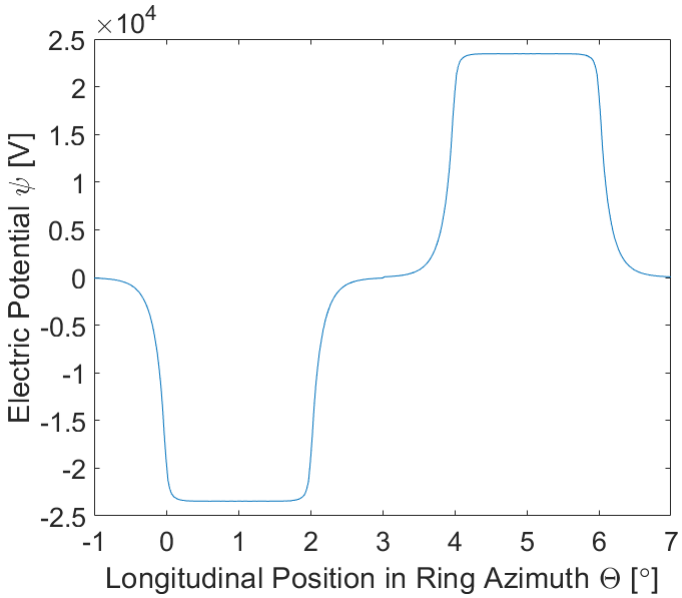

Figure 3.6: The region of field map required for fitting the potential ψ, shown for $u = 5.737$ and $v = 0$. The original upstream field map extends $2°$ in ring azimuth (from $\Theta = -1°$ to $1°$ in the plot), which has then been reflected to produce the downstream field map (between $\Theta = 1°$ and $3°$ in the plot). This combination is then mirrored in both axes (potential and longitudinal position) to form the other half of the field map (between $\Theta = 3°$ and $7°$ in the plot). To obtain a suitable potential for fitting, a constant of $-40.7544\,\mathrm{V}$ is added to the original upstream fringe field map, such that the potentials along the fitted surface at $\Theta = -1$ average to zero, so that the potential can more accurately be described by sine functions longitudinally.

(described in Section 2.3.4).

The residuals with respect to the field map (the latter shown in Figure 2.12 in Chapter 2) were also calculated in the plane transverse to the design orbit, at $0.5°$ before the quadrupole plates, at the end of the plates and at $0.5°$ within the quadrupole. These are shown in Figure 3.9, and again show a very similar level of discrepancy to that for the cylindrical harmonic fit.

Also analysed is the residual of the on-axis electric field component E_x, in Figure 3.10, which exhibits similar rises at the quadrupole ends as were seen with the cylindrical harmonic fit, on the same scale.

As the residuals are of similar magnitude to those from the cylindrical harmonic fits in Section 2.3.4, we consider this method to have compara-

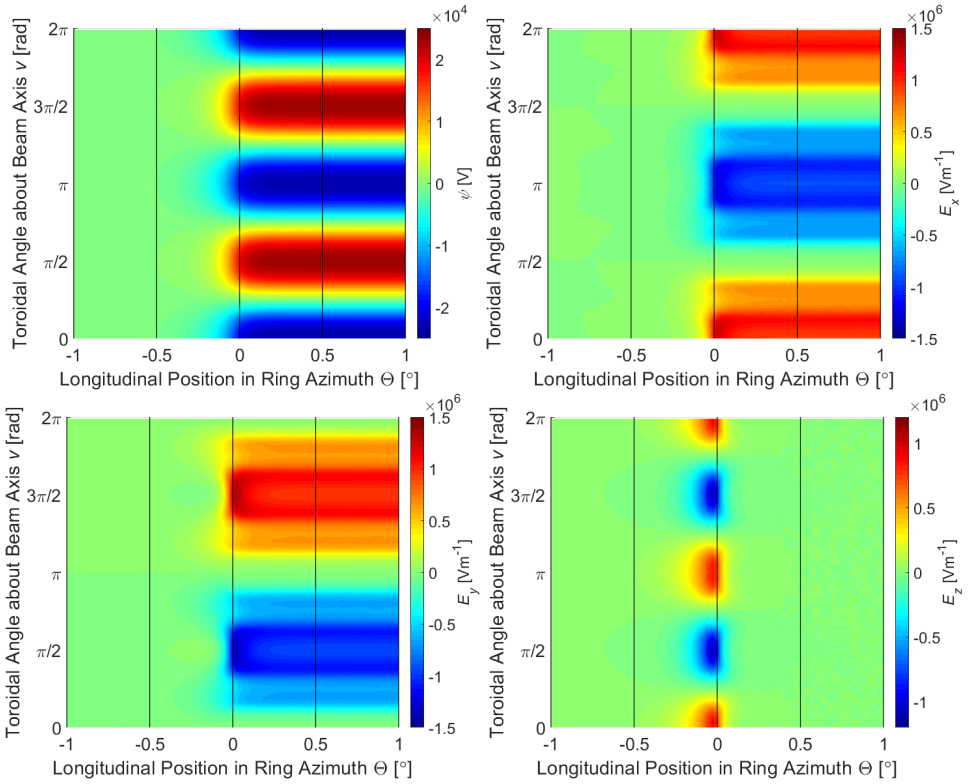

Figure 3.7: Interpolated field map values for ψ (top-left), E_x (top-right), E_y (bottom-left) and E_z (bottom-right) on the fitted surface between $\Theta = -1°$ (1° of azimuth before the quadrupole plates start) and $\Theta = 1°$ (1° of azimuth within the quadrupole).

ble accuracy. However, the toroidal multipoles derived here obey Maxwell's equations for all n and m and in a curved reference frame. Thus, for a strictly physical model, it is preferable to use the toroidal multipoles.

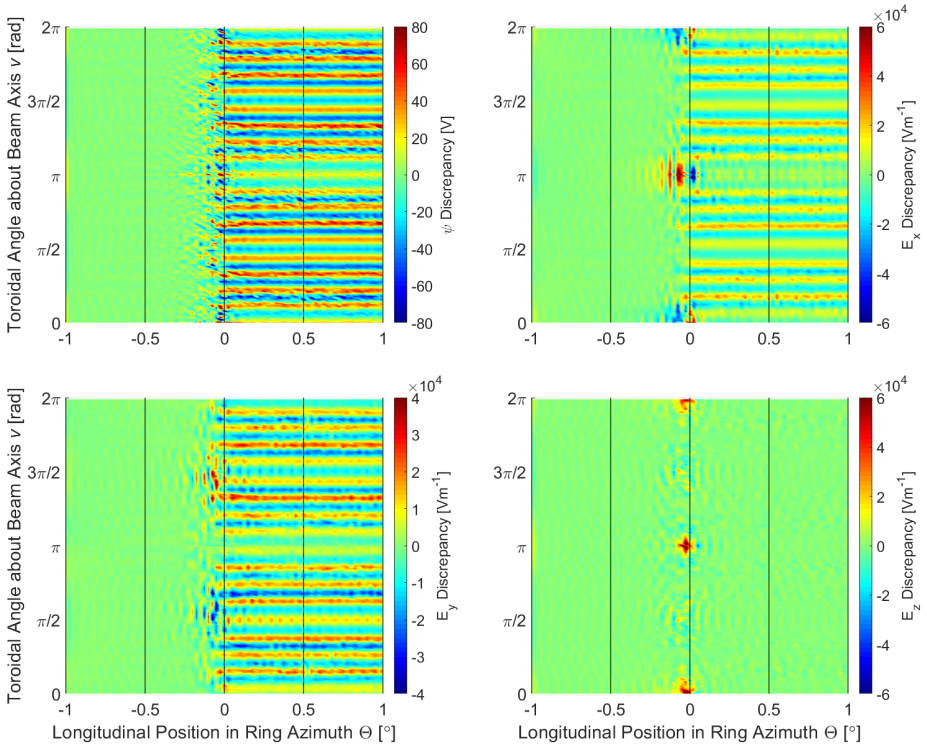

Figure 3.8: Fit residuals of ψ (top-left), E_x (top-right), E_y (bottom-left) and E_z (bottom-right) on the fitted surface between $\Theta = -1°$ (1° of azimuth before the quadrupole plates start) and $\Theta = 1°$ (1° of azimuth within the quadrupole), for which the field map values are shown in Figure 3.7. The residuals for ψ should be compared to the peak potential, which is 23 kV on the fitted surface (27.2 kV at the plates), while the field should be compared with the on-surface peak value of $10^6\,\mathrm{Vm}^{-1}$. We note the clear "horizontal" lines indicating variations in ψ within the quadrupole (top-left). The number of these lines suggests that the dominant residual is due to an omitted $m = 18$ (36-pole) term: to include this term, the fit would have to be performed at higher order. The number of faint vertical lines, particularly visible in E_x just outside the quadrupole (where we see ten oscillations within 0.5°), indicates that these are caused by an omitted $n = 160$ longitudinal mode.

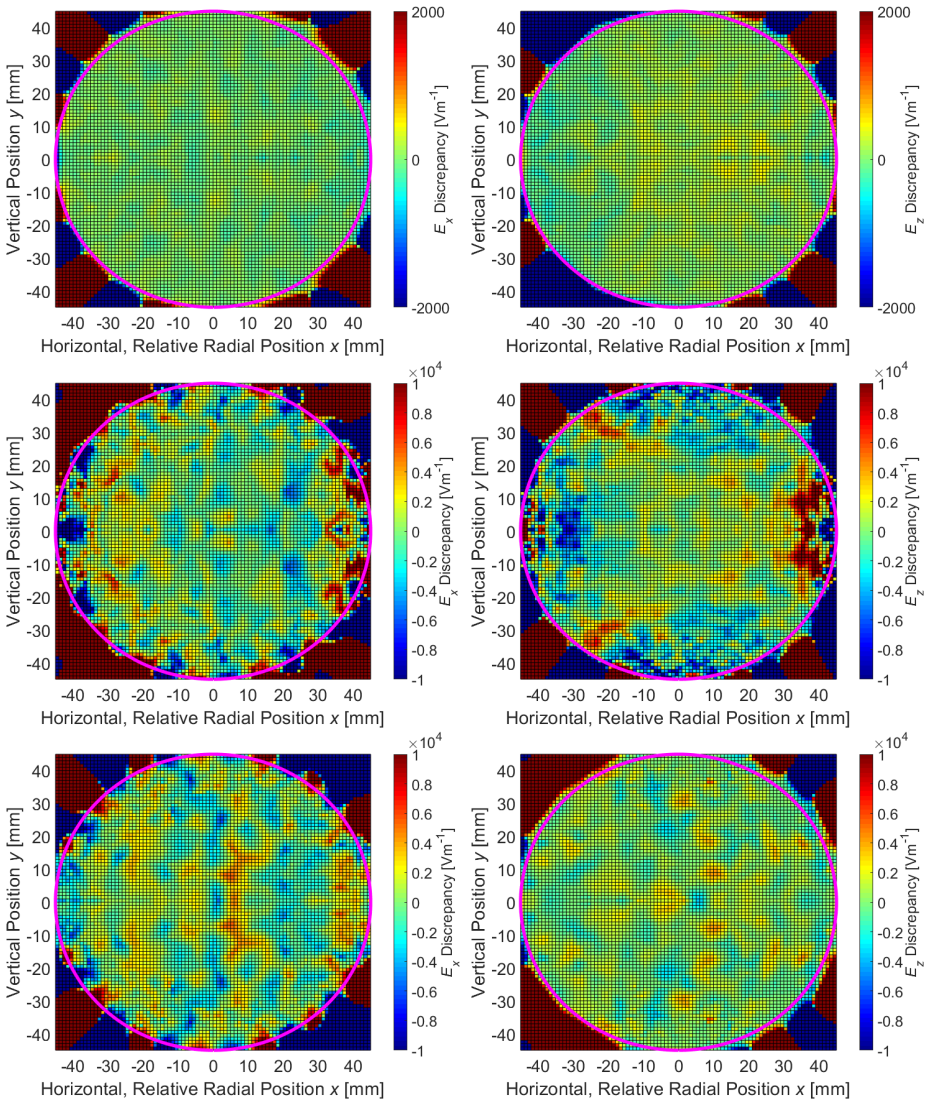

Figure 3.9: Residuals of E_x (left column) and E_z (right column) with respect to the field map (shown in Figure 2.12 in Chapter 2) on the transverse plane at 0.5° of ring azimuth before the quadrupole (top row), at the start of the quadrupole (middle row) and 0.5° of ring azimuth within the quadrupole (bottom row). The residuals of the potential within the storage volume do not exceed 274 V and have an RMS of 16 V, while the residuals of E_x do not exceed $6 \times 10^4\,\mathrm{Vm}^{-1}$ and have an RMS of $2 \times 10^3\,\mathrm{Vm}^{-1}$. For context, residuals should be compared to the peak field of $10^6\,\mathrm{Vm}^{-1}$ and the apparent field map noise of approximately $10^3\,\mathrm{Vm}^{-1}$.

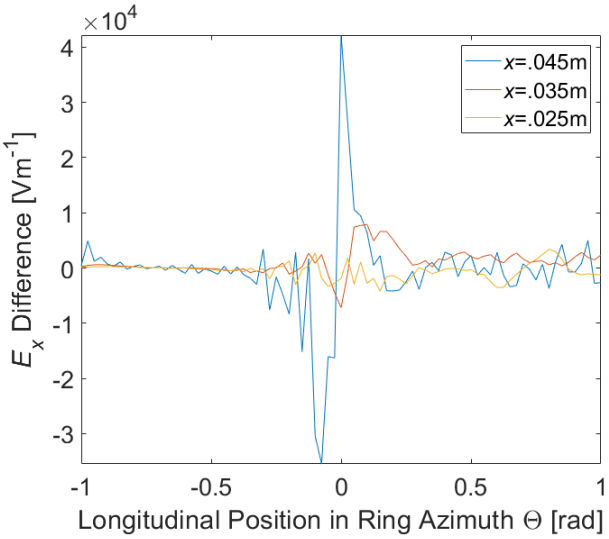

Figure 3.10: Residuals of on-axis field component E_x, along fringe field ring azimuth, at $y = 0$ and $x = .045\,\mathrm{m}$ (blue), $x = .035\,\mathrm{m}$ (red) and $x = .025\,\mathrm{m}$ (orange). We see the residuals, which peak at the quadrupole plate ends, are on the same scale as those from the cylindrical harmonic fits in Figure 2.14.

3.3.3 Application to Bulk Fields

It is also possible to apply this toroidal multipole description to the bulk (longitudinally uniform) field case. To do this, we select only the solutions in (3.80) which do not vary in Θ (longitudinally), ie. where $n = 0$:

$$\begin{aligned}\psi &= \sum_{m=-\infty}^{\infty} f_m \sqrt{\frac{\cosh(u)-\cos(v)}{\sinh(u)}}(-i)^m P_{-\frac{1}{2}}^{-|m|}\left(\frac{1}{\tanh(u)}\right) e^{imv} \\ &= \sum_{m=-\infty}^{\infty} f_m \sqrt{\frac{\rho}{\rho+x}}\tilde{P}_{-\frac{1}{2}}^{m} e^{imv},\end{aligned} \tag{3.103}$$

where we have again used the shorthand form $\tilde{P}_n^m = (-i)^m P_n^{-|m|}(\coth(u))$, and f_m is now only dependent on m.

As with the fringe field case, we can take the Fourier transform to isolate f_m. This is simply (3.86) with an integral over Θ performed (noting that $n = 0$):

$$f_m = \frac{\sqrt{\sinh(u_0)}}{2\pi \tilde{P}_{-\frac{1}{2}}^{m}(u_0)} \int_0^{2\pi} \frac{\psi(u_0, v) e^{-imv} dv}{\sqrt{\cosh(u_0)-\cos(v)}}. \tag{3.104}$$

Fitting to Field Maps

With the bulk (2D, transverse) field map $\psi(u, v)$ in toroidal coordinates u, v, we make a suitable choice of $u = u_0$ such that we can use (3.104) to obtain the coefficients f_m which describe the field.

Using the same value of $u_0 = 5.737$ (and $\rho = 7.112\,\text{m}$) as for the fringe field case, the bulk (2D, transverse) field map was interpolated on to the line of $u = u_0$ using the 2D spline interpolation method in MatLab [53]. The integration in (3.104) was then performed using the trapezoidal method, over 180 evenly-spaced sample points in v.

The fit was calculated up to $m = 14$. This choice was again due to the accuracy of the fit degrading substantially below this value, and the increased computation overhead for marginal improvements in accuracy of the fit for larger values of m. The resulting values for f_m are given in Appendix H.7, with the residuals on the line of the fit shown in Figure 3.11. The residuals along the fit line have an RMS value of 31 V and a peak value of 62 V, which are 0.11% and 0.22% respectively of the plate potential of 27.2 kV.

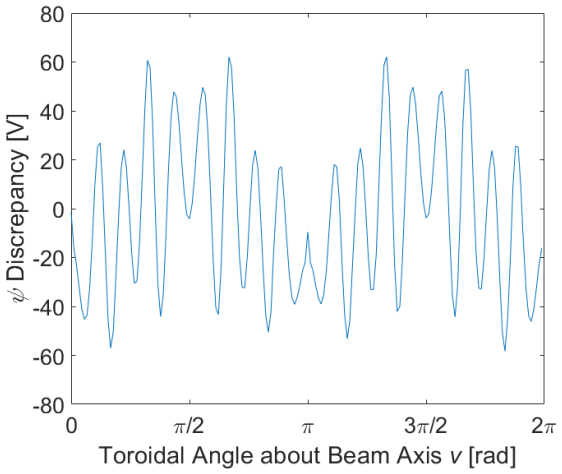

Figure 3.11: Residual of ψ along the fitted line at $u = u_0 = 5.737$, for $0 \leq v < 2\pi$ with a fit up to order $m = 14$. The plot exhibits oscillations corresponding to $m = 18$, suggesting that increasing the fit to this order would improve agreement. The RMS discrepancy along the fitted line is 31 V which, compared to the plate potential of 27.2 kV, corresponds to a 0.11% discrepancy.

Residuals were also calculated over the entire 2D plane, covering the range $-45\,\text{mm} \leq x \leq 45\,\text{mm}$, $-45\,\text{mm} \leq y \leq 45\,\text{mm}$, and are shown in Fig-

ure 3.12 (for which the field map values are shown in Figure 2.7 in Chapter 2). These exhibit a very similar level of agreement to the standard multipole fit in Section 2.3.3. In particular, within the storage region they exhibit RMS deviations of $2.5 \times 10^3\,\mathrm{Vm}^{-1}$ and $2.2 \times 10^3\,\mathrm{Vm}^{-1}$, with peak values of $1.6 \times 10^4\,\mathrm{Vm}^{-1}$ and $1.8 \times 10^4\,\mathrm{Vm}^{-1}$ for E_x and E_y respectively. Overall, we compare these with the field at the plate edges of $1 \times 10^6\,\mathrm{Vm}^{-1}$, and so the RMS values correspond to approximately 0.25% and 0.22%, respectively, of this. However, we also note that the electric field on the design trajectory in these plots is on the order of $10^3\,\mathrm{Vm}^{-1}$, which is comparable to the noise in the field map (taken as the random fluctuations in E_y along the x-axis, approximately $500\,\mathrm{Vm}^{-1}$ to $1000\,\mathrm{Vm}^{-1}$).

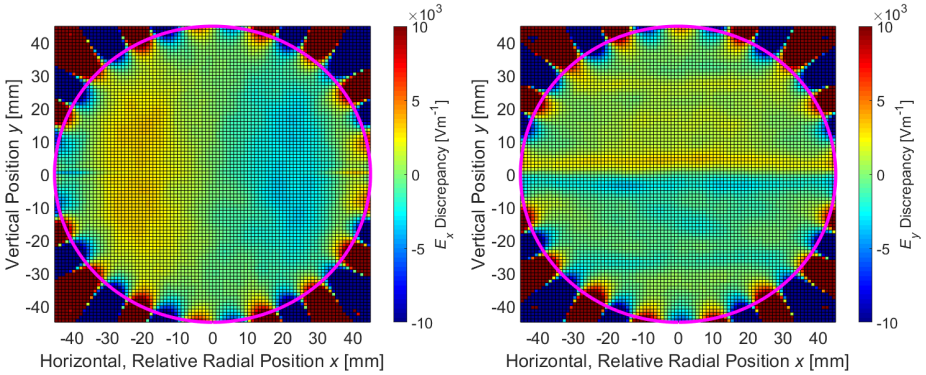

Figure 3.12: Residuals of E_x (left) and E_y (right) with respect to the field map (shown in Figure 2.7 in Chapter 2) in the plane transverse to the beam axis within the quadrupole bulk, for a fit up to $m = 14$. The edge of the storage region of radius 45 mm is shown in magenta. The number of poles along the storage region edge corresponds to an $m = 18$ multipole, suggesting that the residuals could be reduced by including this order of multipole to the fit. The RMS discrepancies within the storage region are $2.5 \times 10^3\,\mathrm{Vm}^{-1}$ and $2.2 \times 10^3\,\mathrm{Vm}^{-1}$ for E_x and E_y respectively, with peak discrepancies within the storage region of $1.6 \times 10^4\,\mathrm{Vm}^{-1}$ and $1.8 \times 10^4\,\mathrm{Vm}^{-1}$ respectively. Compared to the fields at the plate edges of $1 \times 10^6\,\mathrm{Vm}^{-1}$, the RMS values correspond to 0.25% and 0.22% discrepancies for E_x and E_y, respectively. These RMS values are very close to the noise level of the field map of $10^3\,\mathrm{Vm}^{-1}$, and so we consider the fit to be in good agreement. While the features visible within the storage region appear to have some symmetry, they do not correspond to any single multipole and are of such a low level that they are ignored.

The curvature of the design trajectory (a 0.1 m aperture with a bending radius of 7.112 m) should be significant feature over the 140° of ring azimuth

covered by the quadrupole bulk regions in the short and long quadrupoles (11° and 24° each, respectively). This suggests that, in the interest of strictly obeying Maxwell's equations, we should use the toroidal multipole description.

However, there is significant computation overhead in using toroidal multipoles over such a large proportion of the ring azimuth. Given the residuals are similar to those from the multipole fit in Section 2.3.3, we consider the standard multipole fit to be sufficient, and can use this to free computation time for use of continuous mathematical models of the fringe field regions.

3.3.4 Optimisation for Tracking

Discontinuity at Origin

As the values of x and y go to zero, u diverges (tends to infinity). This causes problems in the calculation of the field at distances of less than 1.3×10^{-5} m from the origin, as shown in Figure 3.13. To rectify this, we must analyse the behaviour of the functions appearing in the expressions for the potential and field at the origin.

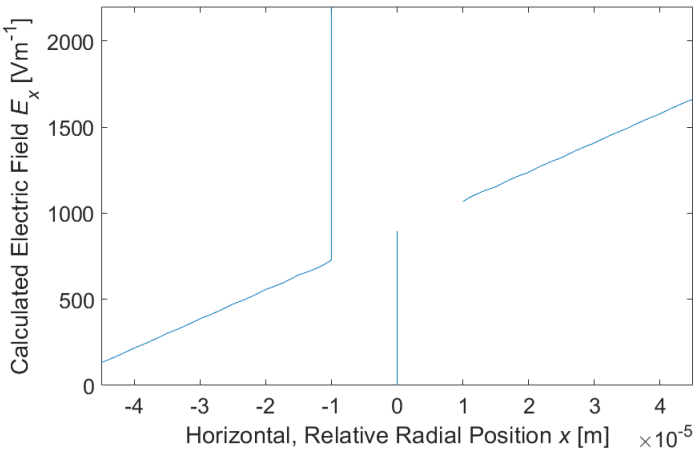

Figure 3.13: Electric field component E_x as calculated at $y = 0$ for 1×10^{-6} m intervals in x near the origin, using the standard calculations for toroidal multipoles. We see a clear and abrupt divergence between $x = -1.3 \times 10^{-5}$ m and $x = 1.3 \times 10^{-5}$ m, which must be removed.

For the case of $x = y = 0$ (where $u \to \infty$), we may use the identities:

$$\lim_{u \to \infty} \tilde{P}^0_{n-\frac{1}{2}}(u) = 1, \tag{3.105}$$

and:

$$\lim_{x\to 0}\left(\frac{\partial}{\partial x}\tilde{P}^{1}_{n-\frac{1}{2}}\big(u(x)\big)\Big|_{y=0}\right)=\lim_{y\to 0}\left(\frac{\partial}{\partial y}\tilde{P}^{1}_{n-\frac{1}{2}}\big(u(y)\big)\Big|_{x=0}\right)=\frac{1}{2\rho},\quad(3.106)$$

where these expressions are zero for all other values of m. The former makes use of $\lim_{u\to\infty}(\tanh(u))=1$ and is calculable by WolframAlpha [69], and the latter has been deduced from qualitative analysis of the function as it approaches $x=0$ as in Figure 3.14.

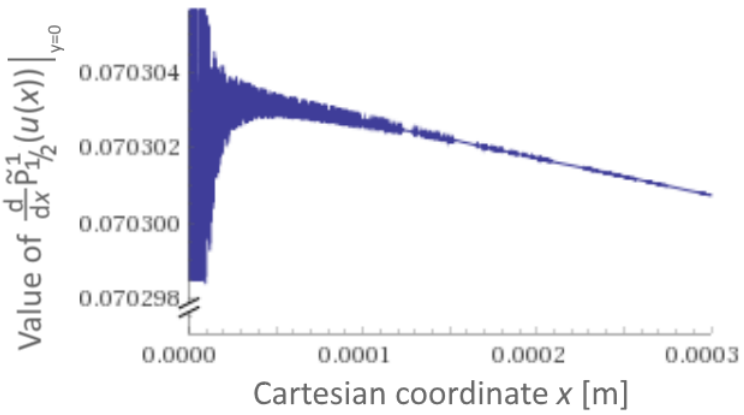

Figure 3.14: Plot of the derivative of $\tilde{P}^{1}_{1/2}(u(x))$ with respect to x, where $\rho = 7.112\,\mathrm{m}$, as calculated using WolframAlpha [69]. From this plot we determine that the function should cross the axis at approximately $0.0703037 = 0.5/7.112 = (2\rho)^{-1}$. Notably, the noise amplifies closer to the origin, demonstrating the divergence of the toroidal coordinate system at this point (where $x \to 0$).

This type of analysis is required due to increasing noise in the evaluation of the associated Legendre polynomials close to the origin ($u=\infty$), evident in Figure 3.14. Using these in the derivation of E_x from ψ in (3.91), shown in Appendix H.8, leads to the result:

$$\begin{aligned}E_x(x{=}0,y{=}0) \;=\; &\frac{1}{2\rho}\sum_{n=-\infty}^{\infty}\Bigg(\Big(A_{n,0}\,\mathbb{R}\mathrm{e}\,(f_{n,0})-A_{n,1}\,\mathbb{R}\mathrm{e}\,(f_{n,1})\Big)\cos(n\Theta)\\&-\Big(A_{n,0}\,\mathbb{I}\mathrm{m}\,(f_{n,0})-A_{n,1}\,\mathbb{I}\mathrm{m}\,(f_{n,1})\Big)\sin(n\Theta)\Bigg),\quad(3.107)\end{aligned}$$

where we notice contributions from the solenoid, as well as dipole components. This could be attributed to the zero-field point in a curved solenoid not being at its centre. Similar to that performed for E_x, the derivation of E_y from ψ (shown in Appendix H.9) produces:

$$E_y(x{=}0, y{=}0) \ = \frac{1}{2\rho} \sum_{n=0}^{\infty} A_{n,1} \Big(\mathbb{R}\mathrm{e}\,(f_{n,m}) \sin(n\Theta) + \mathbb{I}\mathrm{m}\,(f_{n,m}) \cos(n\Theta) \Big), \tag{3.108}$$

while for E_z we obtain (by setting $\coth(u) = 1$ and, due to (3.105), set $m = 0$ in (3.101)):

$$E_z(x{=}0, y{=}0) \ = \frac{1}{\rho} \sum_{n=0}^{\infty} n A_{n,0} \Big(\mathbb{R}\mathrm{e}\,(f_{n,0}) \sin(n\Theta) + \mathbb{I}\mathrm{m}\,(f_{n,0}) \cos(n\Theta) \Big). \tag{3.109}$$

By a similar derivation, shown in Appendix H.10, for ψ at the origin we obtain:

$$\psi(x{=}0, y{=}0) \ = \sum_{n=0}^{\infty} A_{n,0} \Big(\mathbb{R}\mathrm{e}\,(f_{n,0}) \cos(n\Theta) - \mathbb{I}\mathrm{m}\,(f_{n,0}) \sin(n\Theta) \Big). \tag{3.110}$$

In the event that the field is evaluated within $1.4 \times 10^{-5}\,\mathrm{m}$ of the origin, these equations are first used to calculate the field at the origin. This is then interpolated linearly with the field at a distance $1.4 \times 10^{-5}\,\mathrm{m}$ from the origin in the direction of the point at which the field is required. For this reason, in tune calculations it was decided to configure BMAD to use deviations in the orbit vector of 1.5×10^{-4}, so that tracking through this interpolated region has a minimal effect on the results.

Caching Function Values

For the tracking studies reported here, the associated Legendre polynomials were evaluated using the Fortran script developed by J. Segura and A. Gil [70]. Unfortunately, use of this script makes simulations with toroidal multipoles untenably slow.

In order to avoid the time-consuming calculation of associated Legendre polynomials for each field query, values of the function $\tilde{P}^m_{n-1/2}(u(x, y))$ are cached for x intervals of $10^{-4}\,\mathrm{m}$ at $y = 0$, for $n \leq 100$ and $m \leq 14$. This provides a consistent resolution in $\tilde{P}$ along the x-axis, and thus also an approximately consistent resolution with distance from the design trajectory (as inferred by Figure 3.5).

For a query of $\tilde{P}$ during a simulation run, we calculate the value of x corresponding to the queried u if the queried point of same u were instead

along the $y = 0$ (x-) axis. The two cached values of the function closest to this value of x are then linearly interpolated, and the result returned.

One drawback of this method is the potential lack of continuity in parameters sensitive to field continuity, such as tune. Fortunately, the fine grid and slow variation of the function avoid such problems on the scale of interest here, and adjusting the BMAD tune calculations to use orbits of larger deviation from the design orbit does not change the result beyond the fourth significant figure.

This method also vastly increases the size of the files needed for an effective toroidal multipole simulation. However, the resolution of cached values may be reduced for cases of large transverse oscillations. Overall, computer memory permitting, the simulation times with this method are similar to using field maps in BMAD.

3.3.5 Verification and Spin Dynamics Considerations

Having implemented the toroidal multipoles in BMAD, the tunes of the storage ring were calculated for cases using different permutations of toroidal multipoles, standard multipoles and field maps to describe quadrupole fringe and bulk fields. The tunes were calculated from the tracking results of particles tracked with coordinate deviations of 1.5×10^{-4} m from the design orbit, so as to minimise the effect of the near-origin field interpolation for the toroidal multipoles. The results are shown in Figure 3.15, including tune resonance lines.

The results suggest that minimal differences (0.0003 for ν_x and 0.0008 for ν_y for 15 kV quadrupole plate potential) occur by changing from the standard multipole to the toroidal multipole bulk description. This can be expected due to the fields both having similar agreement with the field map close to the design trajectory (although the tune calculation for the field map description itself is affected by the map interpolation scheme).

3.4 Discussion of Magnetic Dipole Field Non-Uniformities

The magnetic dipole field in the storage ring has been measured with various instruments [16], and a map of the non-uniformities in magnetic field magnitude in the storage volume around the ring has been produced (see Figure 3.16).

The objective of these measurements is to calibrate and configure a coil system in the vacuum chamber walls within the ring, to compensate the larger

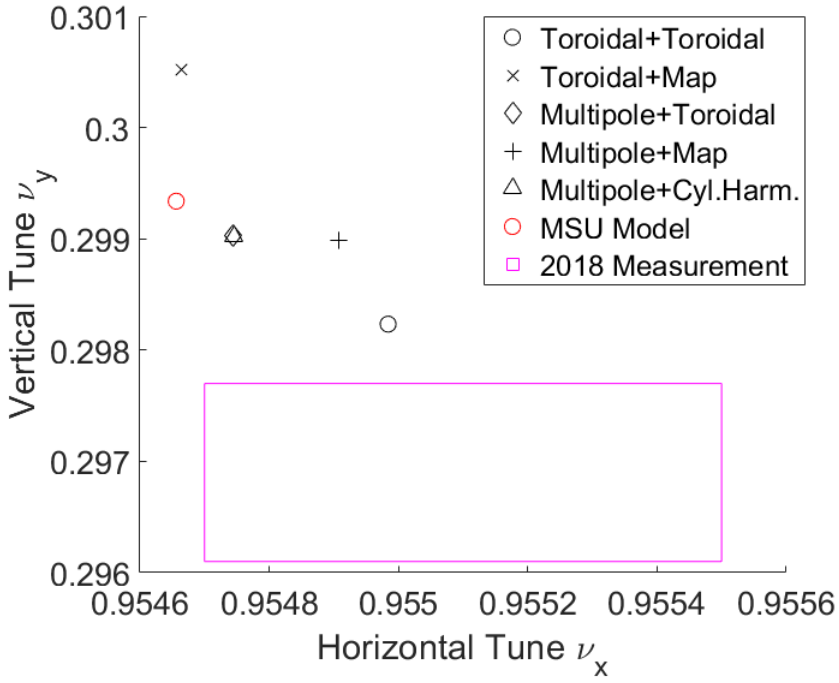

Figure 3.15: Plot of tune space, showing the measured values (in the centre of the violet box, which displays the error bounds), the values from the MSU model [56] (red circle), and cases of a field map fringe field with standard multipole bulk field (the plus), toroidal multipole fringe field with standard multipole bulk field (the diamond), field map fringe with toroidal multipole bulk field (the cross), toroidal multipole fringe and bulk fields (the circle) and cylindrical harmonic fringe (from Chapter 2) with standard multipole bulk field (the triangle), for a quadrupole plate potential of 15 kV. We see that the tunes from the five descriptions and the MSU model mostly differ on the level of the fourth siginificant figure, while the full toroidal multipole description is the closest to the measured value. Decreasing the simulated quadrupole potential by 1.3% results in agreement with measurement.

field non-uniformities. However, there appears to be a relatively large, random variation in the field between azimuthal measurement points. Combined with the fact that only the magnitude is measured, this makes it impossible to determine the components of magnetic field, required to fit accurately a 3D field description such as toroidal multipoles.

It is possible to make assumptions about the field, for example that the longitudinal magnetic field is zero such that the field can be processed in

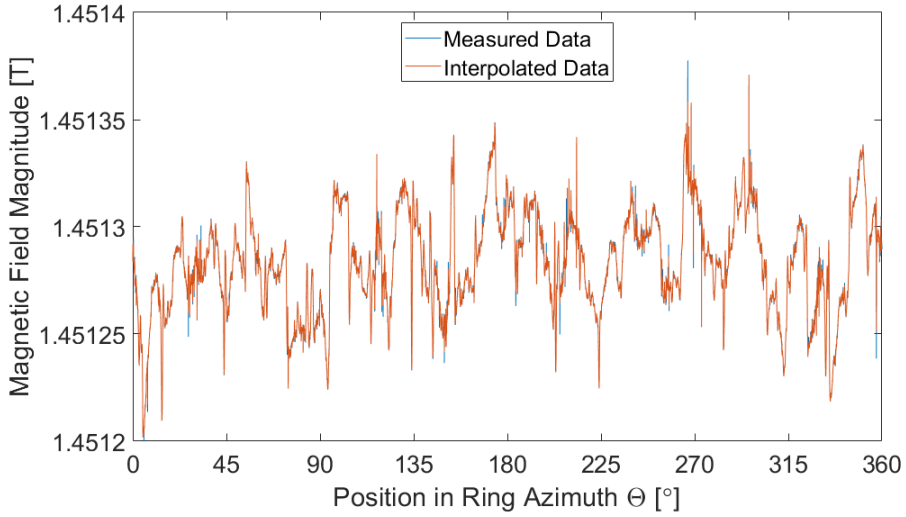

Figure 3.16: Field variations around the ring as measured [51] to 20 ppb accuracy [71] (at points of nonumiform spacing in ring azimuth) by one of the outermost NMR probes on the field measurement trolley within the storage region (blue), with a MatLab 1D interpolation of that data calculated at a similar number of points with uniform spacing (orange). We see very rapid, high-amplitude variations in field with respect to ring azimuth at various points, which the interpolation cannot follow. Such variations make this field difficult to fit or interpolate accurately.

to a transverse magnetic field map, or that the variations are mostly in the radial (x) direction. However, as these field components are not measured separately, further investigations in to the magnetic field would be required before such assumptions could be considered robust. Such studies are beyond the scope of research presented here.

Chapter 4

Simulation Studies

With the versatile model described over the previous two chapters, able to simulate the measured time dependency of the injection kickers, as well as the consistent curvature of the design trajectory and time-varying electric fields from the quadrupoles (during the injection scraping regime), we can perform studies on how the machine may behave given different values of these machine parameters.

To provide a benchmark of the model, we wish to study the lattice properties, particularly the beta functions, tunes and dispersion for the steady-state ring for various values of the electrostatic quadrupole potential. This allows comparison with other machines and other models of the same machine.

To make use of the model, we will also perform tracking studies for various configurations for the injection channel (kickers and injection angle) and collimators. We will also analyse the tracking results from a long-term (2000-turn) simulation.

4.1 Lattice Properties

4.1.1 Twiss Parameters and Dispersion

Due to (de-)focusing, the β, α and γ functions in the x- and y- axes vary around the ring. BMAD can calculate the values of these functions at any point in ring azimuth by tracking particles of some small deviation from a closed orbit, as described in Section 1.3. To minimise any inaccuracies resulting from the near-origin implementation of the toroidal multipole description investigated in the previous chapter, we choose a deviation from the design orbit of 1.5×10^{-4} for all phase space coordinates.

As the β function is proportional to the square of the beam size in the specified axis, we would expect this to tend towards increasing values whilst

inside the (defocusing) quadrupoles for β_x, and tend to decreasing values within the quadrupoles for β_y. Outside the quadrupoles, weak focusing occurs in the x direction, so we would expect β_x to tend towards decreasing values.

The calculated β_x and β_y functions for quadrupole plate potentials of 32 kV, 27.2 kV, 20.2 kV and 15 kV are plotted in Figure 4.1 (along with the lattice layout), where we see the expected behaviour in both β_x and β_y. The α_x and α_y functions are plotted in Appendix I.

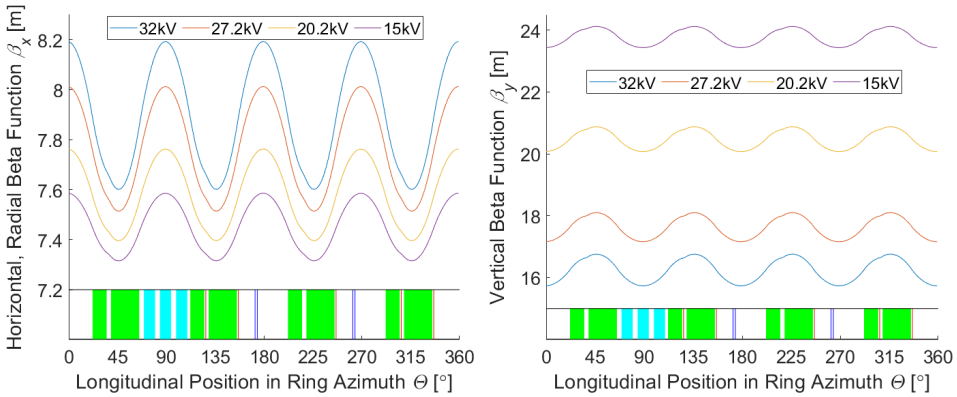

Figure 4.1: Beta functions of the storage ring model (using multipoles and toroidal multipoles for the bulk and fringe regions of the quadrupoles, respectively) for the horizontal, radial motion in x (left) and vertical motion in y (right) as calculated for quadrupole plates at 32 kV, 27.2 kV, 20.2 kV and 15 kV. The lattice is shown beneath each plot with quadrupoles (green), kickers (cyan), fibre harps (blue) and collimators (red). As can be expected, the horizontal and vertical betatron functions tend towards increasing (concave-up) and decreasing values (concave-down) respectively, when inside the quadrupoles. Due to the weak focusing of the dipole magnet, β_x tends towards decreasing values (concave-down) when outside the quadrupoles where, due to natural bunch divergence, β_y tends towards increasing values (concave-up). The β_x function is also less affected by variation in quadrupole strength than β_y, which is again expected due to the magnetic weak focusing in the x direction, while the only force in the y direction (in this particular set-up) is from the quadrupoles.

Another parameter of interest is the dispersion. Along with the betatron functions, this can also be used to compare models. We consider the argument that, for a higher quadrupole focusing strength (defocusing in x), the dispersion in that direction should be greater due to a particle with nonzero δ (relative momentum) being pulled further away from the design orbit, to-

wards the electrodes.

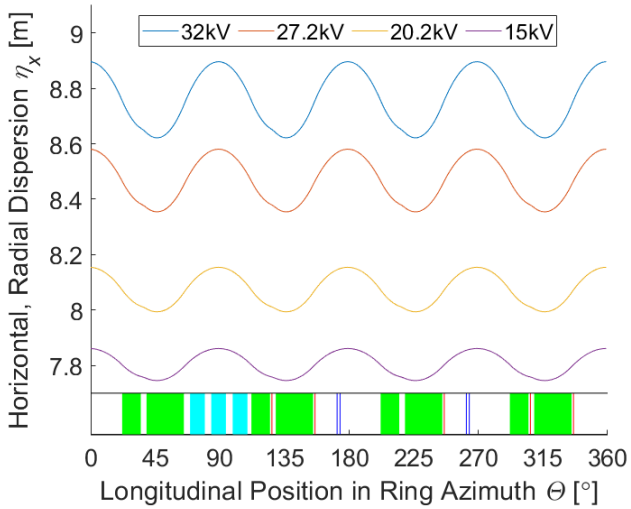

Figure 4.2: Dispersion in the radial direction x as calculated for quadrupole plates at 32 kV, 27.2 kV, 20.2 kV and 15 kV. The lattice is shown beneath with quadrupoles (green), kickers (cyan), fibre harps (blue) and collimators (red). As the electrodes positioned radially outward and inward from the design trajectory attract particles with a radial offset from this trajectory, the increaed dispersion with increased plate potential visible here is expected.

As can be seen in Figure 4.2, where we compare η_x for quadrupole plate potentials of 32 kV, 27.2 kV, 20.2 kV and 15 kV, our expectations have again been met with agreement from the simulation. Now that they are understood, these computed lattice functions provide a suitable basis for comparison between models.

Comparison with Other Models

The beta functions and x-dispersion at 32 kV can be compared to those from a similar, simpler model devised at Cornell University [72]. At time of comparison, for the quadrupoles this used a simple multipole fit based on a two-fold rotational symmetry, using a 2D field map of a straight quadrupole, without fringe fields.

Due to the lack of fringe fields, which contain a peak in electric field at the ends of the electrodes, we would expect a reduction in effective focusing strength. We also must shift the values in s, as the positioning of the elements

in the two models are offset by some small amount. The results are shown in Figure 4.3 and Figure 4.4.

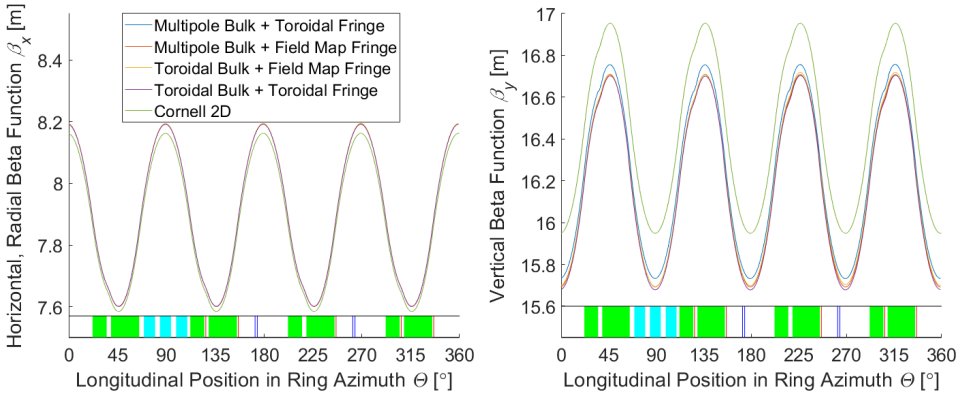

Figure 4.3: x- (left) and y- (right) betatron functions with quadrupole potential of 32 kV for this model with multiple permutations of quadrupole field descriptions, and the simple Cornell model where the quadrupoles consist only of a multipole bulk field based on a 2D (transverse) description of the quadrupoles, with no fringe fields. The lattice is shown beneath each plot with quadrupoles (green), kickers (cyan), fibre harps (blue) and collimators (red). As the Cornell 2D model excludes the peak in field caused by the ends of the electrodes, we expect the effective focusing to be weaker, which corresponds to the difference seen here of β_x being smaller and β_y being larger than for models containing fringe field descriptions. The different field descriptions from this model are too close to decipher in β_x. However, small differences can be seen in β_y, which is more sensitive to the quadrupole fields.

The results appear to confirm this hypothesis, with a difference of less than 1% noticeable between the β_y for various permutations of multipole and toroidal bulk field, and toroidal and field map fringe field descriptions. The furthest outlier is the standard multipole bulk with toroidal multipole fringe. However, as this case does not also stand out in β_x, we accept this as being within an acceptable difference for the modelling method.

4.1.2 Tune and Chromaticity

The betatron tunes ν_x and ν_y can also be calculated for the lattice. These also form a simple benchmark to allow model comparison. Although relying on only the tunes to describe the ring could potentially ignore substantial

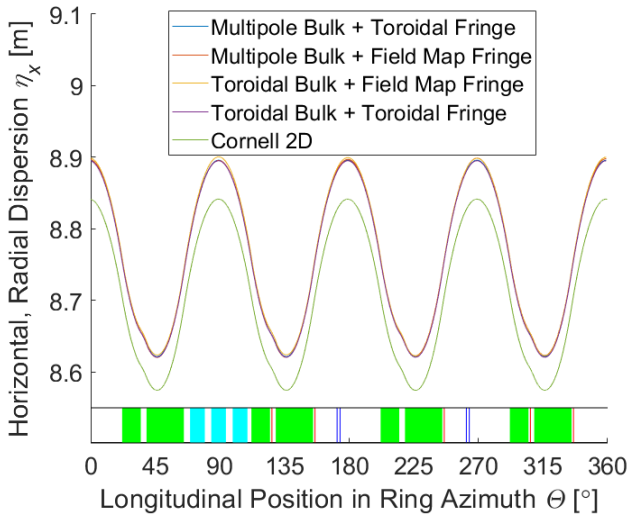

Figure 4.4: Dispersion in the radial direction x as calculated for quadrupole plates at 32 kV, for this model with multiple permutations of quadrupole field descriptions, and the simple Cornell model where the quadrupoles consist only of a multipole bulk field based on a 2D (transverse) description of the quadrupoles, with no fringe fields. The lattice is shown beneath with quadrupoles (green), kickers (cyan), fibre harps (blue) and collimators (red). Due to the lack of a field peak in the Cornell 2D model, exhibited by the fringe fields, we expect the effect of a weaker quadrupole, exhibited by a lower dispersion (which is increased by the electrically attractive radially inner and outer plates), which is seen here.

differences between models, calculation of the tunes are important for determining the proximity of the operating point of the ring to a resonance. The on-axis tunes (on the design trajectory) of the experiment ring have been measured [24], so models which differ from this beyond a few percent in plate potential should not be regarded as reliable.

The tunes were calculated for all four configurations of the model, at the measured quadrupole plate potentials of 20.5 kV, 20.2 kV, 19 kV, 17.6 kV, 15 kV and 13 kV. These tune values have been plotted in tune space in Figure 4.5.

From these plotted tune values we see that, for a given quadrupole plate potential, there is greater variation in ν_x than in ν_y between the different descriptions available in the model. We also notice that the different models converge as the quadrupole plate potential reduces, which is expected, since the models should be identical for zero plate potential.

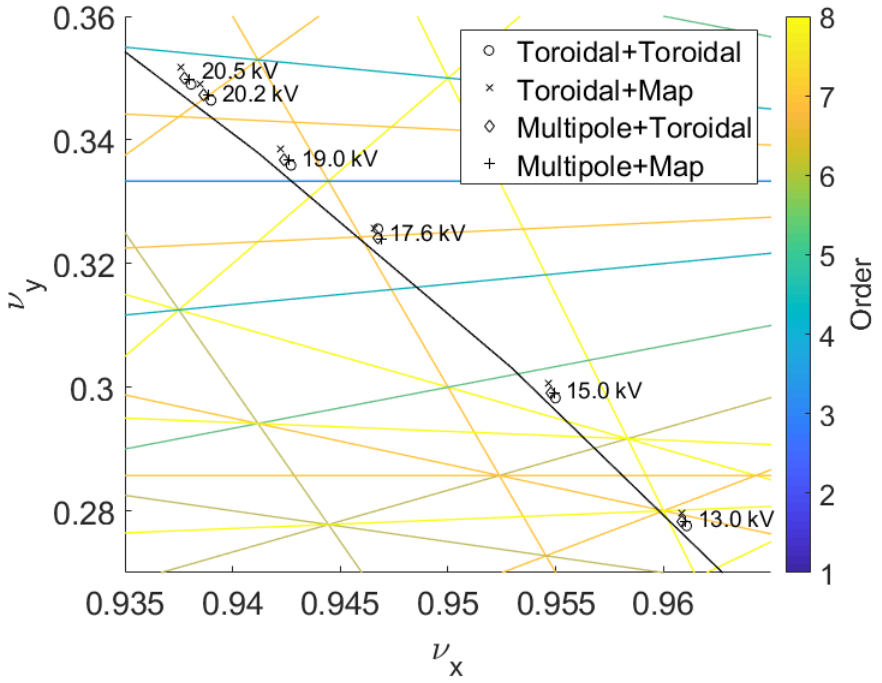

Figure 4.5: Location in tune space of models where the quadrupoles comprise of toroidal multipole bulk and fringe descriptions, toroidal multipole bulk with field map fringes, standard multipole bulk with toroidal fringes and standard multipole bulk with field map fringes. The values for the analytical case of a continuous quadrupole (covering the entire ring azimuth) are shown as a black line [73], while the resonances are shown as coloured lines, up to eighth order. We see the differences between the descriptions grows as the quadrupole strength increases, which may be expected as all descriptions are equivalent when the quadrupole plates are at 0 kV. We also note that the description with standard multipole bulk with toroidal fringes is consistently closer to the continuous quadrupole approximation, although the measured values from the experiment are not shown here.

As the bunch in the ring has a large spread in momentum of about 0.3%, we also wish to analyse the effect this may have on the spread of particles in tune space. To do this, in Figure 4.6 we show the variation in tune with momentum for the closed-orbit case of different momenta with the quadrupoles at 19 kV as this is closest to a low-order resonance.

We see that orbits of much increased or decreased momentum (and thus radii with respect to the design trajectory) cause larger values of ν_x, and

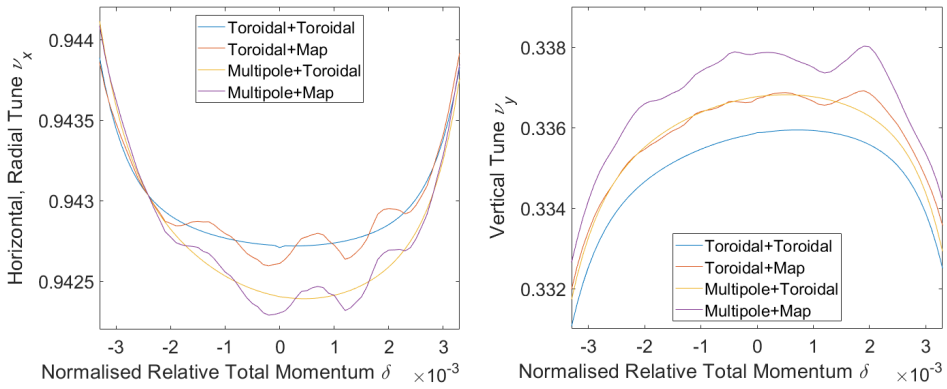

Figure 4.6: Horizontal, radial tune ν_x (left) and vertical tune ν_y (right) as a function of closed orbit momentum, with the quadrupoles at 19 kV, where the quadrupoles comprise of toroidal multipole bulk and fringe descriptions, toroidal multipole bulk with field map fringes, standard multipole bulk with toroidal fringes and standard multipole bulk with field map fringes. The behaviour of ν_x can be understood as particles with closed orbits radially further out (higher momentum) have time to undergo more betatron oscillations in a rotation period, whereas those radially further inward also have time for more betatron oscillations due to having lower momentum. We see that models containing field maps exhibit turbulent chromaticity, while the analytic field models produce smooth lines. This is expected due to the simple interpolation performed, and due to noise in the field map. We notice a consistent difference between the standard multipole and toroidal multipole bulk field descriptions, although this can be expected given the difference in tune.

lower values for ν_y. This is caused by the weakening of the field close to the plates by high-order multipoles (as in Figure 3.1 in Chapter 3), with respect to what it would be if only the quadrupole term were present.

For the on-axis tunes (at $\delta = 0$), the vertical tune ν_y exhibits a small, positive slope (chromaticity). This can be understood as the particles with higher momentum having to spend more time within the (vertically focusing) quadrupoles before completing an orbit, and thus undergoing more oscillation, while the opposite is the case for the lower momentum particles. The horizontal tune ν_x exhibits a negative on-axis slope (chromaticity), due to the very slight decrease in strength of electric quadrupole defocusing relative to magnetic weak focusing with increasing momentum.

We also notice that using the field maps for the fringe fields introduces

turbulence in the chromaticity (characterised by the slope in the plots). This is a feature we expect, due to the field maps having some level of noise, but also as there will be some imperfect, computationally inexpensive interpolation used which will result in the field not being entirely smooth in all derivatives.

Another feature visible in Figure 4.6 is the difference in tunes between the standard multipole bulk field description and the toroidal multipole bulk field description. This can only be attributed to the properties of the fits and/or accuracy of the fit methods with the given field maps.

In Figure 4.7 the closed orbit tunes have been plotted with the possible spread caused by momentum, for a quadrupole potential of 19 kV.

Taking momentum spread into account, we see that, for a quadrupole potential of 19 kV, the vertical tunes ν_y can coincide with the third-order resonance at $\nu_y = 0.3333$. This could cause substantial storage losses, hampering the statistics and long-term measurements made by the experiment.

4.2 Injection Offsets

To determine the angle and position of the injected beam, the simulated beam behaviour of the ring can be compared to the behaviour of the beam in the physical ring. The most readily available quantity characterising relevant beam behaviour is the number of measured calorimeter hits. The injection kicker and quadrupole strengths provide two independent machine parameters. By tracking particles with different values for these parameters, with different incoming beam angles, and finding the number of surviving antimuons for each configuration, we can obtain results which can be compared directly to measured values from the experiment.

Due to the narrow aperture of the inflector magnet, through which many of the incoming antimuons are collimated, the position of the beam exiting the inflector is effectively fixed. An unintended radial momentum component on injection will have the effect of shifting the optimal kicker strength.

However, what was observed in the experiment was that the storage fraction would drop linearly with decreasing quadrupole strength, with a zero storage at approximately 6 kV quadrupole potential. Due to it being a potential cause of this phenomenon, studies on the effects of average vertical momentum on injection (being considered to be limited to the range $0 \leq p_y \leq 0.003$), is the main focus of the injection studies presented here.

To this end, we vary the vertical momentum p_y in the range $0 \leq p_y \leq 0.003$ with increments of 0.001, for the quadrupoles at 11 kV, 15 kV, 18 kV, 21 kV and 25 kV. For each of these cases, a bunch of 168924 antimuons taken

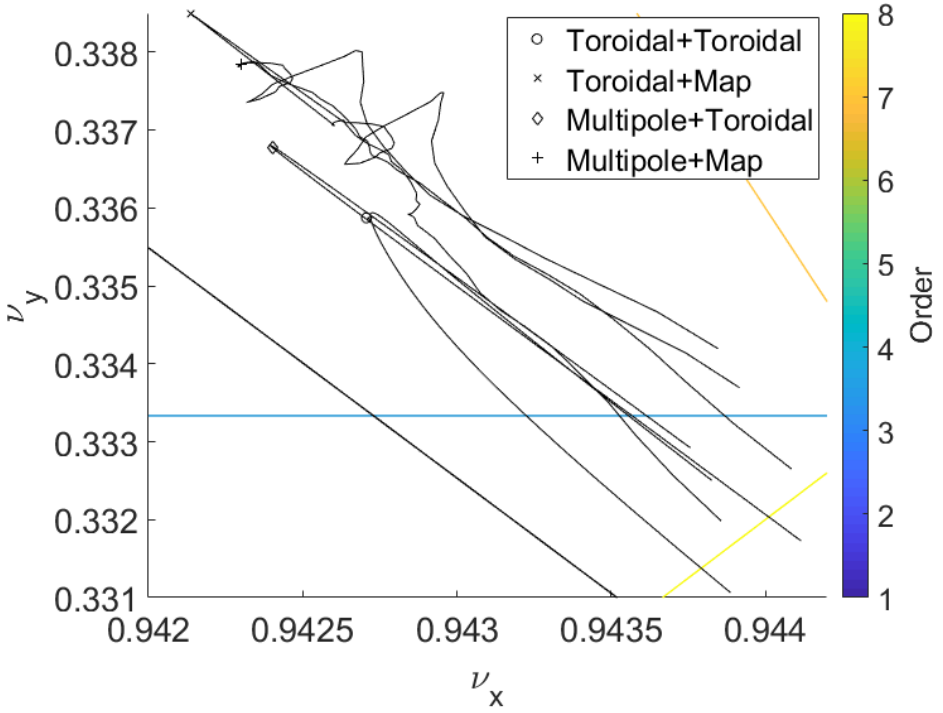

Figure 4.7: Position of the ring in tune space, with quadrupoles at 19 kV, where the quadrupoles comprise of toroidal multipole bulk and fringe descriptions, toroidal multipole bulk with field map fringes, standard multipole bulk with toroidal fringes and standard multipole bulk with field map fringes. The spreads of closed orbit tunes caused by the permitted momentum range of the ring are shown as lines passing through those tunes. We see that both descriptions involving field maps exhibit erratic behaviour in tune space, while the continuous descriptions have smooth behaviour. The effect of chromaticity on the tunes for the continuous descriptions is to extend them in the positive direction in ν_x and in the negative direction in ν_y, in line with the effects visible in Figure 4.6. We notice that the chromaticity may cause particles to have tunes on the $N_y = 3$ resonance ($\nu_y = 0.3333$), which could cause substantial storage losses.

from the Cornell University injection simulation [41] was tracked from the downstream end of the inflector around the ring 20 times. The kicker strength for this simulation was set to 50% of the (near optimal) 270 gauss peak kick, as this is considered to be approximately the strength of kick used during the gathering of the experiment data. Here, we use the straight multipole de-

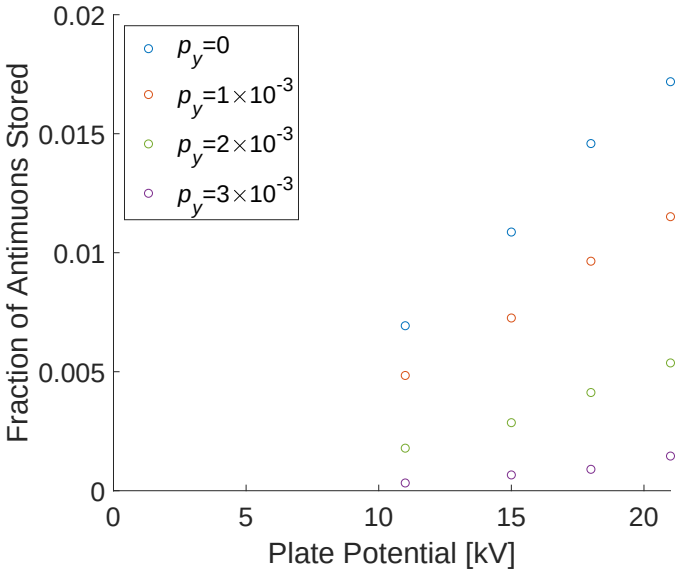

Figure 4.8: Stored antimuon fraction after 20 turns as a function of quadrupole plate potential as simulated for a beam injected with vertical momenta p_y of 0, 0.001, 0.002 and 0.003 applied, with kicker strength set at 50% of the (near optimal) 270 gauss peak. The value of 50% is chosen in an attempt to coincide with the kicker strength used for the measured data whose absolute value is unknown, but is known to be 75% of the kicker strength available during the commissioning run, with 100% known to be insufficient for optimal injection. We see that the $p_y = 0.003$ simulation produces different storage behaviour to the other simulations, which have an almost linear relationship between storage fraction and quadrupole potential. This difference in behaviour may help to determine which simulation agrees best with the measured data (with a factor proportional to detector acceptance applied), allowing us to uniquely determine p_y of the injected beam in the storage ring.

scription of the quadrupole bulk fiends, and the field map descriptions of the quadrupole fringe fields to save computation time. As we only consider storage over 20 turns in these simulations, the field map description is considered sufficiently accurate for such an analysis.

The results are shown in Figure 4.8, where we see that the variation in

the number of stored antimuons versus plate potential is similar for all cases where $p_y \leq 0.002$. This is a useful feature, as the measured values from the experiment must be multiplied by a single factor (dependent on features such as detector acceptance and relative numbers of antimuons used in the simulation and experiment), and so the problem is to find a factor at which both the shape and values of the data sets agree, resulting in a uniquely determined value of p_y. Comparison with data from the experiment will be performed in Section 5.2.

Analysis of radial angle of injection and kicker strength was also performed. Different combinations of peak kicker strength, in 27 gauss steps, and radial injection angle, in 1 mrad steps, were simulated for the first ten turns with an injected bunch of 32201 antimuons. The optimal point was found by populating different points in Figure 4.9 and manually choosing the next simulation configuration accordingly.

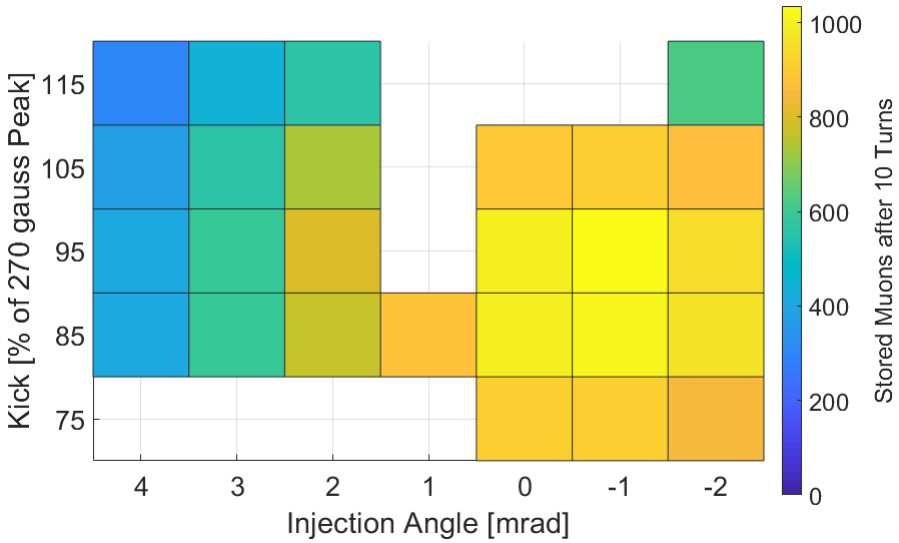

Figure 4.9: Simulated antimuon capture efficiency as a function of radial injection angle and kicker strength, as found from an injected bunch of 32201 antimuons. The optimisation started at 105% kick and 3 mrad injection angle, from which steps of 5% and 1 mrad were taken to simulate adjacent configurations, and a path made manually towards the optimal point of 95% (256.5 Gauss peak) kick and radial injection angle of -1 mrad (radially inward). We note that configurations adjacent to the optimal point differ in efficiency by up to 15%.

This optimisation procedure found the best conditions consisted of $-1 \pm$

1 mrad of radial momentum on injection, and a kicker peak field of 257 ± 27 gauss, with deviations from these conditions of 1 mrad or 27 gauss having less than a 15% effect on storage efficiency. Although this study was performed with limited statistics, similar studies performed with BMAD [32] and with Geant4 [28] predict the same optimal value of injection angle [74, 75].

To confirm these results experimentally would be highly desirable. However, at time of writing, the absolute magnetic field of the kickers is not known to within 10%, and while the angle of the inflector can be adjusted to scan different injection angles, this requires disassembly of the experiment. Therefore, the agreement with another model is deemed sufficient confirmation of this study.

4.3 Collimator Configurations

Another study of importance to gauge the accuracy of the data gathered by the experiment is to compare how systematics are affected by changes in experiment configuration (changeable as components can fall in to disrepair) as compared to the design. In this case, we wish to compare the temporal distributions of antimuon collimations (a potential cause of increased experimental error due to antimuon loss during the measurement period) between the cases of two and five collimators inserted.

The two configurations studied correspond to the designed experiment (with five collimators) and the experiment running at the end of the commissioning period, with one collimator between the second short and long quadrupoles (the first of the five collimators), and the other collimator between the fourth short and long quadrupoles (the fourth of the five collimators). For each of these, a bunch from the end of the Cornell University beamline simulation (at the downstream end of the inflector) containing 32201 antimuons was tracked from the inflector exit around the ring 500 times, with quadrupoles at 20.5 kV, leaving approximately 1000 antimuons in the storage region in both cases.

The losses from the tracking as a function of azimuth in the ring are shown in Figure 4.10, also showing how the losses are split between the top, bottom, radial outside and radial inside of the apertures. We see that, in the two collimator case, collimator four must absorb much of the load of the missing collimators, with the remaining load being taken by the first collimator and chamber walls. It is important to point out that fewer losses occur in the two collimator case over the period of tracking. However, the same (or even greater) losses may occur over a longer period, increasing the number of antimuons lost during data taking (and thus the associated

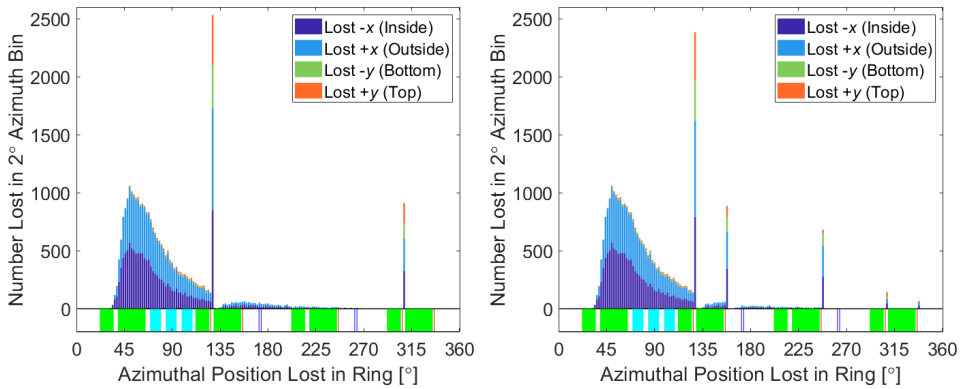

Figure 4.10: Histograms of antimuons lost over 500 ring turns at different locations in ring azimuth, collected in 2° bins for the cases of two (the first and fourth) collimators (left) and all five collimators (right). The bins are each split in to four, showing collimation at the positive and negative x and y apertures. The lattice is shown beneath with quadrupoles (green), kickers (cyan), fibre harps (blue) and collimators (red). We see that the two collimator case slightly increases the load on the first collimator, while increasing the load on the fourth collimator by a factor of 6.3. We also note that the five collimator case removes load on the vacuum chamber walls betwen the second collimator and the 180° fibre harps. It should be noted that fewer losses occur in this range for the two collimator case, although more losses may occur later. Although one can suggest that much of the load up to the first collimator would be from the injection (first turn), a time analysis of the collimations must also be performed to confirm this.

systematic error).

To investigate this further, we can also study the losses as a function of time. The same loss data were plotted against time, over a period just more than the first turn ($0\,\text{ns} < t < 150\,\text{ns}$) and is shown for the two cases in Figure 4.11 and for the first 70 µs in Figure 4.12.

We see that there is minimal difference over the first turn, which is expected as this is when antimuons with momentum outside the ring acceptance will be collimated, which will happen continuously as the beam passes all collimators around the ring with little impact on the time distribution from the number of collimators. However, at times approaching the measurement period (from 35 µs onwards) we see more antimuons being collimated at later times in the two collimator case. This is expected, as antimuons which would hit one of the three missing collimators must orbit more times before hitting

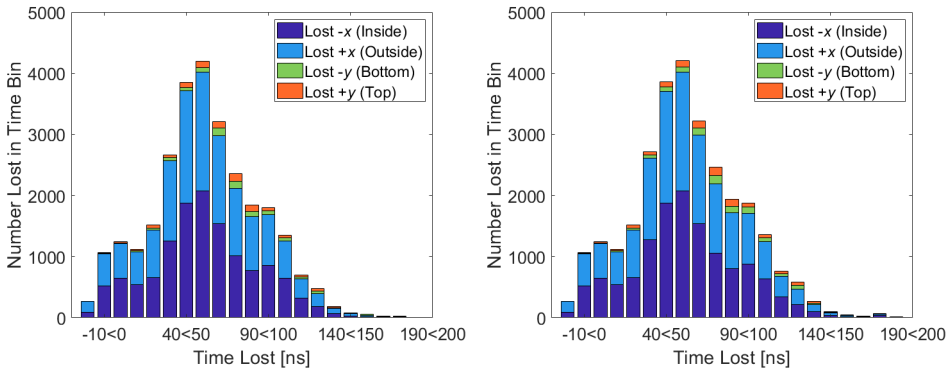

Figure 4.11: Histograms of antimuons lost over 500 ring turns at different times, collected in 10 ns bins for the cases of two (the first and fourth) collimators (left) and all five collimators (right). The bins are each split in to four, showing collimation at the positive and negative x and y apertures. We see minimal difference here between the two cases, which is understood due to the losses in the first turn being dominated by hits on the walls due to the large momentum spread. However, analysing the losses in this time period does show the signal that could be expected in the calorimeters from the particles with momentum outside the acceptable range.

one of the remaining two.

While the statistics are not high (due to the simulation time), we see many trends which are all intuitive. It is understood that fewer collimators results in longer collimation time, and therefore a higher lost antimuon systematic error for the experiment. It is also clear that much of the collimation in all cases will occur on the first turn, in the vacuum chambers housing the first long quadrupole and the kickers, although the beam intensities are not high enough for this to be of concern.

4.4 Long-Term Storage Simulation

In a final demonstration of the use of the model, a long-term simulation, including spin tracking, was performed over one month with 168924 antimuons. The initial states of the particles were taken from the results of the Cornell University beamline simulation [76], at the downstream end of the inflector, which include the phase-space, spin and arrival time of each particle. These were tracked over 2000 turns of the storage ring, corresponding to approximately 300 µs which, as the experiment measurement period starts at 35 µs and ends at 699 µs, covers approximately half of the measurement period.

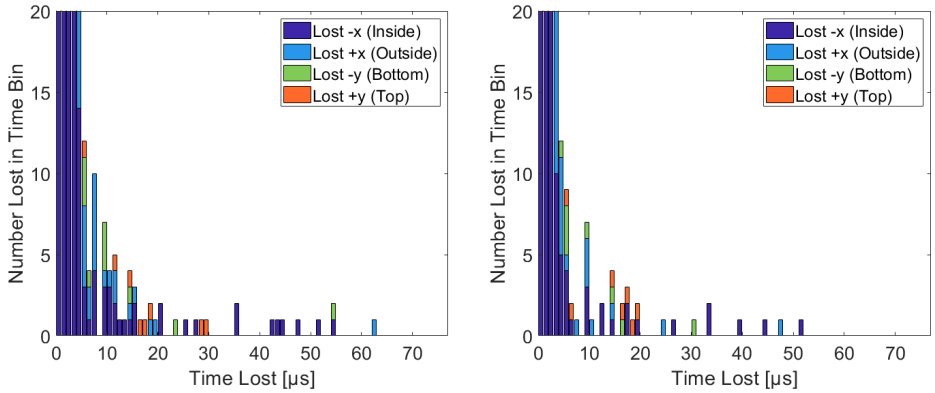

Figure 4.12: Histograms of antimuons lost over 500 ring turns at different times, collected in 1 μs bins for the cases of two (the first and fourth) collimators (left) and all five collimators (right). The bins are each split in to four, showing collimation at the positive and negative x and y apertures. In this range, we see a difference in the number of antimuons being lost at later times, within the measurement period, which starts at 35 μs after injection. For the two collimator case, more losses occur at later times than for the five collimator case. We expect this trend to continue (albeit with lower statistics) beyond the time range shown, well in to the measurement period.

The quadrupole potential was set at 18.06 kV which, due to the difference with the effective operating point of the ring in tune space discussed in Section 5.1.1, represents the ring with quadrupole potentials at the experiment value of 18.3 kV. The static scraping case was used, with first step potential of 12.93 kV to represent a quadrupole potential of 13.1 kV. The kicker pulses were all set to coincide with the middle of the bunch reaching the centrepoint of the middle kicker, and with peak fields of 270 gauss.

As the (asymmetric quadrupole) scraping and consequent transition to symmetric quadrupoles occur over the first 35 μs, we use the field map descriptions of the quadrupole bulk and fringe fields for the first 235 turns of the storage ring. After this, the continuous descriptions are used for the remaining 1765 turns, whereby we use a standard multipole description of the bulk fields, and toroidal multipoles for the fringe fields.

Our particular aim is to investigate particle loss, with the data obtained for this allowing for analysis of the evolution of polarisation and any correlations between phase-space and polarisation.

4.4.1 Mid- to Long-Term Muon Losses

Due to the impact on the experiment of particle collimation during data taking, which starts at 35 µs after injection, mid- and long-term antimuon loss is of substantial interest. We analyse particle losses from the 2000-turn run and, as we see in Figure 4.13, the distribution of losses about the ring is similar to that for the five collimator study in the previous section.

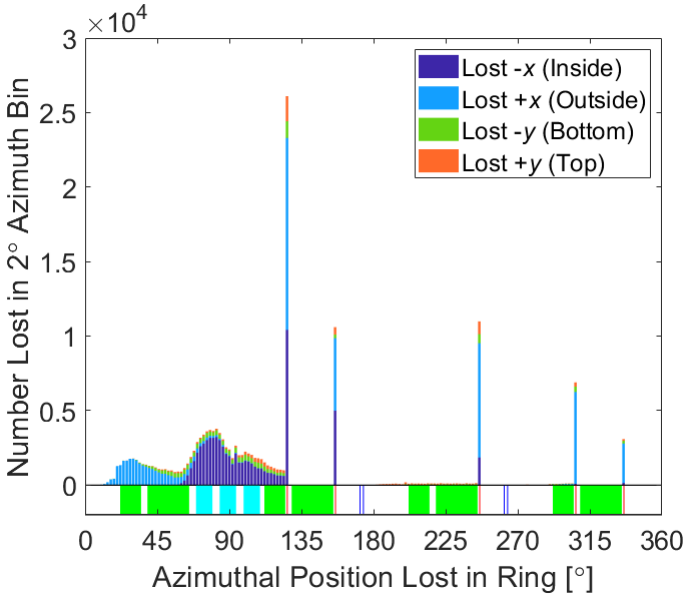

Figure 4.13: Histogram of antimuons lost over the long simulation run (2000 ring turns) at different locations in ring azimuth, collected in 2° bins. The bins are each split in to four, showing collimation at the positive and negative x and y apertures. The lattice is shown beneath with quadrupoles (green), kickers (cyan), fibre harps (blue) and collimators (red). We see that the distribution is similar to the five collimator case in Figure 4.10, with high load on the first collimator (within the second quadrupole pair) and many losses incurred through the first quadrupole and kickers on the first turn. The difference in distibution of the losses within the first quadrupole are attributed to use of a slightly reduced global aperture which, as the particles striking this at the inflector exit have too great action in the radial axis to be stored, makes no difference to storage during the measurement period.

This is unsurprising, as the difference in simulation time produces few more collimated antimuons. However, those few antimuons are of interest for the lost particle systematic, whereby antimuons lost during the data-taking

may affect average properties of the stored particles, and thus the measured result for $g-2$. The losses are plotted versus time for the full simulation period in Figure 4.14.

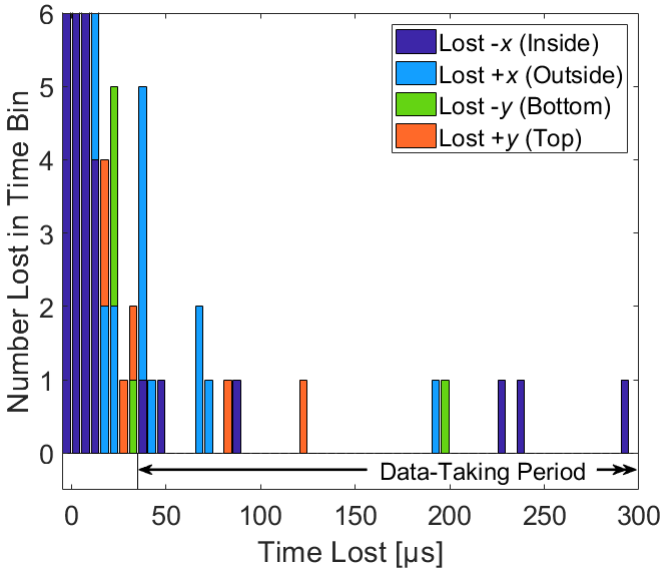

Figure 4.14: Histogram of antimuons lost over the long simulation run (2000 ring turns) at different times, collected in 5 μs bins. The bins are each split in to four, showing collimation at the positive and negative x and y apertures. The start of the experiment data-taking period is shown at the bottom, and extends up to 699 μs. We see a total of 18 antimuons collimated during the data-taking period, with no clear preference of aperture struck. Investigating these losses is a high priority for the experiment.

There are 18 antimuons lost after the start of the measurement period (at 35 μs). Plotting these losses in x and y phase space, as in Figure 4.15, reveals they do not necessarily undergo high amplitude betatron oscillations in either x or y individually. However, when the oscillations in position peak simultaneously, as shown in Figure 4.16 for one such case, the particle can occasionally be just outside the storage region for a short period of time.

The oscillations in x and y individually are of much higher frequency than their combined "beat" pattern, and so particles with too great a betatron amplitude in either x or y are lost shortly after injection. However, if only the combination of these can be enough to place the particle outside the storage region, it can take many microseconds before the particle can hit a collimator.

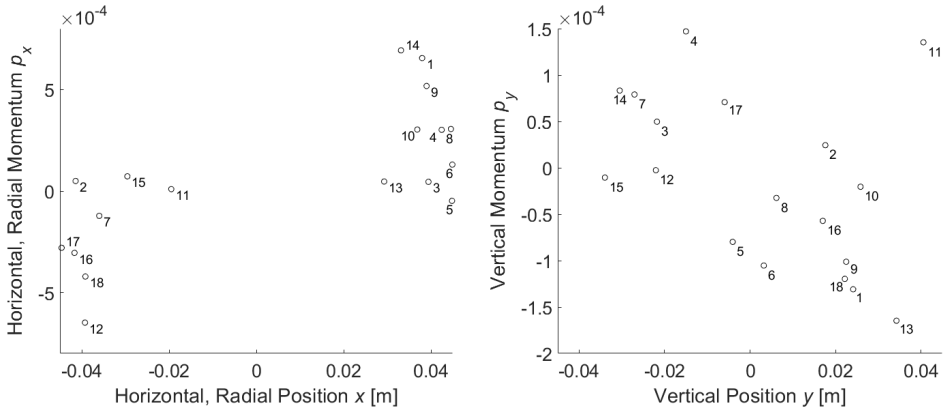

Figure 4.15: Labelled x- (left) and y- (right) phase space locations of the 18 lost antimuons at time of loss. For these particles (lost at late times), we notice that particles with high-amplitude orbits in x phase space have low-amplitude orbits in y phase space and vice-versa. From this, we suggest that the combination of both oscillation amplitudes is relevant to collimation by the (circular) collimators.

From the same analysis of all 18 late-loss antimuons, the same pattern emerges as in Figure 4.16: the distance from the design orbit develops a beat frequency, and only leaving the storage region when the x and y betatron phases match – on the order of tens of μs after injection. The scraping period after injection is designed to collimate particles with too high a betatron amplitude in either x or y. However, the 3 μs beat period observed in Figure 4.16 is too large to effectively collimate particles when the betatron phases in x and y only match (taking the particle outside the storage region) on some of these peaks, as this must occur at a collimator within the 35 μs scraping period to safely remove the particle before data-taking.

Two methods are possible to mitigate this problem. The first is changing the collimator shape to have a square aperture, which would prevent this combined phase effect although it would reduce the total storage volume and thus the number of stored antimuons (due to vacuum chamber rails existing toward the corners of such an aperture). The other is to attempt to target these particles with RF-pulse scraping with the aim of damping their oscillation amplitude or to collimate them within the pre-data scraping period. However, this would be difficult to do in the 35 μs before data taking.

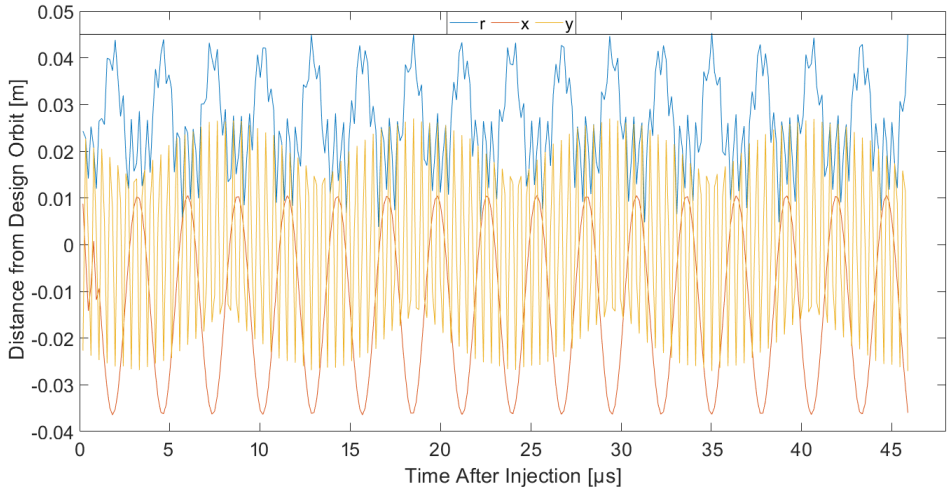

Figure 4.16: Horizontal (x, orange) and vertical (y, yellow) coordinates of one of the particles lost during the measurement period, along with the distance r (blue) from the design orbit. The samples are taken at the point in azimuth of the injection point, and the last sample is the point of collimation. The edge of the (circular) storage region is shown as a black line at 0.045 m. We see that peaks in r occur with extrema in either x or y, whichever has greatest amplitude. However, the maximum values of r are only reached when the extrema of both x and y occur simultaneously. It is evident from this plot that this occurance is rare, and much less frequent than extrema in x or y individually.

4.4.2 Evolution of Polarisation

We wish to investigate how the average spin direction (polarisation) of the beam changes over time. Naturally, we expect the polarisation to precess in the horizontal plane with frequency proportional to a_μ. However, the statistical properties of the polarisation may also change over the circa 300 μs period simulated due to the electric fields from the quadrupoles and a net movement parallel to the magnetic field (the "pitch correction" term) as in the latter two terms of (1.3). While our expectation is for these effects to be negligible, we must show this to be the case in the simulations.

As the spin vector in BMAD is stored as a normalised 3-vector, for analysis this must be decomposed in to two angles: the vector's angle in the horizontal plane (relative to the z axis), and the angle between the spin vector and the horizontal plane. The latter is simply the arcsine of the vertical component. However, the angle in the horizontal plane continually precesses

with the $g-2$ frequency ω_a.

Although the experiment allows measurement of a particle's approximate spin angle in the range 0 to 2π only, we convert the horizontal spin angle in to a total phase advance. This is because a collective oscillation between $-\pi$ and π would complicate the statistical analysis when the polarisation angle is close to $\pm\pi$.

We again use the simulation samples taken from the azimuthal coordinate of the injection point (exit of the inflector). We average the processed spin angle values in to 300 ns width bins, taken between 0 µs and 300 µs. With knowledge of the orbit time (149 ns) and the number of particles surviving (7675) this then leads to an approximate population of 15400 to 15600 per bin. The results are shown in Figure 4.17.

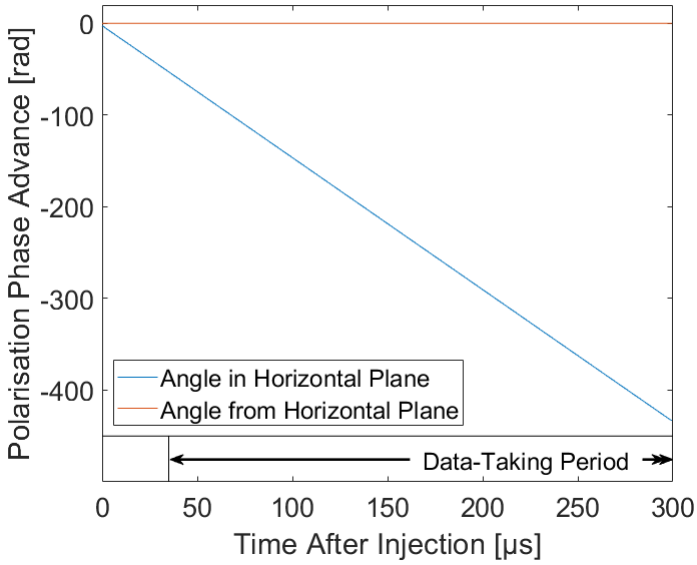

Figure 4.17: Bunch polarisation angle in the horizontal plane, from the longitudinal $+z$-axis in the direction of the $+x$-axis (blue), and angle in the vertical direction "from the horizontal plane" (orange). The angle in the horizontal plane has been converted to a total phase advance for analysis. The data-taking period starts at 35 µs and continues to 699 µs. We observe that the angle from the horizontal plane is constant while precession occurs in the horizontal plane. Given that the only magnetic field within the measurement period is the perfectly vertical dipole field, this behaviour is expected.

A closer look at the vertical angle in Figure 4.18 shows a small but steady vertical polarisation angle of 2.8 mrad, which differs from the average verti-

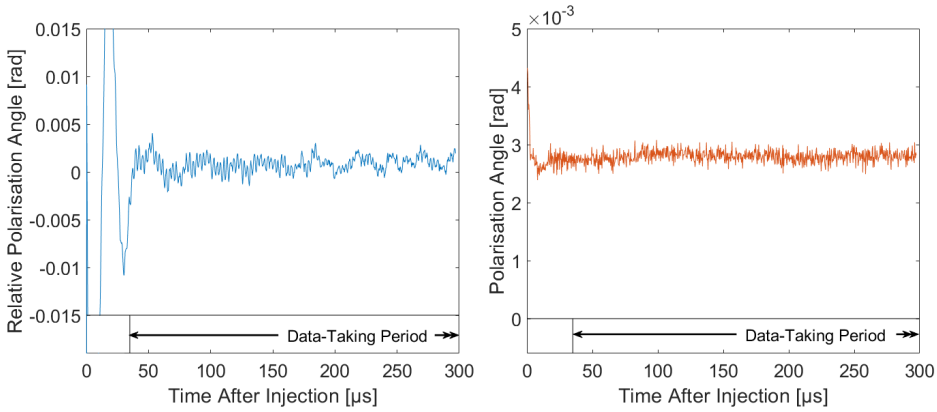

Figure 4.18: Bunch polarisation angle in the horizontal direction, relative to a linear fit of $-1.43935\,\text{rad}\,\mu\text{s}^{-1}$ (left) and bunch polarisation in the vertical direction, where zero is parallel to the horizontal plane (right). The measurement period starts at 35 μs and continues to 699 μs. We see minimal variation after scraping, with the polarisation settled at 2.8 mrad from the horizontal plane for the measurement period. The variation of approximately 0.2 mrad on both angles is largely due to the chosen binning. Although increasing the bin size to 0.4 μs can halve this variation during the measurement period for the horizontal polarisation, it increases the variation in the vertical angle. Thus, we conclude that the residuals are due to a conbination of bin choice and effects from the electric field and the "pitch correction" term of the magnetic field (the latter two terms in (1.3)). It is noted that the horizontal polarisation angle does not settle until approximately 1.5 μs after the start of the measurement period. Although binning does not change this, it may be due to sampling the beam at a single location in ring azimuth.

cal polarisation angle of the incoming beam of 0.28 mrad. Analysis of the initial spin vectors of the particles surviving the simulation confirms that they started with a vertical polarisation of 2.6 mrad, so we conclude that the vertical polarisation of the incoming beam is modified on injection, possibly by collimation and/or by the non-uniform magnetic field of the kicker.

For the horizontal polarisation in Figure 4.18, we have subtracted a fit consisting of a constant spin precession angular frequency of $-1.43935 \times 10^6\,\text{rad}\,\text{s}^{-1}$. Using only the first term in (1.3), this corresponds to a value of $a_\mu = 0.00116592$, which matches the experimental value of a_μ to that level of precision. From this, we deduce that there are no features in the model, during the data-taking period, which affect the polarisation precession to greater than the level of 1 ppm. If decays are included in the simulation, we note

that this relatively constant residual may change based on the polarisation-momentum correlations discussed in Section 4.4.3.

The apparent erratic behaviour of the horizontal polarisation during the scraping period in Figure 4.18 continues to approximately 1.5 µs in to the measurement period. Changing the time-bin size has little effect on the duration of this erratic behaviour, although it does affect the number of high-amplitude oscillations performed in that space of time. This suggests that it may be an artefact of taking these values at a single location in ring azimuth. However, if confirmed as a real effect, shifting the start of the measurement period by a few microseconds will mitigate any effect on the experiment.

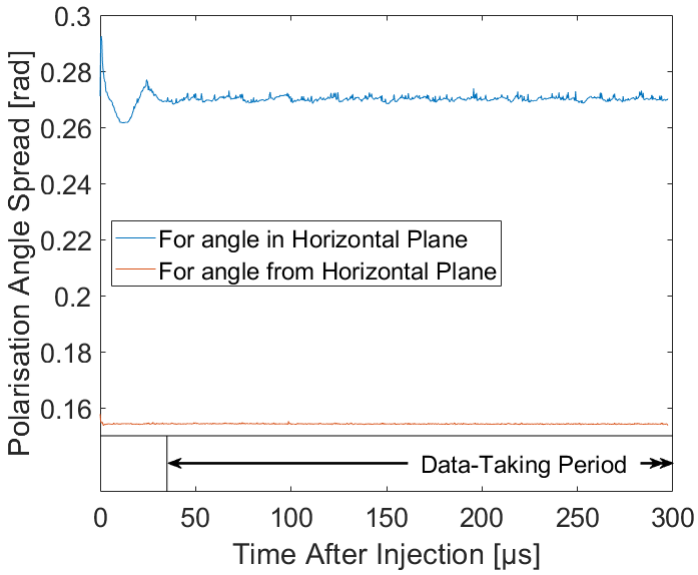

Figure 4.19: Standard deviation of the simulated polarisation in the horizontal plane (blue) and horizontal plane (orange). The measurement period starts at 35 µs and continues to 699 µs. We notice that, despite the exclusion of decays from this simulation, there is no evident change in polarisation spread during the measurement period for either angle. We also notice a variation in spread for the polarisation angle in the horizontal plane up to the start of the measurement period, similar to the behaviour of the angle itself in Figure 4.18.

We also wish to investigate the polarisation spread as described by the standard deviation, as having a weak polarisation may also affect the results. The polarisation spread is plotted in Figure 4.19 for both the polarisation

angle in the horizontal plane and that in the vertical direction.

From Figure 4.19 we see no change in the spread in polarisation over the measurement period. As uniformity during the measurement period is desired to avoid potential additional systematics in the measurement of the precession frequency over time, this is encouraging. However, we do see fluctuations in the horizontal polarisation spread similar to those in the polarisation angle itself in Figure 4.18, up to around the start of the measurement period. Due to the persistence of this feature, it would be appropriate to compare this behaviour with that of different models.

4.4.3 Phase-Space to Spin Correlations

In the interests of understanding the precession of the bunch polarisation in the storage ring, we wish to investigate correlations between particle spins and their phase-space coordinates. As antimuons passing through different field non-uniformities may undergo spin precession at different rates, finding ways to isolate those which traverse a more uniform field can help to reduce the systematic error of the experiment.

Of all possible correlations between the six-dimensional phase space and polarisation angles, the most relevant for the experiment is that between the momentum δ and the horizontal polarisation angle. This is because δ determines the equilibrium radius (position in x) of a particle orbit, which can be determined experimentally from the detections of the decay positron. If there is a known correlation between the equilibrium radius and measured spin precession, this tool can be used to isolate particles with the most desirable orbits, and thus reduce this as a source of systematic error in the result for a_μ.

To investigate this, we divide the tracked antimuons in to ten momentum bins and analyse the evolution of the polarisation angles of each bin over the simulated period. To maintain sufficient bin population for statistical analysis, the bin width increases with δ values further from zero. As such, we choose the following bin ranges in δ: [-0.0034 to -0.0013], [-0.0013 to -0.0009], [-0.0009 to -0.0006], [-0.0006 to -0.0003], [-0.0003 to 0], [0 to 0.0003], [0.0003 to 0.0006], [0.0006 to 0.0009], [0.0009 to 0.0013] and [0.0013 to 0.0034]. We also extend the length in time of each time bin from 0.3 μs to 1.6 μs, in order to increase the bin populations.

For the horizontal polarisation, again subtracting the same fit line (corresponding to spin precession with the expected value of $a_\mu = 0.00116592$), we can plot the residual polarisations for the highest and lowest momentum bins (relative to the overall average residual) to obtain Figure 4.20. While also plotting the further eight bins increases the data shown in this plot, they

show no difference in behaviour with respect to time, and the overlap would make the plot difficult to interpret.

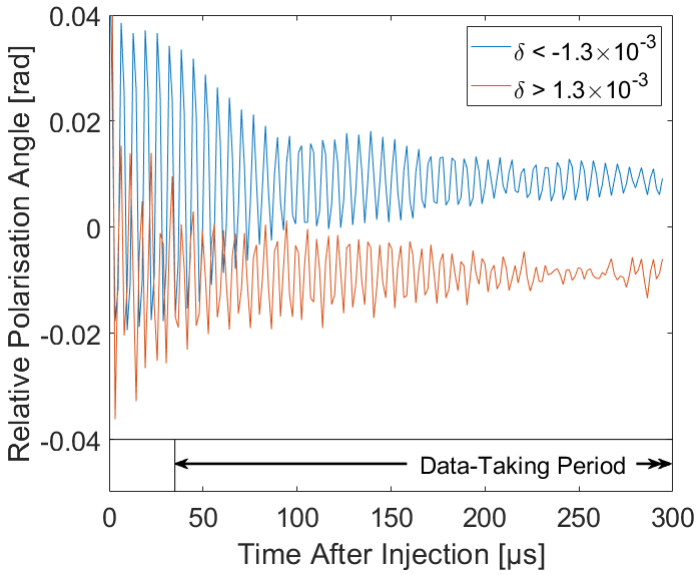

Figure 4.20: Simulated bunch polarisation angle in the horizontal direction, relative to a linear fit of $-1.43935\,\text{rad}\,\mu\text{s}^{-1}$, for particles with momenta $\delta < -.0013$ (numbering approximately 12600) and $\delta > .0013$ (numbering approximately 9400), taken at the point in ring azimuth of injection (downstream end of the inflector). The relative polarisation angle is zeroed on the average polarisation of the entire particle ensemble, relative to the ω_a precession fit. The measurement period starts at 35 μs and continues to 699 μs. We see a high-amplitude oscillation in polarisation, relative to the fit, which damps rapidly towards the measurement period. This is associated with the azimuthal spreading of the beam with time, and damps to a level where the relative polarisations are clearly of different value. For both momentum bins these oscillations are about the same polarisation angles. As such, assuming these are to be fit to constants, we can be confident of the difference between the values.

The main source of oscillations in the plot is due to the bin population and sampling. In particular, we are again sampling a single point in ring azimuth, so bin widths in time must be chosen so as not to coincide with an integer number of orbit periods (indeed, these oscillations get smaller as the bunch spreads out about the ring azimuth). Despite the existence of these small oscillations, we can perform linear fits within the data-taking period as

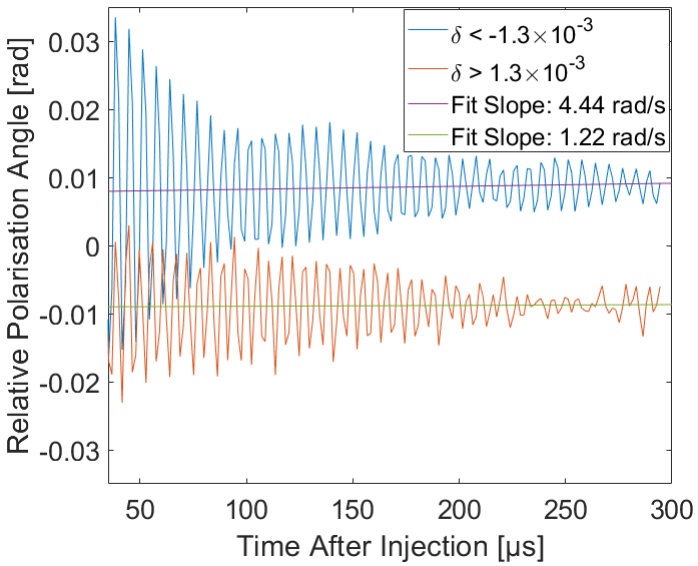

Figure 4.21: Simulated bunch polarisation angle in the horizontal direction, relative to a linear fit of $-1.43935\,\mathrm{rad}\,\mu\mathrm{s}^{-1}$, for particles with momenta $\delta < -.0013$ (blue, numbering approximately 12600) and $\delta > .0013$ (orange, numbering approximately 9400), taken at the point in ring azimuth of injection (downstream end of the inflector) during the first 265 μs of the measurement period. The relative polarisation angle is zeroed on the average polarisation of the entire particle ensemble, relative to the ω_a precession fit. The measurement period starts at 35 μs and continues to 699 μs. By performing a linear fit to the data in the measurement period, it is even clear that each of the two bins converge to different, constant values of phase relative to the average. The linear fits here have slopes of $4.4\,\mathrm{rad}\,\mathrm{s}^{-1}$ (for the low δ) and $1.2\,\mathrm{rad}\,\mathrm{s}^{-1}$ (for the high δ) relative to the expected spin precession of $-1.43935 \times 10^6\,\mathrm{rad}\,\mathrm{s}^{-1}$. However, the expected spin precession (subtracted from the data to produce this plot) is precise only to the order of $10^0\,\mathrm{rad}\,\mathrm{s}^{-1}$ and removing the last few microseconds of data varies the slopes by approximately $1\,\mathrm{rad}\,\mathrm{s}^{-1}$, so we cannot conclusively claim the slopes (spin precession) to be different from each other or from the expected precession for these two momentum bins.

in Figure 4.21. We associate with these slopes an uncertainty of $\pm 1\,\mathrm{rad}\,\mathrm{s}^{-1}$, found by taking the fits including and excluding the last half oscillations in the data.

We note that these slopes are so small that they are on the same level of

precision as our subtracted precession. If we include seven significant figures in all quantities, we find that the deviations from the mean of the simulated precessions of our two bins are:

$$4.4 \pm 1\,\text{rad}\,\text{s}^{-1} \text{ for } \delta < -1.3 \times 10^{-3},$$
$$1.2 \pm 1\,\text{rad}\,\text{s}^{-1} \text{ for } \delta > 1.3 \times 10^{-3}.$$

Using the equation for the measured spin precession (1.3) to analyse the effect of off-momentum particles in an electric field, we find that the $a_\mu - (\gamma^2 - 1)^{-2}$ term is negative for $\gamma < \gamma_0$, and positive for $\gamma > \gamma_0$. However, we also find that $\boldsymbol{E} \times \boldsymbol{\beta}$ is positive for low-momentum particles (which predominantly experience an electric field pointing radially inwards), and negative for high-momentum particles (which predominantly experience an electric field pointing radially outwards). The combination of these is that both low- and high-momentum particles should undergo a reduced spin precession, which would be expressed in the results above as a positive deviation from the average spin precession (as in Figure 4.21).

Quantitative analysis of these cases in the electric field term of the equation for ω_a (1.3) yield effects of approximately 0.0003% of the spin precession calculated from the (dominant) first term. This results in a reduction in precession frequency of approximately $4\,\text{rad}\,\text{s}^{-1}$ for both the high- and low-momentum particles. This suggests that the results listed above are indeed the result of the effects of the electric field on spin precession, although it is again important to note the large relative uncertainty on these figures of 1 ppm. Further investigations would have to improve upon this scale to determine a definite correlation between particle spin precession and momentum in the storage ring (beyond the effects of particle decays). We note that simulations on this scale would also require a much larger complement of antimuons for the required statistics.

One clear conclusion that can be drawn from Figure 4.20 is the difference in polarisation phase between the highest and lowest momentum bins. To investigate this further, we take the residual horizontal polarisation phases during the measurement period (as in Figure 4.21) of all bins, and average them over the measurement period. This provides us with Figure 4.22, where we see the relative widths of the momentum bins and the phase of each bin relative to the overall average.

As the oscillations in Figure 4.20 produce very large standard deviations for a fit to a constant, the (vertical) error bars in Figure 4.22 are taken as twice the variation in the average polarisation when half a period is subtracted from the end of the data.

We see a tendency for antimuons of higher energy to have a time-averaged difference in polarisation phase from the average phase by approximately

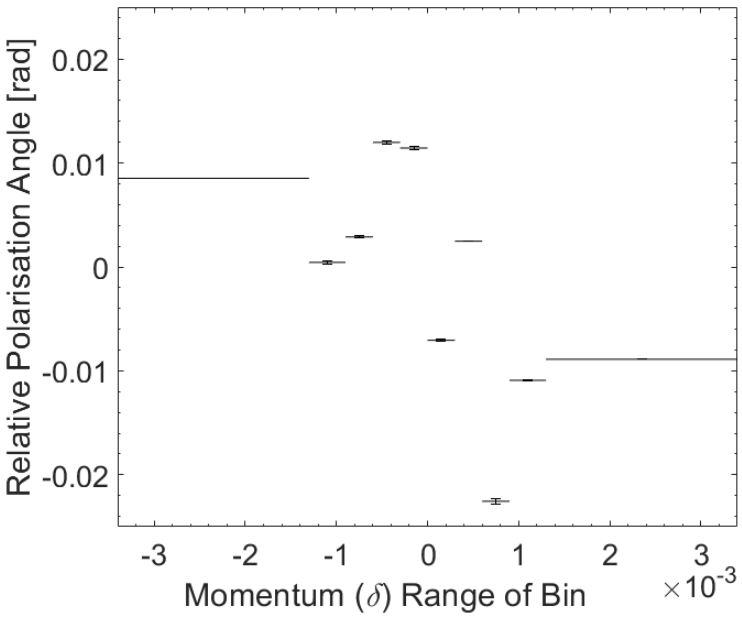

Figure 4.22: Simulated bunch polarisation angle in the horizontal direction, relative to a linear fit of $-1.43935\,\mathrm{rad}\,\mu\mathrm{s}^{-1}$, for particles in different bins of momentum δ (shown as width on this plot), taken at the point in ring azimuth of injection (downstream end of the inflector) averaged over the first 265 μs of the measurement period. Values are relative to the average polarisation of the entire particle ensemble, relative to the ω_a precession fit. Uncertainties are taken as the variation in average value when the last half oscillation is subtracted (from the apparent wave forms in Figure 4.20). This presents a clear trend for higher momentum particles to have a polarisation angle which leads the average spin precession of the ensemble by approximately 8 mrad, while the polarisation of the lower momentum particles trails the spin precession by the same amount. This suggests that collimating particles with high or low momenta will affect the horizontal polarisation of the beam.

8 mrad, and for the lower energy antimuon polarisation to trail the average by approximately the same amount (as in Figure 4.21). While this may not have any direct effect on the measurement of a_μ (if we ignore particle decays), it does help to explain the erratic behaviour of the polarisation during the scraping, where higher- and lower-momentum particles are collimated.

A similar analysis of the vertical polarisation of the momentum bins in

Figure 4.23 shows that any such trends for the vertical polarisation are hidden in noise. Indeed, the bins at the maximum and minimum values of momentum exhibit almost identical vertical polarisation, within the level of noise visible.

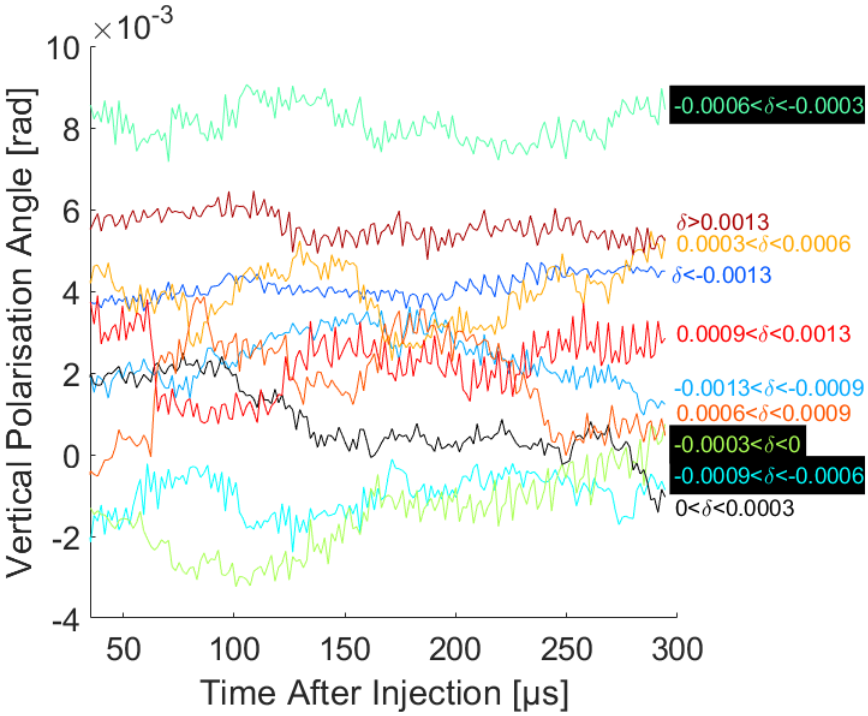

Figure 4.23: Simulated bunch polarisation angle in the vertical direction for particles in different bins of momentum δ (labelled to the right of this plot), taken at the point in ring azimuth of injection (downstream end of the inflector) during the first 265 μs of the measurement period. The measurement period starts at 35 μs and continues to 699 μs. We see no notable trends between momentum and vertical polarisation, as the vertical polarisations of each bin are erratic in time and often cross. If a trend were visible, then the particles with vertical polarisations further from zero could be targeted and collimated to reduce vertical polarisation of the bunch, although such a trend is not discernible from this data.

The lack of high-amplitude oscillation at the start of the measurement period in Figure 4.23 can be associated with the fact that the vertical polarisation, unlike the horizontal, is constant with respect to time and so is not affected by the azimuthal spread of the beam (or location of sampling of the beam).

The polarisations of the surviving antimuons at injection have a much narrower spread, with the lowest momentum bin starting with only a 3 mrad difference in horizontal polarisation from the highest momentum bin, and 2 mrad difference in vertical polarisation. This leads to the conclusion that the differences between the bins seen in Figure 4.22 are due to the nature of the storage ring (including injection), and the statistics of the 6D phase space of the particular bunch studied. As such, study of other bunches in other simulations would be required to confirm these features.

The apparent difference in precession frequency between the high-/low-momentum antimuons and the average is not substantial enough with respect to the statistics offered by the simulation to claim a clear correlation. However, analysis of the equation for ω_a does suggest that such a correlation exists, on the same order of magnitude as the results here.

It is also important to point out that antimuon decay will occur preferentially among the lower momentum particles which trail the average spin precession, as in Figure 4.20, resulting in a slightly lower measured precession frequency at earlier times. At later times, when the average momentum of the decaying antimuons increases (due to the lower momentum particles having already decayed), this will change to a higher measured precession frequency. For the vertical polarisation, the lack of any clear correlation between angle and momentum suggests that including decays would leave vertical polarisation unaffected.

While decays themselves are not included directly in the simulation due to the associated loss of statistics for beam properties at later times, it may be possible to include the effect on top of the momentum-bin populations presented here, although this is considered outside the scope of this body of work.

With the studies performed, we wish to validate as many of the results as possible with data from the experiment.

Chapter 5

Comparisons with Machine Measurements

Given the studies of the model performed in the previous chapter, we wish to investigate how these compare to the behaviour of the real machine.

Although not all of the studies performed in the previous chapter have corresponding processed data from the experiment, we present here measurements of ring tunes, resonances and a discussion of results from injection studies performed on the machine and compare these to the results of studies presented in the previous chapter.

5.1 Tunes and Resonances

The fibre harps described in Section 1.4.5 enable us to measure the beam shape and position at two points in the ring, while Fourier decomposition of signals from individual fibres can be used to determine the tunes of particles with closed orbits at the radial position of the fibre.

Lost antimuons can be quantified by studying hits in multiple adjacent calorimeters (given a suitable relative time cut), which can be used to study the relative numbers of antimuons lost with different configurations of the long-term storage systems in the ring. In particular, studying these losses with respect to the electrostatic quadrupole potential is essentially a study of the location of betatron resonances in the space of quadrupole potential set in the machine.

5.1.1 Tunes at Different Focusing Strengths

Measurements have been performed using signals from the central fibres of the fibre harps to calculate the on-axis betatron tunes of the machine [24]. These take account of the fact that the fibre harps degrade the beam with time, and so measurements at earlier times are more heavily weighted.

The results, with associated uncertainties (symmetric in ν_x and ν_y) given by the bounds of the relevant box, are shown in Figure 5.1 with the predicted values of the model from the previous chapter.

In these results, there appears to be a relatively small, yet systematic, difference between the measured values and those from the corresponding model configurations. By adjusting the quadrupole potentials in the model and recalculating the tunes, we find that this difference represents a change of approximately 1.3% in the plate potential of the electrostatic quadrupoles.

It is estimated [77] that a drop in potential of up to about 1% could occur between the potential measured in the high-voltage cabinets and the quadrupole plates. This alone can account for a large discrepancy in tunes between the model and experiment.

The positions of the quadrupole plates have been measured around the ring, such that the average spacings between the quadrupole plates in the horizontal and vertical directions, x_{Plates} and y_{Plates} respectively, can be calculated (as in Appendix J) to be:

$$\Delta x_{\text{Plates}} = 99.9 \pm 0.4\,\text{mm}, \tag{5.1}$$

$$\Delta y_{\text{Plates}} = 99.8 \pm 0.8\,\text{mm}. \tag{5.2}$$

As this is a quadrupole, we can assume the spacing scales approximately linearly with effective quadrupole strength for plates at the same potential. This gives us a range in potentials at the ideal plate positions of roughly $\pm 0.6\%$.

Together, the difference in potential between the high-voltage cabinet and quadrupole plates, and the uncertainty in plate positions, can account for the differences between the tunes calculated from the model (as described in the previous chapter) and those found from the physical storage ring. The tunes from the different models demonstrated in Figure 5.1 are consistent with the physical experiment.

Due to this difference being potentially explained by features of the experiment apparatus, the decision was made to run the long-term simulations in the previous chapter with a factor of -1.3% applied to all plate potentials, so as to more closely replicate the physical experiment.

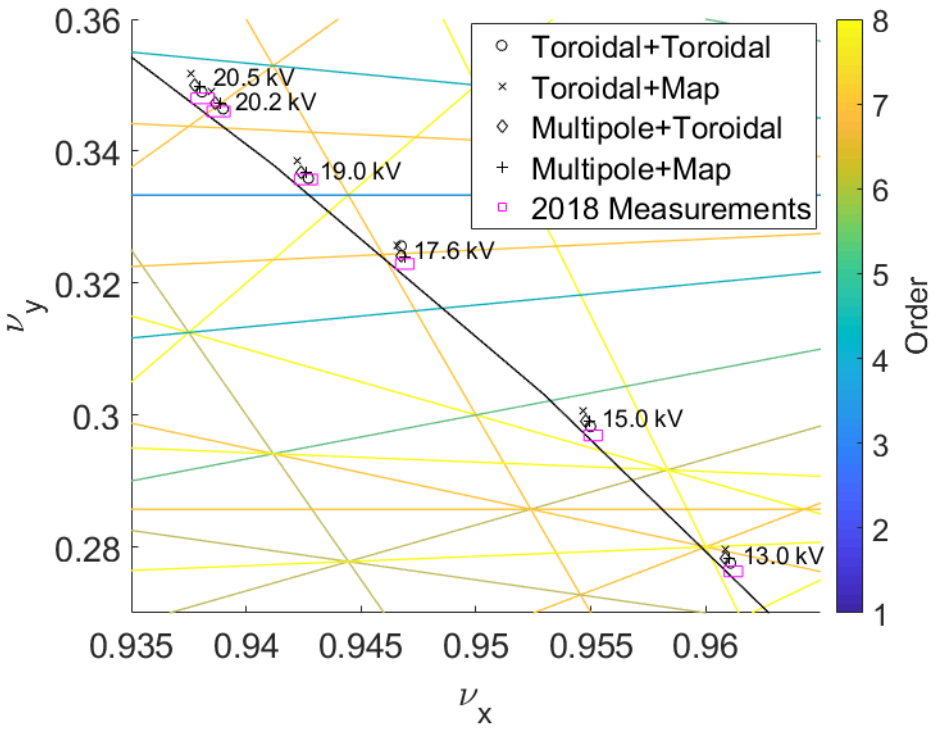

Figure 5.1: Locations in tune space of the physical storage ring (purple) and models where the quadrupoles are comprised of toroidal multipole bulk and fringe drescriptions, toroidal multipole bulk with field map fringes, standard multipole bulk with toroidal fringes and standard multipole bulk with field map fringes. The measured values were provided with uncertainties of $\pm 5 \times 10^{-4}$ for ν_x at plate potentials of 20.5 kV, 20.2 kV and 19.0 kV and $\pm 4 \times 10^{-4}$ for ν_x at plate potentials of 17.6 kV, 15.0 kV and 13.0 kV, with an uncertainty of $\pm 8 \times 10^{-4}$ for ν_y values at all plate potentials. We see a general trend for the model configurations to be at a slightly higher effective quadrupole potential than the measured results by about 1.3%. This can be explained by the quadrupole potential of the physical plates being slightly lower than that in the high-voltage cabinets by approximately 1.3%, or by the quadrupole plates in the experiment being separated by approximately an additional 1.3 mm, or a combination of both. The latter explanation need apply only to the vertical plates, as this affects the vertical tune the most, which is where we see the largest discrepancy. Due to the discrepancy here, the long-term simulations in the previous chapter were performed with a -1.3% factor applied to the plate potentials for both scraping and long-term storage.

5.1.2 Measured Resonances by Particle Loss

To investigate the location of resonances in the parameter space of the physical storage ring, researchers have measured the numbers of antimuons lost at different quadrupole potentials. In these studies, the number of detected decay positrons was used as a means to quantify the relative number of antimuons being successfully stored in the ring [78].

In addition to this, correlated hits in two and three adjacent calorimeters were used to directly detect antimuon losses [79]. Several quadrupole potentials were found to cause up to three times the number of antimuons detected in this way [79, 80], which are listed in Table 5.1.

Table 5.1: Quadrupole potentials at which resonances were detected in the experiment [79, 80] through time-correlated coincidences in adjacent calorimeters, with the relative increase in these "doubles" given for each resonance found. The tunes for these potentials are calculated for the toroidal multipole description, and the closest resonance lines (plotted in Figure 5.1) to these are given for each observed resonance. The found tunes satisfy the resonance conditions to the third significant figure.

Quadrupole Potential [kV]	Rel. Increase in "Doubles"	(ν_x, ν_y) Calc'd from Tor.Multip.	Nearest Resonance
16.8 ± 0.2	4.5	$(0.9495, 0.3157)$	$-\nu_x + 3\nu_y = 0$
18.8 ± 0.1	7.0	$(0.9433, 0.3341)$	$3\nu_y = 1$
21.1 ± 0.2	6.6	$(0.9362, 0.3541)$	$\nu_x + 3\nu_y = 2$

By comparing the measured resonances in Table 5.1 with the tune plot in Figure 5.1, we can see that the resonance at 16.8 kV resonance corresponds to the fourth-order $-\nu_x + 3\nu_y = 0$ resonance, the 18.9 kV resonance corresponds to the third-order $3\nu_y = 1$ resonance, and the 21.1 kV resonance corresponds to the fourth-order $\nu_x + 3\nu_y = 2$ resonance.

Studies performed [55] have indicated that the fourth-order $\nu_x + 3\nu_y = 2$ and $-\nu_x + 3\nu_y = 0$ resonances are driven by the $n = 10$ (20-)pole component of the electric field. Similar studies [81] suggest that the observed magnitude of the$3\nu_y = 1$ resonance can be explained if driven by a 20 ppm magnetic skew sextupole component or an electric skew sextupole component strength of approximately 0.1 kV (as measured at 0.045 m from the beam axis), given that these cover at least 13° of ring azimuth.

In the case of the electric field, if such a component is distributed through all quadrupoles in the ring (twelve times 13°), then we estimate the electric field skew sextupole component need only be approximately 8 V (as measured at 0.045 m from the beam axis). The skew sextupole component given from

Table 5.2: Potentials required in the different descriptions of the quadrupole fields (described in Chapters 2 and 3) to achieve vertical betatron tune of $\nu_y = 0.3333$ in the storage ring model. We add the 1.3% correction factor, established in Section 5.1.1, to these in the final column.

Model Quadrupole Description		Potential at	+1.3%
Bulk Fields	Fringe Fields	$3\nu_y = 1$ [kV]	Correction [kV]
Toroidal	Toroidal	18.42	18.66
Toroidal	FieldMap	18.43	18.67
Multipole	Toroidal	18.60	18.84
Multipole	FieldMap	18.50	18.74

the field map fit in Table 2.1 in Chapter 2 provides a magnitude of 4 V (as measured at 0.045 m from the beam axis), although this is comparable to the fit residual.

In the case of the magnetic field, the average skew sextupole component required around the entire ring azimuth is 0.7 ppm (as measured at 0.045 m from the beam axis). As the azimuthally averaged uniformity of the field measured in the experiment is on the order of 1 ppm (at 0.032 m from the beam axis) [71], it is probable that the magnetic field contributes substantially to driving this resonance, although a contribution from the electric field remains possible.

Assuming the resonance at 18.8 kV is the $3\nu_y = 1$ resonance, it provides confirmation that both the tunes interpreted from measurement and those from the model are in this case very close to the real value. To quantify this, all four model configurations were run to find the quadrupole potential required to obtain a vertical tune of $3\nu_y = 1$. The results are shown in Table 5.2.

With the 1.3% correction factor applied, these models are distributed around the 18.8 kV at which we observe the resonance. This leads us to the conclusion that there is no severe discrepancy beyond the correction factor.

Due to the resolution of the quadrupole potential for the lost antimuon studies being 0.1 kV, conclusions regarding the difference between model tunes and machine tunes cannot be reached with as high confidence as in Section 5.1.1. Nonetheless, these experiment studies have been shown to be consistent with the coordinates in tune space of the models and fibre harp tune measurements.

5.2 Injection Offsets

During the commissioning run in 2017, it was found that the number of stored particles decreased linearly with quadrupole potential, with an extrapolated point of no storage at approximately 6 kV [82]. The relevant simulations, presented in Section 4.2, showed how both the magnitude and behaviour of storage efficiency with respect to quadrupole potential changed depending on the vertical angle of the incoming beam.

The storage efficiency values for a number of quadrupole potentials from the machine (incorporating features such as detector acceptance and geometry) can be scaled such that both magnitude and behaviour match a simulation. The experiment data, scaled to best fit simulation results, is shown with the simulation results in Figure 5.2.

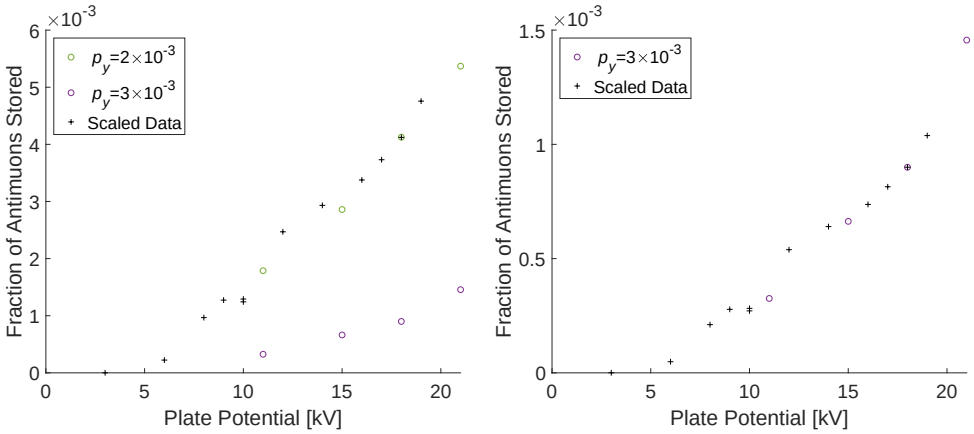

Figure 5.2: Stored antimuon fraction after 20 turns as a function of quadrupole plate potential as simulated for a beam injected with vertical momenta p_y of 0.002 and 0.003 applied, with kicker strength set at 50% of the (near optimal) 270 gauss peak. Also plotted are measured data from the commissioning run with kickers at 75% of their available range (with 100% during the commissioning run known to be below the optimum for injection) [83], scaled manually to best fit both the apparent behaviour (slope) and zero-storage quadrupole potential of the $p_y = 0.002$ simulation (left) and the $p_y = 0.002$ simulation (right). It was concluded in this study that the agreement was best with the $p_y = 0.003$ simulation.

We see from this that the best agreement is found with the $p_y = 0.003$ simulation, as in other cases (shown in Appendix K) the behaviour does not match the data from the experiment. Although it would be interesting to investigate larger injection angles, the agreement with the $p_y = 0.003$

simulation is sufficient such that additional study is not necessary.

Indeed, on conclusion of this study it was realised that the physical ring was positioned between 4 mm and 5 mm lower than the beamline [84], and as such the beam was angled vertically by approximately 3 mrad to navigate the injection channel and obtain maximum particle flux in the ring. In conclusion, this study was successful in predicting the behaviour of a beam injected with non-zero vertical momentum.

5.3 Collimator Configurations

The study of different collimator configurations presented in Section 4.3 was carried out due to the lack of all five of the collimators being available during the first run of the experiment.

In the second run, all five collimators were used. However, many changes were made to the machine between the first and second runs. It is therefore difficult to make a direct comparison between the different collimator configurations based on existing experimental data.

Nevertheless, comparisons of the two experiment configurations thus far have found a smaller fraction of antimuons being collimated during data-taking with the five-collimator configuration. Although this supports the results from Section 4.3, confirmation can only be provided by a dedicated study in the machine (using similar machine configurations, differing only in the arrangements of the collimators).

Chapter 6

Conclusion

The aim of the project was to produce a model which can simulate the injection process (through the injection kickers and scraping), and accurately simulate the magnetic field of the dipole magnet and electric field of the curved electrostatic quadrupoles. Once such a model had been constructed, the aim was then to investigate systematic effects in the measurement of the muon $g-2$, and suggest methods to mitigate them.

6.1 Summary and Conclusions

In the course of constructing an accurate model of the Fermilab Muon $g-2$ Experiment (E989) in BMAD, we have found cause to use continuous descriptions of electro- and magneto-static fields from curvilinear beamline elements, in place of field maps.

In Chapter 2, we found that fitting standard mutlipoles to field maps produced from models of the curved electrostatic quadrupoles (using an FEA code) provides a description of the transverse, bulk field, accurate to the level of approximately twice the field map noise (and peaking, at the edge of the fit region, at 0.5% of the field at the plates). We found the tune values for the multipole description exhibit a systematic difference from the measured machine tunes, small on the level of the uncertainties of those measurements. We also developed a novel "cylindrical harmonics" method of describing longitudinally-varying fields, which fit the fringe field maps of the quadrupoles well, with peak residuals (at the edge of the fit area) of approximately 5% of the fields at the plates and had an average field deviation over the storage region of 2.7% if the fields at the plates, or about three times the level of noise in the field maps.

The accuracy of the fits performed in Chapter 2 is perhaps surprising,

given that the design trajectory of the storage ring is curved with radius $\rho = 7.112\,\mathrm{m}$, and the storage aperture is 0.1 m. Indeed, the standard multipole fit was expected to perform poorly in comparisons with machine data and curvilinear field descriptions (given that the bulk field covers 140° of ring azimuth). This was not the case, and the fit was so accurate that there was sufficient confidence to use it in the simulation runs in Chapter 4. The "cylindrical harmonics" method was found to model the fringe fields as well as the toroidal multipoles. Despite the latter being considered more suitable for application here (due to the ring curvature), this new method may also be suitable for applications in straight beamlines.

The novel third-order symplectic integrator in a bend developed towards the end of Chapter 2, and the more versatile version developed in Chapter 3, were both found to produce results for particle action and angle in agreement with those of a fourth-order Runge–Kutta integrator, for non-uniform electric and (in the latter case) magnetic fields. For 1 mm integration steps, the deviations found in particle phase were on the order of 0.1 mrad after 30 ring turns, for both horizontal and vertical phase, with no clear increase with tracked distance. This suggests that the integrators would be suitable for tracking particles through thousands of turns of the storage ring and still agree with the Runge–Kutta integrator. However, it was found that the relative longitudinal position z would drift on the order of 10 mm for tracking over such a distance.

While the more versatile of these integrators was found in Chapter 3 to be very computationally expensive for varying magnetic fields, the integrators both exhibited excellent agreement with the fourth-order Runge–Kutta integrator, with the noted exception of relative longitudinal coordinate z. This could be considered surprising, as both integrators were derived using the paraxial approximation, and the coordinates for stored particles in the $g-2$ Experiment can be large in comparison to most cases where this approximation is applied. We list the qualities of each integrator used here in Table 6.1, to outline the benefits and drawbacks of each. In conclusion, these integrators could be readily applied to storage rings (where symplecticity can be considered an important requirement), as well as curved elements in standard beamlines, ideally in cases where the integral of the magnetic vector potential (required for the more general version of the integrator) can easily be calculated analytically.

In Chapter 3, we found that existing descriptions of fields in a curved trajectory [35, 36, 37] provided an insufficient description of the field map to which they were fit, due to the difficulty of fitting. We also noted that they could not describe longitudinally-varying (fringe) fields in a bend. Due to these problems, we developed the "toroidal multipoles" method of describ-

Table 6.1: Comparison of the available features of the different integrators used. Spin tracking is a feature that can be added, but this is beyond the scope of work presented here.

Feature	Runge–Kutta	New Integrator	General New Integrator
Curvature	Yes	Inherent	Inherent
Arbitrary $\boldsymbol{E}$	Yes	Yes	Yes
Arbitrary $\boldsymbol{B}$	Yes	Dipole Only	Yes
Symplectic	No	Yes	Yes
Spin Tracking	Yes	Not Implemented	Not Implemented

ing longitudinally-varying electrostatic fields in a bend, and applied this by fitting relevant coefficients to the field maps calculated for the electrostatic quadrupoles. In the case of the fringe fields, fit discrepancies within the storage region had a maximum, found at the edge of the fit area in the region of greatest variation, of about 6% of the fields at the plates, and an average discrepancy of about twice the noise level in the field maps. For the bulk fields, described by a longitudinally static case of the toroidal multipoles, the fit was found to have a maximum residual, at the edge of the fitted surface, of approximately 2% of the fields near the plates. The average discrepancy was again of about twice the level of field map noise, representing similar performance to the standard multipole fits.

Given the ability of this novel "toroidal multipole" decomposition to describe longitudinally varying (fringe) fields in a bend, the accuracy of the fits shown in Chapter 3 support the conclusion that this method could be of great use in curved (sections of) beamlines. The case of (bulk) fields which are invariant down a curved beamline can also be described accurately by toroidal multipoles. We compare the properties of these with the other field descriptions studied, in Table 6.2. While the diverging of the toroidal coordinate system towards the beam axis has caused computational difficulty (discussed in Section 3.3.4), it is considered a problem which can potentially be solved through further research. Using a list of values for the associated Legendre polynomials and linearly interpolating, rather than calculating them at each field point, has proven to be an accurate and fast approximation, which could be applied when integrating this description in a tracking code.

In Chapter 4, we looked at the various properties of the model of the storage ring using different descriptions of the electrostatic quadrupole fields, and found that the beta functions and dispersions all appeared to be consistent with a simpler model, using 2D field maps for the quadrupoles (without fringe

Table 6.2: Comparison of the different field-modelling methods used. The ability of cylindrical harmonics to describe (transverse-only) bulk fields has not been investigated, as this is already described by the standard multipoles (in Chapter 2, Section 2.3.3). Surface fitting refers to the ability to perform a fit on a surface in multiple dimensions (to better reflect the behaviour of the field), rather than the fitting being confined to the field behaviour along a single axis.

Feature	Multipoles	Cylindrical Harmonics	Curvilinear Multipoles	Toroidal Multipoles
Bulk/Fringe	Bulk	Fringe	Bulk	Bulk+Fringe
Curvature	No	No	Yes	Yes
Fitting Method	Surface	Surface	Axis	Surface

fields). We also found that using field maps in any of the descriptions caused artefacts in the chromaticity. Using a multipole description of the quadrupole bulk fields and field maps for the fringe fields, the model was found to predict an ideal injection angle of -1 mrad (1 mrad radially inward) and kick with peak of approximately 256 gauss. It also predicts that using all five collimators leads to fewer antimuon collimations during the data-taking period than using two (specifically, the two placed within the second and fourth quadrupole pairs). Of particular note, the long-term simulations (where we used a multipole description of the quadrupole bulk and toroidal multipole description of the fringe fields) provided some insight into the mechanism behind collimation of antimuons during the data-taking period.

While we also found the prediction of ideal injection angle and kick to be supported by a further model, sufficient machine data was not available to compare with these results. The two- and five-collimator studies conclude that running with five is optimal for the experiment. We conclude that the long-term collimations are due to the use of circular collimators, which are sensitive to the horizontal and vertical betatron oscillation amplitudes adding when in phase, and placing the particle temporarily and infrequently outside of the storage region. We also conclude that, while using square collimators would mitigate this, there may be other effects which cause this to be an unfavourable option.

In Chapter 5, we found that the tunes calculated from the simulations match up with the measured tunes from the experiment, if the quadrupole potential is adjusted by -1.3%. Possible sources of this factor were identified in the machine, so it is considered realistic. Quadrupole potentials at which resonances occurred in the experiment were also found to coincide with model

predictions, once the correction factor was applied. The injection studies to understand the nonzero zero-storage quadrupole potential that was observed in the experiment commissioning run, also demonstrated agreement with experiment, correctly predicting the nonzero vertical injection angle. While insufficient data from the experiment exists to be compared with the two- versus five-collimator studies, a dedicated study is being considered by the experiment collaboration [85].

Having identified possible causes of a 1.3% decrease of potential between the experiment readout and the quadrupole plates in the machine, we have confidence in the accuracy of the tunes predicted by the models, for the studied quadrupole potentials of 13kV, 15 kV, 17.6 kV, 19 kV, 20.2 kV and 20.5 kV. As the tunes from the model using toroidal multipoles were closest to those measured, we conclude that this is the most accurate description of the electrostatic quadrupoles of those considered. The successes of the vertical injection angle analysis, and the predicted tunes, suggest the model is able to reflect both the injection and steady-state (storage) processes of the machine. The success of the toroidal multipole description of the electrostatic quadrupoles also leads us to suggest that some or all of the bespoke methods developed here can be of wider use in beam dynamics simulations.

6.2 Further Studies and Closing Remarks

From the perspective of beam dynamics simulations, the divergence of the toroidal coordinate system close to the beam axis currently makes toroidal multipoles difficult to implement. It is hoped that further work could produce a simpler, non-divergent calculation for the field close to/on the beam axis. This would remove one of the main obstacles to the more widespread use of the toroidal multipole field description developed here.

Application of toroidal multipoles to the magnetic field in the Fermilab Muon $g-2$ Experiment (E989) storage ring would allow modelling of the non-uniformities in the dipole magnet, such that their effect on the measurement of $g-2$ could be estimated, and any resulting spin to phase-space correlations investigated, along with effects on the beam dynamics. This would require measurements of the magnetic field components, rather than the magnitude (already measured), as then the longitudinal and transverse fields can be separated. However, once such a measurement is made the application of the toroidal multipole description would be similar to that performed in Chapter 3 for the electrostatic quadrupole fringe fields.

The symplectic integrator derived in Chapter 3 could be combined with an adaptive-step algorithm and a spin tracking code, which would make

application to the Fermilab Muon $g-2$ Experiment more tenable. If simple analytical, integrable expressions can be obtained for the vector potentials in the ring, then this may increase the speed of the integrator so as to be competitive with the fourth-order Runge–Kutta integrator used here.

For direct application to the Fermilab Muon $g-2$ Experiment, a further investigation of collimator shape, based on the study results here, would be useful. We have found that circular collimators remove particles that may have an amplitude in one axis which takes them to the edge of the storage region, using some slight amplitude in the other axis to cause them to exit the storage region and hit a collimator at some point in time. However, the combinations of these amplitudes may cause particles to be collimated during the data-taking period. Changing the collimators to a square shape should reduce this coupling, and so reduce collimations during data-taking. Given this suggestion has also been made by the COSY model simulation team, this is a probable change to be made in a consequent revision of the Fermilab Muon $g-2$ Storage Ring, as the formal design/production time for new collimators would not be short enough to include them in the current experiment.

Once experimental studies of the two- and five-collimator configurations of the experiment have been performed, a comparison can be made with the simulation results in Chapter 4. These studies are currently expected to occur in late 2019.

Further investigations into the correlations between particle phase space coordinates and spin can also be performed, using the data produced by the simulations in Chapter 4. While a complete analysis of the data is considered beyond the scope of this thesis, such research may reveal further, important correlations for the running and data-processing/results of the experiment.

The achievements of this project have developed beyond the initial objectives of developing and using a beam dynamics model of the Fermilab Muon $g-2$ Storage Ring. In searching for ways to improve the model, new and potentially useful tracking methods have been developed, as has a method of describing general electric fields in a source-free region, with a curved reference trajectory. These have allowed the construction of a model which better reflects the machine dynamics (in terms of tune and field geometry) than would be possible otherwise. While the research performed with this model has already produced some useful results for the experiment, including studies performed of vertical injection angle and of correlations between phase-space and spin, the tracking data produced during the long-term run of this model may find use in further analysis. However, this lies beyond the scope of the objectives here.

Bibliography

[1] P. A. Moreno Casares, "A review on Loop Quantum Gravity," *arXiv e-prints*, p. arXiv:1808.01252, Aug 2018.

[2] M. Thomson, *Modern Particle Physics*. Cambridge University Press, 2017.

[3] T. Blum, A. Denig, I. Logashenko, E. de Rafael, B. L. Roberts, T. Teubner, and G. Venanzoni, "The muon (g-2) theory value: Present and future," 2013.

[4] The DELPHI Collaboration, "Study of tau-pair production in photon-photon collisions at lep and limits on the anomalous electromagnetic moments of the tau lepton," *The European Physical Journal C - Particles and Fields*, vol. 35, pp. 159–170, Jun 2004.

[5] E. J. Konopinski, "The experimental clarification of the laws of beta-radioactivity," *Annual Review of Nuclear Science*, vol. 9, no. 1, pp. 99–158, 1959.

[6] R. Van de Water, A. El-Khadra, T. Izubuchi, C. Lehner, and L. Roberts, "First Workshop of the Muon g-2 Theory Initiative," June 2017.

[7] A. Denig, F. Mank, G. von Hippel, H. Meyer, A. Nyffeler, M. Vanderhaeghen, and H. Wittig, "Second Workshop of the Muon g-2 Theory Initiative," June 2018.

[8] A. El-Khadra, "The Muon g-2 Theory Initiative," in *APS April Meeting Abstracts*, 2018 Aspen Winter Conference: The Particle Frontier, (Geneva, Switzerland), Indico, CERN, March 2018.

[9] A. Keshavarzi, D. Nomura, and T. Teubner, "Muon $g-2$ and $\alpha(M_Z^2)$: A new data-based analysis," *Phys. Rev. D*, vol. 97, p. 114025, Jun 2018.

[10] G. Charpak, P. J. M. Farley, E. L. Garwin, T. Muller, J. C. Sens, and A. Zichichi, "The anomalous magnetic moment of the muon," *Il Nuovo Cimento (1955-1965)*, vol. 37, pp. 1241–1363, Jun 1965.

[11] J. Bailey, W. Bartl, G. von Bochmann, R. C. A. Brown, F. J. M. Farley, M. Giesch, H. Jöstlein, S. van der Meer, E. Picasso, and R. W. Williams, "Precise measurement of the anomalous magnetic moment of the muon," *Il Nuovo Cimento A (1965-1970)*, vol. 9, pp. 369–432, Jun 1972.

[12] A. Wolski, *Beam Dynamics in High Energy Particle Accelerators*. London: Imperial College Press, 2014.

[13] J. Bailey, K. Borer, F. Combley, H. Drumm, C. Eck, F. Farley, J. Field, W. Flegel, P. Hattersley, F. Krienen, F. Lange, G. Lebée, E. McMillan, G. Petrucci, E. Picasso, O. Rúnolfsson, W. von Rüden, R. Williams, and S. Wojcicki, "Final report on the cern muon storage ring including the anomalous magnetic moment and the electric dipole moment of the muon, and a direct test of relativistic time dilation," *Nuclear Physics B*, vol. 150, pp. 1 – 75, 1979.

[14] G. W. Bennett, B. Bousquet, H. N. Brown, G. Bunce, R. M. Carey, P. Cushman, G. T. Danby, P. T. Debevec, M. Deile, H. Deng, W. Deninger, S. K. Dhawan, V. P. Druzhinin, L. Duong, E. Efstathiadis, F. J. M. Farley, G. V. Fedotovich, S. Giron, F. E. Gray, D. Grigoriev, M. Grosse-Perdekamp, A. Grossmann, M. F. Hare, D. W. Hertzog, X. Huang, V. W. Hughes, M. Iwasaki, K. Jungmann, D. Kawall, M. Kawamura, B. I. Khazin, J. Kindem, F. Krienen, I. Kronkvist, A. Lam, R. Larsen, Y. Y. Lee, I. Logashenko, R. McNabb, W. Meng, J. Mi, J. P. Miller, Y. Mizumachi, W. M. Morse, D. Nikas, C. J. G. Onderwater, Y. Orlov, C. S. Özben, J. M. Paley, Q. Peng, C. C. Polly, J. Pretz, R. Prigl, G. zu Putlitz, T. Qian, S. I. Redin, O. Rind, B. L. Roberts, N. Ryskulov, S. Sedykh, Y. K. Semertzidis, P. Shagin, Y. M. Shatunov, E. P. Sichtermann, E. Solodov, M. Sossong, A. Steinmetz, L. R. Sulak, C. Timmermans, A. Trofimov, D. Urner, P. von Walter, D. Warburton, D. Winn, A. Yamamoto, and D. Zimmerman, "Final report of the e821 muon anomalous magnetic moment measurement at bnl," *Phys. Rev. D*, vol. 73, p. 072003, Apr 2006.

[15] K. Olive, "Review of particle physics," *Chinese Physics C*, vol. 40, p. 100001, Oct 2016.

[16] J. Grange, V. Guarino, P. Winter, K. Wood, H. Zhao, R. M. Carey, D. Gastler, E. Hazen, N. Kinnaird, J. P. Miller, J. Mott, B. L. Roberts,

J. Benante, J. Crnkovic, W. M. Morse, H. Sayed, V. Tishchenko, V. P. Druzhinin, B. I. Khazin, I. A. Koop, I. Logashenko, Y. M. Shatunov, E. Solodov, M. Korostelev, D. Newton, A. Wolski, A. Chapelain, R. Bjorkquist, N. Eggert, A. Frankenthal, L. Gibbons, S. Kim, A. Mikhailichenko, Y. Orlov, D. Rubin, D. Sweigart, D. Allspach, G. Annala, E. Barzi, K. Bourland, G. Brown, B. C. K. Casey, S. Chappa, M. E. Convery, B. Drendel, H. Friedsam, T. Gadfort, K. Hardin, S. Hawke, S. Hayes, W. Jaskierny, C. Johnstone, J. Johnstone, V. Kashikhin, C. Kendziora, B. Kiburg, A. Klebaner, I. Kourbanis, J. Kyle, N. Larson, A. Leveling, A. L. Lyon, D. Markley, D. McArthur, K. W. Merritt, N. Mokhov, J. P. Morgan, H. Nguyen, J.-F. Ostiguy, A. Para, C. C. P. M. Popovic, E. Ramberg, M. Rominsky, D. Schoo, R. Schultz, D. Still, A. K. Soha, S. Strigonov, G. Tassotto, D. Turrioni, E. Villegas, E. Voirin, G. Velev, L. Welty-Rieger, D. Wolff, C. Worel, J.-Y. Wu, R. Zifko, K. Jungmann, C. J. G. Onderwater, P. T. Debevec, S. Ganguly, M. Kasten, S. Leo, K. Pitts, C. Schlesier, M. Gaisser, S. Haciomeroglu, Y.-I. Kim, S. Lee, M.-J. Lee, Y. K. Semertzidis, K. Giovanetti, V. A. Baranov, V. N. Duginov, N. V. Khomutov, V. A. Krylov, N. A. Kuchinskiy, V. P. Volnykh, C. Crawford, R. Fatemi, W. P. Gohn, T. P. Gorringe, W. Korsch, B. Plaster, A. Anastasi, D. Babusci, S. Dabagov, C. Ferrari, A. Fioretti, C. Gabbanini, D. Hampai, A. Palladino, G. Venanzoni, T. Bowcock, J. Carroll, B. King, S. Maxfield, K. McCormick, J. Price, D. Sim, A. Smith, T. Teubner, W. Turner, M. Whitley, M. Wormald, R. Chislett, S. Kilani, M. Lancaster, E. Motuk, T. Stuttard, M. Warren, D. Flay, D. Kawall, Z. Meadows, T. Chupp, R. Raymond, A. Tewlsey-Booth, M. J. Syphers, D. Tarazona, S. Catalonotti, R. Di Stefano, M. Iacovacci, S. Mastroianni, S. Chattopadhyay, M. Eads, M. Fortner, D. Hedin, N. Pohlman, A. de Gouvea, H. Schellman, L. Welty-Rieger, F. Azfar, S. Henry, G. D. Alkhazov, V. L. Golovtsov, P. V. Neustroev, L. N. Uvarov, A. A. Vasilyev, A. A. Vorobyov, M. B. Zhalov, L. Cerrito, F. Gray, G. Di Sciascio, D. Moricciani, C. Fu, X. Ji, L. Li, H. Yang, D. Stöckinger, G. Cantatore, D. Cauz, M. Karuza, G. Pauletta, L. Santi, S. Baeßler, M. Bychkov, E. Frlez, D. Pocanic, L. P. Alonzi, M. Fertl, A. Fienberg, N. Froemming, A. Garcia, D. W. H. J. Kaspar, P. Kammel, R. Osofsky, M. Smith, E. Swanson, T. van Wechel, and K. Lynch, "Muon (g-2) Technical Design Report," *arXiv e-prints*, Jan 2015.

[17] M. Korostelev, "Doc 4614: Beam simulations from pion production target to muon storage ring." Fermilab $g-2$ DocDB, 2016.

[18] F. Bieniosek and K. Anderson, "Note 546: Lithium lens for focusing protons on target in the fermilab antiproton source." Fermilab PBAR

Notes, 1993.

[19] D. Stratakis, B. Drendel, J. P. Morgan, M. J. Syphers, and N. S. Froemming, "Commissioning and first results of the fermilab muon campus," *Phys. Rev. Accel. Beams*, vol. 22, p. 011001, Jan 2019.

[20] M. Korostelev. Private communication, July 2016.

[21] D. Stratakis, "Doc 4189: End to end simulations for g-2 (up to the ring) (v3)." Fermilab $g-2$ DocDB, 2016.

[22] D. Stratakis *et al.*, "Performance Analysis for the New g-2 Experiment at Fermilab," in *Proc. of International Particle Accelerator Conference (IPAC'16), Busan, Korea, May 8-13, 2016*, no. 7 in International Particle Accelerator Conference, (Geneva, Switzerland), pp. 996–998, JACoW, June 2016. doi:10.18429/JACoW-IPAC2016-MOPOY060.

[23] R. Osofsky and Muon g-2 Collaboration, "Improving Magnetic Field Uniformity in the Muon g-2 Storage Ring," in *APS April Meeting Abstracts*, vol. 2018, p. D17.004, Jan 2018.

[24] A. Chapelain, "Doc 11712: On improving the tune/frequency extraction." Fermilab $g-2$ DocDB, 2018.

[25] O. Kim, S. Hacıömeroğlu, Y. Kim, Y. Orlov, and Y. Semertzidis, "Reduction of Coherent Betatron Oscillations Using RF Electric Fields in the Fermilab Muon g-2 Experiment," in *Proc. 9th International Particle Accelerator Conference (IPAC'18), Vancouver, BC, Canada, April 29-May 4, 2018*, no. 9 in International Particle Accelerator Conference, (Geneva, Switzerland), pp. 2961–2964, JACoW Publishing, June 2018. https://doi.org/10.18429/JACoW-IPAC2018-THPAF010.

[26] O. Kim, "Doc 18922: Results of the july rf test runs." Fermilab $g-2$ DocDB, 2019.

[27] A. Fienberg, "Doc 7556: Beam dynamics with the calorimeters." Fermilab $g-2$ DocDB, 2017.

[28] CERN, "Geant 4: A simulation toolkit." `http://web.archive.org/web/20190808211229/http://geant4.web.cern.ch/`. Accessed: 08-08-2019.

[29] F. M. $g-2$ Collaboration, "gm2ringsim software project." `https://web.archive.org/web/20190811190900/https://cdcvs.fnal.gov/redmine/projects/gm2ringsim/`. Accessed: 11-08-2019.

[30] M. Berz and K. Makino, "Cosy infinity." http://web.archive.org/web/20190516204854/https://bt.pa.msu.edu/index_cosy.htm. Accessed: 16-05-2019.

[31] D. T. M. Berz, "Doc 3514: Cosy simulations update." Fermilab $g-2$ DocDB, 2016.

[32] D. C. Sagan, "Bmad: Software toolkit for charged-particle and x-ray simulations." https://www.classe.cornell.edu/bmad. Accessed: 09-08-2019.

[33] D. Rubin, "Doc 2820: Injection and storage in the muon ring." Fermilab $g-2$ DocDB, 2015.

[34] B. Shepherd and N. Marks, "Quadrupole Magnets for the 20 mev ffag, 'emma'," in *Proc. of Particle Accelerator Conference (PAC'07), Albuquerque, New Mexico, USA, 25-29 June, 2007*, no. 22 in Particle Accelerator Conference, (Geneva, Switzerland), pp. 413—-415, JACoW, June 2007.

[35] E. M. McMillan, "Multipoles in cylindrical coordinates," *Nuclear Instruments and Methods*, vol. 127, no. 3, pp. 471 – 474, 1975.

[36] S. Mane, "Solutions of laplace's equation in two dimensions with a curved longitudinal axis," *Nuclear Instruments and Methods in Physics Research Section A: Accelerators, Spectrometers, Detectors and Associated Equipment*, vol. 321, no. 1, pp. 365 – 375, 1992.

[37] T. Zolkin, "Sector magnets or transverse electromagnetic fields in cylindrical coordinates," *Phys. Rev. Accel. Beams*, vol. 20, p. 043501, Apr 2017.

[38] W. H. Press, S. A. Teukolsky, W. T. Vetterling, and B. P. Flannery, *Numerical Recipes in FORTRAN (2Nd Ed.): The Art of Scientific Computing*, p. 708. New York, NY, USA: Cambridge University Press, 1992.

[39] L. Deniau, A. Latina, P. Skowronski, and T. Persson, "Mad - methodical accelerator design." http://web.archive.org/web/20190612224738if_/http://mad.web.cern.ch/mad/. Accessed: 03-03-2019.

[40] M. Korostelev, I. Bailey, A. Herrod, D. Stratakis, V. Tishchenko, and A. Wolski, "Update on Bmad Simulations From Target to Storage Ring

for the New Muon G-2 Experiment at Fermilab," in *Proc. of International Particle Accelerator Conference (IPAC'17), Copenhagen, Denmark, 14-19 May, 2017*, no. 8 in International Particle Accelerator Conference, (Geneva, Switzerland), pp. 791–794, JACoW, May 2017. https://doi.org/10.18429/JACoW-IPAC2017-MOPIK110.

[41] D. Rubin, "Doc 1109: E989 note 43: Tracking and transfer map through injection channel into g-2 ring." Fermilab $g-2$ DocDB, 2014.

[42] D. Stratakis, J. Crnkovic, W. Morse, and V. Tishchenko, "Spin Correlations Study for the New g-2 Experiment at Fermilab," in *Proc. of International Particle Accelerator Conference (IPAC'16), Busan, Korea, May 8-13, 2016*, no. 7 in International Particle Accelerator Conference, (Geneva, Switzerland), pp. 1301–1303, JACoW, June 2016. doi:10.18429/JACoW-IPAC2016-TUPMR028.

[43] M. B. D. Tarazona, "Doc 7475: Cosy end-to-end simulation status." Fermilab $g-2$ DocDB, 2019.

[44] V. T. B. Morse, "Doc 1569: Mars simulations of pion production and capture." Fermilab $g-2$ DocDB, 2014.

[45] A. Keshavarzi, "Doc 9692: E989 note 129: Measurement of the kicker pulse of the muon g-2 experiment (e989) using a faraday magnetometer." Fermilab $g-2$ DocDB, 2018.

[46] D. Stratakis, "Doc 9110: Storage ring beam dynamics." Fermilab $g-2$ DocDB, 2017.

[47] J. Grange, "Vacuum chambers #28, 17/09/2015, 10:19:05: Various info on new collimators." University of Washington $g-2$ E-Log, 2015.

[48] W. Wu, "Doc 9188: 3d_quads_electric_field_maps_beamdynamics_2017-11-16." Fermilab $g-2$ DocDB, 2017.

[49] J. Grange, "Doc 8180: Passive shimming." Fermilab $g-2$ DocDB, 2017.

[50] R. Osofsky, "Doc 8168: Active shimming update." Fermilab $g-2$ DocDB, 2017.

[51] R. O. D. Flay, A.T. Herrod, "Doc 11598: Trolley run field map for beam dynamics." Fermilab $g-2$ DocDB, 2018.

[52] A. J. Dragt, *Lie Methods for Nonlinear Dynamics with Applications to Accelerator Physics*, p. 1235. Maryland: University of Maryland, Department of Physics, 2019.

[53] MathWorks, "Matlab." http://web.archive.org/web/20190717121010/https://uk.mathworks.com/products/matlab.html. Accessed: 17-07-2019.

[54] D. C. Sagan, "Bmad manual, revision: September 25, 2018." https://www.classe.cornell.edu/bmad/manual.html. Accessed: 25-09-2018.

[55] K. M. D. Tarazona, M. Berz, "Doc 12921: Tune/resonances." Fermilab $g-2$ DocDB, 2019.

[56] D. Tarazona. Private communication, September 2019.

[57] G. H. Hoffstaetter, *High-Energy Polarized Proton Beams*. New York: Springer, 2006.

[58] D. T. Abell, D. Meiser, V. H. Ranjbar, and D. P. Barber, "Accurate and efficient spin integration for particle accelerators," *Phys. Rev. ST Accel. Beams*, vol. 18, p. 024001, Feb 2015.

[59] Y. K. Wu, E. Forest, and D. S. Robin, "Explicit symplectic integrator for s-dependent static magnetic field," *Phys. Rev. E*, vol. 68, p. 046502, Oct 2003.

[60] H. Goldstein, J. L. Safko, and C. Poole, *Classical Mechanics*. London: Pearson, 2002.

[61] A. Herrod, I. Bailey, S. Jones, M. Korostelev, and A. Wolski, "Modelling of Curvilinear Electrostatic Multipoles in the Fermilab Muon g-2 Storage Ring," in *Proc. of International Particle Accelerator Conference (IPAC'17), Copenhagen, Denmark, 14-19 May, 2017*, no. 8 in International Particle Accelerator Conference, (Geneva, Switzerland), pp. 3837–3839, JACoW, May 2017. https://doi.org/10.18429/JACoW-IPAC2017-THPAB055.

[62] A. Wolski and A. T. Herrod, "Explicit symplectic integrator for particle tracking in s-dependent static electric and magnetic fields with curved reference trajectory," *Phys. Rev. Accel. Beams*, vol. 21, p. 084001, Aug 2018.

[63] D. C. Sagan, "Bmad manual, revision: September 25, 2018." https://www.classe.cornell.edu/bmad/manual.html. Accessed: 25-09-2018.

[64] E. W. Weisstein, "Toroidal coordinates." http://mathworld.wolfram.com/ToroidalCoordinates.html. Accessed: 27-06-2019.

[65] W. E. Byerly, *An elementary treatise on Fourier's series and spherical, cylindrical, and ellipsoidal harmonics with applications to problems in mathematical physics*, pp. 264—-266. Boston: Ginn & Company, 1893.

[66] E. W. Weisstein, "Laplace's equation–toroidal coordinates." `http://mathworld.wolfram.com/LaplacesEquationToroidalCoordinates.html`. Accessed: 11-08-2019.

[67] E. W. Weisstein, "Toroidal function." `http://mathworld.wolfram.com/ToroidalFunction.html`. Accessed: 11-08-2019.

[68] M. Abramowitz and I. A. Stegun, *Handbook of Mathematical Functions With Formulas, Graphs, and Mathematical Tables*, p. 333. Washington, District of Columbia: United States of America Government Printing Office, 1972.

[69] W. Research, "Wolfram alpha." `http://web.archive.org/web/20190808065400/https://www.wolframalpha.com/`. Accessed: 08-08-2019.

[70] J. Segura and A. Gil, "Evaluation of toroidal harmonics," *Computer Physics Communications*, vol. 124, no. 1, pp. 104 – 122, 2000.

[71] R. Osofsky, "Doc 12993: Magnetic field summary." Fermilab $g-2$ DocDB, 2018.

[72] D. Rubin, "Doc 1740: Ring model." Fermilab $g-2$ DocDB, 2014.

[73] W. T. Weng and S. R. Mane, "Fundamentals of particle beam dynamics and phase space," *AIP Conference Proceedings*, vol. 249, no. 1, pp. 3–45, 1992.

[74] D. Rubin, "Doc 10563: Injection dependencies." Fermilab $g-2$ DocDB, 2018.

[75] N. S. Froemming. Private communication, February 2018.

[76] D. Rubin, "Doc 11703: Phase space at inflector exit." Fermilab $g-2$ DocDB, 2018.

[77] H. Nguyen. Private communication, March 2019.

[78] W. W. J.D. Crnkovic, "Doc 10027: quad-scan-update2018jan." Fermilab $g-2$ DocDB, 2018.

[79] S. Ganguly, "Doc 19583: 2nd fine quad scan from run 2 with offline data." Fermilab $g-2$ DocDB, 2019.

[80] S. Ganguly, J. Crnkovic, K. T. Pitts, and C. C. Polly, "Lost Muon Studies for the Muon g-2 Experiment at Fermilab," in *Proc. 9th International Particle Accelerator Conference (IPAC'18), Vancouver, BC, Canada, April 29-May 4, 2018*, no. 9 in International Particle Accelerator Conference, (Geneva, Switzerland), pp. 3573–3576, JACoW Publishing, June 2018. https://doi.org/10.18429/JACoW-IPAC2018-THPAK139.

[81] K. M. D. Tarazona, M. Berz, "Doc 12416: 3qy=1 and collimation studies with cosy." Fermilab $g-2$ DocDB, 2019.

[82] E. Barlas, "Doc 6686: Quad commissioning status." Fermilab $g-2$ DocDB, 2017.

[83] V. Tishchenko, "The muon g-2 collaboration electronic logbook, entry 8567, 06/19/2017, 14:03:21: Quad scan." Fermilab Muon g-2 Collaboration Electronic Logbook, 2017.

[84] H. Friedsam, "Doc 2853: Results of the the g-2 pole alignment from 5-20-2015." Fermilab $g-2$ DocDB, 2015.

[85] C. C. Polly. Private communication, July 2019.

[86] W. R. Inc., "Besseli function." `http://functions.wolfram.com/Bessel-TypeFunctions/BesselI/introductions/Bessels/ShowAll.html`. Accessed: 2-07-2019.

[87] W. D. D'haeseleer, W. N. G. Hitchon, J. D. Callen, and J. L. Shohet, *"Proper" Toroidal Coordinates*, pp. 179–185. Berlin, Heidelberg: Springer Berlin Heidelberg, 1991.

[88] P. Winter, "Doc 2418: Change request for vacuum chamber rail/cage/quadrupole survey activities." Fermilab $g-2$ DocDB, 2014.

[89] M. Kargiantoulakis, "Doc 16970: E989 note 177: Alignment survey results for the electrostatic quadrupole system of the muon g-2 experiment." Fermilab $g-2$ DocDB, 2019.

Appendix A

Derivation of the Measured Spin Precession Frequency ω_a

We start with the equation for T-BMT spin precession frequency ω_s of a particle with velocity vector $\boldsymbol{\beta}c$ and lorentz factor γ in electric field $\boldsymbol{E}$ and magnetic field $\boldsymbol{B}$ [12]:

$$\omega_s = \frac{-q}{\gamma m}\left((1+\gamma a_\mu)\boldsymbol{B}_\perp + (1+a_\mu)\boldsymbol{B}_\parallel + \left(\frac{1}{\gamma+1}+a_\mu\right)\frac{\gamma \boldsymbol{E}}{c}\times\boldsymbol{\beta}\right), \quad \text{(A.1)}$$

where $\boldsymbol{B}_\perp$ and $\boldsymbol{B}_\parallel$ are the magnetic fields perpendicular and parallel to the particle momentum, respectively. The quantity a_μ is referred to as the anomalous magnetic moment, and satisfies:

$$a_\mu = \frac{g_\mu - 2}{2} \quad \text{(A.2)}$$

where g is the gyromagnetic ratio used in the equation for magnetic moment $\boldsymbol{\mu}$:

$$\boldsymbol{\mu} = \frac{ge}{2m}\boldsymbol{S} \quad \text{(A.3)}$$

where e, m and $\boldsymbol{S}$ are the electric charge, the mass and the spin vector of the particle, respectively.

The components of the magnetic field can be written as:

$$\boldsymbol{B}_\parallel = \frac{(\boldsymbol{B}\cdot\boldsymbol{\beta})}{\beta^2}\boldsymbol{\beta} = \frac{\gamma^2(\boldsymbol{B}\cdot\boldsymbol{\beta})}{\gamma^2-1}\boldsymbol{\beta},$$

$$\boldsymbol{B}_\perp = \boldsymbol{B} - \boldsymbol{B}_\parallel = \boldsymbol{B} - \frac{\gamma^2(\boldsymbol{B}\cdot\boldsymbol{\beta})}{\gamma^2-1}\boldsymbol{\beta},$$

which can be substituted in to (A.1) to produce:

$$\omega_s = \frac{-q}{\gamma m}\left((1+\gamma a_\mu)\boldsymbol{B} + \frac{\gamma^2 a_\mu(1-\gamma)}{\gamma^2-1}(\boldsymbol{B}\cdot\boldsymbol{\beta})\boldsymbol{\beta} + \left(\frac{1}{\gamma+1}+a_\mu\right)\frac{\gamma\boldsymbol{E}}{c}\times\boldsymbol{\beta}\right)$$

$$= \frac{-q}{\gamma m}\left((1+\gamma a_\mu)\boldsymbol{B} - \frac{\gamma^2 a_\mu}{\gamma+1}(\boldsymbol{B}\cdot\boldsymbol{\beta})\boldsymbol{\beta} + \left(\frac{1}{\gamma+1}+a_\mu\right)\frac{\gamma\boldsymbol{E}}{c}\times\boldsymbol{\beta}\right). \quad \text{(A.4)}$$

We then use the cyclotron frequency ω_c which, in both electric and magnetic fields, takes the form:

$$\omega_c = \frac{-q}{\gamma m}\left(\boldsymbol{B} + \frac{\gamma}{\gamma^2-1}\left(\frac{\gamma\boldsymbol{E}}{c}\times\boldsymbol{\beta}\right)\right), \quad \text{(A.5)}$$

and note that what is actually measured in the experiment is the difference of spin precession and cyclotron frequencies, as the particles spins are precessing at a smooth rate (due to the uniform dipole magnet) whilst they orbit the ring, and the calorimeters are only on the inside of the ring.

We obtain the measured frequency ω_a from the difference of (A.4) and (A.5):

$$\omega_a = \omega_s - \omega_c \quad \text{(A.6)}$$

$$= \frac{-q}{\gamma m}\left(\gamma a_\mu \boldsymbol{B} - \frac{\gamma^2 a_\mu}{\gamma+1}(\boldsymbol{B}\cdot\boldsymbol{\beta})\boldsymbol{\beta} + \left(\frac{1}{\gamma+1} - \frac{\gamma}{\gamma^2-1} + a_\mu\right)\frac{\gamma\boldsymbol{E}}{c}\times\boldsymbol{\beta}\right)$$

where, in the third term, we can use the identity:

$$\frac{1}{\gamma+1} - \frac{\gamma}{\gamma^2-1} = \frac{\gamma^2-1-\gamma^2-\gamma}{(\gamma+1)(\gamma^2-1)} = \frac{-(\gamma+1)}{(\gamma+1)(\gamma^2-1)} = \frac{-1}{\gamma^2-1} \quad \text{(A.7)}$$

to leave us with the final result for ω_a:

$$\omega_a = \frac{-q}{\gamma m}\left(\gamma a_\mu \boldsymbol{B} - \frac{\gamma^2 a_\mu}{\gamma+1}(\boldsymbol{B}\cdot\boldsymbol{\beta})\boldsymbol{\beta} + \left(a_\mu - \frac{1}{\gamma^2-1}\right)\frac{\gamma\boldsymbol{E}}{c}\times\boldsymbol{\beta}\right) \quad \text{(A.8)}$$

Appendix B

Testing the Physical Validity of Field Maps

To verify that the given electric fields satisfy Maxwell's equations in the static case, we check that the field is divergence-free in the region between the plates. We take a cylindrical surface of radius $r_m = .045\,\mathrm{m}$, with curved axis following the design orbit. The ends of the cylinder correspond to the ends of the upstream fringe field map. However, as the design orbit is not straight, we must take into account the increased surface area for the surface elements of the cylinder in the $x > 0$ region (radial outside of the ring) as compared to the $x < 0$ region (radial inside of the ring).

To find the correct surface element, we first take the surface element of the side of a cylinder to be a square of area:

$$dA_{\mathrm{Cyl}} = r_m d\phi dz \tag{B.1}$$

where ϕ is the "minor azimuth" angle about the design orbit (assumed straight here), r_m is the radius of the cylinder and z is the length along the design orbit.

To change this to the surface area element of a torus (the curved cylinder), we replace dz with the element of arclength about the centre of the torus. As this element depends on the major-radius (distance from the centre of the torus/ring) of the point studied, in local coordinates it depends on the minor-radius of the cylinder/torus and the minor-azimuth ϕ. This leads us to the substitution:

$$dz \to (\rho + r_m \cos(\phi))d\Theta \tag{B.2}$$

leaving us with the surface element:

$$dA_{\mathrm{Tor}} = r_m d\phi(\rho + r_m \cos(\phi))d\Theta \tag{B.3}$$

where $\rho = 7.112\,\mathrm{m}$. This, and the surface elements of the circular ends of the cylinder:

$$dA_{\mathrm{Cir}} = \pi(r_b^2 - r_a^2)d\phi \tag{B.4}$$

(where r_a and r_b are the previous and current radii sampled, respectively, starting from zero) are multiplied by the field perpendicular to the surface at that point at intervals of $\Delta\Theta = 0.025°, \Delta\phi = 3°, \Delta r = 1\,\mathrm{mm}$, found by interpolating the field map using the MatLab [53] 3D spline method. This resulted in the value of:

$$\oiint_{\mathrm{Tor}} E_\perp dS = -83.3\,\mathrm{Vm} \tag{B.5}$$

which, given a surface area of approximately $0.08\,\mathrm{m}^2$, suggests the field diverges on the level of $10^3\,\mathrm{Vm}^{-1}$ over the whole surface. As this is the understood to be near the noise level of the field map, this result is reassuring.

Closed loops along the surface were also checked to be induction-free, using circles centred on the design orbit and the component of electric field parallel to the line element. The values of this, for three different circles, came to:

$$\oint_{\mathrm{Cir}} E_\parallel dl = 0.80\,\mathrm{V}, 5.9\,\mathrm{V}, 3.8\,\mathrm{V} \tag{B.6}$$

which have been calculated as loops around the design trajectory at 0.5° before the start of the quadrupole plates, at the start of the quadrupole plates, and 0.5° within the quadrupole, respectively. Given these are taken over paths of length $0.28\,\mathrm{m}$, the average field disagreement along the paths are on the order of $10\,\mathrm{Vm}^{-1}$. This is also sufficiently close to zero to claim that the field map satisfies Maxwell's equations.

Similar studies were done for the bulk and downstream field maps, with similar results. To fully verify the physical validity of the field maps would require this procedure to be performed more rigorously, however this was not necessary as the simple tests were deemed sufficient to show that the provided field maps could be used.

Appendix C

Fitting of the Multipole Expansion

C.1 Fourier Transform of the Standard Multipole Expansion

We start with the equation for the field of the multipole expansion (2.3):

$$E_\phi(r,\phi) + iE_r(r,\phi) = \sum_{n=1}^{\infty} c_n \left(\frac{r}{r_0}\right)^{n-1} e^{in\phi}. \tag{C.1}$$

We fix r at some value (we can choose any r_0 here) at which we have measured field values, and wish to replace the angle ϕ with a number of evenly-spaced azimuthal sample points. We wish to take in ϕ, N_ϕ (with azimuthal separation of $2\pi/N_\phi$):

$$\frac{1}{N_\phi}\sum_{n_\phi=0}^{N_\phi-1}\left(E_\phi\Big(r_0, 2\pi\frac{n_\phi}{N_\phi}\Big) + iE_r\Big(r_0, 2\pi\frac{n_\phi}{N_\phi}\Big)\right)e^{-in2\pi n_\phi/N_\phi} = c_n, \tag{C.2}$$

where we have included the normalisation factor N_ϕ^{-1}.

C.2 Multipole Expansion Radius Optimisation

The residuals of the multipole fit were taken using fits of different expansion (fit) radii. These are shown in Figure C.1, and suggest the best expansion radius to be approximately $r_0 = 45\,\text{mm}$. Smaller values than this would cause the field description within the storage region radius to be less accurate.

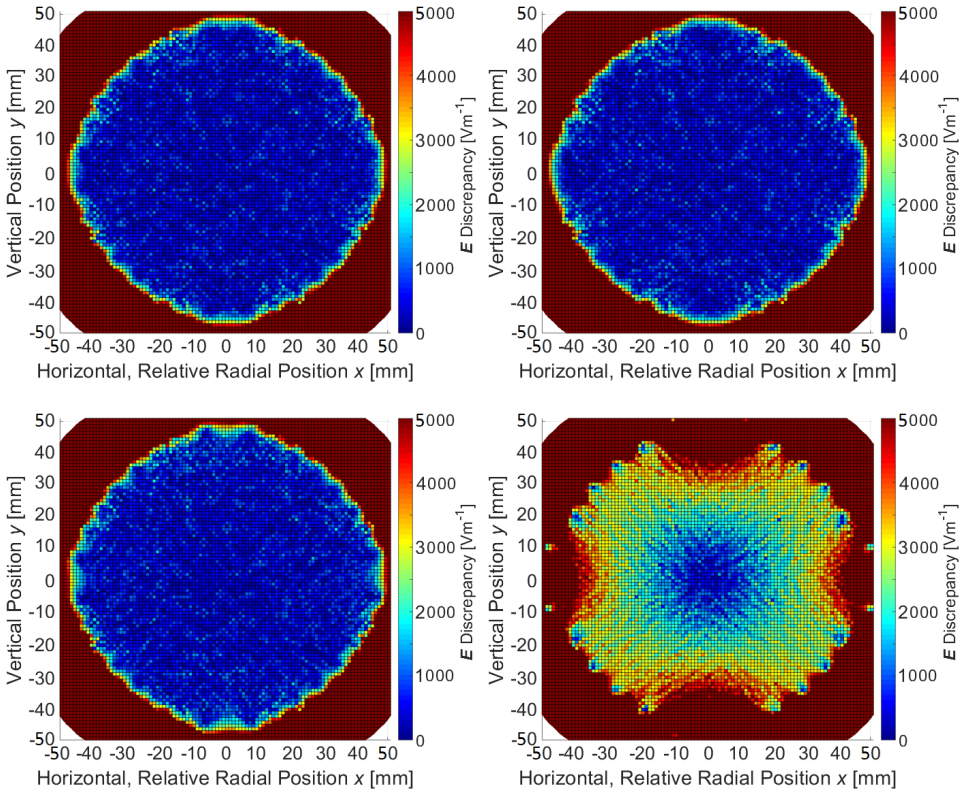

Figure C.1: Magnitude of residual electric field for fits taken at $r_0 = 45\,\text{mm}$ (top-left), $r_0 = 46\,\text{mm}$ (top-right), $r_0 = 47\,\text{mm}$ (bottom-left) and $r_0 = 49\,\text{mm}$ (bottom-right). We see the best expansion radius is at approximately 45 mm. Smaller values than this would cause field inaccuracy within the storage region.

Appendix D

Bessel Expansion Derivations and Fitting

D.1 Recurrence Relation of the Modified Bessel Functions of the First Kind

The recurrence relation, often quoted as [86]:

$$I_m(z) = \frac{2(m+1)}{z} I_{m+1}(z) + I_{m+2}(z), \tag{D.1}$$

can be re-written as:

$$\frac{2(m)}{z} I_m(z) = I_{m+1}(z) - I_{m-1}(z) \tag{D.2}$$

by making the substitution $m \to m - 1$.

D.2 Fourier Transform of Potential to Calculate Coefficients

We wish to Fourier transform (2.9) to obtain the coefficients $c_{n,m}$, given known values of $\psi(r, \phi, z)$. Firstly, we revert the expression for ψ back to the form in which the sums are from $-\infty$ to ∞:

$$\psi = \sum_{m=-\infty}^{\infty} \sum_{n=-\infty}^{\infty} -c_{n,m} \sin(nkz) e^{im\phi} \frac{I_m(nkr)}{nk} \tag{D.3}$$

and set a radius (about the reference trajectory) r_0 at which we will provide field values. As the only dependencies on the other two coordinates are in

complex exponents (including the sine function), the transformation can be performed, where we define N_ϕ and N_z as the number of points along ϕ and z, respectively, at which field values are provided. The factor $I_m(nkr_0)/nk$ is thus a constant with respect to the coordinates we with to iterate over.

The result of the transformation is thus:

$$c_{n,m} = \frac{-nk}{N_\phi N_z I_m(nkr_0)} \sum_{n_\phi=0}^{N_\phi-1} \sum_{n_z=0}^{N_z-1} e^{-im(2\pi n_\phi/N_\phi)} \sin(-n[2\pi n_z/N_z])\psi(r_0,\phi,z), \tag{D.4}$$

where ϕ has been replaced by $2\pi n_\phi/N_\phi$, kz (longitudinal position given as phase angle between 0 and 2π within the described field region) has been replaced by $2\pi n_z/N_z$ and the normalisation factors N_ϕ and N_z have been applied. The final result is thus:

$$c_{n,m} = \frac{nk}{N_\phi N_z I_m(nkr_0)} \sum_{n_\phi=0}^{N_\phi-1} \sum_{n_z=0}^{N_z-1} e^{-im(2\pi n_\phi/N_\phi)} \sin(n2\pi n_z/N_z)\psi(r_0,\phi,z). \tag{D.5}$$

D.3 Field x-Component E_x

For the x-component E_x, separating out the $m = 0$ cases (whose sum is denoted $E_{x,m=0}$), we keep in mind that $r^2 = x^2 + y^2$ and obtain:

$$\begin{aligned} E_x &= -\frac{\partial\psi}{\partial x} \\ &= E_{x,m=0} + \sum_{n=0}^{\infty}\sum_{m=1}^{\infty} A_{n,m}\sin(nkz) \\ &\qquad \times \mathbb{R}\mathrm{e}\left(\frac{c_{n,m}}{nk} I_m(nkr)\left[\frac{\partial}{\partial x} e^{im\phi}\right] + \frac{c_{n,m}}{nk} e^{im\phi}\left[\frac{\partial}{\partial x} I_m(nkr)\right]\right) \end{aligned} \tag{D.6}$$

where the first of the derivatives can be found, using $x = r\cos(\phi)$ and $y = r\sin(\phi)$, as follows:

$$\begin{aligned}
\frac{\partial}{\partial x}e^{im\phi} &= \frac{\partial}{\partial x}\left(\frac{x}{\sqrt{x^2+y^2}} + i\frac{y}{\sqrt{x^2+y^2}}\right)^m \\
&= \left((x+iy)^m\frac{\partial}{\partial x}(x^2+y^2)^{-m/2} + (x^2+y^2)^{-m/2}\frac{\partial}{\partial x}(x+iy)^m\right) \\
&= (x+iy)^m\frac{-mx}{r^{m+2}} + \frac{m}{r^m}(x+iy)^{m-1} \\
&= \frac{(x+iy)^m}{r^m}\left(\frac{-mx}{r^2} + m\frac{x-iy}{r^2}\right) \\
&= e^{im\phi}\frac{-imy}{r^2} \qquad \text{(D.7)}
\end{aligned}$$

and the second can be trivially found using (2.12) (with the differentiation chain rule).

This allows us to continue simplifying the expression for E_x:

$$\begin{aligned}
E_x &= E_{x,m=0} + \sum_{n=0}^{\infty}\sum_{m=1}^{\infty} A_{n,m}\sin(nkz) \\
&\times \mathbb{R}\mathrm{e}\left(\frac{-imy}{nkr^2}I_m(nkr)\left[c_{n,m}e^{im\phi}\right] + \frac{x}{2r}\left[I_{m-1}(nkr) + I_{m+1}(nkr)\right]\left[c_{n,m}e^{im\phi}\right]\right) \\
&= E_{x,m=0} + \sum_{n=0}^{\infty}\sum_{m=1}^{\infty} A_{n,m}\sin(nkz) \\
&\quad\times \mathbb{R}\mathrm{e}\Bigg(\frac{my}{nkr^2}I_m(nkr)\left[\mathbb{R}\mathrm{e}\left(c_{n,m}\right)\sin(m\phi) + \mathbb{I}\mathrm{m}\left(c_{n,m}\right)\cos(m\phi)\right] \\
&\quad+ \frac{x}{2r}\left[I_{m-1}(nkr) + I_{m+1}(nkr)\right]\left[\mathbb{R}\mathrm{e}\left(c_{n,m}\right)\cos(m\phi) - \mathbb{I}\mathrm{m}\left(c_{n,m}\right)\sin(m\phi)\right]\Bigg) \qquad \text{(D.8)}
\end{aligned}$$

where we can use the identity in (D.2) for I_m:

$$E_x = E_{x,m=0} + \sum_{n=0}^{\infty}\sum_{m=1}^{\infty} A_{n,m}\sin(nkz)$$
$$\times\left(\frac{y}{2r}\big[I_{m-1}(nkr) - I_{m+1}(nkr)\big]\big[\mathbb{R}\mathrm{e}\,(c_{n,m})\sin(m\phi) + \mathbb{I}\mathrm{m}\,(c_{n,m})\cos(m\phi)\big]\right.$$
$$\left.+\frac{x}{2r}\big[I_{m-1}(nkr) + I_{m+1}(nkr)\big]\big[\,\mathbb{R}\mathrm{e}\,(c_{n,m})\cos(m\phi) - \mathbb{I}\mathrm{m}\,(c_{n,m})\sin(m\phi)\big]\right) \tag{D.9}$$

and the coordinate definitions for x and y in (2.5), to obtain:

$$E_x = E_{x,m=0} + \sum_{n=0}^{\infty}\sum_{m=1}^{\infty} A_{n,m}\frac{\sin(nkz)}{2}\Bigg($$
$$\mathbb{R}\mathrm{e}\,(c_{n,m})\Big(I_{m-1}(nkr)\cos\big((m-1)\phi\big) + I_{m+1}(nkr)\cos\big((m+1)\phi\big)\Big)$$
$$-\,\mathbb{I}\mathrm{m}\,(c_{n,m})\Big(I_{m-1}(nkr)\sin\big((m-1)\phi\big) + I_{m+1}(nkr)\sin\big((m+1)\phi\big)\Big)\Bigg) \tag{D.10}$$

where the result has been written in terms of the components of $c_{n,m}$.

D.3.1 $m = 0$

Here we treat specially the case of $m = 0$, where the derivative of the Modified Bessel Function I_m is unique (as in (2.12)):

$$E_{x,m=0} = -\left.\frac{\partial\psi}{\partial x}\right|_{m=0}$$
$$= \mathbb{R}\mathrm{e}\left(\sum_{n=0}^{\infty} A_{n,0}c_{n,0}\frac{\sin(nkz)}{nk}\frac{\partial}{\partial x}I_0\left(nk\sqrt{x^2+y^2}\right)\right)$$
$$= \sum_{n=0}^{\infty} A_{n,0}\,\mathbb{R}\mathrm{e}\,(c_{n,0})\,\frac{\sin(nkz)}{nk}\frac{nkx}{r}I_1\,(nkr) \tag{D.11}$$

where, in the last line, we used (2.12). Using the coordinate definition $x = r\cos(\phi)$, this becomes:

$$E_{x,m=0} = \cos(\phi)\sum_{n=0}^{\infty} A_{n,0}\,\mathbb{R}\mathrm{e}\,(c_{n,0})\sin(nkz)I_1\,(nkr)\,. \tag{D.12}$$

D.4 Field y-Component E_y

For the y-component E_y, separating out the $m = 0$ cases (whose sum is denoted $E_{y,m=0}$), we keep in mind that $r^2 = x^2 + y^2$ and obtain:

$$\begin{aligned} E_y &= -\frac{\partial \psi}{\partial y} \\ &= E_{y,m=0} + \sum_{n=0}^{\infty} \sum_{m=1}^{\infty} A_{n,m} \sin(nkz) \\ &\quad \times \mathbb{R}\mathrm{e}\left(\frac{c_{n,m}}{nk} I_m(nkr) \left[\frac{\partial}{\partial y} e^{im\phi} \right] + \frac{c_{n,m}}{nk} e^{im\phi} \left[\frac{\partial}{\partial y} I_m(nkr) \right] \right) \end{aligned} \quad \text{(D.13)}$$

where the first of the derivatives can be found, using $x = r\cos(\phi)$ and $y = r\sin(\phi)$, as follows:

$$\begin{aligned} \frac{\partial}{\partial y} e^{im\phi} &= \frac{\partial}{\partial y} \left(\frac{x}{\sqrt{x^2+y^2}} + i \frac{y}{\sqrt{x^2+y^2}} \right)^m \\ &= \left((x+iy)^m \frac{\partial}{\partial y} (x^2+y^2)^{-m/2} + (x^2+y^2)^{-m/2} \frac{\partial}{\partial y} (x+iy)^m \right) \\ &= (x+iy)^m \frac{-my}{r^{m+2}} + \frac{im}{r^m} (x+iy)^{m-1} \\ &= \frac{(x+iy)^m}{r^m} \left(\frac{-my}{r^2} + im \frac{x-iy}{r^2} \right) \\ &= e^{im\phi} \frac{imx}{r^2} \end{aligned} \quad \text{(D.14)}$$

and the second can be trivially found using (2.12) (with the differentiation chain rule).

This allows us to continue simplifying the expression for E_y:

$$\begin{aligned}
E_y &= E_{y,m=0} + \sum_{n=0}^{\infty}\sum_{m=1}^{\infty} A_{n,m}\sin(nkz) \\
&\quad \times \mathbb{R}\mathrm{e}\left(\frac{imx}{nkr^2} I_m(nkr)\left[c_{n,m}e^{im\phi}\right] + \frac{y}{2r}\left[I_{m-1}(nkr) + I_{m+1}(nkr)\right]\left[c_{n,m}e^{im\phi}\right]\right) \\
&= E_{y,m=0} + \sum_{n=0}^{\infty}\sum_{m=1}^{\infty} A_{n,m}\sin(nkz) \\
&\quad \times \left(\frac{mx}{nkr^2} I_m(nkr)\left[-\mathbb{R}\mathrm{e}\left(c_{n,m}\right)\sin(m\phi) - \mathbb{I}\mathrm{m}\left(c_{n,m}\right)\cos(m\phi)\right]\right. \\
&\quad \left. + \frac{y}{2r}\left[I_{m-1}(nkr) + I_{m+1}(nkr)\right]\left[\mathbb{R}\mathrm{e}\left(c_{n,m}\right)\cos(m\phi) - \mathbb{I}\mathrm{m}\left(c_{n,m}\right)\sin(m\phi)\right]\right)
\end{aligned} \tag{D.15}$$

where we can use the identity in (D.2) for I_m:

$$\begin{aligned}
E_y &= E_{y,m=0} + \sum_{n=0}^{\infty}\sum_{m=1}^{\infty} A_{n,m}\sin(nkz) \\
&\quad \times \left(\frac{x}{2r}\left[I_{m-1}(nkr) - I_{m+1}(nkr)\right]\left[-\mathbb{R}\mathrm{e}\left(c_{n,m}\right)\sin(m\phi) - \mathbb{I}\mathrm{m}\left(c_{n,m}\right)\cos(m\phi)\right]\right. \\
&\quad \left. + \frac{y}{2r}\left[I_{m-1}(nkr) + I_{m+1}(nkr)\right]\left[\mathbb{R}\mathrm{e}\left(c_{n,m}\right)\cos(m\phi) - \mathbb{I}\mathrm{m}\left(c_{n,m}\right)\sin(m\phi)\right]\right)
\end{aligned} \tag{D.16}$$

and the coordinate definitions for x and y in (2.5), to obtain:

$$\begin{aligned}
E_y &= E_{y,m=0} + \sum_{n=0}^{\infty}\sum_{m=1}^{\infty} A_{n,m}\frac{\sin(nkz)}{2}\Bigg(\\
&\quad - \mathbb{R}\mathrm{e}\left(c_{n,m}\right)\Big(I_{m-1}(nkr)\sin\big((m-1)\phi\big) - I_{m+1}(nkr)\sin\big((m+1)\phi\big)\Big) \\
&\quad - \mathbb{I}\mathrm{m}\left(c_{n,m}\right)\Big(I_{m-1}(nkr)\cos\big((m-1)\phi\big) - I_{m+1}(nkr)\cos\big((m+1)\phi\big)\Big)\Bigg)
\end{aligned} \tag{D.17}$$

where the result has been written in terms of the components of $c_{n,m}$.

D.4.1 $m = 0$

We treat separately the case of $m = 0$, where the derivative of the Modified Bessel Function I_m is unique (as in (2.12)):

$$\begin{aligned} E_{y,m=0} &= -\left.\frac{\partial\psi}{\partial y}\right|_{m=0} \\ &= \mathbb{R}\mathrm{e}\left(\sum_{n=0}^{\infty} A_{n,0}c_{n,0}\frac{\sin(nkz)}{nk}\frac{\partial}{\partial y}I_0\left(nk\sqrt{x^2+y^2}\right)\right) \\ &= \sum_{n=0}^{\infty} A_{n,0}\,\mathbb{R}\mathrm{e}\left(c_{n,0}\right)\frac{\sin(nkz)}{nk}\frac{nky}{r}I_1\left(nkr\right) \end{aligned} \tag{D.18}$$

where, in the last line, we used (2.12). Using the coordinate definition $y = r\sin(\phi)$, this becomes:

$$E_{y,m=0} = \sin(\phi)\sum_{n=0}^{\infty} A_{n,0}\,\mathbb{R}\mathrm{e}\left(c_{n,0}\right)\sin(nkz)I_1\left(nkr\right). \tag{D.19}$$

D.5 Fit Residuals

The residuals for E_x, E_y and E_z on the fitted surface are shown in Figure D.2, with residuals calculated on transverse (x, y) planes at $\Theta = -0.5°$, $\Theta = 0°$ and $\Theta = 1°$.

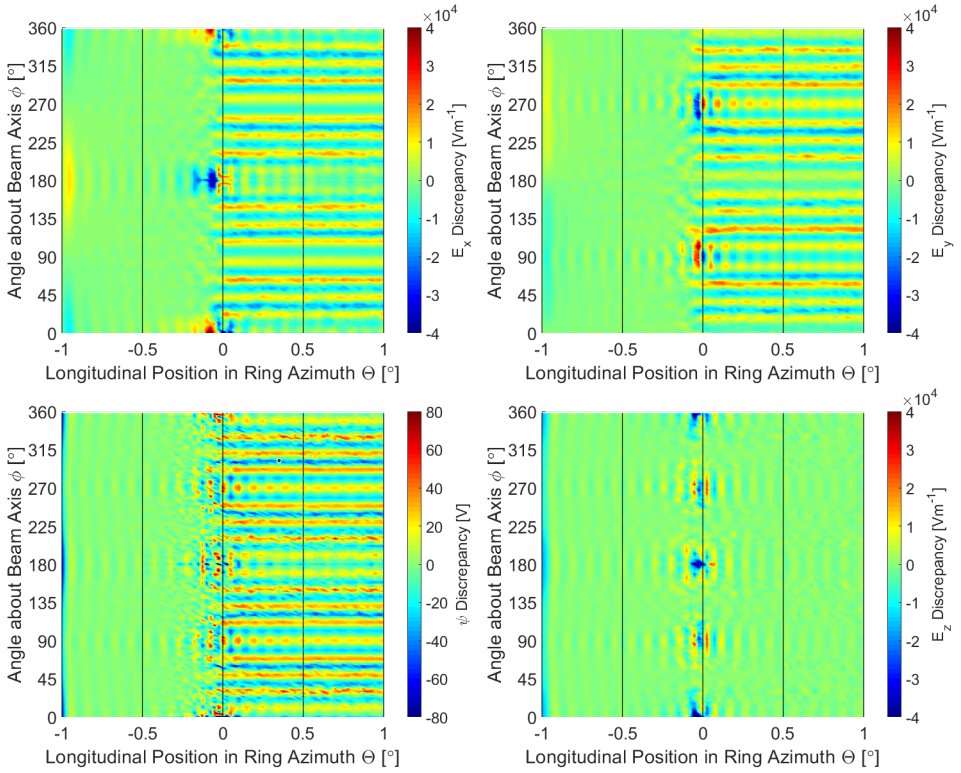

Figure D.1: Residuals on the $r_0 = .045\,\text{m}$ fitted surface for (clockwise from top-left): E_x, E_y, E_z and ϕ respectively. Residuals should be compared to the peak field of $10^6\,\text{Vm}^{-1}$.

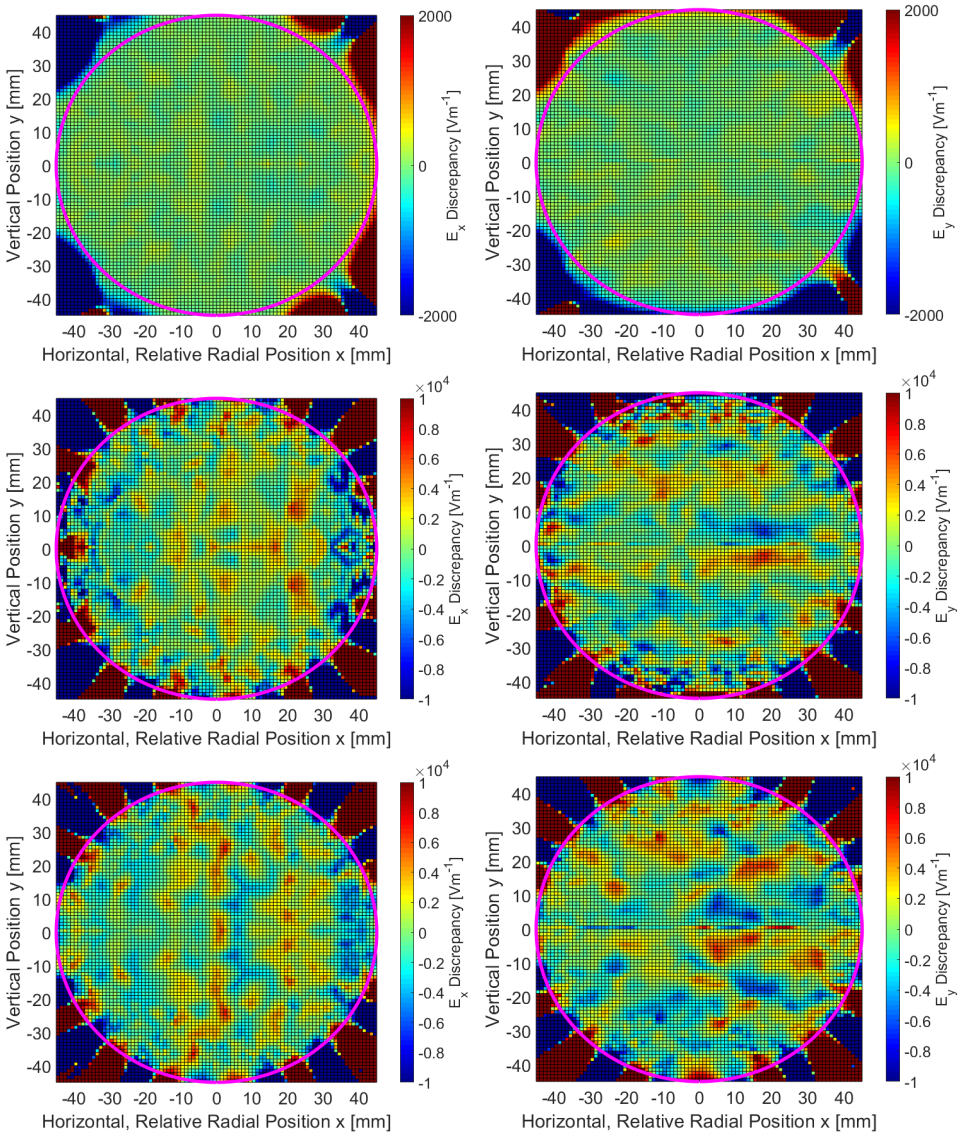

Figure D.2: Residuals of E_x (left column) and E_y (right column) on the transverse plane at 0.5° of ring azimuth before the quadrupole (top row), at the start of the quadrupole (middle row) and 0.5° of ring azimuth within the quadrupole (bottom row). Residuals should be compared to the peak field of $10^6\,\mathrm{Vm}^{-1}$.

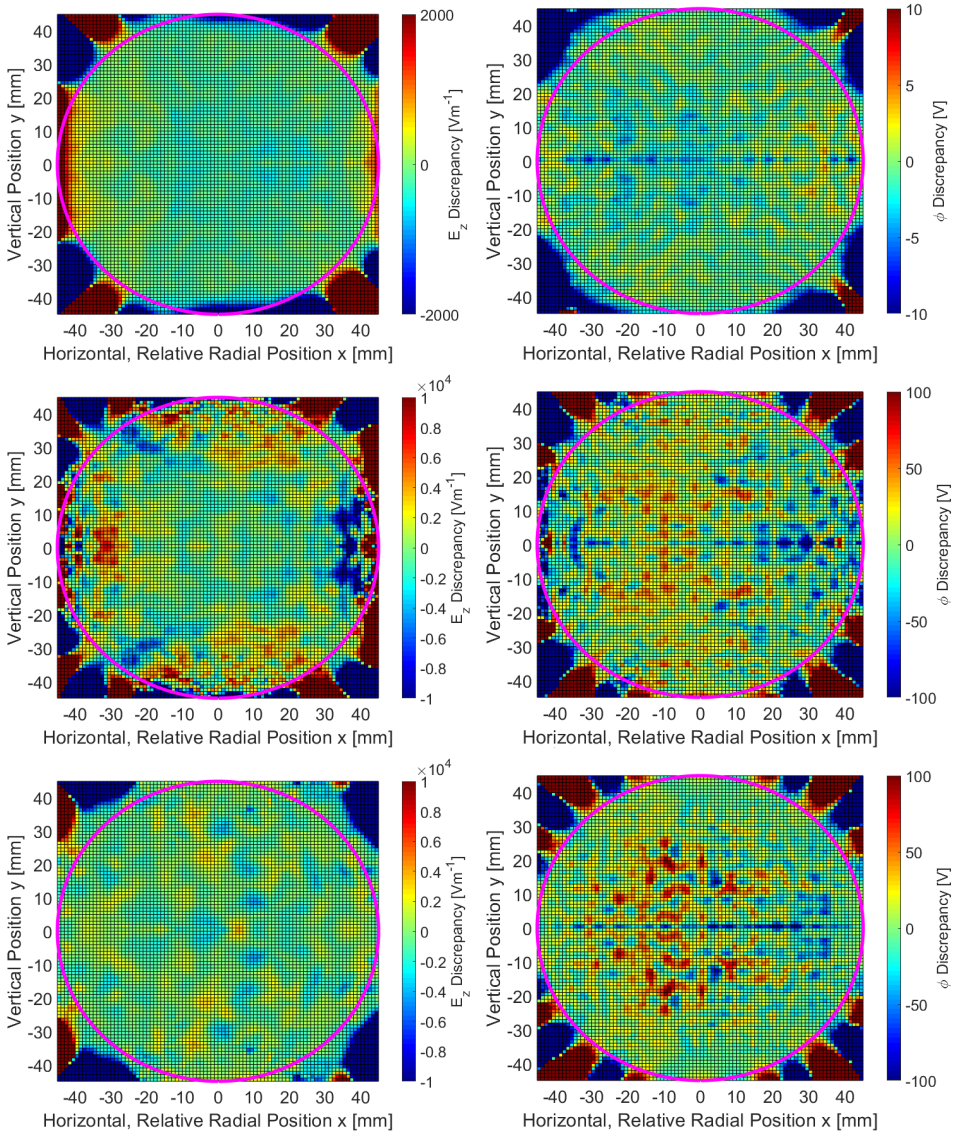

Figure D.3: Residuals of Ez (left column) and ϕ (right column) on the transverse plane at 0.5° of ring azimuth before the quadrupole (top row), at the start of the quadrupole (middle row) and 0.5° of ring azimuth within the quadrupole (bottom row). Residuals should be compared to the peak field of $10^6\,\mathrm{Vm}^{-1}$.

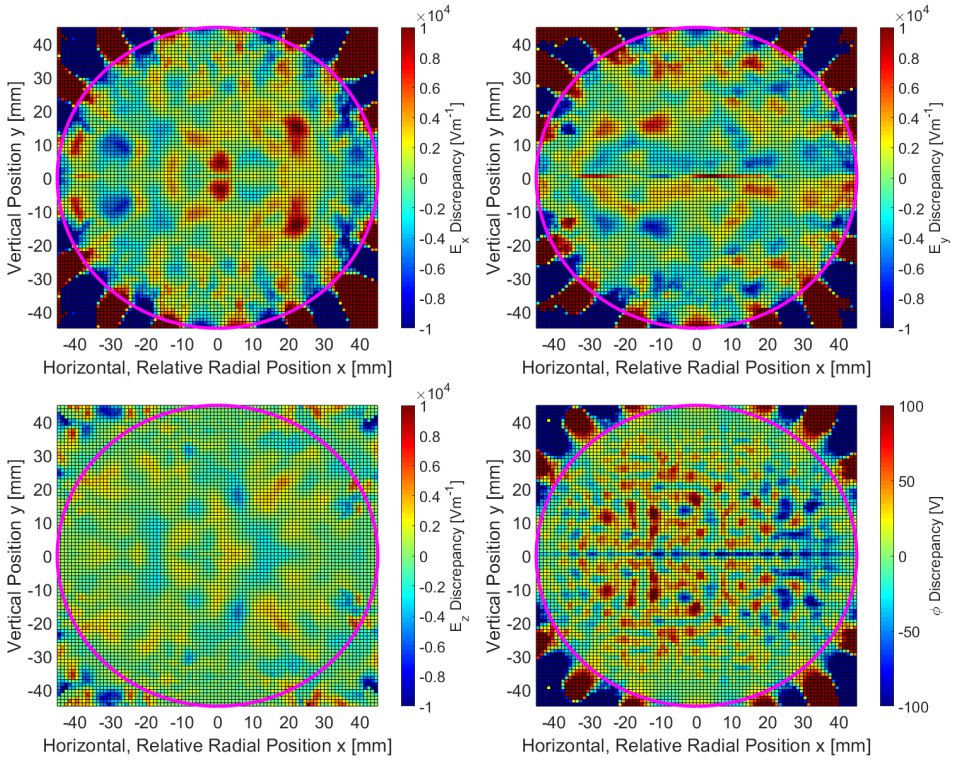

Figure D.4: Residuals on the transverse plane at 1° of ring azimuth within the quadrupole for (clockwise from top-left): E_x, E_y, E_z and ϕ respectively. Residuals should be compared to the peak field of $10^6\,\mathrm{Vm}^{-1}$.

Appendix E

Derivations for the New Symplectic Integrators

E.1 Dipole Vector Potential in a Bend

We use a global cylindrical coordinate system, with the Z-axis in the vertical direction (y-axis), and the angle Φ is parallel to the design orbit (such that vector components in Φ are equal to those in s). The Z- (y-) component of the curl of $\boldsymbol{a} = (0, 0, a_s)$ in this coordinate system is then:

$$(\nabla \times \boldsymbol{a})_Z = \frac{qB_Z}{P_0} = \frac{1}{R}\frac{\partial(Ra_s)}{\partial R}, \tag{E.1}$$

where the normalisation of B is from (2.20) and a_s from (2.25). Converting the coordinates in the expression for a_s to those of the global cylindrical system, the above expression becomes:

$$\frac{1}{R}\frac{\partial(Ra_s)}{\partial R} = \frac{1}{R}\frac{\partial}{\partial R}\left(Rk_0(R-\rho)\left(\frac{h(R-\rho)}{2(1+h(R-\rho))} - 1\right)\right) \tag{E.2}$$

$$= \frac{1}{R}\frac{\partial}{\partial R}\left(\frac{k_0 h}{2}\frac{R(R-\rho)^2}{1+h(R-\rho)} - k_0 R(R-\rho)\right). \tag{E.3}$$

Substituting the value $h = 1/\rho$, this becomes:

$$\frac{1}{R}\frac{\partial(Ra_s)}{\partial R} = \frac{1}{R}\frac{\partial}{\partial R}\left(\frac{k_0}{2\rho}\frac{R(R-\rho)^2}{R/\rho} - k_0 R(R-\rho)\right) \tag{E.4}$$

$$= \frac{1}{R}\frac{\partial}{\partial R}\left(\frac{k_0}{2}(R-\rho)^2 - k_0 R(R-\rho)\right). \tag{E.5}$$

Differentiating each term with respect to R gives:

$$\frac{1}{R}\frac{\partial(Ra_s)}{\partial R} = \frac{1}{R}\left(\frac{k_0}{2}2(R-\rho) - k_0(2R-\rho)\right), \tag{E.6}$$

which leaves us with:

$$= \frac{1}{R}\Big(k_0(R-\rho) - k_0(2R-\rho)\Big) = \frac{-k_0 R}{R} = -k_0. \tag{E.7}$$

This is a constant, and so the potential a_s is indeed the vector potential for a dipole. There are also no variables in a_s other than radial position, so the other components of $\boldsymbol{B}$ from this potential are zero.

However, we can go further and write the value for B_Z:

$$B_Z = -\frac{P_0}{q}k_0. \tag{E.8}$$

Using the equation for beam rigidity ($B\rho = p/q$), we can express k_0 as:

$$k_0 = \frac{-1}{\rho'} \tag{E.9}$$

where ρ' is the orbit radius of a particle with momentum P_0, caused by the dipole of strength k_0. So, for an ideal dipole field in the experiment, we should have a value of $k_0 = -h = -1/\rho$ everywhere.

E.2 Taylor Expansion of Hamiltonian K to Third Order

We start with (2.24), in which we expand the brackets in the square root to obtain:

$$K = p_s + \frac{\tilde{\delta}}{\beta_0} - (1+hx)\left(a_s + \sqrt{(\tilde{\delta}-\tilde{\psi})^2 + \frac{1}{\beta_0^2} + 2\frac{\tilde{\delta}-\tilde{\psi}}{\beta_0} - p_x^2 - p_y^2 - \frac{1}{\beta_0^2\gamma_0^2}}\right)$$

where we can re-write the factor of β_0^{-2}:

$$\frac{1}{\beta_0^2} = 1 + \left(\frac{1}{\beta_0^2} - 1\right) = 1 + \frac{1-\beta_0^2}{\beta_0^2} = 1 + \frac{1}{\beta_0^2\gamma_0^2}, \tag{E.10}$$

giving for the square-root:

$$\sqrt{1 + (\tilde{\delta}-\tilde{\psi})^2 + 2\frac{\tilde{\delta}-\tilde{\psi}}{\beta_0} - (p_x^2 + p_y^2)} \tag{E.11}$$

which, taking the form of a Taylor expansion of $\sqrt{1+x}$, can be approximated as:

$$1 + \frac{x}{2} - \frac{x^2}{8} + \frac{x^3}{16} - ... \tag{E.12}$$

given that all of the dynamic variables, and $\tilde{\psi}$, are small (the paraxial approximation). This results in the square root being approximated as:

$$1 + \frac{(\tilde{\delta}-\tilde{\psi})^2}{2} + \frac{\tilde{\delta}-\tilde{\psi}}{\beta_0} - \frac{p_x^2+p_y^2}{2} - \frac{1}{8}\left((\tilde{\delta}-\tilde{\psi})^2 + 2\frac{\tilde{\delta}-\tilde{\psi}}{\beta_0} - (p_x^2+p_y^2)\right)^2 + \frac{1}{16}\left((\tilde{\delta}-\tilde{\psi})^2 + 2\frac{\tilde{\delta}-\tilde{\psi}}{\beta_0} - (p_x^2+p_y^2)\right)^3 \tag{E.13}$$

where the only terms we need concern ourselves with are those of third order in the dynamic variables. This then becomes:

$$1 + \frac{(\tilde{\delta}-\tilde{\psi})^2}{2} + \frac{\tilde{\delta}-\tilde{\psi}}{\beta_0} - \frac{p_x^2+p_y^2}{2} - \frac{(\tilde{\delta}-\tilde{\psi})^3}{2\beta_0} + \frac{\tilde{\delta}-\tilde{\psi}}{2\beta_0}(p_x^2+p_y^2) - \frac{(\tilde{\delta}-\tilde{\psi})^2}{2\beta_0^2} + \frac{(\tilde{\delta}-\tilde{\psi})^3}{2\beta_0^3}. \tag{E.14}$$

Feeding our approximated value for the square-root back in to K, we obtain:

$$K \approx p_s + \frac{\tilde{\delta}}{\beta_0} - (1+hx)\Bigg(a_s + 1 + \frac{(\tilde{\delta}-\tilde{\psi})^2}{2} + \frac{\tilde{\delta}-\tilde{\psi}}{\beta_0} - \frac{p_x^2+p_y^2}{2} - \frac{(\tilde{\delta}-\tilde{\psi})^3}{2\beta_0} + \frac{\tilde{\delta}-\tilde{\psi}}{2\beta_0}(p_x^2+p_y^2) - \frac{(\tilde{\delta}-\tilde{\psi})^2}{2\beta_0^2} + \frac{(\tilde{\delta}-\tilde{\psi})^3}{2\beta_0^3}\Bigg). \tag{E.15}$$

Given the value of a_s for a dipole field, in (2.25), this becomes:

$$\begin{aligned} K &\approx p_s + \frac{\tilde{\delta}}{\beta_0} - (1+hx)\Bigg(\frac{hk_0x^2}{2(1+hx)} - k_0x + 1 + \frac{(\tilde{\delta}-\tilde{\psi})^2}{2} + \frac{\tilde{\delta}-\tilde{\psi}}{\beta_0} - \frac{p_x^2+p_y^2}{2} \\ &\qquad - \frac{(\tilde{\delta}-\tilde{\psi})^3}{2\beta_0} + \frac{\tilde{\delta}-\tilde{\psi}}{2\beta_0}(p_x^2+p_y^2) - \frac{(\tilde{\delta}-\tilde{\psi})^2}{2\beta_0^2} + \frac{(\tilde{\delta}-\tilde{\psi})^3}{2\beta_0^3}\Bigg) \\ &= p_s + \frac{\tilde{\delta}}{\beta_0} - \frac{hk_0x^2}{2} + (1+hx)\Bigg(k_0x - 1 - \frac{(\tilde{\delta}-\tilde{\psi})^2}{2} - \frac{\tilde{\delta}-\tilde{\psi}}{\beta_0} + \frac{p_x^2+p_y^2}{2} \\ &\qquad + \frac{(\tilde{\delta}-\tilde{\psi})^3}{2\beta_0} - \frac{\tilde{\delta}-\tilde{\psi}}{2\beta_0}(p_x^2+p_y^2) + \frac{(\tilde{\delta}-\tilde{\psi})^2}{2\beta_0^2} - \frac{(\tilde{\delta}-\tilde{\psi})^3}{2\beta_0^3}\Bigg), \end{aligned} \tag{E.16}$$

in which we expand the outermost brackets:

$$= p_s + \frac{\tilde{\delta}}{\beta_0} - \frac{hk_0x^2}{2} + k_0x - 1 - \frac{(\tilde{\delta}-\tilde{\psi})^2}{2} - \frac{\tilde{\delta}-\tilde{\psi}}{\beta_0} + \frac{p_x^2+p_y^2}{2} + \frac{(\tilde{\delta}-\tilde{\psi})^3}{2\beta_0}$$
$$- \frac{\tilde{\delta}-\tilde{\psi}}{2\beta_0}(p_x^2+p_y^2) + \frac{(\tilde{\delta}-\tilde{\psi})^2}{2\beta_0^2} - \frac{(\tilde{\delta}-\tilde{\psi})^3}{2\beta_0^3} + hk_0x^2 - hx - \frac{(\tilde{\delta}-\tilde{\psi})^2}{2}hx - \frac{\tilde{\delta}-\tilde{\psi}}{\beta_0}hx$$
$$+ \frac{p_x^2+p_y^2}{2}hx + \frac{(\tilde{\delta}-\tilde{\psi})^3}{2\beta_0}hx - \frac{\tilde{\delta}-\tilde{\psi}}{2\beta_0}(p_x^2+p_y^2)hx + \frac{(\tilde{\delta}-\tilde{\psi})^2}{2\beta_0^2}hx - \frac{(\tilde{\delta}-\tilde{\psi})^3}{2\beta_0^3}hx. \tag{E.17}$$

Factoring similar terms together, we have:

$$= -1 + p_s + \frac{p_x^2+p_y^2}{2}\left(1 - \frac{\tilde{\delta}-\tilde{\psi}}{\beta_0} + hx - hx\frac{\tilde{\delta}-\tilde{\psi}}{\beta_0}\right) + \frac{hk_0x^2}{2} + \frac{\tilde{\delta}}{\beta_0} - \frac{\tilde{\delta}-\tilde{\psi}}{\beta_0}$$
$$+ (k_0-h)x - \frac{\tilde{\delta}-\tilde{\psi}}{\beta_0}hx$$
$$+ \frac{(\tilde{\delta}-\tilde{\psi})^2}{2\beta_0^2} - \frac{(\tilde{\delta}-\tilde{\psi})^2}{2} - \frac{(\tilde{\delta}-\tilde{\psi})^3}{2\beta_0^3} + \frac{(\tilde{\delta}-\tilde{\psi})^3}{2\beta_0} + \frac{(\tilde{\delta}-\tilde{\psi})^2}{2\beta_0^2}hx - \frac{(\tilde{\delta}-\tilde{\psi})^2}{2}hx, \tag{E.18}$$

where the terms containing a factor of $(\tilde{\delta}-\tilde{\psi})^3x$ have been removed due to being of fourth order, and the last line contains factors of $(\beta^{-2}-1)$. As this is also equal to $\beta_0^{-2}\gamma_0^{-2}$ (shown in (E.10)), we obtain:

$$K \approx -1 + p_s + \frac{p_x^2+p_y^2}{2}\left(1 - \frac{\tilde{\delta}-\tilde{\psi}}{\beta_0} + hx - hx\frac{\tilde{\delta}-\tilde{\psi}}{\beta_0}\right) + \frac{hk_0x^2}{2} + \frac{\tilde{\psi}}{\beta_0}$$
$$+ (k_0-h)x - \frac{\tilde{\delta}-\tilde{\psi}}{\beta_0}hx + \frac{(\tilde{\delta}-\tilde{\psi})^2}{2\beta_0^2\gamma_0^2} - \frac{(\tilde{\delta}-\tilde{\psi})^3}{2\beta_0^3\gamma_0^2} + \frac{(\tilde{\delta}-\tilde{\psi})^2}{2\beta_0^2\gamma_0^2}hx, \tag{E.19}$$

which can be further factorised, to form our final result:

$$K \approx -1 + p_s + \frac{p_x^2+p_y^2}{2}\left(1 - \frac{\tilde{\delta}-\tilde{\psi}}{\beta_0} + hx - hx\frac{\tilde{\delta}-\tilde{\psi}}{\beta_0}\right) + \frac{hk_0x^2}{2} + \frac{\tilde{\psi}}{\beta_0}$$
$$+ (k_0-h)x - \frac{\tilde{\delta}-\tilde{\psi}}{\beta_0}hx + \frac{(\tilde{\delta}-\tilde{\psi})^2}{2\beta_0^2\gamma_0^2}\left(1 + hx - \frac{\tilde{\delta}-\tilde{\psi}}{\beta_0}\right). \tag{E.20}$$

E.3 Deriving Equations of Motion for H_1

Using the expression for H_1 in (2.27), we can use Hamilton's equations (2.31) for the canonical variables in the x-axis:

$$p_x' = -\frac{\partial H_1}{\partial x} = -hk_0 x \tag{E.21}$$

$$x' = \frac{\partial H_1}{\partial p_x} = \left(1 - \frac{\delta}{\beta_0}\right) p_x \tag{E.22}$$

which have the appearance of a set of harmonic oscillators. We will put in the trial solutions $x(\sigma) = A\sin(\omega\sigma) + B\cos(\omega\sigma)$ and $p_x(\sigma) = C\sin(\omega\sigma) + D\cos(\omega\sigma)$:

$$p_x' = \omega C\cos(\omega\sigma) - \omega D\sin(\omega\sigma) = -hk_0\big(A\sin(\omega\sigma) + B\cos(\omega\sigma)\big) \tag{E.23}$$

$$x' = \omega A\cos(\omega\sigma) - \omega B\sin(\omega\sigma) = \left(1 - \frac{\delta}{\beta_0}\right)\big(C\sin(\omega\sigma) + D\cos(\omega\sigma)\big). \tag{E.24}$$

From these, we obtain two pairs of simultaneous equations:

$$-hk_0 B = \omega C, \qquad -\omega B = \left(1 - \frac{\delta}{\beta_0}\right) C \tag{E.25}$$

and

$$\omega D = hk_0 A, \qquad \left(1 - \frac{\delta}{\beta_0}\right) D = \omega A. \tag{E.26}$$

Solving the first of these gives:

$$C = \frac{-hk_0}{\omega} B \qquad \text{and} \qquad \omega = \sqrt{\left(1 - \frac{\delta}{\beta_0}\right) hk_0}, \tag{E.27}$$

where the result for ω can be used in the second pair of equations to obtain:

$$D = A\sqrt{\left(1 - \frac{\delta}{\beta_0}\right)^{-1} hk_0}. \tag{E.28}$$

Now, we take the boundary conditions that $x(\sigma) = x(0)$ when $\sigma = 0$, and similarly for p_x:

$$x(0) = B, \qquad p_x(0) = D,$$

with which we arrive at our results for $x(\sigma)$ and $p_x(\sigma)$:

$$x(\sigma) = p_x(0)\frac{hk_0}{\omega}\sin(\omega\sigma) + x(0)\cos(\omega\sigma), \tag{E.29}$$

$$p_x(\sigma) = x(0)\frac{-hk_0}{\omega}\sin(\omega\sigma) + p_x(0)\cos(\omega\sigma). \tag{E.30}$$

These are the expressions for $e^{-\sigma:H_1:}x$ and $e^{-\sigma:H_1:}p_x$, in (2.32) and (2.36), respectively.

Transformations for the other canonical variables are found by the same method, albeit with simpler solutions.

Appendix F

Calculating Twiss Parameters from Tracking

We wish to extract the Twiss parameters β, α and γ, and phase advance μ, from the tracking results of particles tracked around the ring with a small deviation. This can be done by reproducing the transport matrices $\mathcal{M}_x$ and $\mathcal{M}_y$, defined in (1.10).

Particles with deviations on the order of 1 mm in the transverse axes (and zero total momentum deviation) were tracked using each of the new integrators. Using the transport matrices, in the x-axis we have:

$$x_1 = x_0\mathcal{M}_{x,11} + p_{x,0}\mathcal{M}_{x,12}, \tag{F.1}$$

$$p_{x,1} = x_0\mathcal{M}_{x,21} + p_{x,0}\mathcal{M}_{x,22}, \tag{F.2}$$

and similarly for the y-axis. If we select particles such that some of the initial momenta and positions are zero, we can determine the components of $\mathcal{M}_x$ and $\mathcal{M}_y$ by simultaneous equations.

We are then left with the transport matrices $\mathcal{M}_x$ and $\mathcal{M}_y$. The phase advances μ_i for each axis $i \in x, y$ can be obtained using:

$$\cos(\mu_i) = \frac{\mathcal{M}_{i,11} + \mathcal{M}_{i,22}}{2} \tag{F.3}$$

and then the β, γ and α Twiss parameters can be obtained with:

$$\beta_i = \frac{\mathcal{M}_{i,12}}{\sin(\mu_i)}, \qquad \gamma_i = -\frac{\mathcal{M}_{i,21}}{\sin(\mu_i)}, \qquad \alpha_i = \frac{\mathcal{M}_{i,11} - \cos(\mu_i)}{\sin(\mu_i)}, \tag{F.4}$$

for $i \in x, y$. It is noted that tracking more particles and taking the average provides more accurate results, given the particles are very close to the design trajectory.

Appendix G

Expansion of Curvilinear Multipole Potential Skew Components

We wish to expand the potential for even multipole components only, for which we shall determine an expression.

Using (3.10) for $m = 2$, we obtain:

$$\begin{aligned}
\psi_{m=2}(x=0) &= -\rho^2 \frac{b_2}{2} \left(\begin{pmatrix} 2 \\ 0 \end{pmatrix} \sum_{n=0}^{1} \beta_{m-2p,n} + (i\tilde{y})^2 \begin{pmatrix} 2 \\ 2 \end{pmatrix} \beta_{0,0} \right) \\
&= -\rho^2 \frac{b_2}{2} \left(\sum_{n=0}^{1} \beta_{m-2p,n} + (i\tilde{y})^2 \beta_{0,0} \right) \\
&= -\rho^2 \frac{b_2}{2} \left(\beta_{2,0} + \beta_{2,1} - \tilde{y}^2 \right) \\
&= -\rho^2 \frac{b_2}{2} \left(2\frac{\alpha_{0,0} - \beta_{0,0}}{4} + 2\frac{\beta_{0,0} - \alpha_{0,0}}{4} - \tilde{y}^2 \right) \\
&= \frac{b_2}{2} \rho^2 \tilde{y}^2 \quad \text{(G.1)}
\end{aligned}$$

where we used (3.6) and (3.7) to find $\beta_{2,0}$ and $\beta_{2,1}$.

For the $m = 4$ term, we obtain:

$$\psi_{m=4}(x=0) = -\rho^4 \frac{b_4}{4}\Bigg(\begin{pmatrix} 4 \\ 0 \end{pmatrix} \sum_{n=0}^{2} \beta_{m-2p,n} - \tilde{y}^2 \begin{pmatrix} 4 \\ 2 \end{pmatrix} \sum_{n=0}^{1} \beta_{m-2p,n} + \tilde{y}^4 \begin{pmatrix} 4 \\ 4 \end{pmatrix} \beta_{0,0} \Bigg)$$

$$= -\rho^4 \frac{b_4}{4} \left((\beta_{4,0} + \beta_{4,1} + \beta_{4,2}) - \tilde{y}^2 6 (\beta_{2,0} + \beta_{2,1}) + \tilde{y}^4 \beta_{0,0} \right)$$

$$= -\rho^4 \frac{b_4}{4}\Bigg(12 \left(\frac{\alpha_{2,0} - \beta_{2,0}}{4} + \frac{\alpha_{2,1} - 2\beta_{2,1}}{32} + \frac{\beta_{2,0} - \alpha_{2,0}}{4} + \frac{2\beta_{2,1} - \alpha_{2,1}}{32} \right) - \tilde{y}^2 12 \left(\frac{\alpha_{0,0} - \beta_{0,0}}{4} + \frac{\beta_{0,0} - \alpha_{0,0}}{4} \right) + \tilde{y}^4 \Bigg)$$

$$= -\frac{b_4}{4} \rho^4 \tilde{y}^4. \quad \text{(G.2)}$$

Indeed, as is evident from [36], when one uses $x = 0$, the even normal component coefficients become:

$$\psi_m(x=1) = (-1)^{\frac{m}{2}+1} \frac{b_m}{m} \rho^m \tilde{y}^m = (-1)^{\frac{m}{2}+1} \frac{b_m}{m} y^m \qquad \text{for even } m. \quad \text{(G.3)}$$

Appendix H

Toroidal Multipole Derivations and Fitting

H.1 Coordinate Reverse Derivation

$$X = (\rho + x)\cos(\Theta) = \rho\frac{\sinh(u)\cos(\Theta)}{\cosh(u) - \cos(v)} \tag{H.1}$$

$$Y = (\rho + x)\sin(\Theta) = \rho\frac{\sinh(u)\sin(\Theta)}{\cosh(u) - \cos(v)} \tag{H.2}$$

$$Z = y = \rho\frac{\sin(v)}{\cosh(u) - \cos(v)} \tag{H.3}$$

from which we can combine the first two expressions to form:

$$\Theta = \arctan\left(\frac{Y}{X}\right). \tag{H.4}$$

Now, we define the distances d_1 and d_2 to the "foci", which are the two locations where the beam axis intersects the plane of current Θ. Focal point d_2 is on the opposite side of the ring from the point studied, whereas d_1 is on the same side of the ring, so we have:

$$d_1^2 = x^2 + y^2, \tag{H.5}$$

$$d_2^2 = (2\rho + x)^2 + y^2. \tag{H.6}$$

With these, the geometric definitions of u and v are [87]:

$$u = \log\left(\frac{d_2}{d_1}\right) = \frac{1}{2}\log\left(\frac{(2\rho + x)^2 + y^2}{x^2 + y^2}\right) \tag{H.7}$$

and

$$v = \arccos\left(\frac{d_1^2 + d_2^2 - (2\rho)^2}{2d_1 d_2}\right) = \arccos\left(\frac{x^2 + y^2 + (2\rho + x)^2 + y^2 - 4\rho^2}{2\sqrt{(x^2 + y^2)((2\rho + x)^2 + y^2)}}\right)$$
$$= \arccos\left(\frac{x^2 + y^2 + 2\rho x}{\sqrt{(x^2 + y^2)\big((2\rho + x)^2 + y^2\big)}}\right)$$
$$= \arccos\left(\frac{r^2 + 4\rho x}{r\sqrt{r^2 + 4\rho x + 4\rho^2}}\right) \tag{H.8}$$

where the definition of v comes from use of the cosine rule to determine the angle between d_1 and d_2 from the point studied.

H.2 Laplacian

The Laplacian in toroidal coordinates can be expressed as [65]:

$$\Delta\psi = 0 = \frac{\big(\cos(v) - \cosh(u)\big)^3}{\sinh(u)}\left[\frac{\partial}{\partial v}\left(\frac{\sinh(u)}{\cosh(u) - \cos(v)}\frac{\partial}{\partial v}\right)\right.$$
$$\left. + \frac{\partial}{\partial u}\left(\frac{\sinh(u)}{\cosh(u) - \cos(v)}\frac{\partial}{\partial u}\right) + \frac{\partial}{\partial \Theta}\left(\frac{1}{\sinh(u)\big(\cosh(u) - \cos(v)\big)}\frac{\partial}{\partial \Theta}\right)\right]\psi. \tag{H.9}$$

H.3 Associated Legendre Polynomial Symmetry in n

WolframAlpha [69] was used to query the values of:

$$P^m_{n-1/2}(z) - P^m_{-n-1/2}(z) \tag{H.10}$$

for incrementing values of $m \leq 0$. The results all returned zero, for $|m| \leq 6$ and $n \leq 6$ (or for all n in the case of $m = 0$, as in Figure H.2). For $m \neq 0$ the values of n had to be evaluated separately (as in Figure H.1), so the general case could not be fully verified. However, this provides evidence strong enough to be confident that replacing n with $-n$ returns the same result.

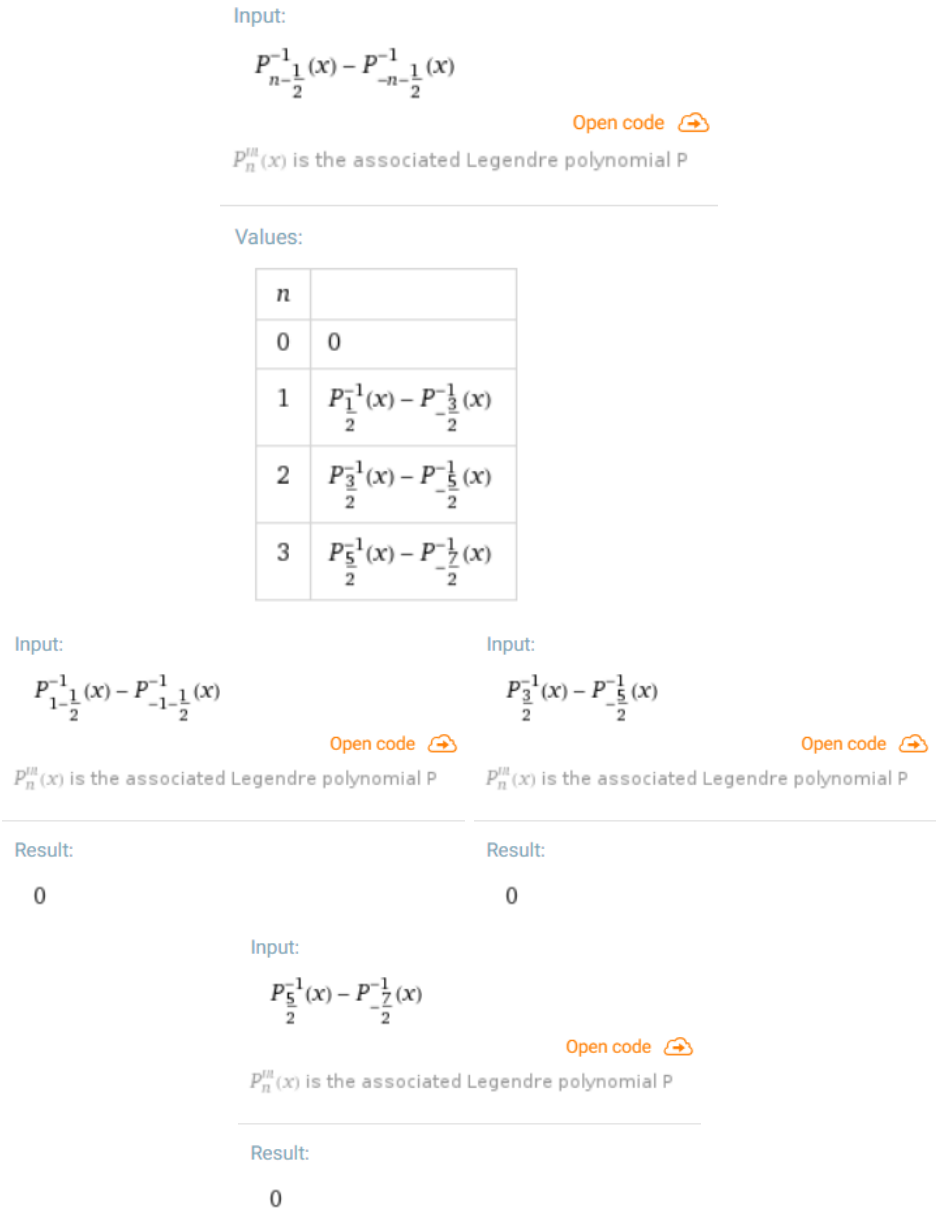

Figure H.1: Results from WolframAlpha [69] showing that the Associated Legendre polynomial is unchanged for $n \to -n$ in the case of $m = -1$, for $n = 0, 1, 2, 3$.

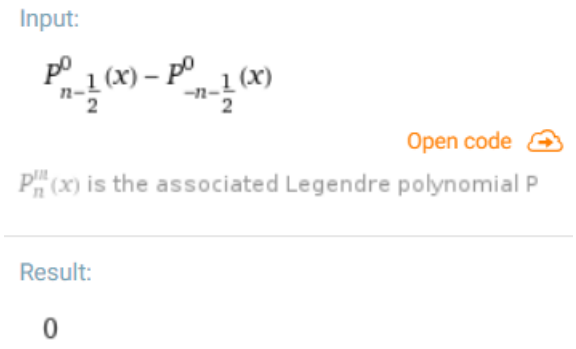

Figure H.2: Result from WolframAlpha [69] showing that the Associated Legendre polynomial is unchanged for $n \to -n$ in the case of $m = 0$.

H.4 Symmetry in Toroidal Multipole Coefficients

We wish to find the relationship between $f_{n,m}$ for where n and/or m change sign. To do this, we can try to use the definition for $f_{n,m}$ in (3.86) wherein we only look at the integral (as the factor of $\tilde{P}$ only changes the overall sign):

$$\int_0^{2\pi}\int_0^{2\pi} \psi(u_0, v, \Theta)\frac{e^{-imv}e^{-in\Theta}dvd\Theta}{\sqrt{\cosh(u_0)-\cos(v)}}. \tag{H.11}$$

However, decomposing the complex exponents in to sines and cosines reveals that changing the sign of n or m leads to some non-trivial results:

$$\begin{aligned} e^{-imv}e^{-in\Theta} = &\Big(\cos(mv)\cos(n\Theta) - \sin(mv)\sin(n\Theta)\Big) \\ &+ i\Big(-\cos(mv)\sin(n\Theta) - \sin(mv)\cos(n\Theta)\Big). \end{aligned} \tag{H.12}$$

Due to this difficulty, coefficients were calculated for both positive and negative m and n to fit to the Fermilab Muon $g-2$ Electrostatic Quadrupoles. The resulting coefficients exhibited the following symmetries between different signs of m and n:

$$f_{n,m} = -f^*_{-n,-m} = -f_{n,-m} = f^*_{-n,m}, \tag{H.13}$$

which are used to simplify the calculations in Section 3.3 and, ultimately, to increase the speed of field calculations in the simulations.

H.5 Derivation of E_y

The equation for E_y can be derived from ψ in (3.91) as:

$$\begin{aligned} E_y = -\frac{\partial \psi}{\partial y} &= \sum_{n=-\infty}^{\infty} \sum_{m=-\infty}^{\infty} -A_{n,m}\, \mathbb{R}\mathrm{e}\left(f_{n,m} e^{in\theta}\right) \sqrt{\frac{\rho}{\rho + x}} \\ &\quad \times \left(\left(\frac{\partial u}{\partial y} \frac{\partial}{\partial u} \tilde{P}^m_{n-\frac{1}{2}} \right) \cos(mv) + \tilde{P}^m_{n-\frac{1}{2}} \left(\frac{\partial v}{\partial y} \frac{\partial}{\partial v} \cos(mv) \right) \right) \\ &= \sum_{n=-\infty}^{\infty} \sum_{m=-\infty}^{\infty} -A_{n,m}\, \mathbb{R}\mathrm{e}\left(f_{n,m} e^{in\theta}\right) \sqrt{\frac{\rho}{\rho + x}} \Bigg(- \tilde{P}^m_{n-\frac{1}{2}} \frac{\partial v}{\partial y} m \sin(mv) \\ &\qquad + \frac{\partial u}{\partial y} \left(\frac{n + \frac{1}{2}}{\tanh(u)} \tilde{P}^m_{n-\frac{1}{2}} - \left(m + n + \tfrac{1}{2}\right) \tilde{P}^m_{n+\frac{1}{2}} \right) \cos(mv) \Bigg). \end{aligned} \tag{H.14}$$

Again, substituting the derivatives from (3.78) and (3.79), we get:

$$\begin{aligned} E_y &= \sum_{n=-\infty}^{\infty} \sum_{m=-\infty}^{\infty} A_{n,m}\, \mathbb{R}\mathrm{e}\left(f_{n,m} e^{in\theta}\right) \sqrt{\frac{\rho}{\rho + x}} \\ &\quad \times \Bigg(\frac{\sinh(u)\sin(v)}{R} \left(\frac{n + \frac{1}{2}}{\tanh(u)} \tilde{P}^m_{n-\frac{1}{2}} - \left(m + n + \tfrac{1}{2}\right) \tilde{P}^m_{n+\frac{1}{2}} \right) \cos(mv) \\ &\qquad - \tilde{P}^m_{n-\frac{1}{2}} \frac{m}{R} \big(1 - \cosh(u)\cos(v)\big) \sin(mv) \Bigg), \end{aligned} \tag{H.15}$$

which can be re-written as:

$$
\begin{aligned}
E_y = & \sum_{n=-\infty}^{\infty} \sum_{m=-\infty}^{\infty} A_{n,m}\, \mathbb{R}\mathrm{e}\left(f_{n,m} e^{in\theta}\right) \sqrt{\frac{\rho}{\rho + x}} \\
\times & \left(\left(\frac{\sinh(u)\sin(v)}{R\tanh(u)} (n + \tfrac{1}{2}) \cos(mv) - m \frac{1 - \cosh(u)\cos(v)}{R} \sin(mv) \right) \tilde{P}^m_{n-\frac{1}{2}} \right. \\
& \left. - \frac{\sinh(u)\sin(v)}{R} \left(m + n + \tfrac{1}{2}\right) \cos(mv) \tilde{P}^m_{n+\frac{1}{2}} \right) \\
= & \sum_{n=-\infty}^{\infty} \sum_{m=-\infty}^{\infty} \frac{A_{n,m}}{2} \big(\mathbb{R}\mathrm{e}\left(f_{n,m}\right) \cos(n\theta) - \mathbb{I}\mathrm{m}\left(f_{n,m}\right) \sin(n\theta) \big) B \\
& \times \left(\Big(J(2n+1)\cos(mv) - 2mG\sin(mv) \Big) \tilde{P}^m_{n-\frac{1}{2}} \right. \\
& \left. - F\left(2m + 2n + 1\right) \cos(mv) \tilde{P}^m_{n+\frac{1}{2}} \right) \qquad \text{(H.16)}
\end{aligned}
$$

H.6 Coefficients from Fringe Fit

Table H.1: Coefficients $\mathbb{R}\mathrm{e}\,(f_{n,m})$ for the toroidal multipole fringe description of the electrostatic quadrupoles in Section 3.3. Columns are longitudinal mode number n, rows are transverse order m. See Table H.3 for factors to apply.

	0	1	2	3	4	5	6	7	8
0	-1472	-7493	340	2107	2188	51	179	-27	100
1	1062	79	264	-119	229	-23	-17	3	-3
2	-1968	929	1457	-29	1004	66	1330	-1098	-651
3	-3541	-2620	1648	-231	-1513	-419	-59	145	-60
4	-1500	-2434	-5284	728	-1032	-41	69	259	312
5	-2655	-1576	1910	-2132	3883	-946	-879	-75	-152
6	-2145	473	124	788	425	-215	212	828	-1966
7	3975	1360	284	-753	603	280	-392	311	705
8	1086	-376	383	-137	-123	92	-12	-66	94
9	-5646	2560	1331	-379	183	447	-77	-469	375
10	6568	-6455	723	-2601	5415	1220	-1187	2120	-4316
11	1192	-168	-195	151	-10	-18	-177	-66	125
12	-5912	1407	1169	-682	296	652	1108	255	-551
13	1597	-241	-236	412	126	29	73	-58	253
14	3188	-1128	-965	646	275	-440	-343	62	615

Table H.2: Coefficients $\mathbb{I}\mathrm{m}\,(f_{n,m})$ for the toroidal multipole fringe description of the electrostatic quadrupoles in Section 3.3. Columns are longitudinal mode number n, rows are transverse order m. See Table H.3 for factors to apply.

	0	1	2	3	4	5	6	7	8
0	1631	1181	71	-352	-121	55	36	-7	-9
1	3597	-1692	-996	408	431	-76	-180	15	61
2	1081	-240	-190	45	64	-9	-21	2	7
3	7738	-2124	-1570	544	728	-190	-309	43	139
4	-4843	7512	2411	-3543	-2296	1245	1404	-280	-670
5	-1910	2535	-54	-1248	-399	785	250	-279	-321
6	169	1040	-971	-555	935	289	-703	-153	461
7	2834	7353	-7414	-2817	5625	2037	-4886	-348	2561
8	-1326	-8435	34	3740	196	-1807	491	559	-483
9	-3133	-283	1884	-995	-487	801	402	-398	-829
10	-3593	989	764	-312	-396	133	224	-59	-125
11	-4174	1024	1044	-364	-614	262	278	-119	-143
12	1873	-318	-327	52	125	7	-76	-9	41
13	1979	1396	-1991	-854	2102	-465	-275	-626	437
14	1014	-302	-196	105	87	-45	-43	21	20

Table H.3: Factors to apply to each row in Table H.1 (real components of $f_{n,m}$) and Table H.2 (complex components of $f_{n,m}$).

m	$\mathbb{R}\mathrm{e}\,(f_{n,m})$ [V]	$\mathbb{I}\mathrm{m}\,(f_{n,m})$ [V]
0	10^{-17}	10^{-1}
1	10^{-13}	10^{0}
2	10^{-10}	10^{6}
3	10^{-8}	10^{6}
4	10^{-5}	10^{9}
5	10^{-2}	10^{11}
6	10^{2}	10^{16}
7	10^{5}	10^{17}
8	10^{9}	10^{21}
9	10^{12}	10^{24}
10	10^{15}	10^{30}
11	10^{20}	10^{32}
12	10^{23}	10^{36}
13	10^{27}	10^{38}
14	10^{30}	10^{44}

H.7 Coefficients from Bulk Fit

Table H.4: Coefficients f_m for the toroidal multipole bulk description of the Fermilab Muon $g-2$ Electrostatic Quadrupoles in Section 3.3.3.

Order m	$\mathbb{R}\mathrm{e}\,(f_m)$ [V]	$\mathbb{I}\mathrm{m}\,(f_m)$ [V]
0	-1.8268×10^{2}	0.0000
1	-8.5087×10^{3}	1.1570
2	-2.2693×10^{9}	4.1218×10^{4}
3	-1.6528×10^{10}	1.9332×10^{7}
4	1.7232×10^{13}	-1.7520×10^{10}
5	7.8927×10^{14}	-2.7916×10^{13}
6	1.9262×10^{19}	-7.0163×10^{15}
7	4.1012×10^{20}	-1.2328×10^{20}
8	-6.2222×10^{24}	5.6903×10^{23}
9	5.0058×10^{27}	4.5551×10^{26}
10	7.5350×10^{33}	2.3280×10^{29}
11	8.5817×10^{35}	-8.7145×10^{33}
12	-3.8487×10^{39}	-2.4275×10^{37}
13	-7.9134×10^{41}	-1.3434×10^{41}
14	-2.1393×10^{47}	-4.2477×10^{44}

H.8 Evaluation of E_x on Design Trajectory

We start with the expression for the potential:

$$\psi = \sum_{n=0}^{\infty}\sum_{m=0}^{\infty} A_{n,m}\sqrt{\frac{\rho}{\rho+x}}\tilde{P}^{m}_{n-\frac{1}{2}}(u)\cos(mv)\,\mathbb{R}\mathrm{e}\left(e^{in\Theta}f_{n,m}\right), \tag{H.17}$$

and set $v = 0$, which is the value for points on the positing x-axis.

We can differentiate the above expression for ψ with respect to x:

$$\begin{aligned} E_x(x=0,y=0) &= -\left.\frac{\partial\psi}{\partial x}\right|_{\substack{x=0\\y=0}} \\ &= -\sum_{n=0}^{\infty}\sum_{m=0}^{\infty} A_{n,m}\,\mathbb{R}\mathrm{e}\left(e^{in\Theta}f_{n,m}\right) \\ &\qquad \times\left(\frac{-1}{2\rho}\left(\frac{\rho}{\rho+x}\right)^{3/2}\tilde{P}^{m}_{n-\frac{1}{2}}(u(x)) + \sqrt{\frac{\rho}{\rho+x}}\frac{\partial}{\partial x}\tilde{P}^{m}_{n-\frac{1}{2}}\big(u(x)\big)\right)\Bigg|_{x=0}. \end{aligned} \tag{H.18}$$

Making use of the identities (3.105) and (3.106), this becomes:

$$\begin{aligned} E_x(0,0) &= -\sum_{n=0}^{\infty}\left(\frac{-1}{2\rho}A_{n,0}\,\mathbb{R}\mathrm{e}\left(e^{in\Theta}f_{n,0}\right) + \frac{1}{2\rho}A_{n,1}\,\mathbb{R}\mathrm{e}\left(e^{in\Theta}f_{n,1}\right)\right), \\ &= \frac{1}{2\rho}\sum_{n=0}^{\infty}\Big(A_{n,0}\,\mathbb{R}\mathrm{e}\left(e^{in\Theta}f_{n,0}\right) - A_{n,1}\,\mathbb{R}\mathrm{e}\left(e^{in\Theta}f_{n,1}\right)\Big). \end{aligned} \tag{H.19}$$

Which is the result for the E_x on the design trajectory, and may also be expressed:

$$\begin{aligned} E_x(0,0) \;= \frac{1}{2\rho}\sum_{n=-\infty}^{\infty}\Bigg(&\Big(A_{n,0}\,\mathbb{R}\mathrm{e}\left(f_{n,0}\right) - A_{n,1}\,\mathbb{R}\mathrm{e}\left(f_{n,1}\right)\Big)\cos(n\Theta) \\ &- \Big(A_{n,0}\,\mathbb{I}\mathrm{m}\left(f_{n,0}\right) - A_{n,1}\,\mathbb{I}\mathrm{m}\left(f_{n,1}\right)\Big)\sin(n\Theta)\Bigg). \end{aligned} \tag{H.20}$$

H.9 Evaluation of E_y on Design Trajectory

We start with the expression for potential in (3.80) (with the square-root term substituted for $\sqrt{\rho/(\rho+x)}$ as in (3.82)):

$$\psi = \sum_{n=-\infty}^{\infty} \sum_{m=-\infty}^{\infty} f_{n,m} \sqrt{\frac{\rho}{\rho+x}} \tilde{P}^m_{n-\frac{1}{2}}(u) e^{imv} e^{in\Theta}. \tag{H.21}$$

We differentiate the above expression for ψ with respect to y:

$$\begin{aligned} E_y(x=0,y=0) &= -\left.\frac{\partial \psi}{\partial y}\right|_{\substack{x=0\\y=0}} \\ &= -\sum_{n=-\infty}^{\infty} \sum_{m=-\infty}^{\infty} e^{in\Theta} f_{n,m} \left(e^{imv} \frac{\partial}{\partial y} \tilde{P}^m_{n-\frac{1}{2}}(u) + \tilde{P}^m_{n-\frac{1}{2}}(u) \frac{\partial}{\partial y} e^{imv} \right)\Bigg|_{y=0} \\ &= -\sum_{n=-\infty}^{\infty} \sum_{m=-\infty}^{\infty} e^{in\Theta} f_{n,m} \left(e^{imv} \frac{\partial}{\partial y} \tilde{P}^m_{n-\frac{1}{2}}(u) + \tilde{P}^m_{n-\frac{1}{2}}(u) ime^{imv} \frac{\partial v}{\partial y} \right)\Bigg|_{y=0}, \end{aligned} \tag{H.22}$$

where we note that, considering (3.105) in the second term, $\tilde{P}$ is only non-zero for $m=0$, so that term disappears:

$$\begin{aligned} E_y(0,0) &= -\sum_{n=-\infty}^{\infty} \sum_{m=-\infty}^{\infty} e^{in\Theta} e^{imv} f_{n,m} \left. \frac{\partial}{\partial y} \tilde{P}^m_{n-\frac{1}{2}}(u) \right|_{y=0}, \\ &= -\sum_{n=0}^{\infty} A_{n,1} e^{in\Theta} f_{n,1} \left. \frac{1}{2\rho} e^{iv} \right|_{y=0}, \end{aligned} \tag{H.23}$$

where we have used the identity in (3.106), reduced the sums (from being from $-\infty$ to being from 0) and introduced the factor $A_{n,m}$ (introduced in Chapter 3) to adjust the coefficients accordingly. We have also taken $m=1$ as the only non-zero set of terms.

We now note that, for y tending towards zero (from the positive direction) with $x=0$, we obtain a value of $v=\pi/2$ from (3.76). This is also clearly visible from Figure 3.5. Using this value yields:

$$\begin{aligned} E_y(0,0) &= -\sum_{n=0}^{\infty} A_{n,1} e^{in\Theta} f_{n,m} \frac{i}{2\rho} \\ &= -\sum_{n=0}^{\infty} A_{n,1} \Big(i\,\mathbb{R}\mathrm{e}\left(f_{n,m}\right) \sin(n\Theta) + i\,\mathbb{I}\mathrm{m}\left(f_{n,m}\right) \cos(n\Theta) \Big) \frac{i}{2\rho}, \end{aligned} \tag{H.24}$$

where we have considered only the components which will produce a real value for the result:

$$E_y(0,0) = \frac{1}{2\rho}\sum_{n=0}^{\infty} A_{n,1}\Big(\,\mathbb{R}\mathrm{e}\,(f_{n,m})\sin(n\Theta) + \mathbb{I}\mathrm{m}\,(f_{n,m})\cos(n\Theta)\Big). \quad \text{(H.25)}$$

H.10 Evaluation of V on Design Trajectory

We start with the expression for potential in (3.80) (with the square-root term substituted for $\sqrt{\rho/(\rho+x)}$ as in (3.82)):

$$\psi = \sum_{n=-\infty}^{\infty}\sum_{m=-\infty}^{\infty} f_{n,m}\sqrt{\frac{\rho}{\rho+x}}\tilde{P}^m_{n-\frac{1}{2}}(u)e^{imv}e^{in\Theta}, \quad \text{(H.26)}$$

where the only non-zero terms are where $m = 0$, due to (3.105), for which $\tilde{P} = 1$. We can also note the factor of $\sqrt{\rho/(\rho+x)}$ is one for $x = 0$:

$$\begin{aligned}\psi(x=0,y=0) &= \sum_{n=-\infty}^{\infty} f_{n,0}e^{in\Theta} \\ &= \sum_{n=0}^{\infty} A_{n,0}\Big(\,\mathbb{R}\mathrm{e}\,(f_{n,0})\cos(n\Theta) - \mathbb{I}\mathrm{m}\,(f_{n,0})\sin(n\Theta)\Big), \quad \text{(H.27)}\end{aligned}$$

which is our result.

Appendix I

Alpha Functions for the Storage Ring Model

For the case of uncoupled motion, where particle motions in the x, y and z directions are independent, we can obtain [12]:

$$\alpha = -\frac{1}{2}\frac{d\beta}{ds}. \tag{I.1}$$

Naïvely, we may expect this function to change in one direction within the quadrupoles, and in the other outside, due to the way in which the beta functions change between these regions. In a particular example: as the β_x function tends towards higher values (is concave-up) when inside the quadrupole, we would expect the α_x function to decrease, as it is the negative of the s-derivative.

From the calculated α_x and α_y functions, plotted in Figure I.1 for quadrupole plate potentials of 32 kV, 27.2 kV, 20.2 kV and 15 kV, we see the expectation for α_x confirmed. We also see the opposite behaviour in α_y, which is justified by the opposite argument as for α_x.

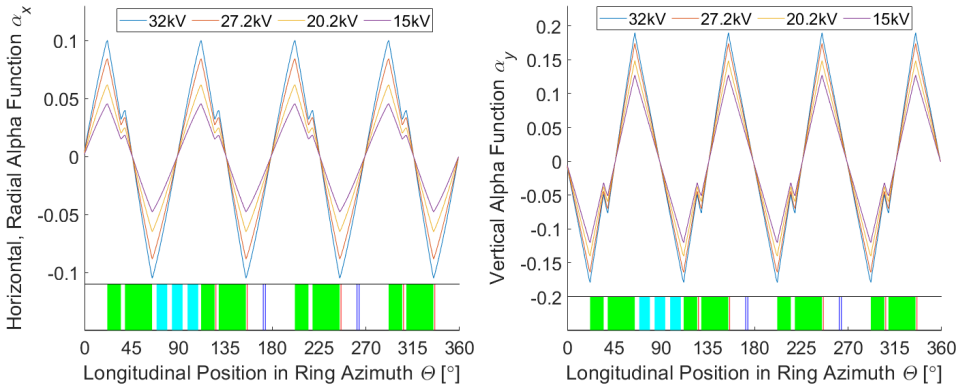

Figure I.1: Twiss alpha functions for the horizontal, radial motion in x (left) and vertical motion in y (right) as calculated for quadrupole plates at 32 kV, 27.2 kV, 20.2 kV and 15 kV. The lattice is shown beneath each plot with quadrupoles (green), kickers (cyan), fibre harps (blue) and collimators (red). Similar to what can be expected from Figure 4.1 and (I.1), α_x and α_y decrease and increase respectively whilst inside the quadrupoles, with the opposite outside the quadrupoles.

Appendix J

Average Quadrupole Plate Spacing

The measured average values of plate position are given in Table J.1 for each plate of each quadrupole.

The values for each plate can then be averaged over the 4 quadrupoles of the same length to give the average plate positions in Table J.2.

Combining the distances from the centroid in to plate separations along x (between inner and outer plates) and y (between the upper and lower plates) leads to the results in Table J.3.

From this, using the relative lengths of each of the short and long quadrupoles (13° and 26° of ring azimuth, respectively), we can calculate the average plate separation around the ring. These results are displayed in Table J.4.

Table J.1: Measured average positions of each plate [88, 89]. Values for inner and outer plates are given as average radial position of each plate. Values for upper and lower plates are given as average deviation in y from their intended location.

Plate	Quoted Position [mm]	Distance from Centroid [mm]	Uncertainty [mm]
Q1Short Inner	7061.58	50.42	0.99
Q1Short Outer	7161.44	49.44	0.99
Q1Short Upper	2.42	52.42	0.75
Q1Short Lower	2.05	47.95	0.75
Q1Long Inner	7061.47	50.53	0.53
Q1Long Outer	7162.04	50.04	0.83
Q1Long Upper	-1.12	48.88	0.75
Q1Long Lower	-0.84	50.84	0.75
Q2Short Inner	7061.30	50.70	0.50
Q2Short Outer	7160.71	48.71	0.70
Q2Short Upper	-0.86	49.14	0.75
Q2Short Lower	-0.49	50.49	0.75
Q2Long Inner	7062.06	49.94	0.58
Q2Long Outer	7161.87	49.87	0.71
Q2Long Upper	0.09	50.09	0.75
Q2Long Lower	0.67	49.33	0.75
Q3Short Inner	7061.60	50.40	0.51
Q3Short Outer	7162.00	50.00	0.81
Q3Short Upper	0.34	50.34	0.75
Q3Short Lower	1.16	48.84	0.75
Q3Long Inner	7062.31	49.69	0.51
Q3Long Outer	7161.92	49.92	0.71
Q3Long Upper	-2.09	47.91	0.75
Q3Long Lower	-1.84	51.84	0.75
Q4Short Inner	7061.61	50.39	0.99
Q4Short Outer	7161.70	49.70	0.99
Q4Short Upper	-1.47	48.53	0.75
Q4Short Lower	-1.16	51.16	0.75
Q4Long Inner	7062.20	49.80	0.67
Q4Long Outer	7161.92	49.97	0.80
Q4Long Upper	0.00	50.00	0.75
Q4Long Lower	-0.44	50.44	0.75

Table J.2: Plate distances from the beam centroid, derived from the measured values in Table J.1 averaged over each quadrupole.

Plates	Average Distance from Centroid [mm]
Short Inner	50.48 ± 0.39
Short Outer	49.46 ± 0.44
Short Upper	50.11 ± 0.75
Short Lower	49.61 ± 0.75
Long Inner	49.99 ± 0.29
Long Outer	49.95 ± 0.38
Long Upper	49.22 ± 0.75
Long Lower	50.61 ± 0.75

Table J.3: Average horizontal apertures (between the inner and outer plates) and vertical apertures (between the upper and lower plates) for the short and long quadrupoles, as calculated from the average plate locations in Table J.2.

Aperture	Average Distance Between Plates [mm]
Short Horizontal Aperture	99.94 ± 0.59
Short Vertical Aperture	99.72 ± 1.06
Long Horizontal Aperture	99.94 ± 0.48
Long Vertical Aperture	99.83 ± 1.06

Table J.4: Overall average horizontal apertures (between the inner and outer plates) and vertical apertures (between the upper and lower plates), as calculated from the average separations for the short and long quadrupoles in Table J.3. The averaging takes in to account the relative length of the short and long quadrupoles (of 13° and 26° of ring azimuth, respectively).

Aperture	Average Distance Between Plates [mm]
Horizontal Aperture	99.9 ± 0.4
Vertical Aperture	99.8 ± 0.8

Appendix K

Injection Angle Fitting

In addition to the fit to $p_y = 0.003$, the experiment data in Chapter 5, Section 5.2 was also scaled in an attempt to fit it to the model data for a vertical injection momentum of $p_y = 0.002$. The best manual fit found is shown in Figure K.1.

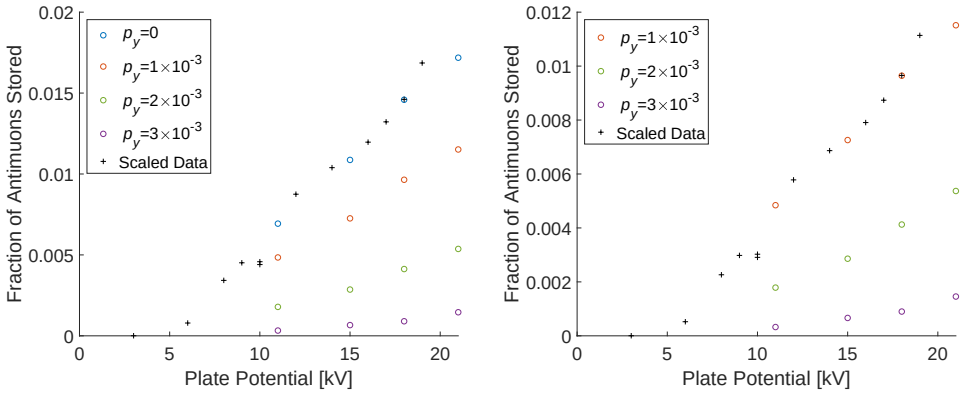

Figure K.1: Stored antimuon fraction after 20 turns as a function of quadrupole plate potential as simulated for a beam injected with vertical momenta p_y of 0 and 0.001, with kicker strength set at 50% of the (near optimal) 270 gauss peak. Also plotted are measured data from the commissioning run with kickers at 75% of their available range (with 100% during the commissioning run known to be below the optimum for injection) [83], scaled manually to best fit both the apparent behaviour (slope) and zero-storage quadrupole potential of the $p_y = 0$ simulation (left) and the $p_y = 0.001$ simulation (right). It was concluded in this study that the agreement was best with the $p_y = 0.003$ simulation.

Appendix L

Ring Component Positions

Component	Length [°]		Pos'n: Ring Azim. [°] (rel. to infl. end)		Pos'n: Radial [m] (rel. to beam)		Pos'n: Vertical [m] (rel. to beam)		Angle: Horizntl [mrad] (rel. to orbit tanjent)		Angle: Verticl [mrad] (rel. to orbit tanjent)	
	Value	Source	Value	Source	Value	Source	Value	Source	Value	Source	Value	Source
Inflector	-		0	By Definition	0.077	Meas[DB#?]	0	TDR	-2.4	Meas[DB#?]	0	TDR
1st Bellows Ctr ("FBC")	-		6.00	Meas[DB#?]	-							
~~Collimator 1~~												
Q1S Plates	13	TDR	21.9	Meas[DB#?]	0	TDR	0	TDR	0	TDR	0	TDR
Q1L Plates	26	TDR	38.9	(=Q1S+13°+4°)	0	TDR	0	TDR	0	TDR	0	TDR
K1 Plates	10.23	Schematic[DB#?]	69.23	Schematic[DB#?]	0	TDR	0	TDR	0	TDR	0	TDR
K2 Plates	10.23	Schematic[DB#?]	83.96	Schematic[DB#?]	0	TDR	0	TDR	0	TDR	0	TDR
K3 Plates	10.23	Schematic[DB#?]	98.90	Schematic[DB#?]	0	TDR	0	TDR	0	TDR	0	TDR
Q2S Plates	13	TDR	111.9	(=Q1S+90°)	0	TDR	0	TDR	0	TDR	0	TDR
Collimator 2	~0.113	Design[DB4399]	126.2	Meas[DB5955]+FBC	0.00013	Meas[DB5955]	-0.00038	Meas[DB5955]	0	TDR	0	TDR
Q2L Plates	26	TDR	128.9	(=Q2S+13°+4°)	0	TDR	0	TDR	0	TDR	0	TDR
Collimator 3	~0.113	Design[DB4399]	156.2	Meas[DB5955]+FBC	0.00008	Meas[DB5955]	-0.00025	Meas[DB5955]	0	TDR	0	TDR
Fiber Harp 180 Y	-		171.60	Meas[DB6728]+FBC	0	TDR	Configurable		0	TDR	Configurable	
Fiber Harp 180 X	-		173.6	Meas[DB6728]+FBC	Configurable		0	TDR	Configurable		0	TDR
~~Collimator 4~~												
Q3S Plates	13	TDR	201.9	(=Q1S+180°)	0	TDR	0	TDR	0	TDR	0	TDR
~~Collimator 5~~												
Q3L Plates	26	TDR	218.9	(=Q3S+13°+4°)	0	TDR	0	TDR	0	TDR	0	TDR
Collimator 6	~0.113	Design[DB4399]	246.2	Meas[DB5955]+FBC	0.00003	Meas[DB5955]	-0.00008	Meas[DB5955]	0	TDR	0	TDR
Trolley Garage?	~4.8	Diagram	~249.6	Diagram	0.15	APPROXIMATE	0	TDR	0	TDR	0	TDR
Fiber Harp 270 Y	-		261.6	Meas[DB6728]+FBC	0	TDR	Configurable		0	TDR	Configurable	
Fiber Harp 270 X	-		263.6	Meas[DB6728]+FBC	Configurable		0	TDR	Configurable		0	TDR
Tracker?	~7.8	Diagram	264.4	Diagram	0.10	Diagram	0	TDR	0	TDR	0	TDR
~~Collimator 7~~												
Q4S Plates	13	TDR	291.9	(=Q1S+270°)	0	TDR	0	TDR	0	TDR	0	TDR
Collimator 8	~0.113	Design[DB4399]	306.2	Meas[DB5955]+FBC	-0.00028	Meas[DB5955]	0.00008	Meas[DB5955]	0	TDR	0	TDR
Q4L Plates	26	TDR	308.9	(=Q4S+13°+4°)	0	TDR	0	TDR	0	TDR	0	TDR
Collimator 9	~0.113	Design[DB4399]	336.2	Meas[DB5955]+FBC	0.00013	Meas[DB5955]	-0.00023	Meas[DB5955]	0	TDR	0	TDR